European Conference on Multifunctional Structures

EMuS 2019

11 – 12 June 2019, Barcelona, Spain

Xavier Martinez and Harmen Schippers (Eds.)

European Conference on Multifunctional Structures

EMuS 2019

Barcelona, Spain
June 11 - 12, 2019

congress.cimne.com/emus2019/

A publication of:

International Centre for Numerical Methods in Engineering (CIMNE)
Barcelona, Spain

ISBN: 978-84-949194-4-2

Printed by: Artes Gráficas Torres S.L., Huelva 9, 08940 Cornellà de Llobregat, Spain

TABLE OF CONTENTS

Preface 7

Supporting Organizations 9

Summary 11

Contents 13

Lectures 15

Authors Index 169

PREFACE

This book contains the full papers accepted for presentation at the European Conference on Multifunctional Structures (EMuS2019), held in Barcelona on June 11-12, 2019.

The main aim of this conference was to share among the scientific and the industrial community the recent advances made on mechanical structures with multiple functions. Recent advances in material technology have improved the additional capacities of such structures in a way in which now, their added functionalities can be as important as their mechanical performance.

At the conference a wide range of papers has been presented about structural systems serving different purposes. The following topics are addressed in the papers:

- Novel multifunctional structures with integrated antennas
- Fuselage panels with active acoustic linings for reduction engine noise
- Multifunctional materials for structural applications
- Structural biocomposites
- Special multifunctional structures with stealth properties
- Manufacturing processes for multifunctional structures
- Simulation and analysis of multifunctional structures

This conference was organized as part of the EU H2020 ACASIAS project. The conference was also supported by ECO-COMPASS Multifunctional Structures experts.

The organizers would like to thank all authors for submitting their contributions, as well as the supporting organizations for their help in making EMuS2019 possible

This conference is partly funded from European Union's Horizon 2020 research and innovation programme under grant agreement No 723167.

Supporting Organizations

The EMuS 2019 is partially financed and supported by the ACASIAS project (www.acasias-project.eu) ECO-COMPASS project (http://www.eco-compass.eu), also support EMuS 2019 with conference materials.

EMUS 2019 is organized by the ACASIAS partner CIMNE (International Centre for Numerical Methods in Engineering Barcelona), in cooperation with ACASIAS coordinator NLR (Netherlands Aerospace Centre, Amsterdam) and ACASIAS partner L-Up (Consultancy in European and national public funding, Paris).

Advanced Concept for Aero-Structures with Integrated Antennas and Sensors (ACASIAS)

International Center for Numerical Methods in Engineering (CIMNE)

Netherlands Aerospace Center (NLR)

L-UP

ECO-COMPASS Project

TRACKWISE

CONTENTS

Active Acoustic Panels **17**
Aircraft with conformal anntennas **38**
Composite Panels with integrated antenna tiles **54**
Eco-composite Structures **75**
Fibre-Metal Laminate Panels with integrated antennas **102**
Multifunctional Materials **114**
Technology for integrated antenna tiles **147**
Winglet with integrated VHF antenna **153**

CONTENTS

Active Acoustic Panels

Manufacturing aspects of active acoustic lining panel.....17
K. Gonet, S. Steeger, S. Algermissen and V. Lungaho

Remote Sensing for a Lining Integrated Active Structural Acoustic Control System.....24
M. Misol and S. Algermissen

Towards a Lining Integrated Active Structural Acoustic Control System.....30
S. Algermissen, M. Misol, A. Kokott, T. Haase, K. Gonet and V. Lungaho

Aircraft with conformal anntennas

Contribution of conformal antennas towards sustainable aircraft.....38
P. Vrchota, A. Prachař, M. Šmíd and J. Middel

Design Consideration for Fully Embedded Electronically Steerable SATCOM Airborne Antenna.....48
G. Expósito, J. M. Abellán, A. E. Jiménez, F. Martín, J. Menéndez, F. Cano, F. J. Jiménez and A. Gal

Composite Panels with integrated antenna tiles

Automated manufacture of grid stiffened panels.....54
J.M. Müller and P. Nijhuis

Structural Analyses of Orthogrid Fuselage Panel for Integrated Ku-band SatCom Antenna......62
F. Turon, F. Otero and X. Martinez

Structural Integration of a Ku-band SATCOM antenna into novel Fuselage Panel.....68
J. Verpoorte and A. Hulzinga

Eco-composite Structures

Application and evaluation of density measurement methods for measuring flax-epoxy polymer composite density.....75
Y. Saadati, J-F. Chatelain, G. Lebrun and Y. Beauchamp

Electrical Conductivity and Electromagnetic Shielding Effectiveness of Bio-Composites.....81
K. Tserpes, V. Tzatzadakis and J. Bachmann

Functionalization of carbon nanotubes and mechanical characterisation of bio-based epoxy nano-composites.....90
A. Singh, C. Sguazzo, C.F.R.A.C. Lima, L.M.N.B.F. Santos, P.J.S. Tavares and P.M.G.P. Moreira

The ECO-COMPASS EU-China Project 96
J. Bachmann and X. Yi

Fibre-Metal Laminate Panels with integrated antennas

Integrating electromagnetic functions into Fiber Metal Laminates - the structural challenge 102
C. van Hengel, C. Heuts and J. Verpoorte

Radiating Aerostructures 108
Y. Konter, C. Heuts and C. van Hengel

Multifunctional Materials

Analysis of Radar Absorbing FSS on foldcores and honeycombs 114
J.J.P. van Es, A. Hulzinga, P. Tensen, H. Schippers, R.M.H. Heijmans and M.J.G. Journee

Development of multifunctional materials and structures with improved capacities in aerodynamics, icing, acoustics or electromagnetism for civil and military aircrafts 122
B. Berton

New Enhanced Acoustic Damping Composite Material for the Aeronautics Industry 132
D. Pastorino, J. Di Lorenzo, B. López-Romano, P. Hadley and T. Blanco

Textile-Integrated Transmitting Unit 142
M. Cupal, J. Dřínovský, T. Götthans, J. Láčík, J. Prášek, Z. Raida, D. Kráčalová, Z. Ledrová, J. Procházka and D. Krutílek

Technology for integrated antenna tiles

Cooling of Active Components in Structurally Integrated Phased Arrays Antennas 147
J. Leiß, T. Ebert, M. Martínez-Vázquez and R. Baggen

Winglet with integrated VHF antenna

From design towards manufacturing of winglets with integrated VHF antenna 153
K. Gonet, S. Steeger, M. Martínez-Vázquez , J. Balcells-Ventura, P. Vrchota, Z. Řezníček and V. Lungaho

Towards Multi-objective Design of EV55 Winglet with integrated VHF antennas 162
Z. Řezníček, S. Steeger, K. Gonnet, M. Martínez-Vázquez , J. Balcells-Ventura, P. Vrchota and V. Lungaho

LECTURES

Manufacturing aspects of active acoustic lining panel EMUS 2019

KAI GONET[*], STEFAN STEEGER[*], STEPHAN ALGERMISSEN [†], VICTOR LUNGAHO [††]

[*]INVENT GmbH
38112 Braunschweig, Germany
e-mail: kai.gonet@invent-gmbh.de, web page: http://www.invent-gmbh.de

[†] Deutsches Zentrum für Luft- und Raumfahrt
38108 Braunschweig
e-mail: stephan.algermissen@dlr.de, web page: http://www.dlr.de

[††] Trackwise
Gloucestershire GL20 8NB
United Kingdom
e-mail: victor.lungaho@trackwise.co.uk - web page: www.trackwise.co.uk

Key words: Interior Design, Aviation Engineering, Noise Reduction

Abstract. This paper shows the technical aspects and the progress of manufacturing a lining concept with actuators and sensors for noise reduction within the cabin of aircraft with CROR engine. The structural integration, the repair possibilities and the serial production of such a lining are focused.

1 INTRODUCTION

One of the possibilities of reducing exhaust gases and fuel consumption are new propulsion concepts in the transport sector. Even in aviation it does not stop for engineering efforts to break new ground. Unfortunately, some of the new concepts offer the desired improvement, but with unwanted side effects for pilots and/or passengers.

One of these examples for a new fuel saving concept are counter rotating open rotors (CROR). This engine concept has one negative side effect. The engines with the two propellers generate unpleasant vibrations and noise for passengers in a frequency band of 500Hz. These vibrations are transmitted by the complex vortex of the propellers from the engine nacelles through the structure right into the cabin, affecting the passengers.

Within the EU project ACASIAS an active structural acoustic control system (ASAC) is being integrated within a lining of an aircraft. The task of the active fairing structure is to detect the vibrations and to eliminate these with oscillations.

Some of the mayor issues like structural integration, repair and maintenance is being presented in this paper.

Figure 1: Closer look to an engine with counter-rotating propellers. Aircraft AN-70 (taken from internet picture research [2])

2 CURRENT PRODUCTION PROCESS

In order to realize this concept of a new lining and to be able to manufacture it for test purposes according to a real environment, it is necessary to analyze an inventory of the current production methods of these parts. State of the art for production such a lining is realized with presses.

In the manufacturing process, a layer of phenolic resin impregnated glass fabric (GFRP) is pressed onto a paper honeycomb. The prepreg, which will later be inside the aircraft, is very finely meshed and is painted in a separate working process according to customers order. The outer fabric layer is very roughly woven fabric and remains untreated. The two fabric layers are pressed at high temperature (approx. 170°C) and high pressure (approx. 12bar) onto the paper honeycomb to form a sandwich panel. Since this process involves pressing at a preset distance, the honeycomb remains largely intact. The honeycomb is only pressed together in areas where greater strength is required (e.g. at the fastening points). In this area compressed honeycomb in combination with the GFRP is referred to as a "crushed core" process. The entire hardening process is called HIHO (hot in, hot out).

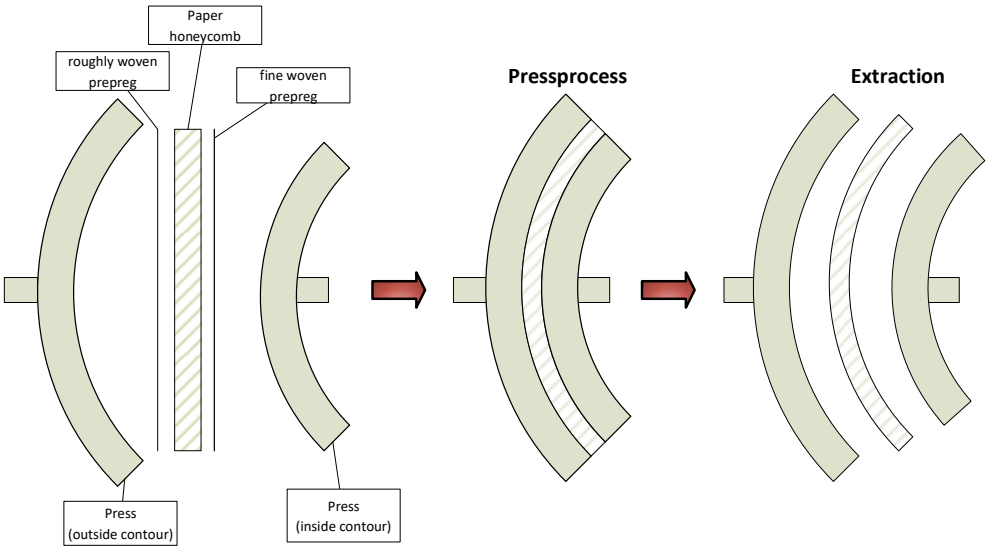

Figure 2: State of the art manufacturing process of aircraft interior lining panels.

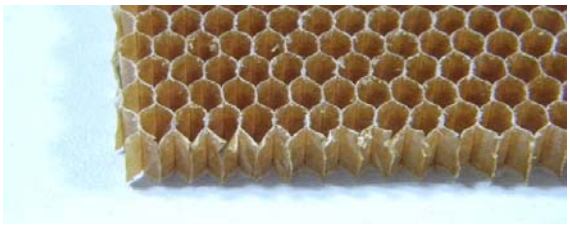

Figure 3: paper honeycomb. 6,5mm thickness. Can be used as a sandwich core, healthy or crushed

3 STRUCTURAL INTEGRATION

The aim of this project is to produce an active lining that reduces noise inside the cabin. This requires both: sensors and actuators. The vibrations must be transmitted directly from the lining to the sensors. The signals from the sensor array are then transmitted to the control unit. This signal will be analyzed. As response to these vibrations the actuators will be activated in the corresponding bandwith. The forces of the actuators have to be transduced into the structure of the lining. As with any industrial application, installation should be simple. The manufacturing processes should not deviate too much from the current work steps. In addition, the devices must be protected from dirt and moisture.

In order to have a fast repair possibility and to be able to flexibly design the positions of the sensors/actuators, a concept with inserts is pursued at ACASIAS. The inserts consist of plastic holders that form the housing for the needed devices. They also include the electrical connection to the control unit. For the test samples of the real linings the inserts are glued in pre-pressed slots inside the lining. The force transmission in both integration types is friction-locked. Stamps corresponding to the size of the inserts are incorporated into the paper honeycomb sandwich structure. These are additionally reinforced on the outside with fine glass fabric prepregs. Later, in an industrial application, the inserts can be integrated into the lining during the press process.

The connection between the devices and the lining is realized on the outside of the lining. There they are virtually invisible to the passenger.

In ACASIAS the array of sensors and actuators consists of 4 actuators and 6 sensors each. The size of the lining itself is about 1.3m x 1.7m. After the production of this test sample at INVENT, the whole device is ready for tests at the DLR.

4 PRODUCTION OF A LINING WITH INSERTS

As mentioned, a lining is normally produced in a pressing cycle. For this purpose, the moulds that later form the contour of the lining are heated to the curing temperature of the resin. The materials are placed in the mould and pressed together with the paper honeycomb to form a lining. In this pressing process, the connections and screwing points can also be placed in the mould and then bonded in the same curing process.

Unfortunately, this is not possible within the scope of this research project. Creating new moulds with heating would be beyond the budget. Therefore, we have to validate the curing as well as the shaping for small quantities by alternative processes.

The first tests for gluing and handling such an insert were performed on a press with a straight plate. Different stamp shapes were tested. However, the round shape quickly proved

to be the best form-fit variant. Reinforcements with finely woven prepreg fabric in this area supports connection to the sandwich structure of the lining for better force transmission (form factor).

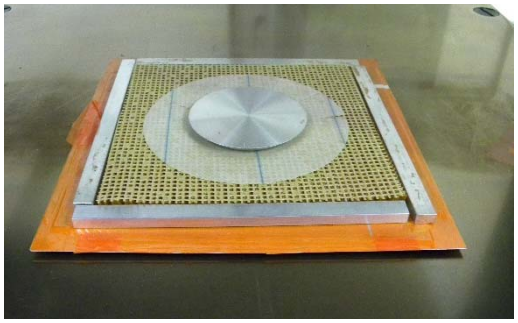

Figure 4: Test sample on a press with preset distance before curing

Figure 5: Test sample after curing with a bonded insert

Within this research project, however, no original molds can be used. Therefore, care is taken of other manufacturing processes. However, these should definitely be very close to the real lining structure. In other words, the product should have a realistic structure.

In the manufacturing process a mould is built which corresponds to the curvature of a lining. A comparative lining is available. Based on the design data, a positive mold is milled from an epoxy reinforced PU foam. This mould reproduces the inside of the lining (passenger side). The fine glass fiber prepreg is placed on this mold. The paper honeycomb cut to size forms the core of the sandwich. The coarse-meshed fabric is used to form the outer layer of the lining. There, the reinforcements for the inserts are placed at the points determined by DLR and the slots for the crush core are positioned.

Since the original press moulds cannot be used within the context of the project, a suitable hardening process with suitable contact pressures must be found. In the manufacturing process, the mould halves are pressed to distance with 17 bar pressure. Available infrastructure only allows for a manufacturing process in an autoclave with a vacuum setup, like in Figure 6. The pressure inside the autoclave must not be too high, because the paper honeycomb must not be damaged under the pressure. But the pressure must be large enough so that the stamps for the deepening of the inserts can be crushed.

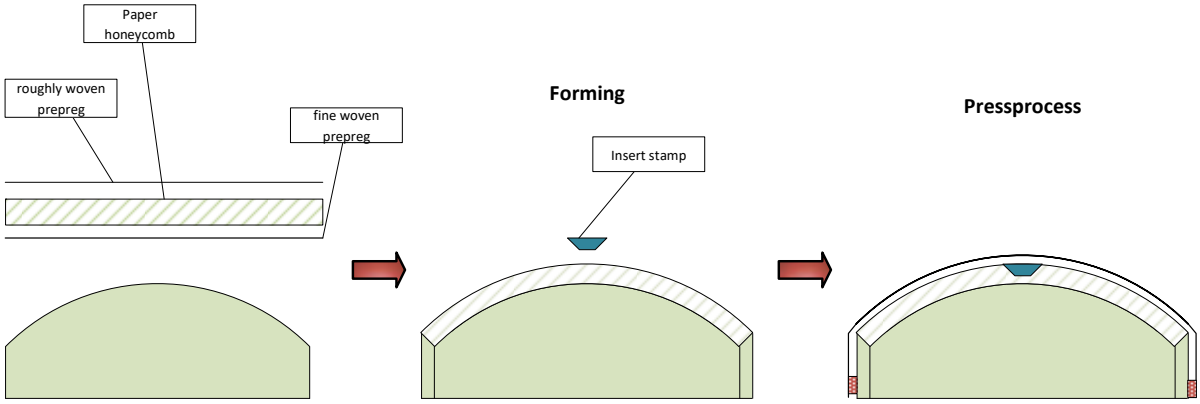

Figure 6: Alternatively curing process and the stamps within the vacuum buildup

First, a material had to be found that was easy to mill, resistant to pressure and that could retain its shape at high temperatures, to be seen at Figure 7. We achieved the best results with an epoxy reinforced PU foam.

Figure 7: Test samples to verify if the PU foam can be induced with high temperature and pressure. These samples were tested at 160°C with 2 bar. The material on the left side failed, the other material passed the test

Another challenge for this alternative hardening process was the setting of the correct pressure or the choice of the correct top layer of the sandwich construction. If a too high pressure in the autoclave is chosen, a compression of the sandwich construction and loss of the part would be a result.

Since the pressure must not be as high as in closed moulds in press production, the areas for the stamps of the inserts must be able to be crushed (pre-damaged). The relatively low pressure compared to the industry standard must still be able to push the stamps into the sandwich construction. Therefore, the paper honeycomb must be pre-damaged. There are two ways to do this:

1. a hole is cut in the intact paper honeycomb where the stamp for production will later also be located. in a separate step, an additional honeycomb piece is pre-damaged (pre-crushed) in a press. The filling piece corresponding to the hole in the paper honeycomb is then cut out of this pre-damaged piece of paper honeycomb and prepared into the intact lining. Figure 8.
2. The cut-out paper honeycomb is machined with a milling cutter at the places for the inserts and material is removed at these places. This does not correspond later to the material

density of a crushed core, but the bond of the paper honeycomb is not so severly damaged and the force distribution within the honeycomb is not interrupted.

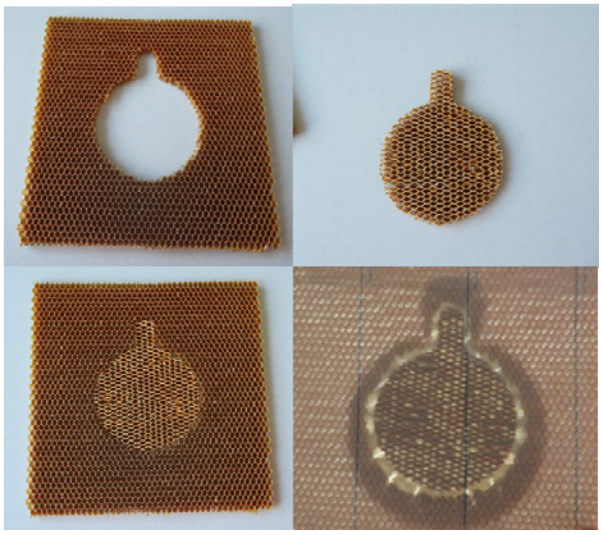

Figure 8: Precutted core, precutted and predamaged inlet for the insert, combined cut outs, pressed and glued sample with interrupted force distribution within the honeycomb

5 REPAIR POSSIBILITES

Due to the fact that the inserts are glued in and the actuators/sensors are connected in these inserts, a necessary repair can be carried out relatively quickly, when necessary. The housing of the components not only protects these devices, they also allow quick access for replacement. Cosmetic repairs to the passenger side are not necessary.

6 MANUFACTURING INTEGRATION

Many of the results presented here can be significantly simplified in the production with presses. In serial production, the inserts described here can be bonded in place during the pressing process using a backdrop. This would require only minor changes to one of the two forms.

7 CONCLUSION AND OUTLOOK

It has been shown that a lining with an array of sensors and actuators can also be produced in small quantities for test purposes. The technical challenges and their solutions have been demonstrated. A manufacturing process as alternative to heated press manufacturing has been developed. With the help of this knowledge, such a lining is produced within the framework of the ACASIAS project and the possibilities of noise reduction are tested in a special sound chamber.

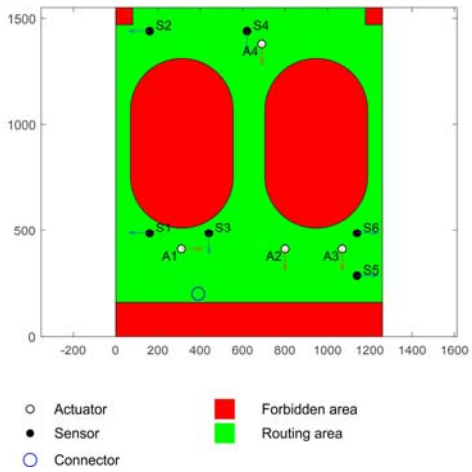

Figure 10: Array of sensors and actuators for the final test sample, view from the pax side

8 ACKNOWLEDGEMENTS

All work described in this paper has received funding from the European Union's Horizon 2020 research and innovation programme under grant agreement No 723167, ACASIAS project.
DIEHL, as an industrial partner for this project, supported us with material such as prepregs and paper honeycomb.

REFERENCES

[1] NOISE-CON 2017, Grand Rapids, MI, 2017 June 12-14, Active Control of Vibrations Using an Audio Signal Processor, Stephan Algermissen, Hans Peter Monner, Institute of Composite Structures and Adaptive Systems, German Aerospace Systems (DLR), Braunschweig

[2] https://wordlesstech.com/revolutionary-airplane-propeller-action/

[3] Stephan Algermissen, et al, "Towards a Lining Integrated Active Structural Acoustic Control System", paper EMuS 2019, June 2019

European Conference on Multifunctional Structures
EMuS 2019
X. Martinez and H. Schippers (Eds)

REMOTE SENSING FOR A LINING INTEGRATED ACTIVE STRUCTURAL ACOUSTIC CONTROL SYSTEM

Malte Misol* **AND Stephan Algermissen†**

Institute of Composite Structures and Adaptive Systems
German Aerospace Center (DLR)
Braunschweig, Germany
e-mail: *malte.misol@dlr.de, †stephan.algermissen@dlr.de
web page: http://www.dlr.de/fa/en

Key words: active noise control, aircraft, lining, remote microphone technique

Abstract. In the framework of the EU project ACASIAS an aircraft sidewall panel (lining) with structurally integrated actuators and sensors is developed. Each lining has a digital unit which samples the sensor signals, performs filtering operations and supplies the actuators with control signals. The whole system makes up an active structural acoustic control system aiming at the reduction of low-frequency multi-tonal aircraft interior noise. The novelty of this approach compared to past implementations of active noise control (ANC) systems in aircraft is its modularity. Each so-called smart lining is autonomous in the sense that it processes only structural sensor data from its own integrated sensors. The use of external microphones for error sensing is avoided because this conflicts with the modularity of the smart lining. Hence, one important design task is the replacement of the physical error microphones by the integrated structural sensors and an acoustic filter (observer) running on the digital unit. This method, which is called the remote microphone technique for active control, has never been applied to an aircraft interior structure so far. The detailed design of the smart lining module comprises several steps which are taken within work package 3 of the ACASIAS project. Experimental data of an aircraft typical double panel system is captured in a sound transmission loss facility. The system is excited with a loudspeaker array placed directly in front of the fuselage structure. Different acoustic load cases are used for the definition of the sensors and the actuators. A multi-tonal excitation with high sound pressure level is relevant for the actuator dimensioning and a broadband excitation with multiple independent sound sources is relevant for the sensor definition. 19 accelerometers are mounted on the lining and 20 microphones are placed in front of it. All sensor signals are sampled simultaneously for deterministic and broadband load cases. The lining is equipped with two inertial mass actuators which are used for the active control. Measured frequency response functions of actuators at 39 positions are used for the optimization of the actuator locations. The measurement data is also used for the derivation of an observer and for the simulation of a smart lining with remote microphones. In this contribution, the steps undertaken for the detailed design will be described and simulation results of the noise reduction performance of the smart lining with remote microphones will be presented.

1 INTRODUCTION

The active control of rotor noise in aircraft is an ongoing research topic for more then thirty years. Some of these approaches have been successfully implemented in aircraft (e.g. Saab 2000 or Bombardier Dash 8 Q 400). A common solution uses loudspeakers in the cabin to reduce the interior sound pressure by so-called anti-sound (ANC). Early results of ANC in aircraft are documented by Elliott et al. [1]. An alternative approach is the active structural acoustic control (ASAC) of the fuselage by means of shakers or piezoelectric patch actuators. Early results on ASAC in aircraft are documented by Fuller and Jones [2]. A similar approach for active interior noise reduction uses active trim panels (linings) instead of actuated fuselage structures. Experimental work on aircraft interior noise reduction with active linings is reported by Tran and Mathur [3]. More recent work on this topic is published by Misol et al. [4, 5]. Misol et al. [4] use a serial production Airbus A350 lining augmented with actuators, sensors and an active control system. The experiments are done in a sound transmission loss facility. Full-scale tests in a Dornier Do728 aircraft (on the ground) with two active lining modules are documented in Misol [5]. The acoustic effect of the rotor engines on the fuselage is mimicked by means of a loudspeaker array. A maximum (mean) SPL reduction of 11.3 dB (6.8 dB) is achieved in the Do728 cabin in front of the active linings. All of the mentioned active noise control systems have in common that they use microphones as error sensors. These microphones are distributed all over the cabin which is considered undesirable because it contradicts the approach of a modular so-called smart lining concept. Therefore, the remote microphone technique (RMT) for active control proposed by Roure and Albarrazin [6] is applied to substitute the error microphones. The RMT uses accelerometers on the lining in combination with an observer filter within the controller as suggested by Cheer and Daley [7]. The present contribution focuses on the noise reduction capability of an active lining system using the RMT. Simulations are performed based on measurement data of the Airbus A350 lining system formerly described in Misol et al. [4].

2 EXPERIMENTAL SETUP

Figure 1 shows a scheme of the experimental setup in a sound transmission loss facility. The loudspeaker array (LSA) is placed in front of the fuselage structure with approx. 0.15 m offset. Out of the 112 loudspeakers 72 are used (yellow area). Two different acoustic load cases are considered. First, the lowest five harmonics of a counter rotation open rotor (CROR) engine (119.4 Hz, 149.2 Hz, 268.6 Hz, 388 Hz and 417.9 Hz) are synthesized (see Algermissen et al. [8]) and second, all 72 loudspeakers are controlled with uncorrelated bandlimited white noise signals. The test specimen consisting of a carbon fiber reinforced plastics (CFRP) fuselage structure and a coupled lining is mounted in the test opening of the facility. Figure 2 shows the experimental setup seen from the semi-anechoic room. From a total of 19 accelerometers, 16 are selected as potential remote sensors for the RMT (the discarded ones are marked with an X). Although 35 out of 39 different actuator positions are considered (the discarded ones are marked with an X), the acoustic frequency response function (FRF) is available only for actuators 1 and 12. For the other actuators the structural FRF to the grid points (grey dots on the lining in Fig. 2) are known from scanning laser vibrometer measurement. If the grid points are assumed

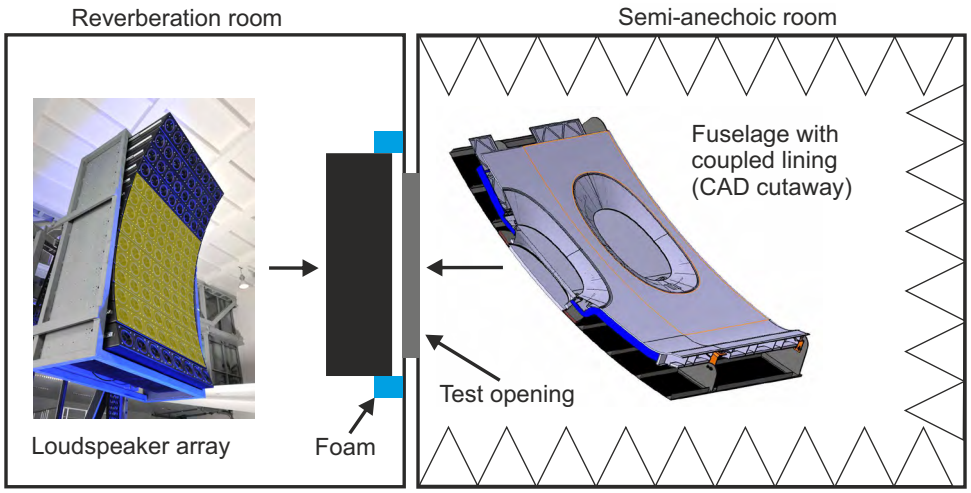

Figure 1: Top view schematic of the experimental setup in the transmission loss facility showing the loudspeaker array in the reverberation room and the fuselage-lining-system mounted in the test opening between the reverberation and the semi anechoic room. The selected loudspeakers are highlighted in yellow. The gap between the fuselage structure and the loudspeaker array is proofed with foam to reduce reverberation.

as elemental radiators of a baffled surface (i.e. the lining), an approximation of the acoustic FRF is obtained from the structural FRF and a radiation impedance matrix. The 20 microphones are arranged in two lines as shown in Fig. 2 (c). It is assumed that the vertical ear locations of passengers sitting in an aircraft will usually be between these two lines. The microphones are placed in three distances from the lining to capture SPL variations from the window seats to the aisle seats. This leads to 60 different microphone positions in total.

3 SENSORS AND ACTUATORS

The defining load case for the sensors is the broadband excitation. In that case, an accurate pressure estimate requires a sufficient number of remote sensors. A quantification of sufficiency is provided by the multiple coherence function. Therefore, it is applied as a metric to, firstly, define the required number and, secondly, the best combination of remote sensors. In Eq. (1), $\mathbf{x}$ is the vector of accelerometer signals and y is the sound pressure at one of the 60 microphone positions. The spectra of these signals are denoted by $\mathbf{X}$ and Y.

$$\bar{C} = \frac{1}{n_2 - n_1 + 1} \sum_{k=n_1}^{n_2} \frac{\mathbf{S}_{xy}(k)\mathbf{S}_{xx}^{-1}(k)\mathbf{S}_{xy}^{H}(k)}{S_{yy}(k)} \tag{1}$$

The multiple coherence function is averaged twice. First, over the discrete frequency k (from 50 Hz to 500 Hz) leading to $\bar{C}$ as given by Eq. (1) and second, over all 60 microphone positions leading to $\bar{C}_{avg}$. The power spectral densities (PSD) are defined as: $\mathbf{S}_{xy} = E\{Y\mathbf{X}^H\}$, $\mathbf{S}_{xx} = E\{\mathbf{X}\mathbf{X}^H\}$ and $S_{yy} = E\{YY^H\}$ with $E\{\cdot\}$ being the expectation operator. A target value of $\bar{C}_{avg} = 0.8$ is chosen. This corresponds to an explanation of roughly 90% of the sound pressure amplitude by the remote sensors. The calculation of $\bar{C}$ for different sensor configurations

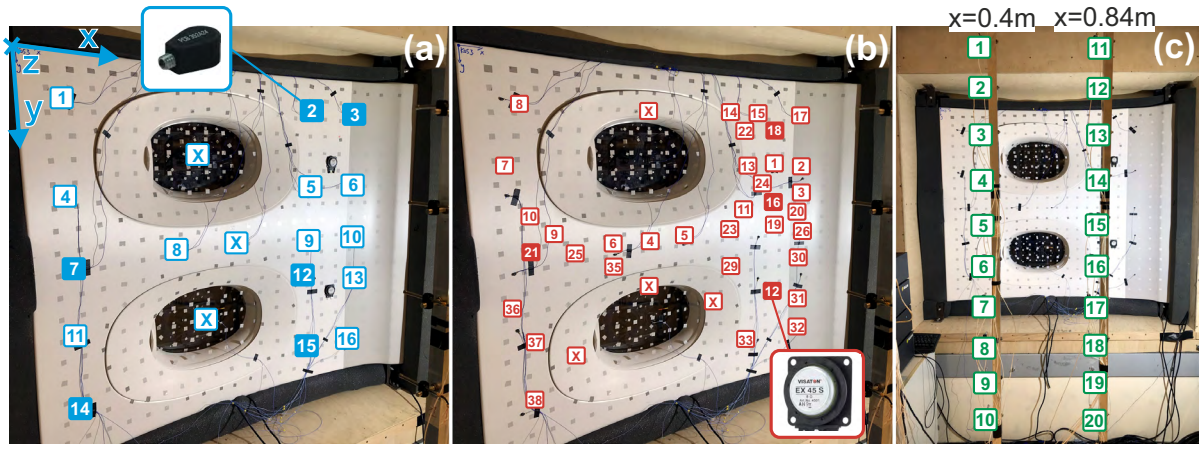

Figure 2: Experimental setup in the transmission loss facility seen from the semi anechoic room. The accelerometers are indicated in blue, the actuators in red and the microphones in green. The accelerometers chosen for the observer of the remote microphone method are 2, 3, 7, 12, 14, 15. The selected actuators are 12, 16, 18 and 21. The microphones are positioned z=–0.5 m, z=–1 m or z=–1.5 m in front of the lining along two vertical lines at x=0.4 m and x=0.84 m spanning two surfaces used for control performance evaluation. Discarded transducer positions are marked with X.

suggests that a number of six accelerometers is adequate. The best combination of six sensors out of 16 is found by combinatorics. The selected combination of six accelerometers (see Fig. 2 (a)) has an average mean coherence of $\bar{C}_{avg} = 0.8021$ compared to the worst combination with $\bar{C}_{avg} = 0.7488$.

The actuators must be powerful enough to counteract the disturbance SPL in front of the lining. A CROR engine is assumed to produce an exterior SPL of 130 dB in front of the fuselage. These high SPL can not be realized with the LSA. The SPL produced in the laboratory by the LSA in front of the fuselage is roughly 113 dB. Therefore, the selected actuator configuration must provide a stroke excess of at least 17 dB. In the experiments two actuators of the type Visaton® EX45S are attached to the lining at positions 1 and 12 (see Fig. 2 (b)). The calculation of the control voltage $\mathbf{U}$ needed to counteract the CROR induced pressure field $\mathbf{D}_a$ in front of the lining results from Eq. (2).

$$\mathbf{D}_a(k) \stackrel{!}{=} \hat{\mathbf{G}}_a(k)\mathbf{U}(k) \rightarrow \mathbf{U}(k) = \left[\hat{\mathbf{G}}_a(k)^H \hat{\mathbf{G}}_a(k)\right]^{-1} \hat{\mathbf{G}}_a(k)^H \mathbf{D}_a(k) \tag{2}$$

The acoustic FRF of the two actuators are denoted with $\hat{\mathbf{G}}_a$. The inverse Fourier transform of $\mathbf{U}$ containing the values from Eq. (2) for the five CROR frequency lines yiels the control voltage $\mathbf{u}$ in the time domain. The required voltage amplitude is 0.924 V which is far below the maximum value of 8.9 V. Assuming a safety factor of two on the voltage, this corresponds to a actuator stroke margin of 13.7 dB. Since the difference between the real and the laboratory SPL is assumed 17 dB or more, the number of actuators is doubled resulting in a actuator stroke margin of roughly 20 dB. The 35 actuator positions are ranked according to the amplitudes of the estimated acoustic FRF. The four actuator locations associated with the highest mean values are considered the most suitable. These are the ones at the positions 12, 16, 18 and 21. The

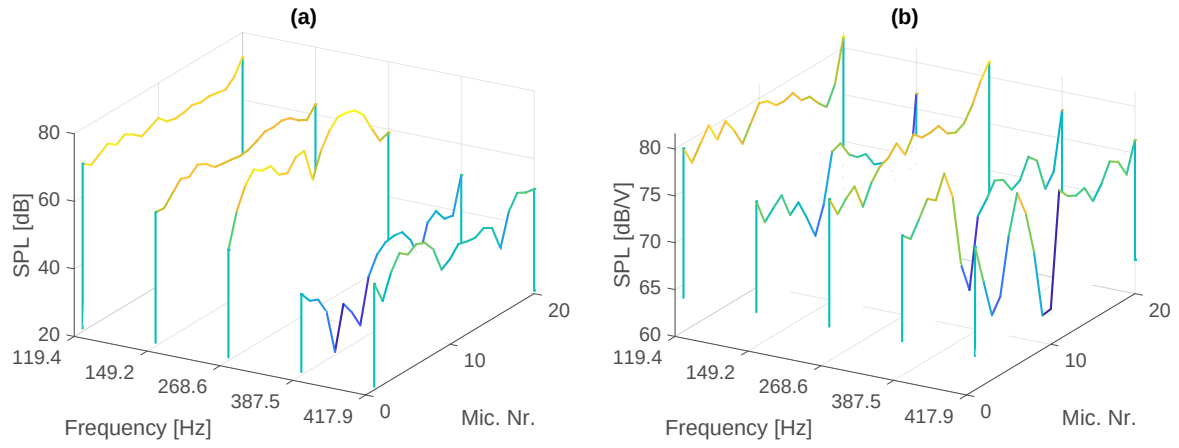

Figure 3: SPL at the CROR frequencies measured by 20 microphones at z=−1 m with the LSA turned on (a) and with actuators 1 and 12 (b).

amplitude difference between the best and the worst location out of 35 is 7.8 dB.

Figure 3 shows the SPL in front of the lining at the CROR frequencies measured by 20 microphones at a distance of one meter. The SPL on the sending side measured between the LSA and the fuselage panel is 104.4 dB at 119.4 Hz, 110.5 dB at 149.2 Hz, 105.9 dB at 268.6 Hz, 78.6 dB at 387.5 Hz and 104.4 dB at 417.9 Hz. The SPL per unit voltage in Fig. 3 (b) shows the theoretical maximum tonal stroke amplitude of the actuators 1 and 12 together. The exakt value of the required voltage amplitude is obtained from Eq. (2).

4 RESULTS

Simulations are performed based on measurement data of the system shown in Fig. 2 with actuators 1 and 12 and remote sensors 2, 3, 7, 12, 14 and 15. The final actuator configuration 12, 16, 18 and 21 is not simulated because the exact acoustic FRF are unavailable. It is assumed that the noise reduction performance will improve due to the increased number of control sources. Results are given for two different virtual microphone configurations. Configuration one uses 30 virtual microphones in the plane at x=0.4 m and configuration two uses 30 virtual microphones in the plane at x=0.4 m and 30 virtual microphones in the plane at x=0.84 m. The plane dimensions of both configurations are $L_y \times L_z = 1.35 \times 1\ m^2$. Configuration one achieves a mean SPL reduction of 6.4 dB (3.8 dB(A)) and a maximum SPL reduction of 17 dB or (13 dB(A)). Configuration two achieves a mean SPL reduction of 7.9 dB (5.2 dB(A)) and a maximum SPL reduction of 12 dB (11 dB(A)). Since configuration two uses virtual microphones in both planes, it achieves a more homogenous SPL reduction then configuration one. This is reflected in an increased mean and a decreased maximum SPL reduction. More information on the simulation can be found in Misol [9].

5 CONCLUSIONS

This contribution describes research activities regarding the detailed design of an active lining module for aircraft interior noise reduction. The derived actuator and sensor configuration is suitable for a CROR engine load case with exterior SPL up to 130 dB. Simulation results show that the active lining reduces the mean SPL by 7.9 dB or 5.2 dB(A) in the controlled volume.

6 ACKNOWLEDGMENTS

This project has received funding from the European Unions Horizon 2020 research and innovation programme under grant agreement No. 723167.

REFERENCES

[1] S. J. Elliott, P. A. Nelson, I. M. Stothers, and C. C. Boucher, "In-flight experiments on the active control of propeller-induced cabin noise," *Journal of Sound and Vibration*, vol. 140, no. 2, pp. 219–238, 1990.

[2] C. R. Fuller and J. D. Jones, "Experiments on reduction of propeller induced interior noise by active control of cylinder vibration," *Journal of Sound and Vibration*, vol. 112, no. 2, pp. 389–395, Jan. 1987.

[3] B. N. Tran and G. P. Mathur, "Aircraft interior noise reduction tests using active trim panels," in *Proceedings of Noise-Con 96*, 1996, pp. 395–400.

[4] M. Misol, T. Haase, S. Algermissen, V. Papantoni, and H. P. Monner, "Lärmreduktion in Flugzeugen mit aktiven Linings," in *Smarte Strukturen und Systeme – Tagungsband des 4SMARTS-Symposiums*, 2017, pp. 329–339.

[5] M. Misol, "EXPERIMENTS ON NOISE REDUCTION IN AIRCRAFT WITH ACTIVE SIDEWALL PANELS," in *Proceedings of the 25th International Congress on Sound and Vibration*, 2018. [Online]. Available: https://elib.dlr.de/121168/

[6] A. Roure and A. Albarrazin, "The remote microphone technique for active noise control," in *PROCEEDINGS OF ACTIVE 99: THE INTERNATIONAL SYMPOSIUM ON ACTIVE CONTROL OF SOUND AND VIBRATION, VOLS 1 & 2*, 1999, pp. 1233–1244.

[7] J. Cheer and S. Daley, "Active structural acoustic control using the remote sensor method," *Journal of Physics: Conference Series*, vol. 744, no. 1, 2016.

[8] S. Algermissen, S. Meyer, C. Appel, and H. P. Monner, "Experimental synthesis of sound pressure fields for active structural acoustic control testing," *Journal of Intelligent Material Systems and Structures*, 2013. [Online]. Available: http://jim.sagepub.com/content/early/2013/06/20/1045389X13493361.abstract

[9] M. Misol, "ACTIVE SIDEWALL PANELS WITH REMOTE MICROPHONE TECHNIQUE FOR AIRCRAFT INTERIOR NOISE REDUCTION," in *Proceedings of the 26th International Congress on Sound and Vibration*, 2019, (accepted for publication).

Towards a Lining Integrated Active Structural Acoustic Control System

– EMuS 2019 -

Stephan Algermissen*, Malte Misol*, Alexander Kokott*, Thomas Haase*, Kai Gonet† and Victor Lungaho‡

*Institute of Composite Structures and Adaptive Systems
German Aerospace Center (DLR)
Braunschweig, Germany
e-mail: stephan.algermissen@dlr.de - web page: www.dlr.de

† Invent GmbH
Braunschweig, Germany
e-mail: kai.gonet@invent-gmbh.de - web page: www.invent-gmbh.de

‡ Trackwise Ltd.
Tewkesbury, UK
e-mail: victor.lungaho@trackwise.co.uk - web page: www.trackwise.co.uk

ABSTRACT

For future aircraft counter-rotating open rotor (CROR) engines are a promising technology to reduce their CO_2 footprint. Since the contribution of CROR engines to the cabin noise is higher than for jet engines, new strategies for the reduction of noise transmissions for frequency bands below 500 Hz are necessary. Active structural acoustic control (ASAC) systems are capable to reduce sound transmission of lining structures in this bandwidth. Sensors measure the vibrations of the lining to estimate its sound emission into the cabin. Based on these signals a controller calculates force signals for actuators on the lining. The actuator forces change the vibration behaviour of the lining in order to reduce its sound emission. For the realization of such a system in a real aircraft, manufacturing and maintenance issues have to be addressed.
Within work package 3 of the EU project ACASIAS an aircraft lining with an integrated ASAC system is developed. The size of the lining is app. 1300 x 1690 mm^2 (W x H) and it is simply curved. The radius of 2980 mm makes it relevant for a twin-aisle aircraft like the Airbus A350. The focus of research activities lies on the integration of components and the industrial manufacturing process of the lining. The components to be integrated are sensors, actuators and the corresponding wiring. A concept is proposed where each actuator and sensor is encapsulated in a kind of insert. The inserts smoothly integrate into the manufacturing process of the lining while they protect the actuators and sensors from humidity, dust, etc. The maintenance aspect is covered by the option to change each actuator or sensor upon insert level. The integrated wiring of the lining is left unaffected during an actuator or sensor replacement since connectors in each insert allow a nearly tool-free assembly/disassembly.
In this paper the progress of work package 3 is presented at a detailed design review (DDR) stage. Finally, the lining will be manufactured and equipped with a full ASAC system. Experiments will be conducted in the acoustic transmission loss facility at the DLR.

Introduction

CROR propulsion systems are a promising concept to reach a resource efficient transport demanded by the European Commission in the Horizon 2020 framework program. Due to their fuel efficiency they are discussed as an alternative to common jet engines. Within in the EU-project ACASIAS the active acoustic lining panel is seen as an enabler for the CROR technology. For sound pressure levels (SPL) of up to 130 dB in the nearfield of the engine [1] and fundamental blade passing frequencies around 100 Hz common insulation strategies fail in reducing the SPL in the cabin to an admissible level for the passengers. Many active methods like ASAC have been developed to reduce the noise transmission through single or double walled structures [2, 3]. In most of the contributions to this

subject laboratory equipment and rapid prototyping controls are used for the realization of the active system. Bringing active systems into real world applications requires small, cost extensive devices and a straight-forward manufacturing concept.
The objective of the ACASIAS project is to go the next step towards the integration of ASAC systems in aircraft linings. This will be achieved by selecting off-the-shelf components for the control system and by creating a production-friendly integration approach. In this paper the setup for an active acoustic lining as technology demonstrator is discussed. First, the dimensions of the lining are defined followed by a component selection process which incorporates different actuator and sensor types. Requirements for the wiring are set which lead to a routing map. Finally, the integration concept for the actuators and sensors in form of an insert is presented, taking maintenance issues into account.

Lining

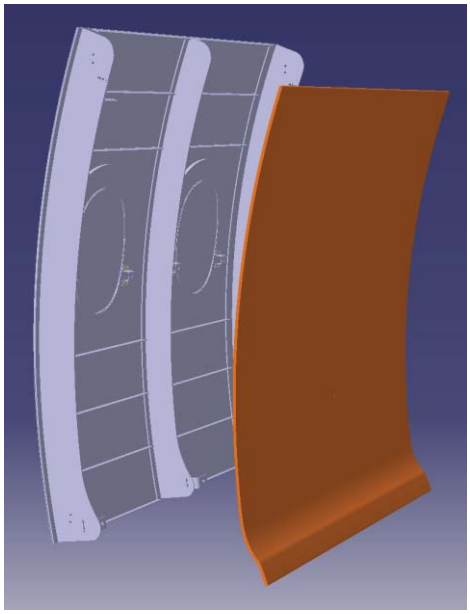

Fig. 1: Lining panel (orange) in front of fuselage

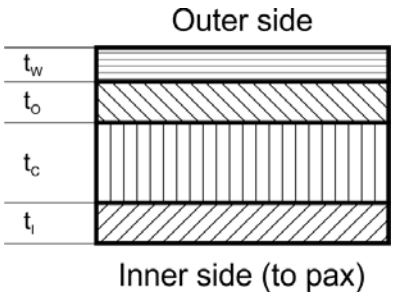

Fig. 2: Lining layup

DLR is able to provide an A350-like fuselage panel with carbon fibre reinforced plastics (CFRP) skin and aluminium stringers and frames, see Fig. 1. It covers two frame widths and has the dimensions 1300 x 1700 mm² (W x H). A wooden framework is available to mount the fuselage panel in the opening of the acoustic transmission loss test stand at DLR. According to the dimensions of the fuselage panel, the dimensions of the lining of app. 1300 x 1690 mm² (W x H) are chosen. The lining is simply curved with a radius of app. 2980 mm. In the lower part of the lining the curvature slightly changes due to air outlets which are present in original linings of an A350. Windows are neglected since the effort and the costs for an adequate mould would be too high.
The lining panel is a sandwich part. Together with the industrial advisory board member Diehl Aviation the layup of the panel has been defined, see Fig. 2. On top of an inner prepreg layer with thickness t_l a honeycomb core of thickness t_c is placed. The core is covered with a single layer of open prepreg of thickness t_o. The wiring of the sensors and actuators is on top of this prepreg. The first idea of placing the wiring between the inner prepreg and the core is rejected since it exists the

Description	Material	Thickness
Wiring		$t_w < 0.04$ mm
Outer layer	Gurit PF811-G231-32	$t_o = 0.2$ mm
Core	Nomex honeycomb	$t_c = 6.5$ mm
Inner layer	Gurit PH600-G227-40	$t_l = 0.19$ mm

Tab. 1: Lining materials

probability that the wiring pushes through the prepreg and becomes visible on the passenger's side. Table 1 summarizes the layup data. The desired thickness of the final lining is 7.0 mm.
The lining is mounted at six points of the fuselage structure. Three clips at the upper and three clips at the lower part of the lining are hooked into shock mounts located at the frames.

Sensors

The objective of the active acoustic lining approach is to provide an autonomous part which is independent from external inputs apart from electrical power. Therefore, microphones sensing the sound pressure level at the passenger's ears are excluded by default. The so-called remote microphone technique [4] enables the estimation of emitted sound of a structure based on acceleration measurements on the specific structure. In case of the active acoustic lining the sensing is realized as follows: The accelerations are input into a pre-calculated observer that estimates the sound pressure levels at selected positions in front of the lining. The accelerations have to be measured in normal direction of the lining's surface.
For the selection of suitable accelerometers, common laboratory equipment is not taken into account. The prices for sensors and cables are too high for any practical application. Instead, micro-electro-mechanical systems (MEMS) accelerometers are a cheaper alternative. Usually, they are provided as integrated circuits (IC) which have to be applied to a printed circuit board (PCB) together with additional electric components and connectors.
The requirements for this application that have to be fulfilled by an accelerometer are limited to the mass, the footprint size and the measurement range. Table 2 summarizes the requirements for the sensor. The measurement range derives from previous projects where experiments at linings were conducted.

Description	**Value**
Mass	max. 20 g
Footprint size	max. 20 x 20 mm²
Measurement bandwidth	min. 500 Hz
Measurement range	min. 2 g = 19,62 m/s²

Tab. 2: Sensor requirements

A market survey based on an internet research is created, where only large suppliers were taken into account. Several types of sensors can be identified which fulfil the given requirements. However, these sensors differ in their connectivity. Three main interfaces are identified: Analogue connection, serial peripheral interface (SPI) and Inter-Integrated Circuit (I²C).

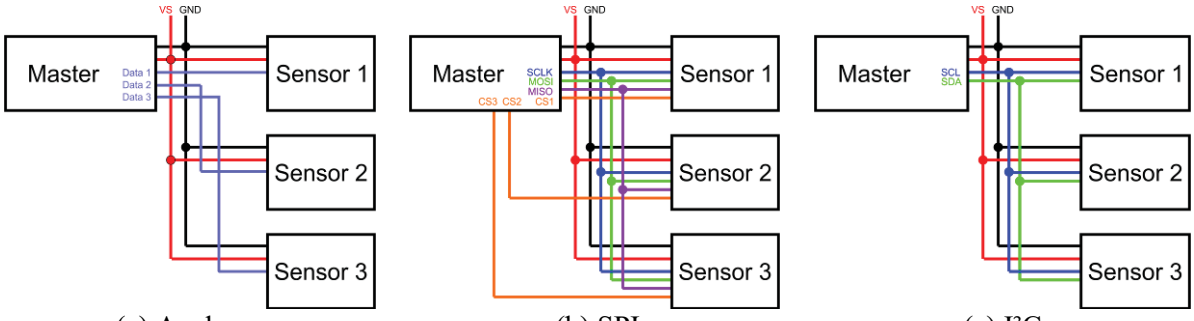

(a) Analogue (b) SPI (c) I²C

Fig. 3: Sensor interface types

Figure 3 compares the wiring effort of the three interface types. While the analogue connection uses only a single data line, the two digital busses SPI and I²C need at least two bus lines. Another benefit of sensors with analogue interface is the easy to implement synchronized sampling of signals. With analogue interfaces the master has to provide synchronized sampling, the data is always available. The sensors with digital busses have to be synchronized by the master and have to be addressed for data transfer. Timing issues are possible and the address space is limited for a larger amount of sensors. Therefore, the analogue interface is preferred for this application.

The further selection process leads to an accelerometer by ANALOG DEVICES®. The ADXL 354 has a measurement range of 2 g and a bandwidth of 1.5 kHz. Its footprint size of 6x6 mm² is ideal suited leaving enough space for additional circuitry. Figure 4 shows the accelerometer on an evaluation board and its pin configuration.

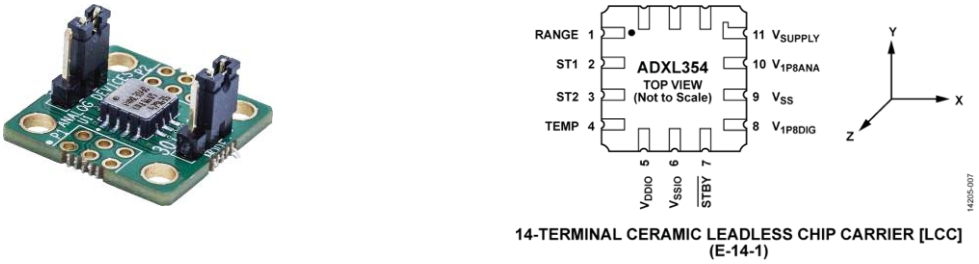

Fig. 4: Accelerometer ADXL 354[1]

Actuators

The fundamental CROR frequencies in the given load case are located close to 120 Hz. The bandwidth of the actuators therefore has to cover the interval from 100 to 500 Hz. Electrodynamic exciters are best suited for this bandwidth. First, piezo actuators were taken into account, but finally fell off due to poor performance in this frequency bandwidth. At best they could complement the exciters as a kind of tweeters for passenger announcements.
As a base line for the selection of an appropriate actuator type the VISATON® EX45S is chosen. Previous experiences from the SYLVIA project [5] show that this type is able to gain sufficient performance and control authority. A market survey among leading exciter manufacturers like DAYTON®, VISATON®, TECTONIC® and ELAC® is compiled to find adequate candidates. The purpose is to identify exciters with higher or equal forces factors (*Bl*) than the base line. Additional requirements are only imposed on the mass and the footprint size, see Tab. 3. The mass is oriented at the mass of the base line exciter.

Description	Value
Mass	max. 100 g
Footprint size	max. 50 x 50 mm²

Tab. 3: Actuator requirements

Different exciters were tested and a few have been selected for further experiments on an iron sprung foundations in the lab. A load cell is attached to the foundation. On top of the load cell four exciter types are mounted successively. Estimation of the exciter current is realized with voltage measurement over a 0.1 Ω resistor. The exciters under test are a DAYTON® DAEX25-VT4, an ELAC® 83005, an ELAC® 84005 and the base line VISATON® EX45S. The frequency response function (FRF) from input current to output force is determined. According to [6] the force factor *Bl* can be estimated from this FRF for frequencies $\omega >> \omega_e$, where ω_e is the exciter eigenfrequency. The result is shown in Fig. 5. The eigenfrequencies ω_e of the exciters under test are located around 100 Hz. The force factor *Bl* can be estimated in the bandwidth 500 – 600 Hz since the FRF is constant and $\omega >> \omega_e$ is valid. Both ELAC® exciters beat the base line exciter from VISATON® while the one from DAYTON® falls short of it. Due to the shown performance, the ELAC® 84005 is chosen for this application.

[1] Image source: analog.com

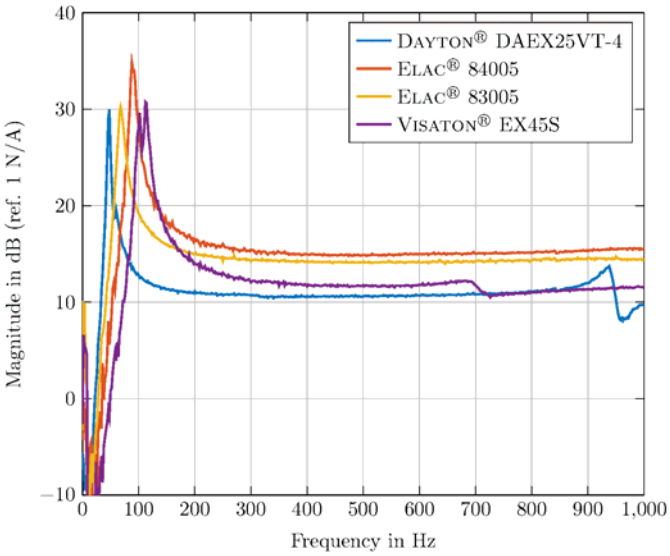

Fig. 5: FRF from exciter current to exciter force

Actuator & Sensor Definition

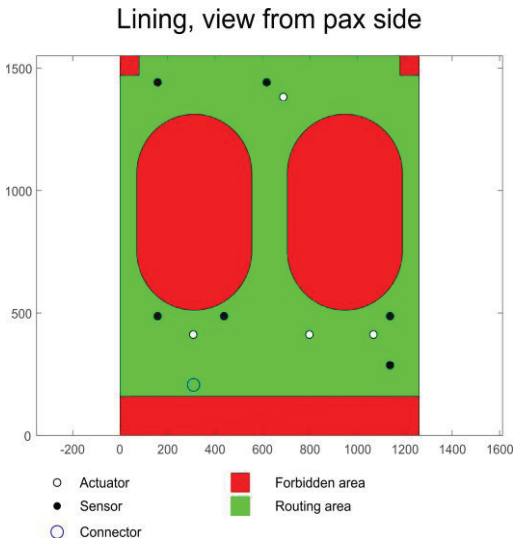

Fig. 6: Placement of actuators and sensors

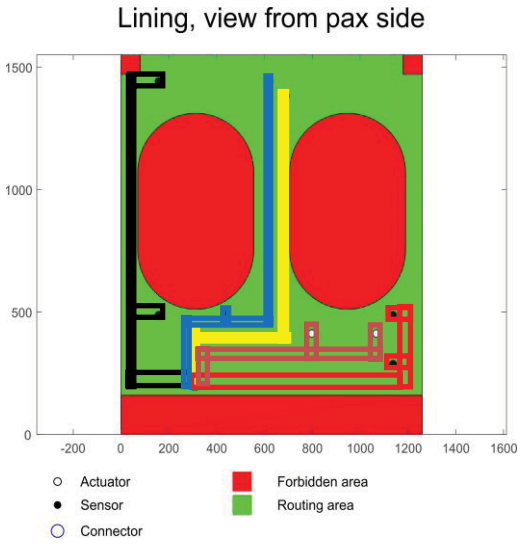

Fig. 7: Routing of wiring

The actuators and sensors are defined in a two-step procedure. Firstly, the required number and secondly, the placement of the transducers is determined. This process is not independent from the dominant noise sources (load case) present in the aircraft. Here, two different load cases are considered for the definition of the remote sensors and the actuators. These are, first, a multi-tonal excitation of a CROR engine and, second, a broadband excitation typical for a turbulent boundary layer excitation (TBL). For the sensor definition, the defining load case is the broadband excitation whereas the actuators are defined for the CROR load case. In both cases the number of transducers is more important than the placement. A detailed description of the process of actuator and sensor definition is provided in [4]. The following description briefly summarizes the main considerations and results of this process.

Theoretically, for the deterministic CROR load case, a single remote sensor is sufficient to estimate the pressure at the virtual locations. However, the use of a single remote sensor is considered unreasonable with regard to robustness because its failure would tie the whole system. Furthermore, in the broadband case, an accurate pressure estimate requires a sufficient number of remote sensors. A quantification of sufficiency is provided by the multiple coherence function. Therefore, it is applied as a metric to, firstly, define the required number and, secondly, the best combination of remote sensors. The best sensor configuration with six remote sensors (see Fig. 6) achieves a mean

coherence value (averaged in the considered frequency range and over all microphones) of app. 80% which explains roughly 90% of the SPL in front of the lining (for the broadband load case).
The number of actuators is determined by the requirement of sufficient control authority to counteract the SPL in front of the lining induced by the CROR engine. The SPL produced in the laboratory by a loud speaker array in front of the fuselage is roughly 113 dB and the SPL estimated for a real CROR engine is 130 dB [1]. Therefore, the selected actuator configuration must provide a stroke excess of at least 17 dB (app. a factor of 7). The evaluation of actuator FRF (voltage to sound pressure) for different positions on the lining provides an estimate of the required actuator number and, furthermore, permits the selection of the most suitable positions. It turns out that four actuators of the type VISATON® EX45S are able to cancel the SPL in front of the lining for external SPL up to 130 dB (with a safety factor of two imposed on the actuator control voltage). See Fig. 6 for the final actuator placement. The results can be transferred to any other actuator type with a known FRF (current to force, see Fig. 5) characteristic. I can be deduced from Fig. 5 that the chosen actuator type ELAC® 84005 is more powerful than the VISATON® EX45S. Hence, the required control authority for external SPL up to 130 dB is guaranteed by this choice.

Wiring

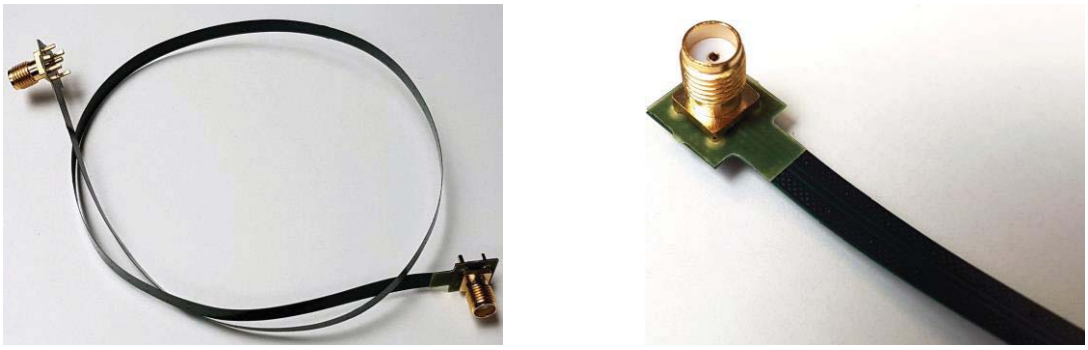

Fig. 8: FPC examples

All sensors and actuators of a single lining have to be connected to the corresponding controller. This is realized by routing all connection lines to a single main connector at the bottom of the lining, see Fig. 6. The wiring and the main connector are placed at the outer side of the lining pointing towards the fuselage, compare Fig. 1. The wiring consists of flexible printed circuits (FPC), see Fig. 8, connecting two actuators/sensors at a time with the lining connector. The objective of the routing is to minimize the width of each FPC since it is limited by the manufacturing process. Figure 7 shows the final routing of the wiring. Two actuator FPC (brown & yellow) and three sensor FPC (black, blue & red) are needed to connect all items.
The requirements on the wiring with respect to voltage and current are estimated roughly using values from the datasheets of the selected actuator and sensor types. For the actuator an absolute peak voltage $U_{\text{peak}} = 15$ V is given [7]. The minimum resistance is the one of the voice coil at DC $R_e = 6.15\ \Omega$. The absolute peak current of the exciter is therefore estimated with

$$I_{\text{peak}} = \frac{U_{\text{peak}}}{R_e} = 2.44\text{A} \tag{1}$$

The maximum supply voltage $U_{\text{supply}} = 3.6$ V is given in the datasheet of the ADXL354 [8]. In measurement mode the chip sinks 150 µA. With a safety factor of two the maximum supply current is estimated with $I_{\text{s,max}} = 300$ µA.
The conductor cross-sections are determined by the maximum currents of actuators and sensors. Figure 9a shows the symbolic cross section of the sensor FPC. The substrate in yellow is the base for the sensor lines. The copper lines are illustrated in orange. The numbers give their width and their distance in mm. According to Fig. 3a four wires are needed to connect two analogue sensors. The common ground and power lines are located in the centre while the data lines are outside.
The actuator FPC has a comparable design. Figure 9b shows four lines on the substrate. Each actuator needs to separate wires. Due to higher currents the width of the lines are significantly higher than for the sensor lines. The height of both FPC is set to 0.035 mm.

2	0,2	0,5	0,2	0,25	0,2	0,5	0,2	2	mm	6,05
	data1		gnd		pwr		data2			

(a)

2	1,7	0,25	1,7	0,5	1,7	0,25	1,7	2	mm	11,8

(b)

Fig. 9: Cross sections of the sensor (a) and the actuator FPC (b)

Inserts

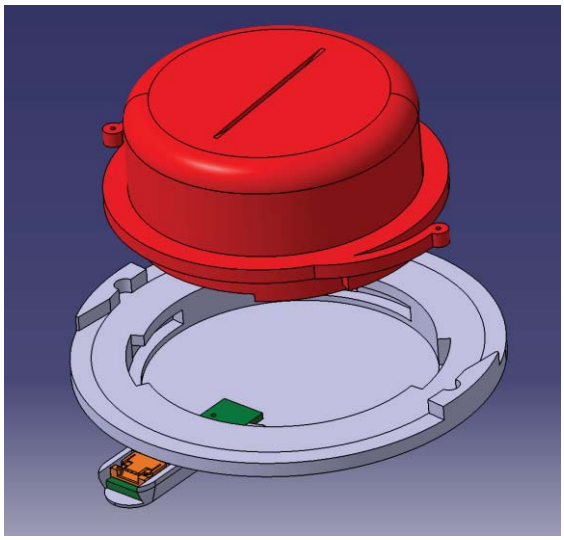

(a) Top (red) and base part (grey)

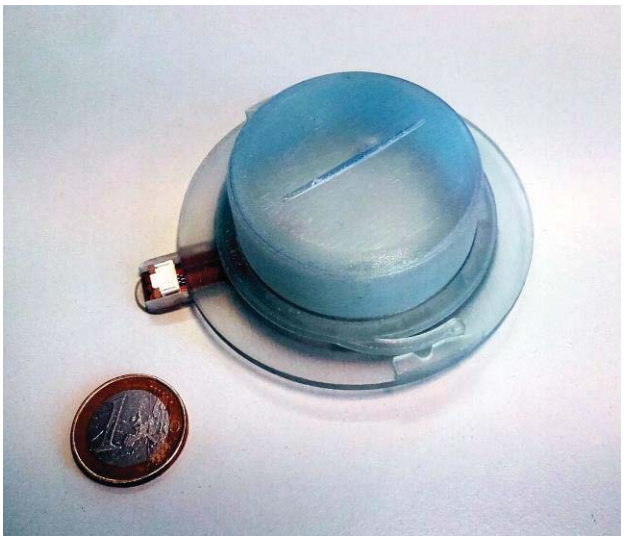

(b) 3D-printed actuator insert

Fig. 10: Concept of the two-part insert

The main aspect of work package 3 of ACASIAS is enabling an industrial manufacturing process for the active lining by integrating actuators, sensors and wiring. The requirements for the integration concepts can be summarized as follows:

- Protection of items from moisture intrusion
- Smooth electrical connection between wiring and items
- Seamless integration into manufacturing process
- Robust mechanical connection for load application (actuator) and signal quality (sensor)
- Repair and maintenance on item level

For the integration of sensors and actuators a concept with inserts is proposed. Each item is enclosed in a two-part insert, see Fig. 10. The base part is integrated into the sandwich panel of the lining. The removable top part houses the sensor or actuator. The mechanical connection of the two parts is realized with a bayonet connector that is inserted and turned for fastening. Two snap connectors prevent the loosening of the parts. Since actuators and sensors have different footprint sizes and heights, two versions of inserts are manufactured. They only differ in dimensions but the design remains the same for both.
The base part is connected to the FPC by an external connector on a printed circuit board (PCB). The connector is mounted on a tab outside of the base part. The PCB, see Fig. 10a in green, reaches through the outer shell of the base part and has contact surfaces on top.
After the insertion process of the FPC the external connector is sealed with resin to prevent moisture intrusion. Depending on the item in the top part, the PCB has two surfaces for an actuator and three for a sensor. Spring contacts in the top part contact to the surfaces during fastening of the bayonet connector and establish the connection between items and wiring. The entire insert is sealed with an

O-ring between top and base part. The application of loads from actuator to lining is accomplished with circumferential shoulders at the top and at the base part.
The industrial integration process therefore roughly outlines as follows:

- Build layup of sandwich lining structure in a mould
- Crush the honeycomb core at actuator and sensor locations to create a sink for all base parts
- Add additional prepreg snippets to reinforce the sinks
- Cure the lining
- Apply the wiring and the main connector
- Integrate all base parts, connect them to the FPC and seal the connectors
- Plug in all top parts

A detailed description of the manufacturing process can be found in [9].

Conclusion & Outlook

Within this paper a concept for the integration of actuators, sensor s and wiring in a lining panel is proposed. Inserts allow the realization of an industrial manufacturing process. The chosen actuator and sensor types enable a cost efficient setup of an ASAC system in a cabin environment comparable to an Airbus A350. Maintenance requirements are met since the top parts of the insert are changeable. The placement of all components of the ASAC system in a lining gives the opportunity to even create a retrofit solution for existing turboprop aircraft.
Next steps in WP 3 will be component test where a base part of an insert is set into a lining sample and connect to an FPC. Function test will approve the concept. In the remaining time of the project an entire lining panel will be manufactured as proposed in the last section. It will be equipped with actuators and sensors. A controller that implements ASAC will be designed and applied to the lining. Acoustic experiments at DLR will prove the performance of the entire system.

Acknowledgments

This project has received funding from the European Union's Horizon 2020 research and innovation programme under grant agreement No. 723167.

References

[1] A. Stürmer, "DLR CROR & propeller noise prediction: Numerical approach requirements & limitations," in *14th CEAS-ASC Workshop*, Warsaw, Poland, 2010.

[2] C. R. Fuller, S. J. Elliott, and P. A. Nelson, *Active Control of Vibration*. London, UK: Academic Press, 1997.

[3] F. Fahy and P. Gardonio, *Sound and Structural Vibration: Radiation, Transmission and Response*, 2nd ed. Oxford, UK: Academic Press, 2007.

[4] M. Misol and S. Algermissen, "Remote sensing for a lining integrated structural acoustic control system," in *Proc. of European Conference on Multifunctional Structures*, Barcelona, Spain, 2019.

[5] M. Misol, S. Algermissen, and M. Rose, "On the noise reduction of active sidewall aircraft panels using feedforward control with embedded systems," in *Proc. of International Conference on Noise and Vibration Engineering (ISMA)*, Leuven, Belgium, 2018.

[6] R. Boulandet, M. Michau, P. Herzog, P. Micheau, and A. Berry, "A sensorless method for measuring the point mobility of mechanical structures," *Journal of Sound and Vibration*, vol. 378, pp. 14 – 27, 2016.

[7] Mechakustik GmbH, "Datasheet airlock exciter 84005", 2013 (Unpublished).

[8] Analog Devices, *ADXL354/ADXL355 datasheet*, downloaded from analog.com at 25.03.2019.

[9] K. Gonet, S. Steeger, S. Algermissen, and V. Lungaho, "Manufacturing aspects of active acoustic lining panel," in *Proc. of European Conference on Multifunctional Structures*, Barcelona, Spain, 2019.

European Conference on Multifunctional Structures
EMuS 2019
X. Martinez and H. Schippers (Eds)

CONTRIBUTION OF CONFORMAL ANTENNAS TOWARDS SUSTAINABLE AIRCRAFT

P. VRCHOTA[*], A. PRACHAŘ[†], M. ŠMÍD[‡] AND J. MIDDEL[§]

*Czech Aerospace Research Centre (VZLU)
Beranovych 130, 199 05 Prague, Czech Republic
e-mail: vrchota@vzlu.cz, web page: http://www.vzlu.cz

† Czech Aerospace Research Centre (VZLU)
Beranovych 130, 199 05 Prague, Czech Republic
e-mail: prachar@vzlu.cz, web page: http://www.vzlu.cz

‡Czech Aerospace Research Centre (VZLU)
Beranovych 130, 199 05 Prague, Czech Republic
e-mail: smid@vzlu.cz, web page: http://www.vzlu.cz

§NLR - Netherlands Aerospace Centre
P.O. Box 90502, 1006 BM Amsterdam, The Netherlands
e-mail: jan.middel@nlr.nl, web page: http://www.nlr.nl

Key words: CFD, radome, drag reduction, emissions

Abstract. This paper shows the drag and emission reduction potential of integrated, flush communication antennas at the surface of an airliner. The CFD simulations of the aircraft model representing a modern airliner with radome in different locations on its upper part of the fuselage have been done. The results have been compared with the baseline configuration of the aircraft without radome. The aerodynamic equivalent weight penalty and additional fuel needed due to the drag of the radome and its weight itself have been calculated by two approaches. The obtained drag reduction potential has been used for the estimation of the CO_2 and NO_x emissions reduction by using integrated antenna.

1 INTRODUCTION

The protection of the environment and reduction of the environmental footprint of air transport is very demanding Among others, growing air traffic also significantly contributes to the emissions contributing to climate change and local air quality issues around airports. Very ambitious goals have been set by politicians; a reduction of 2% in fuel consumption (and thus CO2 emissions) for aviation by 2021 and then by 2% per year until 2050 [1]. Many operational improvements and new technologies have to be adopted to achieve this ambitious goal. One new technology is to replace the protruding communication antennas by integrated one with the aircraft outer skin can be used to contribute to the defined requirements [2, 3]. The structurally integrated antennas cause less additional drag, noise and turbulence in comparison with classical protruding antennas. These antennas also reduce the maintenance costs and possible operational delays by avoiding collisions of protruding parts with airport cargo

vehicles. The European project ACASIAS [4] addresses, among others, the topic of integrated antennas and their effect on aerodynamic performances and environment. The project researches VHF antennas that can be integrated into the fuselage panels or winglet's surface [3], e.g. This paper is focusing on the evaluation of the aerodynamic effect of the integrated antenna with the aircraft fuselage and its impact on the weight and fuel savings by eliminating the need for a radome. The possible emissions reductions by integrated antenna have also been evaluated.

2 METHODS

2.1 Aircraft model

The NASA Common Research Model (CRM) [5] designed by Boeing and among other purposes has been used during the Drag Prediction Workshops (DPW) [6] to obtain the experimental data for CFD code verification. It is based on a transonic transport configuration designed to fly at a cruise Mach number, M = 0.85 at design lift coefficient CL = 0.5. Several configurations of the CRM can be used. The horizontal tail and nacelle/pylon can be integrated into the baseline configuration which contains the wing and body, only. The CRM model used for this study is depicted in Fig. 1. The considered baseline configuration corresponded to the wing, body and horizontal tail, without radome.

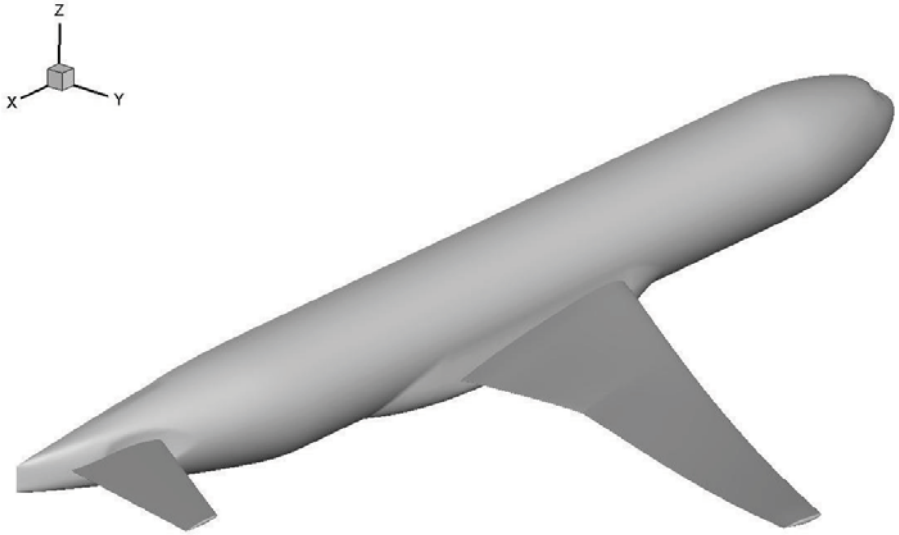

Figure 1: Baseline configuration of Common Research Model

The radome was placed in four locations along the fuselage, two in front of the wing (marked G_0 and G_1), one over the wing (marked G_3) and one in the rear (marked G_2, see Fig. 2). The positions of the radome have been determined according to the Cp distribution (local velocity) along a fuselage of the baseline configuration. The geometry of the radome corresponds to the low-profile Gogo 2Ku antenna [7].

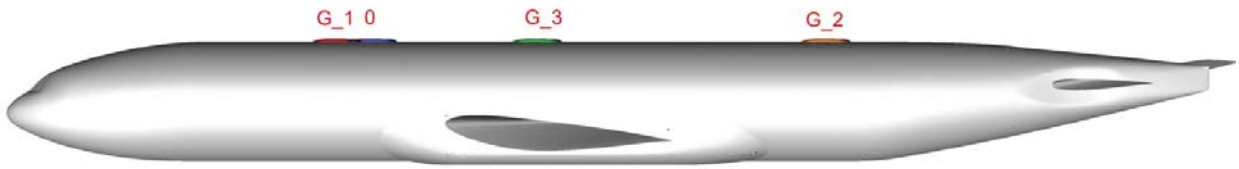

Figure 2: Considered positions of the radome along the fuselage

2.2 Calculation of the Aerodynamic Equivalent Weight Penalty and additional fuel

The weight penalty due to the presence of the radome were calculated by two approaches. The first one was introduced and applied by the radome's producer [7] and is called Aerodynamic Equivalent Drag Penalty (AEDP). It assumes that the value of the lift over drag ratio is constant during the cruise part of the flight.

$$L/D = C \tag{1}$$

If the drag of the aircraft is increased by the contribution of the radome, the lift has to be also increased according to the following equation.

$$L_{New} = (D + D_{Radome}) \cdot C \tag{2}$$

The differences between the new value of lift (L_{New}) and original value of lift is the *AEDP*.

$$AEDP = L_{New} - L \tag{3}$$

The hardware weight has to be also added to the AEDP to obtain the overall increasing of the weight by presence of the radome. The AEDP could be an equivalent to the weight of the fuel which can be saved by integrated antenna.

The second simplified method is based on contribution of the fuel weight to the MTOW of the aircraft and the assumption of the fuel burned in cruise. The additional fuel needed to carry the radome consists of the fuel needed for radome's weight and fuel needed for radome's drag. It can be split into the part needed for the radome's drag itself and part needed for radome's drag fuel (additional fuel needed to carry the extra fuel needed because of the radome's drag – snow ball effect). This method was applied to two aircraft, A350 and B-787 (see Section 3.2). These two aircraft have been selected because of their geometric and also cruise regime similarity in each other and also in CRM.

2.3 Mesh generation, flow solver and flow conditions

The computational grids were generated by Pointwise software [8]. They are unstructured grids with rectangular elements on the model surfaces, prismatic layer and tetrahedron elements in the volume. The height of the first layer was set to fulfill the demand of the turbulence model on the value of the y+ function. The grid topology was the same for all considered configurations. The differences were only in close vicinity of the radome.

The Reynolds average Navier-Stokes (RANS) equations are solved in in-house CFD

program. It is a finite volume Navier-Stokes solver for unstructured meshes. The k-ω EARSM [9] turbulence model was used for this study. All simulations were run as a fully turbulent flow. A farfield boundary condition was used on the outer boundary of the computational domain. This condition is specified by Mach number, flow direction, static pressure and static temperature. The aircraft was treated as no-slip viscous boundary. Symmetry boundary condition was used at the symmetry plane of the half model.

Freestream Mach number 0.85 and the Reynolds number $30 \cdot 10^6$ based on mean aerodynamic chord were used. Angle of attack was varied during the simulations to obtain constant lift coefficient 0.5.

3 RESULTS

3.1 Effect of the location of the radome on the drag

The drag of the aircraft with different locations of the radome was evaluated for the constant lift coefficient (CL = 0.5). It means that the angles of attack were slightly different for different radome locations to obtain the same aerodynamic loading. The drag increment, caused by the presence of the radome in particular locations, is depicted in Fig. 3. The drag is increased from 0.07% up to 0.75% related to the baseline configuration. The best positions of the radome are in the front and in rear part of the fuselage while the overwing position (marked as G_3 in figure 2) is the worst. The higher drag in the overwing position is due to the locally accelerated flow caused by the wing(lift). This shows from the Cp distribution along the fuselage depicted in Fig 4. It can be seen the locally accelerated flow just behind the nose of the fuselage and overwing position (the wing root is between the 25m and 37m in x coordinate). The suitable position for placing the radome can be determined according to the Cp distribution with lower local flow velocity, in front of the wing and in the aft part of the fuselage, respectively. It has to be mentioned, that the drag of the rear position is slightly biased due to the missing the vertical tail plane.

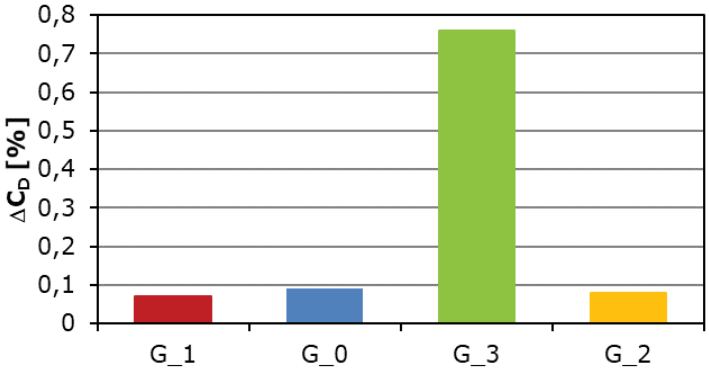

Figure 3: Drag increment by presence of the radome in different locations

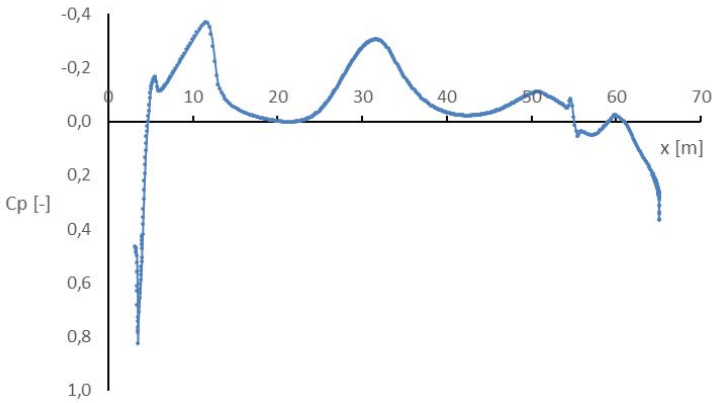

Figure 4: Cp distribution along the fuselage of the baseline configuration

The values of the drag force corresponding to the particular locations of the radome were used for further calculations of the aerodynamic equivalent drag penalty and the additional fuel needed.

3.2 Weight penalty due to the presence of radome

The aerodynamic characteristics of the CRM (lift, drag and radome's drag) have been used to calculate the AEDP. The values of AEDP were calculated by means of the Eq. 1-3. This method takes into account the aerodynamic characteristics of the aircraft only. The hardware weight of the radome has to be also added to the values of AEDP to obtain the full „penalty". The results are depicted in Fig. 5 (left).

The second method of calculation of the weight penalty determines the weight of the additional fuel needed to carry the radome itself (hardware weight and radome's drag) and due to the snow ball effect also some more fuel to carry the additional fuel. This method takes more into account the flight profile and the ratios between maximum take-off weight (MTOW), fuel weight, burned fuel during the cruise, etc. For the purpose of this study two aircraft and their parameters (MTOW, fuel weight, etc.) have been used, A350 and B-787. The value of L/D for cruise condition was considered the same for both aircraft. It could be reason for the differences in calculated weight penalty between these aircraft (see Fig. 5 right). Some other differences are caused by the characteristics of the aircraft themselves (A-350 is slightly larger in comparison with CRM whilst B-787 is slightly smaller). The results of this method are also depicted in Fig. 5 (right). It could be seen that both methods gave similar results and penalize the same configuration.

The results of both methods are rather informative. The precise aerodynamic, geometrical and weight characteristics of the real considered aircraft need to be taken into account to obtain correct absolute values of the weight penalty. On the other hand, the trend of the effect of the radome in particular positions can be used from this procedure.

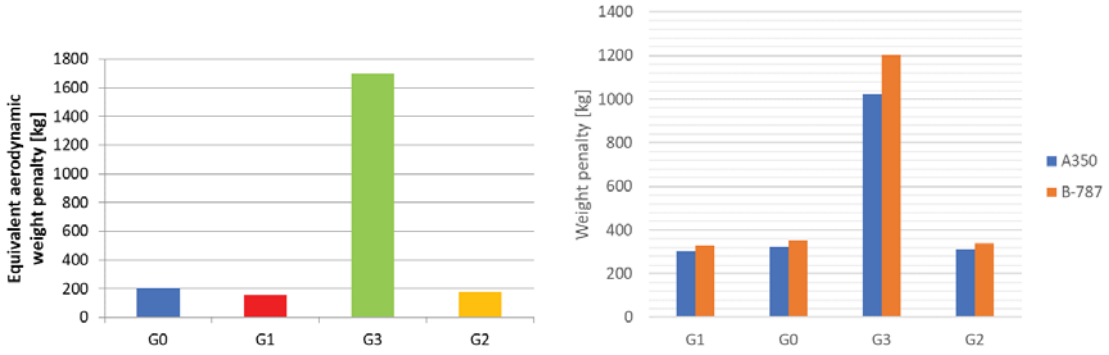

Figure 5: Aerodynamic Equivalent Drag Penalty (left) and weight penalty for two aircraft (right)

3.3 Possible reduction of the CO_2 and NO_x emissions by integrated antennas

The CO_2 and NO_x emissions can be calculated or obtained by several methods. One of these methods is the calculation of the emissions from the chemical reactions inside the combustion chamber using its efficiency and selected regime [10]. Another method is based on the data provided by the engines' manufacturers. International Civil Aviation Organization (ICAO) organization manages the aircraft engine emission databank database [11], where the fuel consumptions and emissions of particular engines are defined and measured in reference static conditions for four thrust settings typical for take-off climb-out, approach and taxi. For low altitude and low speeds, as typical for airports, this database can be directly applied to the effect of integrated antennas with the aircraft's surface in terms of CO_2 and NO_x emissions, if the engine type of the aircraft is known. The example of the estimation of the production of the emissions in dependence on the fuel consumption for an ideal engine is depicted in Fig. 6. Similar graphs of production of CO_2 and NO_x emission in dependence on the thrust can be also drawn.

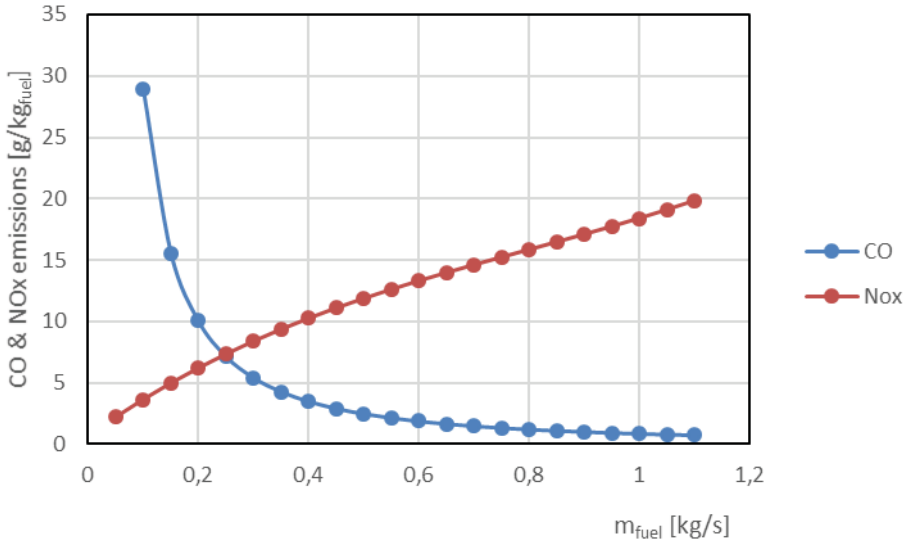

Figure 6: CO_2 and NO_x emissions for ICAO Aircraft Engine Emissions Databank engine [11]

The NO_x emissions production of the A-350-900 aircraft during typical flight (7000 km trip) was calculated. The values of the drag increment have been taken over from the simulations of CRM. These correspond to the worst case (overwing location, G3) and the rear location (G2) of the radome. The results of the estimation of the NO_x production together with the estimation of the fuel consumption are in the following table. It is possible see the savings of the amount of the fuel burned (~0.6%) and NOx emissions produced (~2%) during the flight corresponded to the overwing radome's location and negligible savings for the rear radome's location.

Table 1: Results of the estimation of the emission production for typical flight w/o radome

	no radome	Radome G3	Radome G2	
fuelburn	51760.24	52076.38	51764	[kg]
fuelestimate (incl. reserves)	53871.93	54388.09	53878.39	[kg]
time	530.52	530.65	530.52	[min]
travel distance	7004.09	7004.09	7004.09	[km]
takeoff mass	238153.78	238540.30	238158.76	[kg]
NOx emissions	1900.85	1941.63	1901.36	[kg]

The typical flight parameters, like altitude, velocity, thrust, together with the fuel flow and NOx emission depending on the time of travel is depicted in Fig. 7. A flight profile consists of a chain of flight segments. Generation of a flight profile starts with a first estimate of a take-off weight (based on OEW, payload, distance-based fuel estimate and reserve fuel estimate). During the flight fuel is burned, and the aircraft weight continuous adjusted accordingly. Fuel burn is based on momentary weight, speed, altitude and thrust setting. The resulting momentary (fuel) weight at touchdown is used to correct the initial calculated/estimated fuel weight until remaining fuel after landing equals reserve fuel.

The production of the emissions is based on fuel flow, speed and altitude. The Boeing-2 fuel flow method (e.g. [12]) is used to calculate the NOx emissions along the flight profile. Boeing-2 fuel flow method is a well-accepted, standard method of estimating NOx. Integration along the flight profile yields NOx emissions and fuel burn. The drag difference between the two aircraft configurations is relatively small. The resulting flight profiles and NOx emissions are then hard to distinguish in the graphs depicted in Fig. 7. Visually they coincide.

The CO_2 emissions are proportional to the fuel burn (see [13]). With reference to Table 1 it can be expected that the reduction of CO_2 emissions will be about 0.6% compared to a radome installed at the worse location G3 is being replaced by a conformal (flush integrated) Ku-band antenna as developed in the ACASIAS project. This follows from the relative difference between fuel burn between the radome at location G3 and flush antenna. When the radome is installed at position G2, then the CO_2 savings are negligible

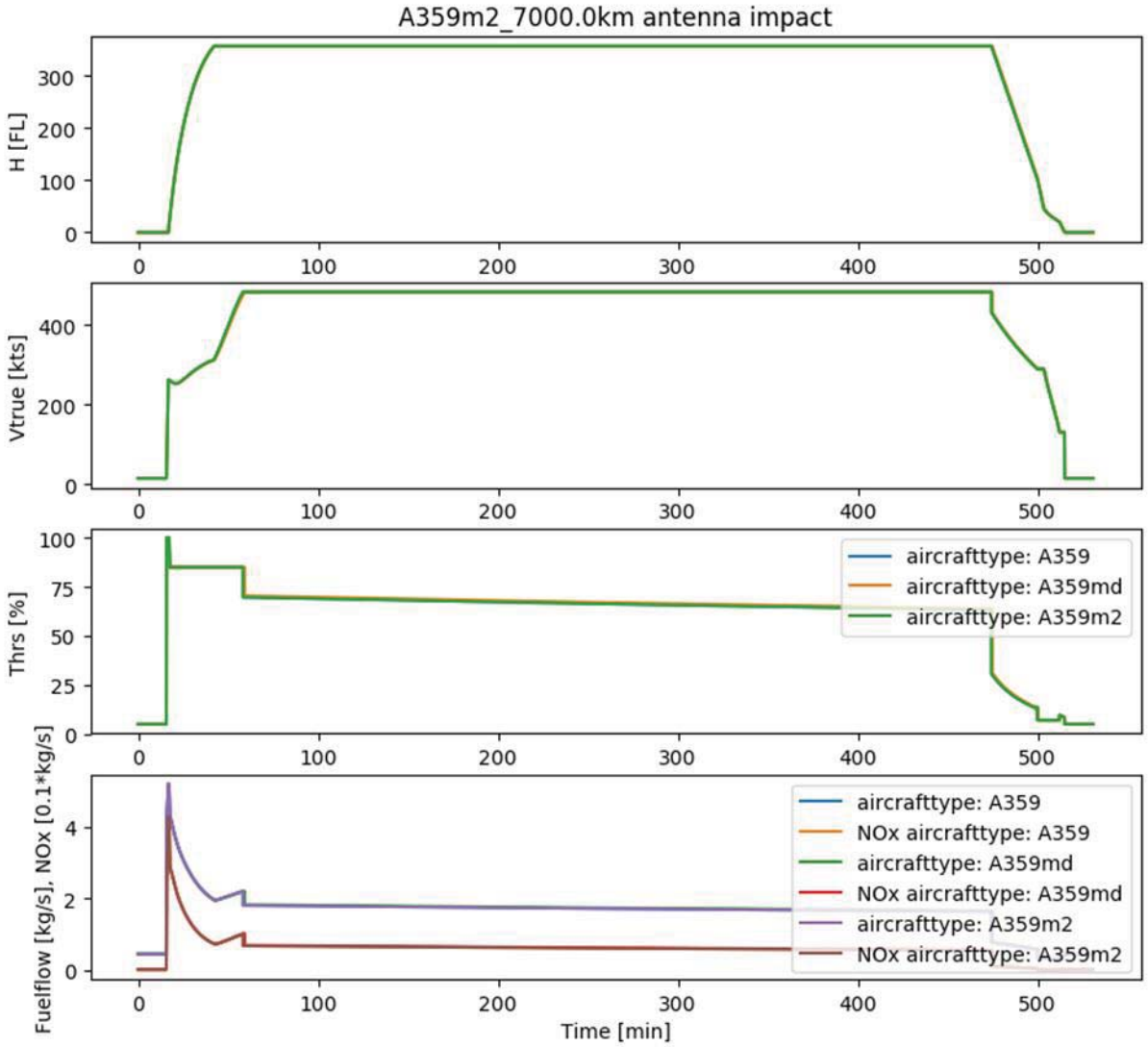

Figure 7: Fuel flow. NOx emissions and parameters of the typical flight of A-350-900

4 CONCLUSIONS

- The effect of the radome on the particular location along the fuselage of the airliner has been evaluated by CFD simulations. NASA Common Research Model has been used as a reference aircraft. The values of the radome's drag and aerodynamic characteristics of the aircraft were used to calculate the AEDP and additional fuel which is needed to carry the radome. The method used for calculation of the fuel needed to carry the radome takes into account the flight profile.
- The aerodynamic effect of the radome or protruding antennas can be expressed by the AEDP or by the weight of the additional fuel needed to carry the radome. It has been found that there can be benefit in hundreds of kilograms in case that the radome will be integrated with the aircraft's surface.
- Another advantage of the integrated antenna is the reduction of the vibration, Noise,

maintenance costs and operational delays reducing risk to protrude parts by collisions with airport cargo cars.

- It has been found that it is possible to reduce the NO_x emission of the typical flight up to 2% and CO_2 emission by about 0.6% by integration of the radome into the fuselage in comparison with the baseline configuration and the worst radome's location. There is negligible saving of the fuel consumption and emissions reduction for the rear location of the radome. The main benefits of this configuration are savings of the additional weight (fuel needed to carry the radome itself) and the other reasons described above.

ACKNOWLEDGMENTS

All work described in this paper has received funding from the European Union's Horizon 2020 research and innovation programme under grant agreement No 723167. ACASIAS project.

This work was supported by The Ministry of Education. Youth and Sports of the Czech Republic from the Large Infrastructures for Research. Experimental Development and Innovations project IT4Innovations National Supercomputing Center LM2015070.

REFERENCES

[1] P. Glowacki. M., Kawalec. S. Czyz, Aviation – Enviromental Threats, Simplified Methodology of NO_x and CO_2 emissions estimation, 5th CEAS Air & Space Conference Challenges in European Aerospace, Delft, 2015

[2] H. Schippers, J. Verpoorte, A. Hulzinga, C. Roeloffzen, and R. Baggen, Towards structural integration of airborne Ku-band SatCom antenna, 7th European Conference on Antennas and Propagation (EuCAP), 2013, pp. 2963-2967.

[3] P. Vrchota, S. Steeger, M. Martínez-Vázquez, M. Světlík, Z. Řezníček, "Aerodynamic and structural design of winglet with integrated VHF antenna", 8th EASN-CEAS Int. Workshop on Manufacturing for Growth & Innovation, Glasgow, 2018, Available: https://doi.org/10.1051/matecconf/201823300018

[4] ACASIAS project website: http://www.acasias-project.eu/

[5] Vassberg, J. C., DeHaan, M. A. Rivers, M. B. and Wahls, M. S., Development of a Common Research Model for Applied CFD Validation Studies, AIAA Paper 2008-6919. 2008.

[6] Drag Prediction Workshop website: http://aaac.larc.nasa.gov/tsab/cfdlarc/aiaa-dpw/Workshop5/

[7] GoGo website: https://www.gogoair.com/commercial/inflight-systems/2ku/

[8] Pointwise website: https://www.pointwise.com/index.html

[9] Wallin, S. and Johansson, A. V., \An Explicit Algebraic Reynolds Stress Model of Incompressible and Compressible Flows," Journal of Fluid Mechanics, Vol. 43, No. 9, 2000, pp. 89{132, also AIAA Paper 89{0269, Jan. 1989.

[10] V. Betak, J. Kubata, Numerical prediction of soot formation in combustion chamber for small jet engines, EFM15 - Experimental Fluid Mechanics 2015, Prague, 2015

[11] ICAO Aircraft Engine Emission Databank: https:// easa.europa.eu/document-library/icao-aircraft-engine-emissions-databank

[12] Schaefer, M., Bartosch, S., Overview on fuel flow correlation methods for the calculation of NOx, CO2 and HC emissions and their implementation into aircraft performance software, 2013

[13] Ashok, A., Dedoussi, I. C., Yim, . H. L., Balakrishnan, H., Barrett, S. R. H., Quantifying the air quality-CO2 tradeoff potential for airports, Atmospheric Environment 99, 2014, pp. 546-555

European Conference on Multifunctional Structures
EMuS 2019
X. Martinez and H. Schippers (Eds)

DESIGN CONSIDERATION FOR FULLY EMBEDDED ELECTRONICALLY STEERABLE SATCOM AIRBORNE ANTENNA EMUS 2019

GONZALO EXPÓSITO *, JUAN M. ABELLÁN*, ANTONIO E. JIMÉNEZ*, FERNANDO MARTÍN*, JOSEFINA MENÉNDEZ*, FERNANDO CANO*, FRANCISCO J. JIMÉNEZ*, AVI GAL†

* EME &Antenna systems, Structural Design, Stress Aerostruct, AIRBUS DEFENCE AND SPACE
Pso. John Lennon, 28906 Madrid, Spain
E-mail: [Gonzalo.exposito; Juan.Abellan; Antonio.e.jimenez; fernando.m.martin; Josefina.menendez; Fernando.cano; Francisco.i.jimenez]@airbus.com - Web page: https://www.e2s2a2project.eu/

†GILAT SATELLITE NETWORKS
21 Yegia Kapayim St., Kiryat Arye Petah Tikva 4913020 Israel
Email: avig@gilat.com

Key words: Embedded Antenna, Flat Ka SATCOM Flat, AESA.

Abstract. in this paper a conceptual design of a SATCOM On The Move (SOTM) system in the Ka band is presented. This system is intended to be airborne and fully integrated in an AIRBUS C295 Flight Test Bench. The system relies in two separated low profile TX and RX antennas (about half a meter size) which reach up to 10Mbps return link and 50Mbps forward link.

1 INTRODUCTION

So far the inflight Internet connectivity for passengers and crew was low or even none at all based on L band SATCOM systems [1]. However, nowadays there are broadband systems, which are based on parabolic antennas located on top of the aircraft covered by a radome, to establish a satellite communication. These antennas are bulky and they introduce an additional aerodynamic drag which can be translated into higher fuel consumption [2]. Low profile antennas based on phase array solutions have been researched for the last years in the X and Ku frequency bands [2] [4] [5]. This new structural embedded Ka SATCOM antenna is a low profile broadband antenna which will overcome the additional aerodynamic drag because it is embedded in the aircraft structure while maintaining the broadband Internet connection. This high data rate communication system will allow the crew and passengers in an aircraft to stay connected anytime anywhere through a satellite communication link. This system is based on an open architecture IP layer protocol, thus allowing all kinds of data traffic.

Airbus DS in order to boost low profile SATCOM antennas leads a project called Embedded Electronically Steerable SATCOM Airborne Antenna ($E^2S^2A^2$) [6]. The project is in line with a new green and intelligent transport such as the new European policies demand, therefore the project is partially funded by the European Commission under the Clean Sky 2 framework. The project is carried out in collaboration with GILAT, RAYSAT and FBM composite partners.

In this paper the progress of the $E^2S^2A^2$ project is presented. The state of the art is summarized in Section 1. The system architecture is described in section 2. Section 3 and 4 shows the airborne design and the structural substantiation. In section 5 the lightning protection is described. Eventually the conclusions are drawn in section 6.

2 SYSTEM DESCRIPTION

The system design is intended to be aligned with the standard described in ARINC 791 [7] in order to achieve equipment interchangeability. The equipment is 28VDC feed and able to withstand the airborne environmental conditions. This system requires the inertial reference and aircraft location, which receives from the Inertial Navigation Unit (INU) according to ARINC 429 protocol. The system performances fulfils the radio electrical regulations ITU-R M1643, ITU-R S2223, ITU-R S580, ECC 184 and ETSI 303978 in order to avoid interferences to satellites located in the Geostationary belt.

According to the standards, the equipment that compounds the system is divided in two mayor groups: the Outside Antenna Equipment (OAE) and the Cabin Enclosed Equipment.

- Outside Antenna equipment
  - TX antenna
  - RX antenna
- Cabin equipment
  - KANDU
  - MODMAN
  - ARINC 429 converter

The system includes two separated TX and RX antennas with an aperture size of half a meter, located in the wing to fuselage fairing WFF. The TX antenna transmits in the 30GHz band and the RX antenna receives in the 20 GHz band. The Antenna performances are shown in Table 1.

Table 1: Embedded Ka SATCOM Antenna parameters

Parameter	RX	TX
Dimensions	447x582x103mm	401x582x104mm
Frequency band	19,7 – 21,2 GHz	29,5 – 31 GHz
Polarization	LHCP (optional)	RHCP (optional)
FOV	Ele: 20-90º Az:360º	Ele: 20-90º Az:360º
XPD	>20 dB	>20 dB
G/T //EIRP	4,4 – 11 dBK	41,6 -49 dBW
Weight	15Kg	13 Kg
Consumption	370 W (avg)	445 W (avg)

The RX antenna includes the steering control by means of several techniques in order to ensure accurate pointing. This equipment includes a local Inertial Unit, receives the KANDU computed steering direction and all these data is integrated additionally to the direction that is based on the Received Signal Strength Indication (RSSI). The TX antenna pointing is

controlled and enabled by means of the RX antenna. The up and down frequency conversion takes place in the TX and RX antennas, therefore Intermediate Frequency is transmitted and received from the antennas to the MODMAN.

The Ka Network Data Unit (KANDU) equipment which stores the satellite ephemeris receives the location and attitude of the aircraft and calculates the steering direction.

The MODEM Manager (MODMAN) interface is based on OpenAMIP ensures total connectivity, management and interoperability. It uses spread spectrum, TX power spectral density enforcement and power limit for skew compensation, overcomes Doppler and supports large number of modulations to ensure adaptive throughput speed depending on radio channel status.

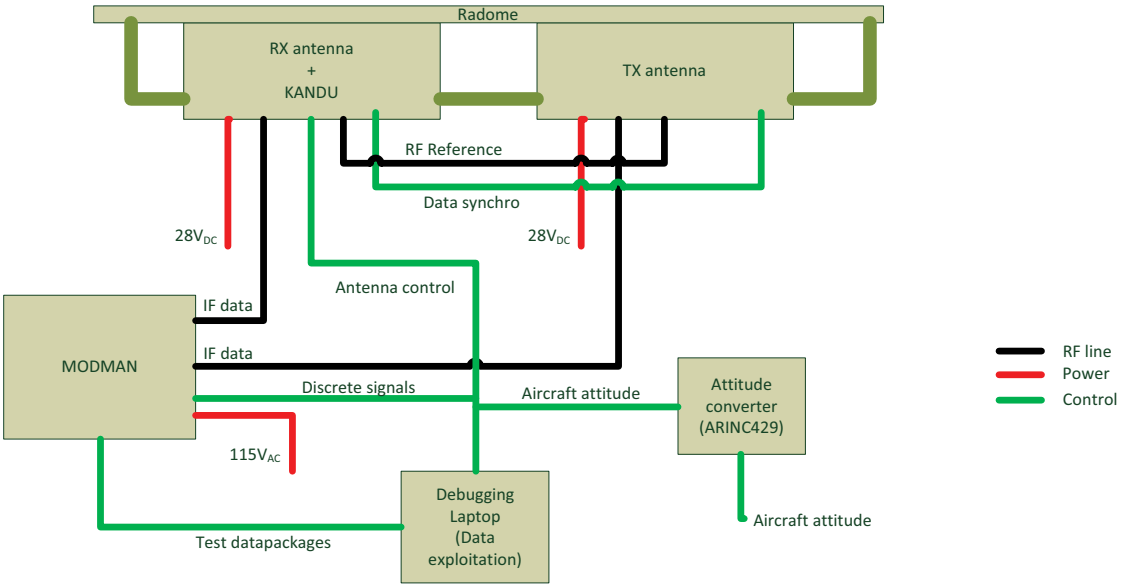

Figure 1: Interface connectivity diagram

3 MECHANICAL DESIGN

The Outside Antenna equipment is located in the external surface of the aircraft in the wing to fuselage fairing area. This zone is environmentally not protected, it is a zone exposed to great temperature changes, weather inclemency's, electromagnetic effects, lightning strike and it is not pressurized.

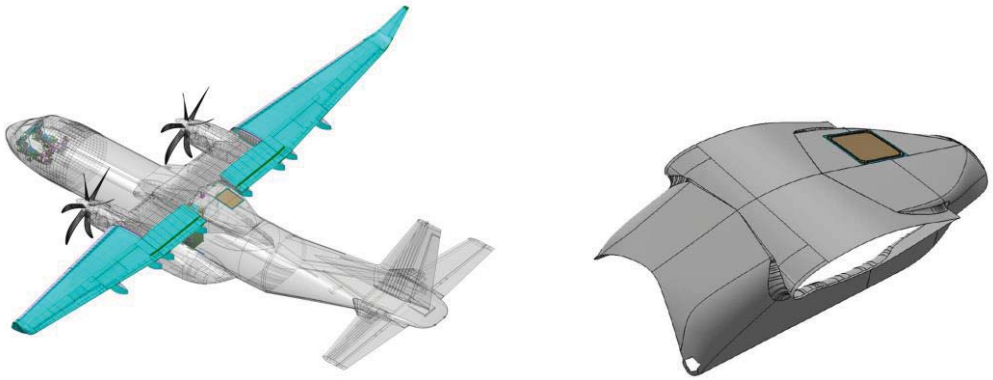

Figure 2: Embedded Ka SATCOM location

One of the old airframe structure sandwich panels that form the wing fuselage fairing structure is replaced by a new subassembly, which incorporates the antenna, and also performs all the structural functions of the substituted panel, respecting the aircraft aerodynamic surfaces. The subassembly if formed by:

- A CFRP solid laminate part to which the antenna equipment's are fixed, and that is installed on the aircraft airframe substructure respecting the replaced sandwich panel's mechanical interfaces. This part of the assembly is called the "Carrier"
- The RX antenna and The TX antenna equipment screwed to the Carrier
- A thin sandwich glass fiber reinforced plastic panel, also attached to the carrier, acting as radome but flush with aerodynamic aircraft surface.

The carrier withstands the antenna equipment loads during aircraft operation to ensure no deformation between TX and RX locations, then not compromising the accurate steering algorithm. The carrier and antennas are covered by a radome transparent to RX and TX frequencies. This radome is a multilayered glass fiber composited with diverter strips located on top and bonded to the carrier panel. All the subassembly parts incorporate electrical bonding means to its connection the to the primary aircraft structure in order to ensure low current path in case of a lightning strike.

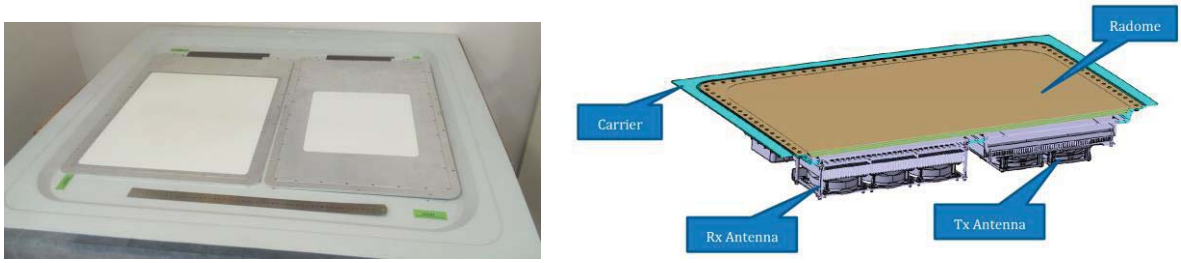

Figure 3: Embedded Ka SATCOM antenna overview

The full subassembly installation process, carrier, antenna equipment, and radome incorporates sealant beads ensuring the full component water tightness, sand or dust ingress and panel edges steps and gaps aerodynamic requirements.

4 STRUCTURAL SUBSTANTIATION

As previously commented, the supporting structure of the outside antenna is joined to the aircraft wing to fuselage fairing so it must comply with common stiffness and strength requirements plus some other specific imposed by the antennas.

Regarding stiffness, radome is directly exposed to the airflow and therefore must guarantee that the aerodynamic shape remains inside tolerances under cruise loads. Carrier, in turn, must resist in-flight inertias of both antennas ensuring small deflections compatible with their correct functionality.

With regards to strength, and despite that both are secondary structural elements, their failure or detachment could indirectly compromise the continuation of safe flight or landing and must be avoided.

4.2 Strength substantiation

Structural strength is to be substantiated by analysis supported by test evidences. Strain fields, deflections and interface loads between components of the assembly (radome to carrier and carrier to fairing) are calculated by using a detailed finite elements model (DFEM) generated on purpose. DFEM reproduces accurately the geometry and thicknesses of the parts accounting also for the laminate stacking sequences and lamina material properties consistent with in-service environmental conditions so that recovered outputs are realistic.

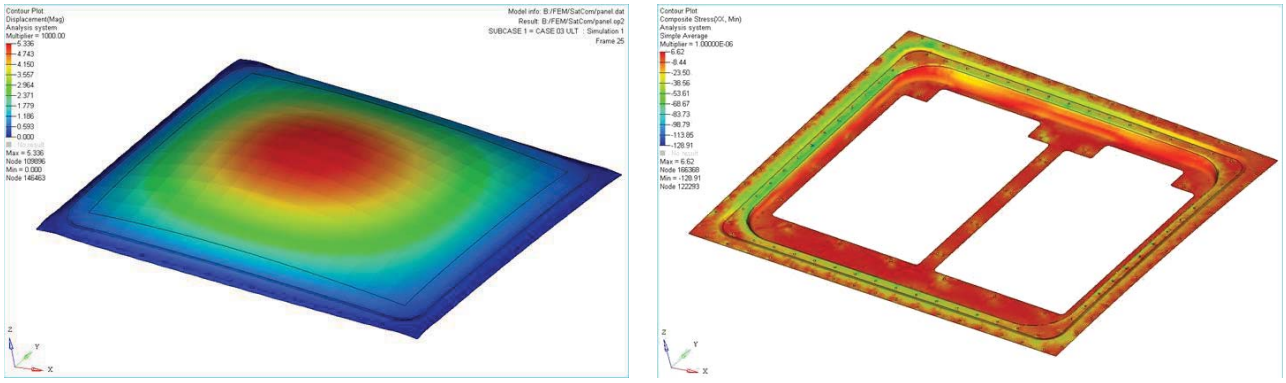

Figure 4: Radome deformed shape (left) and carrier strains distribution (right)

Strength justification is done by classical hand calculations using reliable methods based on worldwide accepted references. Critical failure mode of each particular design detail is identified by exploring all of the relevant.

Testing planned to support the qualification for flight of the supporting structure includes several tests at coupon level to confirm preliminary material allowable values plus one component test at ultimate load to validate DFEM calculations and demonstrate the static strength.

5 LIGHTNING PROTECTION

Aircraft externally mounted equipment are potentially exposed to direct lightning attachment. The consequences of this event are the physical damage on the equipment and the induced current/voltages to internal systems. A concept based on flux antennas reduces the probability of them to suffer a lightning attachment compared with protruding antennas (more attractive for the lightning channel to attach). On the other hand, when the antenna is integrated in the structure, the lightning strike physical damage may have also structural implications that need to be addresses to ensure no compromising structural integrity.

The Outside Antenna equipment is located in the external surface of the aircraft in the wing to fuselage fairing area. This area may be affected by sweeping effect of a lightning channel and it is considered as zone 2A [8]. The design principle in order to ensure minimizing the effects resulting from a lightning strike is based on:

- External metallization of the radome up to a limit to not compromise antenna functionality.

- Lightning unprotected area of the radome with enough dielectric strength so that channel would surface flash over this area to the adjacent metallization instead of puncturing it.
- Provide an electrical bonding path from the radome to the main aircraft structure so the lightning current is transferred in a way that adverse effects are minimized.

6 CONCLUSIONS

In this paper the progress of the $E^2S^2A^2$ project is presented. The design phase is mature and the current solution fulfils the demanding requirements to establish a satellite radio link with an expected throughput of 10Mbps return link and 50Mbps forward link.

REFERENCES

[1] Webpage:www.inmarsat.com/news/successful-airborne-testing-l-band-laisr-service
[2] Webpage:northamerica.airbus-group.com/north-america/usa/Airbus-Defense-and-Space/news/press.20110221_astrium_canada
[3] D. F. Filipovic, "A planar wideband circularly polarized antenna for satellite communications" Technologies for Wireless Applications, IEEE MTT-S Symposium on, Vancouver,BC, Canada. Feb. 1999
[4] W.H. Weedon, S.K. Cheung, "Ku-band low-profile and wideband satellite communication antenna (LPWSA)" Phased Array Systems and Technology (PAST), Waltham, MA, USA. Oct. 2016.
[5] G. M. Rebeiz, L. M. Paulsen, "Advances in SATCOM phased arrays using silicon technologies" Microwave Symposium, Honololu, HI, USA. Jun. 2017
[6] https://www.e2s2a2project.eu/
[7] Aeronautical Radio INCorporation, "791-1 Mark1, Aviation Ku-band and Ka band Satellite communications system" Ago. 2014
[8] EUROCAE ED-91A "Aircraft Lightning Zoning", Jan. 2019

European Conference on Multifunctional Structures
EMuS 2019
X. Martinez and H. Schippers (Eds)

AUTOMATED MANUFACTURE OF GRID STIFFENED PANELS

J. MARCELO MÜLLER,* PETER NIJHUIS*

* Netherlands Aerospace Centre (NLR)
Voorsterweg 31, 8316 PR, Marknesse, The Netherlands
e-mail: peter.nijhuis@nlr.nl, web page: http://www.nlr.org

Key words: Composites Manufacturing, Orthogrid structure, Low cost tooling, Reusable vacuum bag, Conformal antenna, Automated Fibre Placement.

Abstract. *Rib or grid stiffened structures have been investigated for decades, mainly for application in space structures.*

Grid structures offer the possibility to develop more damage tolerant structures as the network of ribs can provide redundant load paths. In an ideal situation, an aircraft fuselage could have a load carrying grid with ribs that carry tensile, compressive and shear loads. The skin would only need to sustain the cabin pressure load.

Such a configuration could lead to significant weight reduction as a different design philosophy can be used. Typically, a damage tolerant design approach allowing a maximum of 3000 μstrain is used for composite aircraft structures. Using a grid structure, a different approach could be developed for a design which could allow strains up to 6000 μstrain.

Automated fibre placement has made composite grid structures an affordable option. However, they pose a major challenge in the development of tooling for cure due to their complex and sometimes irregular structure.

Within the European funded Horizon 2020 ACASIAS programme, square antenna elements are developed to be integrated in a composite aircraft fuselage panel. For this reason, an orthogrid stiffener pattern was chosen. As the skin of the panel must be transparent for the antenna signals, a glass fibre skin is required. A glass fibre skin to carry shear loads and carbon fibre ribs to carry compression and tension loads is therefore being developed to be able to meet structural and electromagnetic requirements.

This paper describes aspects of the ongoing development for the design, manufacture and testing of an orthogrid stiffened structure in an efficient way.

Simple alternating cutting of tapes at the crossing appear to be a suitable solution with a tensile stiffness reduction of 10 % compared to the situation without cuts. These and other details and elements are tested to validate the final design.

The use of reusable silicone vacuum bags was investigated in order to replace complex metal tooling blocks. Besides saving on mould materials and machining, the use of a pre-shaped silicone vacuum bag is expected to reduce labour cost due to a decrease in handling of tooling blocks for positioning and cleaning.

The first trial indicates that good quality laminates can be obtained using reusable vacuum bags. More testing will be carried out to validate the concept for a large 3×1.2 m panel.

1 INTRODUCTION

The European Horizon 2020 ACASIAS programme aims to reduce energy consumption of future aircraft through research into integrated aero-structures with multifunctional capabilities.

One of the subjects within this project is improving aerodynamic performance by integrating antennas in the fuselage. This can not only reduce fuel consumption by reduction of aerodynamic drag**,** but can also make antennas less vulnerable to damage as well, as they do not protrude from the fuselage.

Antennas for communication with Ku-band geostationary satellites are used to provide internet access and entertainment on-board of aircraft. These used to be mechanically steered antennas. Currently, state-of-the-art is the use of hybrid antennas where the horizontal scanning is mechanical and the vertical scanning is electrical. ACASIAS aims to integrate a conformal phased array antenna into the fuselage, thus creating a conformal antenna. See Figure 1 for an illustration.

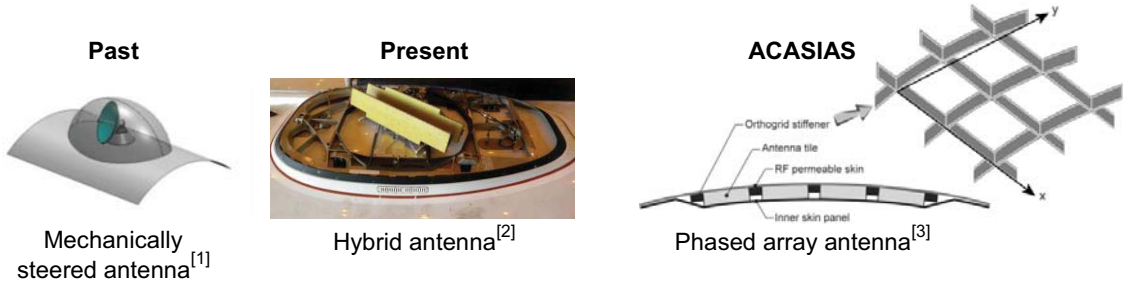

Figure 1: Evolution of Ku-band antennas

Each antenna contains between 24 and 32 antenna tiles. Each antenna tile contains 8×8 antenna elements. The size of an antenna tiles is approximately 100×100 mm. The antenna tiles can be placed in a circular or rectangular aperture, see also Figure 2.

The antenna tiles are square and therefore an orthogrid stiffener pattern was chosen to enable efficient positioning of the antenna tiles.

Rib stiffened structures, also referred to as grid or isogrid structures have been investigated for decades, mainly for application in space structures. Research was initially into metal grid structures and later into composite grid structures in both the USA and USSR[4].

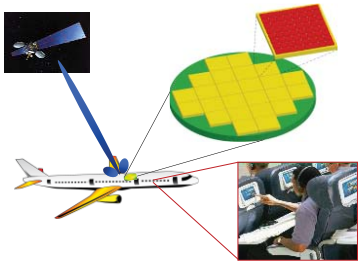

Figure 2: ACASIAS concept for airborne satellite communication

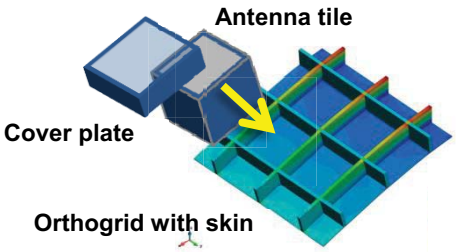

Figure 3: Basic manufacturing concept for fuselage panel

Grid structures offer the possibility to develop more damage tolerant structures as the network of ribs can provide redundant load paths. In an ideal situation, an aircraft fuselage could have a load carrying grid with ribs that carry tensile, compressive and shear loads. The skin would only need to sustain the cabin pressure load.

Such a configuration could lead to significant weight reduction as a different design philosophy can be used. Typically, a damage tolerant design approach allowing a maximum of 3000 μstrain is used for composite aircraft structures. Using a grid structure, a different approach could be developed for a design which could allow strains up to 6000 μstrain.

The skin must be transparent for electromagnetic signals and carry shear loads. The orthogrid must carry compression and tension loads. A hybrid composite structure must therefore be employed to meet these structural and electromagnetic requirements. The requirements can met by using glass fibre reinforced composite for the skins and carbon fibre reinforced ribs. A fuselage panel section with this configuration is being designed, manufactured and tested. The panel section will be 3 m long and 1.2 m wide.

Automated fibre placement (AFP) has made composite grid structures an affordable option. However, they pose a major challenge in the development of tooling for cure due to their complex and sometimes irregular structure.

In the European Union sponsored project LOCOMACHS, it was demonstrated that high quality rib stiffeners can be manufactured in an automated way with relative ease. It is possible to simply place tapes on top of each other, thus forming a stack of thermoset tape that can be cured subsequently, see Figure 4.

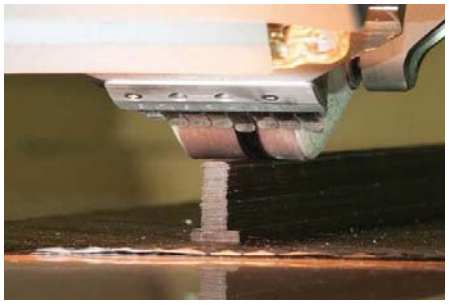

Figure 4: Manufacturing of ribs using automated fibre placement and thermoset material[5]

Figure 5: Advanced Grid-Stiffened Payload Fairing[6]

The deposition method using AFP does not require tooling. However, the cure of the component still requires an extensive tooling set, as tooling blocks must be inserted in all pockets to support the ribs during autoclave cure. This can lead to a large amount of complex tooling blocks. Figure 5 shows the tooling used for the cure of the Advanced Grid-Stiffened Composite Payload Fairing used on the Minotaur 1 launcher. It was developed by the Air Force Research Laboratory (AFRL), Boeing and Orbital Sciences Corp. This large amount of tooling blocks is undesirable, as it increases manufacturing risk and cost.

This paper will describe the ongoing development for the manufacture of an orthogrid stiffened fuselage panel using AFP in an efficient way.

2 ANALYSIS AND DESIGN

A representative section of the fuselage of a regional aircraft was chosen for design, manufacture and testing.

Criteria for selection of the location of the antenna on the aircraft were:

- Aerodynamic and structural loads
- Field of view
- Available space
- Isolation from other antennas
- Location preferably in an area with low loads

For operation at high latitudes, two antennas may be needed, one at each side of the aircraft, to steer the beam to low elevations.

A compromise was reached between field of view vs expected stress and a forward panel with an angle of 30^{o} with regard to zenith was chosen. In Figure 6 the location is shown as a green patch.

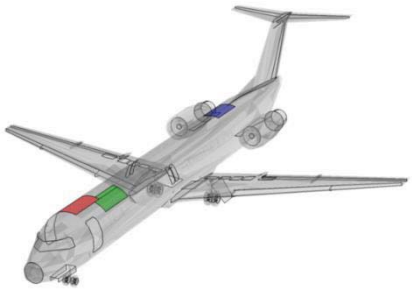

Figure 6: Possible antenna locations indicated by coloured patches.

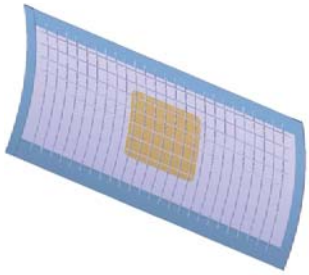

Figure 7: Preliminary design of the carbon fibre fuselage panel. The light brown area is the glass fibre skin section.

As the antenna signals must be able to pass through the skin, it is necessary to incorporate an electromagnetic transparent material in the fuselage skin. As a compromise between functionality and weight, it was chosen to include a section made out of glass fibre into the fuselage skin where the antenna tiles are to be placed.

One major issue with grid stiffened structures is the crossing of the grids. Simply laying crossing tapes on top of each other would lead to an excessive build-up at the crossing, leading to double the thickness of the ribs at the crossings. Spreading tows at the crossings could overcome this, but this will mean that at the crossings, the tape width will be double that of the regular width. The ideal situation would be that the height at the crossing is the same as the rest of the ribs. Preliminary analyses showed that alternate cutting of the tapes, leaving a gap for the transverse tape to pass, would result in a relative small decrease in stiffness at the crossings. This option was examined further.

Two cases were examined in comparison with the theoretical (ideal) case that both tapes would run continuously in both directions. One case is where the tapes are cut in an alternating fashion in each direction: the “real” case. The other is where one rib is kept intact at the crossing and the other rib is complete cut in two: the “worst” case. Figure 8 illustrates this. In Table 1, the results of the finite element analysis on representative material is given. As can be seen, for the alternate cuts, the loss in stiffness is limited. To maintain (buckling) stability, structural aerospace panel designs are normally stiffness driven. Considering the

relative small drop in stiffness and enormous advantages in manufacturing, the alternating cut method was chosen to be implemented.

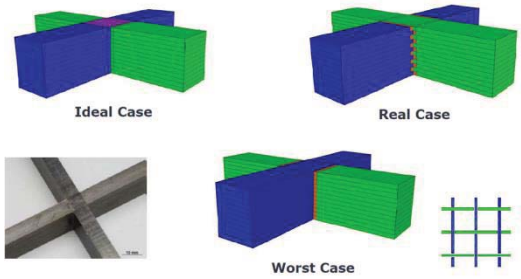

Figure 8: Illustration of crossings and cuts.
The red areas represent cuts in the tape.
Source: CIMNE

	Tension	Bending	Pure shear
Ideal	100	100	100
Real	98	96	97
Worst	90	91	94

Table 1: Calculated stiffness reduction at crossing compared to the ideal case (=100 %).
Source: CIMNE

The decrease in stiffness was compared with an actual test in tension. The average reduction in stiffness between UD coupon tests and actual crossing details with alternating cuts, i.e. the "real" case depicted in Figure 8. It appeared that the stiffness of the crossing was reduced to 90% of the UD coupon test value ("ideal" case in Figure 8). This value is lower than calculated. The calculated value assumes an ideal material, in reality, manufacturing deviations will occur which have to be accounted for. The decrease in stiffness was deemed acceptable and is used for the design of the larger panel.

A number of other detail tests such as the transition zone between carbon and glass fibre and peel strength between ribs and carbon skin were carried out to assess the performance and validate the finite element model.

Using representative loads, a design is being made using finite element analysis. A full-scale test of the 3×1.2 m composite panel will be carried out. The panel will be tested in a test rig with which a combination of pressure, axial and circumferential loads can be applied. Figure 9 gives an overview of the mechanical test that will be carried out.

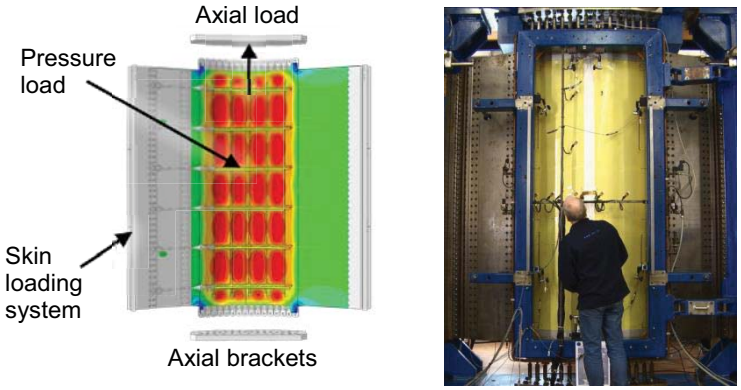

Figure 9: Overview of the panel test set-up. The actual test rig is shown on the right.

3 MANUFACTURING

As discussed in the introduction, a large number of tooling blocks of different shapes and sizes are often necessary to cure an entire grid. The complexity is increased further when the panel is curved and the blocks must be placed on the inner side of the curvature. In this case the blocks must be collapsible and will consist of at least two parts. Although technically feasible, an alternative is desirable that requires less complex tooling and labour at the same or lower risk.

The option of employing reusable vacuum bags was explored to see if they can provide benefit over hard tooling. Reusable vacuum bags are used to replace single use bagging films during composite autoclave cure. They are usually made of silicone rubber and conform to the shape of the product that must be cured. Manufacturing of these vacuum bags is done by either brushing or spraying uncured silicone rubber on a plug in the shape of the final product followed by (often) room temperature cure. The bag obtained is resistant to temperatures of up to 260 °C and can be reused multiple times.

The height of ribs of the orthogrid under investigation is below 10 mm. The grid itself is not a very complex shape in terms of geometry. A flexible vacuum bag could be easily placed over the product and removed afterwards. Compared to the material cost, the machining, cleaning, applying release agent and positioning of metal tooling blocks on the product, the silicone bag is an attractive option to save on material but also, perhaps even more important, on labour cost.

Trials are being carried out to investigate if a reusable silicone bag shaped in the form of an orthogrid could be used for consolidation. The goal is not only to take advantage of the flexibility of the bag to position and remove it from the product, but to use it to simplify the bag manufacture itself as well.

The intention is to manufacture a flat silicone bag that will be placed on the curved product. The diameter of the fuselage under study is 3.3 m. Consequently, the radius of the curvature is relatively large and the deformation of the flexible bag should be limited. In addition to this, the material itself has an elongation at break of over 300 % and should be able to accommodate some deformation. In this way, it is possible to manufacture the vacuum bag in a low-cost way, without the need for a curved plug.

This concept is being tested on a small-scale first. A smaller panel was laid down using fibre placement for this purpose.

A simple plug was made using aluminium strips. Two-component silicone rubber was applied on the plug to form the bag (Figure 10).

Figure 10: Silicone being applied to aluminium plug

Figure 11: Placing vacuum bag over uncured product

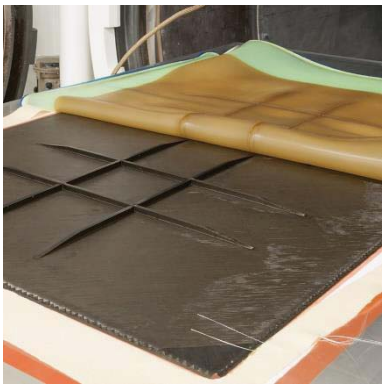

Figure 12: Product after autoclave cure

Figure 13: Detail of crossing after cure

The fibre placed panel was bagged using the silicone bag (Figure 11) and subsequently cured (Figure 12 and Figure 13).

The resulting panel showed some surface roughness at the bagging surface. A C-scan confirmed that the skin laminate quality was good and the imperfections at the bagging side were only superficial. The cause of the surface roughness was not clear and is being investigated further. These first trials indicate that the use of reusable silicone vacuum bags could be an efficient alternative to more traditional moulding blocks.

4 DISCUSSION AND CONCLUSIONS

The goal of this study is to develop, design and a stiffened fuselage panel to incorporate an antenna array.

An orthogrid stiffening pattern was chosen to accommodate the square antenna tiles. The design, manufacture and test of a stiffened orthogrid panel are being investigated with an emphasis on a low-cost manufacturing solution.

Simple alternating cutting of tapes at the crossing appear to be a suitable solution with a tensile stiffness reduction of 10 % compared to the situation without cuts. These and other details and elements are tested to validate the final design.

The use of reusable silicone vacuum bags was investigated in order to replace complex metal tooling blocks. Besides saving on mould materials and machining, the use of a pre-shaped silicone vacuum bag is expected to reduce labour cost due to a decrease in handling of tooling blocks for positioning and cleaning.

The first trial indicates that good quality laminates can be obtained using reusable vacuum bags. More testing will be carried out to validate the concept for a large 3×1.2 m panel.

5 ACKNOWLEDGEMENTS

This project has received funding from the European Union's Horizon 2020 research and innovation programme under grant agreement No 723167.

6 REFERENCES

[1] H. Schippers et al., "Broadband Conformal Phased Array with Optical Beam Forming for Airborne Satellite Communication", IEEE Aerospace Conf., March 2008, Big Sky, MT, USA.

[2] S. Panthi, J. King, and C. McLain. "The eXConnect Broadband Aeronautical Service", 31st AIAA International Communications Satellite Systems Conference (ICSSC), (AIAA 2013-5621), October 14-17, 2013, Florence, Italy. https://doi.org/10.2514/6.2013-5621

[3] ACASIAS web site at http://www.acasias-project.eu/objectives-and-innovations-11, Accessed 21 March 2019.

[4] Steven M. Huybrechts, Steven E. Hahn and Troy E. Meink, "Fabrication, analysis and design methods", ICCM12 Conference, Paris, July 1999, paper 357 , ISBN 2-9514526-2-4

[5] J. M. Müller and W. van den Brink, "Comparison of integrated rib stiffened and L-blade stiffened composite panels manufactured using simple tooling methods," in SAMPE Technical Conference, Long Beach, USA, 2016.

[6] Michael P. Kleiman, "Light carbon-fiber structure protects heavy space cargo", AFRL Space Vehicles Directorate, February 26, 2007. Available at: https://www.wpafb.af.mil/News/Article-Display/Article/401406/light-carbon-fiber-structure-protects-heavy-space-cargo/ Accessed 21 March 2019.

European Conference on Multifunctional Structures
EMuS 2019
X. Martinez and H. Schippers (Eds)

STRUCTURAL ANALYSES OF ORTHOGRID FUSELAGE PANEL FOR INTEGRATED KU-BAND SATCOM ANTENNA – EMUS 2019

FRANCESC TURON*, FERMIN OTERO* AND XAVIER MARTINEZ†*

* International Center for Numerical Methods in Engineering (CIMNE)
Technical University of Catalonia (UPC)
Gran Capitn s/n, 08034 Barcelona, Spain
e-mail: fturon@cimne.upc.edu, fotero@cimne.upc.edu

† Departamento de Ciencia e Ingeniera Nutica, FNB
Technical University of Catalonia (UPC)
Pla de Palau 18, 08003 Barcelona, Spain
e-mail: x.martinez@upc.edu

Key words: Composites, Numerical Methods, Antenna, Panel, Multifunctional, Serial-Parallel Mixing Theory

Abstract. The aim of this work is to describe the structural analysis of a multifunctional aircraft fuselage panel. The structure of the panel has an embedded antenna tiles. The panel consists of UniDirectional (UD) carbon fibre reinforced composite skin stiffened with ortho-grid ribs, and a transparent skin window made using UD glass fibre reinforced composite. The ortho-grid structure is a structural reinforcement but also the antenna tiles support. The presented work proposes a numerical multiscale strategy. The laminate is simulated with solid elements, in order to capture the real kinematics of the material, but several laminas are condensed in a single finite element. The performance of each lamina is obtained using the Serial-Parallel (SP) mixing theory. The specific formulations developed have been very useful to identify and study the mechanical performance of these new structures and the localization of unknown and un-predicted hot-spots in the structure.

1 INTRODUCTION

The Fokker 100 is the target aircraft to integrate the ortho-grid stiffness fuselage panel with the integrated antenna. The forward crown panel at the top of the fuselage is selected for the ortho-grid panel location, as in this section the antenna will have the best performance with the lower loads. It should be noted that in this work no aerodynamic loads are included, and that a variation of temperature conditions is not foreseen.

The panel is manufactured using thermoset prepreg materials, which are suitable for aerospace structural applications. The panel skin and the ortho-grid ribs consist of carbon fibre reinforced material: Hexcel 8552 resin and AS4 fibre. On the other hand, the transparent panel window skin consists of glass fibre reinforced material: Cytec FM906-27 resin and S2 glass 187-460 fibre.The ortho-grid ribs are laid-up using automated fibre placement over the panel skin. The

panel skin has a material transition in the glass window edges through interleave plies of carbon and glass. Finally, the whole fuselage panel is cured in an autoclave.

Even with nowadays computational capacity it is almost impossible to analyse a structural component taking into account a detailed definition of the laminate layup. For this reason, in this work a numerical multiscale strategy is proposed. The laminate is simulated with solid elements, in order to capture the real kinematics of the material, but several laminas are condensed in a single finite element. The performance of each lamina is obtained using the serial-parallel mixing theory.

2 SERIAL-PARALLEL MIXING THEORY

The serial-parallel mixing theory could be defined as a phenomenological homogenization, where the behavior of the composite is obtained from the constitutive response of their materials components. This theory has been developed by Rastellini et al. [1], and is a natural evolution of the parallel mixing theory developed by Car et al. [2]. The theory is based on the compatibility conditions, but introduces a modification in the iso-strain hypothesis. The iso-strain condition is imposed in the reinforcement direction and a new iso-stress condition is imposed in the transversal directions. Commonly, for UD composites, the formulation applies an iso-strain condition in fibre direction and a iso-stress condition in the other ones.

Taking only two composite components, the equations that define the stress (σ) equilibrium and setting up the strain (ε) compatibility between the individual components follow the hypothesis previously described are:

Parallel behavior:

$$\begin{aligned} {}^{c}\varepsilon_p &= {}^{m}\varepsilon_p = {}^{f}\varepsilon_p \\ {}^{c}\sigma_p &= {}^{m}k^{m}\sigma_p + {}^{f}k^{f}\sigma_p \end{aligned} \tag{1}$$

Serial behavior:

$$\begin{aligned} {}^{c}\varepsilon_s &= {}^{m}k^{m}\varepsilon_s + {}^{f}k^{f}\varepsilon_s \\ {}^{c}\sigma_s &= {}^{m}\sigma_s = {}^{f}\sigma_s \end{aligned} \tag{2}$$

where the superscripts c, m and f stand for composite, matrix and fibre, respectively and ${}^{i}k$ is the volume-fraction coefficient of each constituent in the composite.

This theory can predict the linear and non-linear behavior of structural elements made of composite materials. Composite materials that can be modelled are those formed of long fibres embedded in a matrix. The theory predicts the different behavior of the composite, depending on the load direction. The potential of this theory is to predict accurately the response of composites in the linear and non linear range as has been proved in several papers [3, 4]. Among the different failure modes that can be captured, in [5] it is shown that the serial-parallel mixing theory is able to simulate the delamination problem naturally, without having to define specific elements or predefine the path of fracture.

3 NUMERICAL MODEL DESCRIPTION

Finite element numerical models are used to study the structural response of the panel for different loading cases. To reduce the computation time required for the simulations, and to be able to include all details in the models developed, only a reduced section of the fuselage

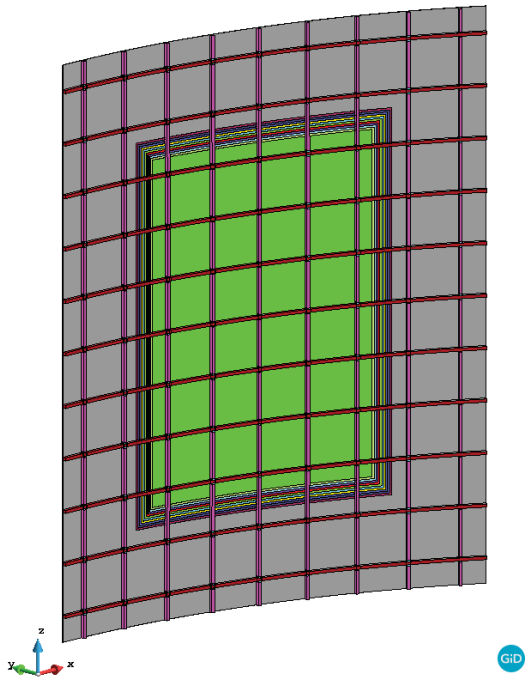

Figure 1: Reduce numerical model for the ortho-grid fuselage panel.

is analysed. In order to obtain the same results that would be reached with the whole panel consistent boundary conditions are imposed.

In the Figure 1, the central green window represents the UD glass fibre reinforced composite transparent window skin. While the grey part of the skin uses UD carbon fibre prepreg material. Figure 2 shows in detail the different geometries in which every part of the model is discretized to model the connection between skin/ribs, rib/rib and the glass/carbon skin transition.

To represent the transition regions, it is necessary to define models with a high level of detail in order to account for changes in layer orientation, composite intersections (glass to carbon), and all different specificities shown in Figure 3. Consequently the quantity of elements required by the model is high, which increases the computational cost of the numerical analysis, in terms of time and memory. In order to improve the machine time and simplify the numerical model a numerical multiscale approach is proposed.

In the numerical model, the laminate is simulated with solid finite elements, to capture the real kinematics of the material, but several layers are condensed in a single finite element. The performance of each lamina is obtained using the SP theory. On the right side of the Figure 3 the homogenized transition zone is shown. As can be seen, there are three element through the thickness, and each one of these elements contains internally several layers. The upper part of the figure shows the numerical model developed while in the lower part are represented the different layers assigned to each region of the model.

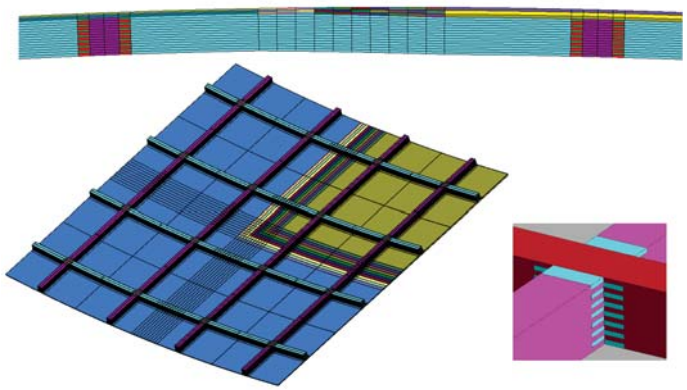

Figure 2: Detailed view of the glass/carbon skin transition, and rib connections.

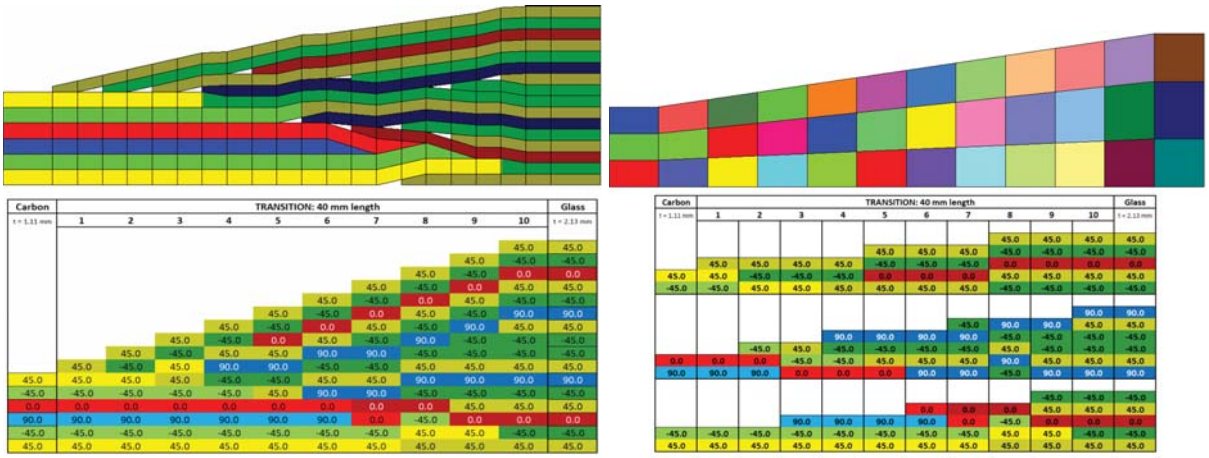

Figure 3: Detailed view of the glass/carbon and homogenized model skin transition.

4 RESULTS

In the following it is presented the numerical results obtained for a tension load case. A tension flow (261.5 N/mm) in the top side and a fixed support in the bottom side of the panel is imposed. It is also applied an the internal pressure (0.08 N/mm^2) of the fuselage. Therefore, specific boundary conditions have to be imposed on both lateral side of the panel.

The total displacement field obtained is shown in Figure 4. The left side shows a inside view of the displacements obtained and the right side a external view of the panel. The maximum values of displacements are presented in the top of the panel because of the tension load, and they are extended to the middle of the panel for the effect of the internal pressure. In Table 1 the most relevant displacement results are presented.

The longitudinal ribs of the panel take most of the load applied. A mean stress value of around 320 MPa is presented in the longitudinal ribs. The maximum value of the principal stress obtained is located on the longitudinal rib close to the Glass/Carbon skin transition in the rib connection. The rib connections have half of the UD carbon plies cut to allow the continuity

Table 1: Relevant displacement results obtained

Max. Long. Displ. (Z dir.) [mm]	2.35
Max. Radial Displ. [mm]	1.85
Mean Radial Displ. [mm]	1.1
Max. Relative Radial Displ. [mm]	0.75

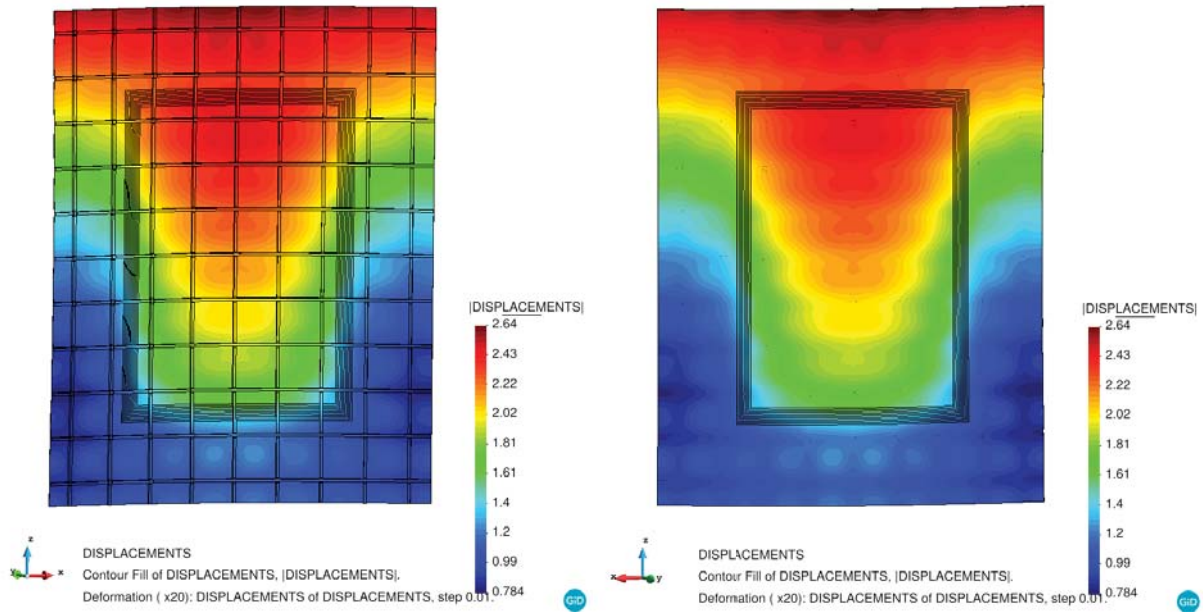

Figure 4: Total displacement field obtained for the tension load case.

of the plies in the perpendicular direction. The maximum stress obtained is around 700 MPa and it is found in the continue layers of the rib connection. The left side of Figure 5 shows the critical zone regarding the stresses level. Another critical area is the region in the connection where the cut layers end, as this region contains only matrix and the stresses are close to 60 MPa. This stress level is close to the maximum ultimate strength of the matrix component.

The skin and the material transition zones do not reach the maximum design strain value (i.e. 3600 μ%). However, in the rib connections and the rib/skin connection the principal strain field presents higher values. An amplified view of the rib connection is shown in the right side of Figure 5. For the additive material in the ribs connection, a higher design value of maximum strain could be accepted. The mentioned figure shows a strain value in this material around 6000 μ%.

5 CONCLUSIONS

A multiscale strategy that combines the finite element method and the SP formulation is proposed. The numerical approach presented allows the analysis of complex composite struc-

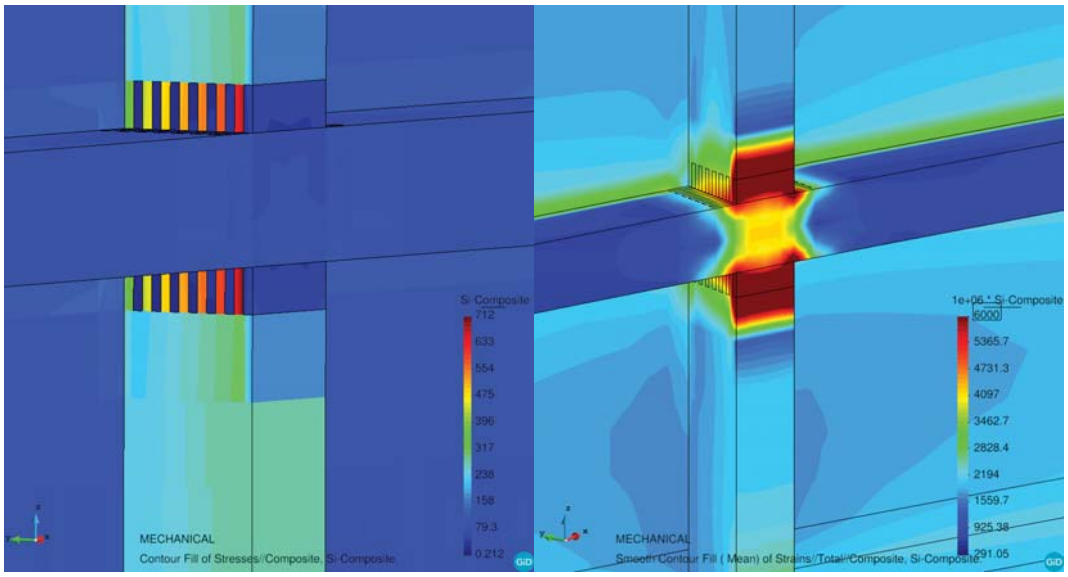

Figure 5: Zone with the maximum value of the principal stresses in the fuselage panel.

tures with an affordable computational cost, which is basic for the development of new multifunctional composite structures. The formulation developed has been very useful to study the mechanical performance of the ortho-gid fuselage panel, and to identify the localization of unknown and un-predicted hot-spots in the structure.

REFERENCES

[1] Rastellini F. and Oller S. and Salomón O. and Oñate, E. Composite materials non-linear modelling for long fibre-reinforced laminates continuum basis, computational aspect and validations. *Computers and Structures.* (2008) **86**:879-896.

[2] Car E. and Oller S. and Oñate, E. An anisotropic elastoplastic constitutive model for large strain analysis of fiber reinforced composite materials. *Computer Methods in Applied Mechanics and Engineering.* (2000) **185**:245-277.

[3] Martinez X. and Oller S. Numerical simulation of matrix reinforced composite materials subjected to compression loads. *Archives of computational methods in engineering.* (2009) **16**:357-397.

[4] Otero F. and Oller S. and Martínez X. and Salomón O. Numerical homogenization for composite materials analysis. Comparison with other micro mechanical formulations. *Composite Structures.* (2015) **122**:405-416.

[5] Martinez X. and Oller S. and Barbero E. Study of Delamination in Composites by Using the Serial/Parallel Mixing Theory and a Damage Formulation. *In: Mechanical Response of Composites. Computational Methods in Applied Sciences*, vol 10. Springer, Dordrecht (2008)

European Conference on Multifunctional Structures
EMuS 2019
X. Martinez and H. Schippers (Eds)

Structural Integration of Ku-band SatCom Antenna into novel Fuselage Panel

J. VERPOORTE, A. HULZINGA

Netherlands Aerospace Centre NLR
Voorsterweg 31, 8316 PR Marknesse, The Netherlands
e-mail: jaco.verpoorte@nlr.nl, adriaan.hulzinga@nlr.nl

Key words: Antenna, integration, lightning protection, Ku-band, satellite communication, orthogrid.

Abstract. This paper addresses the structural integration of a Ku-band SATCOM antenna in the fuselage of an aircraft. The phased array antenna consists of 25 antenna tiles that are integrated in an orthogrid fuselage panel. The specific electromagnetic aspects of the antenna integration will be discussed in this paper; this concerns the lightning protection of the antenna tiles and the electromagnetic interaction of the CFRP orthogrid and GFRP fuselage skin with the array antenna. The structural properties and thermal management of the antenna will be discussed in separate papers [1,2,3].

1 INTRODUCTION

The main objective of the ACASIAS project is to contribute to the reduction of energy consumption of future aircraft by improving the aerodynamic performance through conformal and structural integration of antennas that are normally protruding. This paper deals with the conformal integration of an electronically steerable Ku-band antenna for satellite communication, which does no longer require a protruding radome.

In the ACASIAS project a composite stiffened orthogrid fuselage panel is being developed for integration of Ku-band SATCOM phased array antenna tiles (Figure 1). The Ku-band antenna tiles to be integrated are based on the antenna tiles that were developed in a previous FP7 project called SANDRA. In the SANDRA project the focus was on the functional performance of the antenna tiles. In the ACASIAS project the focus will be on the integration of the antenna tiles in a fuselage panel, taking into account integration aspects like thermal control and lightning protection. The ribs of the orthogrid will be made of Carbon Fibre Reinforced Plastic (CFRP), while the skin will consist partly of CFRP and partly of Glass Fibre Reinforced Plastic (GFRP). The GFRP skin is necessary to enable the electromagnetic radiation from the antenna underneath it. The orthogrid has a pitch of 107 mm. The rib thickness is 7 mm and the rib height is 8 mm. The array consists of 5 by 5 antenna tiles. Each antenna tile has 8 by 8 antenna elements. The tile will have a maximum size of 100 by 100 mm and a thickness of 7.8 mm. The tiles may be made a bit smaller to accommodate tolerances and deformation of the orthogrid.

The structural design and analysis of the orthogrid will be discussed in separate papers [1,2].

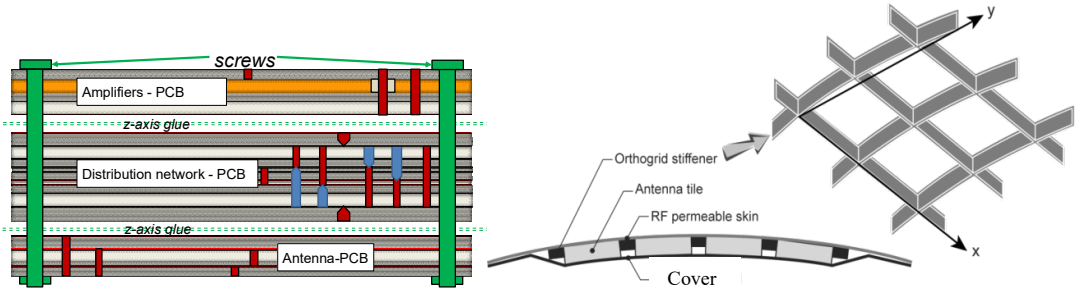

Figure 1. Cross section of antenna tile and orthogrid.

A complete array of 25 antenna tiles will be designed and manufactured. However, not all tiles will be real antennas since the main focus in this project is on cooling solutions and lightning protection. Some tiles will only have passive components (resistors) and will not operate as an antenna. The thermal behaviour of these dummy tiles will be representative for the real antenna tiles. The antenna tiles will have built-in cooling solutions. These cooling solutions and the thermal behaviour of the antenna tiles will be discussed in a separate paper [3]. This paper will focus on the electromagnetic aspects of the antenna integration: the influence of the fuselage structure and of the lightning protection material on the behaviour of the satcom antenna.

2 INFLUENCE OF THE CFRP ORTHOGRID AND GFRP SKIN

In general the radiation pattern of an array antenna depends on the layout of the array and on the radiation pattern of the individual antenna elements. In this case, the radiation pattern of the array antenna will be determined by the layout of the antenna tiles, the separation between the antenna tiles and the radiation pattern of the (stacked) patch antennas. Too large a separation between the antenna tiles may introduce grating lobes in the radiated pattern or increase the side lobe level. The tiles are separated by the ribs of the orthogrid. Therefore the thickness of the ribs of the orthogrid has to be taken into account in the design of the antenna array. In addition, the influence of the material of the ribs on the radiation pattern has to be taken into account. The CFRP ribs of the orthogrid are conductive. In the design of the antenna elements and antenna tiles the conductivity of the ribs will have to be taken into account, especially under scanning conditions of the antenna. The skin of the fuselage panel above the antenna tiles is transparent to enable the electromagnetic radiation by the antenna. Therefore the complex permittivity of the GFRP material will have to be determined to assess the specific transmission, reflection and absorption properties of the GFRP skin for Ku-band waves.

2.1 Influence of tile separation on radiation pattern

The antenna tiles in the orthogrid are separated by the ribs of the orthogrid. In order to obtain sufficient structural strength, the ribs of the orthogrid have a minimum width (7 mm) and height (8 mm). Due to the rib thickness the antenna tiles do not touch but have a separation of 7 mm. This is in the order of a quarter of the wavelength and therefore this gap will have an influence on the radiation pattern. In Figure 2 the influence is shown of the gap between the antenna tiles. When the gap increases from 0 to 3 mm some staircasing becomes

visible in the radiation pattern. This implies that the sidelobe levels increase slightly at some angles. When the gap increases from 3 mm to 7 mm the sidelobes increase even more. Recommendations are given for the radiation pattern of transmit antennas for Ku-band satellite communication [4,5]. In order to meet these standards, the sidelobes have to be suppressed to a certain level. This can be done by applying an amplitude taper over the array. However, this will reduce the gain and broaden the main lobe also. In addition it adds to the system complexity because not only the phase of the antenna elements has to be controlled (for beam steering) but also the amplitude (for side level reduction). As an example, the effect of applying a Chebyshev tapering is shown in Figure 3.

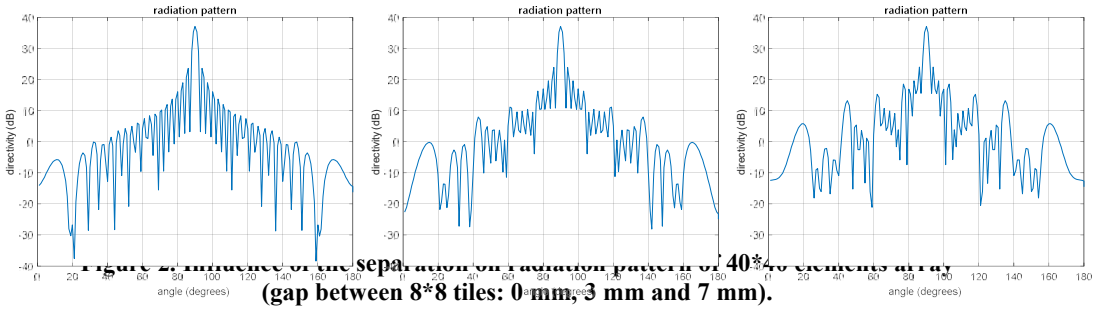

Figure 2. Influence of the separation on radiation pattern of 40*40 elements array (gap between 8*8 tiles: 0 mm, 3 mm and 7 mm).

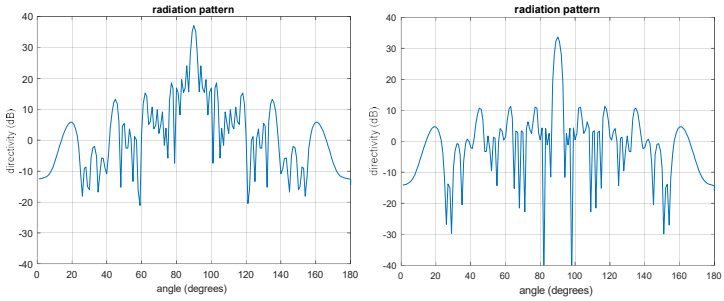

Figure 3. Influence of amplitude tapering on radiation pattern of 40*40 elements array (left uniform illumination and right Chebyshev tapering).

2.2 Influence of CFRP orthogrid on the radiation pattern of antenna tile

The ribs are made of CFRP. This material has a specific conductivity and will therefore have an influence on the input impedance and the radiation pattern. Since the ribs are at the edge of an 8*8 array, the effect will be mainly on the edge elements and less on the centre elements. The antenna tiles will be installed in the orthogrid with a certain air gap between the antenna tile and the skin to accommodate for deformation of the fuselage panel and to decrease the influence of the skin on the antenna performance. In Figure 5 the influence on the radiation pattern for two orthogonal polarisations is given as a function of the height of the rib. The radiation pattern is given for three different rib heights (0, 3 and 6 mm), where the height given is the height of the rib above the antenna tiles (the actual height of the ribs is 8 mm). In Figure 5 the radiation pattern for a corner element of an antenna tile is shown (X11) and in Figure 6 the radiation pattern is given of the second antenna element (X22) along the

diagonal of the antenna tile (Figure 4 shows the position of the antenna elements).

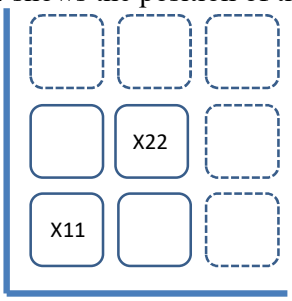

Figure 4. Numbering of antenna elements in array.

The radiation pattern is given for a single antenna element in a small array (4 by 4), therefore this antenna also radiates to the back. The influences of the rib on the forward radiation of the antenna is very small. Some influence can be seen on the backward radiation of the antenna element. In general the influence is larger when the rib height is larger. The influence is most significant for the corner element (X11) and less for elements more to the centre (like X22).

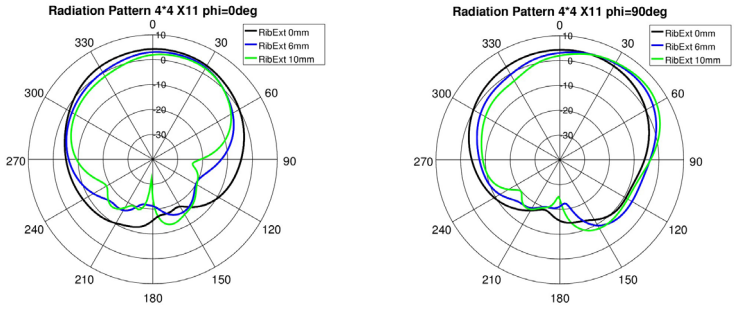

Figure 5. Influence of rib height on the radiation pattern of an antenna element in the corner of the antenna tile X11 (two orthogonal polarisations).

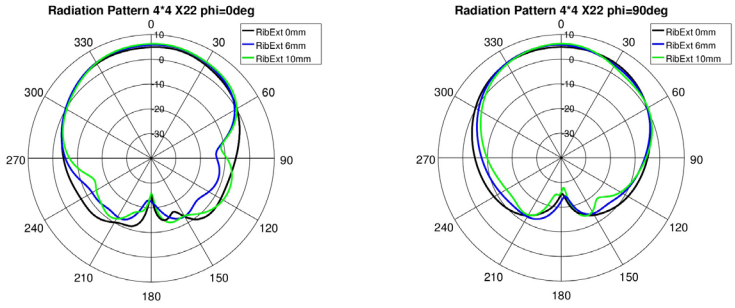

Figure 6. Influence of rib height on the radiation pattern of an antenna element near the corner of the antenna tile X22 (two orthogonal polarisations).

2.3 Influence of the GFRP skin on the input impedance and radiation pattern of the antenna

In Figure 7 the influence of the thickness of and the distance to the GFRP skin is given. The skin is made of S-2 glass fibres. In this case the influence of the skin on the reflection loss (S_{11}) of a single antenna element is given. The antenna element is designed to give a reflection loss less than -10 dB between 10.7 GHz and 12.7 GHz. If the skin has a thickness of 1 mm the S_{11} increases to about -6 dB, which is too high. For larger skin thickness (e.g. 6 mm) the S_{11} shows a better behaviour: the reflection loss is below -10 dB in a larger part of the frequency band. Probably a skin with a thickness of 6 mm resembles a radome with thickness of half a wavelength which has in general good transmission and reflection characteristics. A skin with a thickness of much less than 1 mm will probably also give a good performance. If a skin of 6 mm is too heavy and a skin of less than 1 mm is too thin from a structural point of view, then a sandwich construction could be applied (two thin layers of S-2 glass with a low permittivity material in between having a total thickness of about 6 mm). In the structural design, the thickness of the GFRP layer is currently fixed at 2.1 mm. If the layer is thicker, the glass window will become too stiff and will absorb all the forces in the fuselage panel. To obtain a better S_{11} with a 2.1 mm GFRP skin, material with same permittivity as glass has to be applied between the skin and the antenna tile to get a good performance. Also the design of the antenna element needs to be optimised for the presence of the GFRP skin once the final value for the thickness is known.

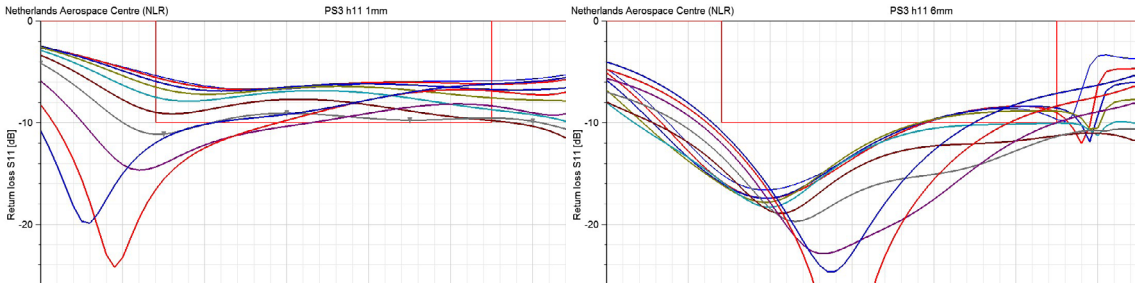

Figure 7. Influence of thickness and distance of GFRP skin on reflection loss (S_{11}) of an antenna element (left thickness 1 mm and right thickness 6 mm).

3 LIGHTNING PROTECTION

The lightning protection for the antenna will be applied in two stages, on element level and on array level.

3.1 Design of antenna elements with lightning protection

The antenna elements (stacked patches) will have both patches grounded using a connecting via in the centre of the patch. In this location the grounding via will have no influence on the electromagnetic performance of the antenna element. In Figure 8 the metal parts of the antenna element are shown. The ground via in the centre of the patches is clearly visible. This via will be used to avoid static charges on the patches and to provide a safe path for lightning currents.

3.2 Lightning protection for the antenna array

In addition some kind of lightning diversion needs to be added to the non-conductive GFRP skin. In general the skin has a copper mesh on the outside to conduct the lightning current. Since a copper mesh would block the electromagnetic waves, lightning diverters (strips) will applied in the GFRP skin just above the ribs of the orthogrid. These strips will be connected to the copper mesh outside the antenna window. To determine the influence of the lightning diverters, an analysis was done on a small array of 4 x 4 antenna elements (instead of 8 x 8 antenna elements). In Figure 9 the small antenna tile is shown with and without ribs and strips. For this simulation the ribs are made of perfectly conducting material (instead of CFRP with a lower conductivity).The ribs are 2 mm higher than the antenna tiles. The lightning strips are 4 mm above the antenna tile. In Figure 10 and Figure 11 the radiation patterns are shown for steering angles of 0 and 45 degrees. The influence of the lightning diverters is visible but the radiation pattern is still acceptable.

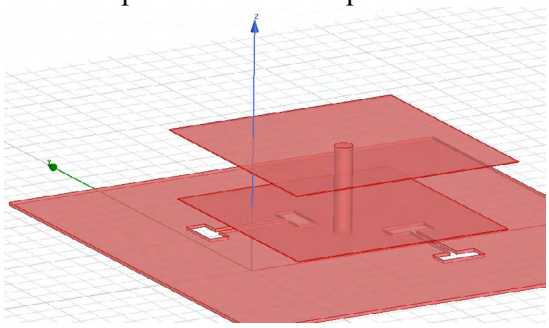

Figure 8. Stacked patch antenna element with ground via in the centre.

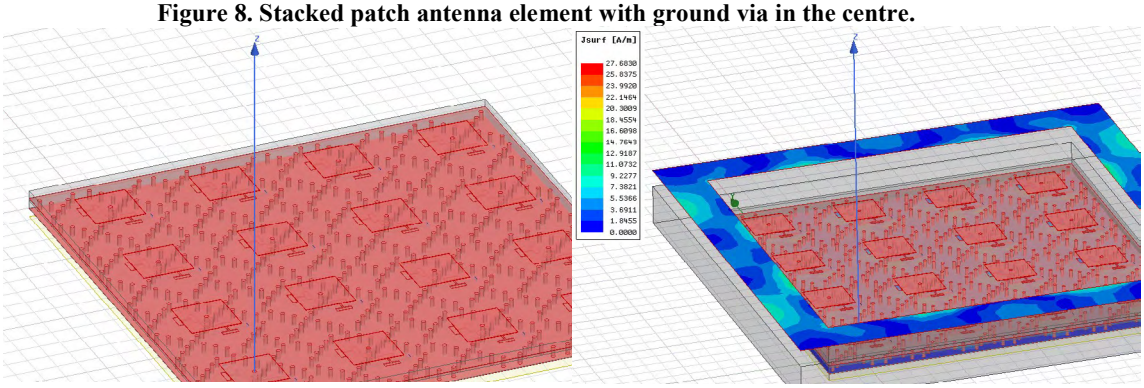

Figure 9. Tile of 4 x 4 antenna elements (left without ribs and strips, right with ribs and strips).

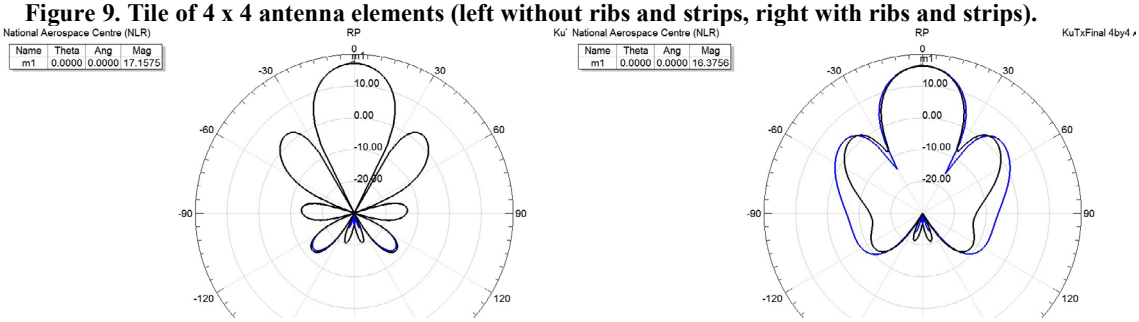

Figure 10. Influence of rib and lighting strip on radiation pattern of 4 x 4 array (left without ribs and strips, right with ribs and strip). Steering angle 0 degrees, two orthogonal polarisations given.

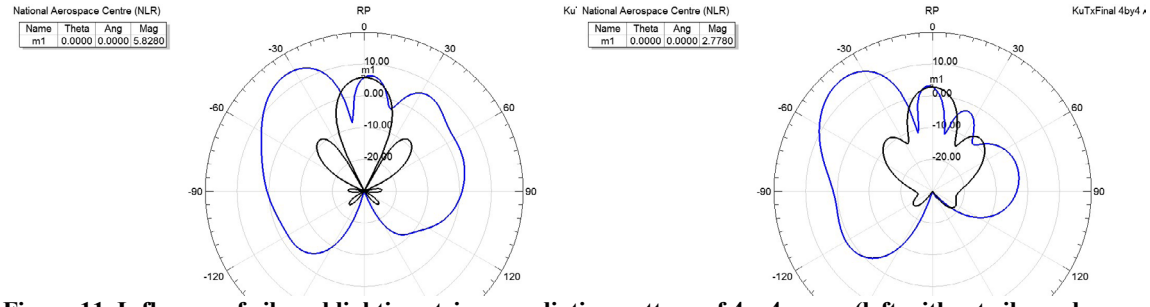

Figure 11. Influence of rib and lighting strip on radiation pattern of 4 x 4 array (left without ribs and strips, right with ribs and strip). Steering angle 45 degrees, two orthogonal polarisations given.

4 CONCLUSIONS

In this paper the structural integration of a Ku-band SATCOM antenna in the fuselage of an aircraft was addressed. In particular the specific electromagnetic aspects of the antenna integration like the lightning protection of the antenna tiles and the electromagnetic interaction of the CFRP orthogrid and GFRP fuselage skin with the array antenna were discussed. The analyses show that the separation of the antenna tiles by the ribs and the proximity of conducting materials like the ribs and the lightning diverters do have an influence on the reflection loss of the antenna elements and on the radiation pattern. This influence however, is acceptable. The GFRP skin has a significant influence on the reflection loss of the antenna element. The design of the skin should take the radome characteristics into account but also additional measures need to be taken to optimise the antenna performance in the presence of the skin.

ACKNOWLEDGMENT

All work described in this paper has received funding from the European Union's Horizon 2020 research and innovation programme under grant agreement No. 723167, ACASIAS project. The authors want to acknowledge the contribution of all the partners in the ACASIAS project.

REFERENCES

[1] "Structural Analyses of Orthogrid Fuselage Panel for Integrated Ku-band SatCom Antenna", Francesc Turon, Fermin Otero and Xavier Martinez

[2] "Automated manufacture of grid stiffened panels", Peter Nijhuis, J. Marcelo Müller

[3] "Cooling of Active Components in Structurally Integrated Phased Arrays Antennas", Jens Leiß, Thomas Ebert, Marta Martínez-Vázquez and Rens Baggen

[4] ITU recommendation S.1428-1 "Reference FSS earth-station radiation patterns for use in interference assessment involving non-GSO satellites in frequency bands between 10.7 GHz and 30 GHz"

[5] ETSI 302 186 "Harmonised Standard for satellite mobile Aircraft Earth Stations (AESs) operating in the 11/12/14 GHz frequency bands"

European Conference on Multifunctional Structures
EMuS 2019
X. Martinez and H. Schippers (Eds)
Barcelona, Spain

COMPARISON OF DENSITY MEASUREMENT METHODS FOR UNIDIRECTIONAL FLAX-EPOXY POLYMER COMPOSITES

YOUSEF SAADATI [†], JEAN-FRANÇOIS CHATELAIN[†*], GILBERT LEBRUN[††] AND YVES BEAUCHAMP[‡]

[†] Mechanical Engineering Department
École de Technologie Supérieure (ÉTS)
1100 Notre-Dame west, Montreal, Quebec, Canada
E-mail: yousef.saadati.1@ens.etsmtl.ca
[*] E-mail: jean-francois.chatelain@etsmtl.ca

[††] Mechanical Engineering Department
Université du Québec à Trois-Rivières (UQTR)
3351, boul. des Forges, Trois-Rivières, Québec, Canada
E-mail: gilbert.lebrun@uqtr.ca, http://www.uqtr.ca/Gilbert.Lebrun

[‡] McGill University
845 Sherbrooke Street West, Montreal, Québec, Canada
E-mail: yves.beauchamp@mcgill.ca

Key words: Natural Fibers, Flax Fiber, Epoxy Composites, Density Measurement, Fiber-reinforced Composites, Physical Properties

Abstract. *Density is a decisive factor in determining one of the most important advantages of flax fiber-reinforced polymer (FFRP) composites, i.e. their relatively low weight leading to high specific properties. As a fundamental physical property of composites, density enters in many engineering design and quality control calculations and its value is a determining factor for several applications. Especially, we need precise material properties including density so as to develop efficient numerical models to these materials. In this work, three density measurement methods were evaluated and compared: Helium-gas pycnometry and Archimedes with two different immersing liquids, water and ethanol. The results show that Helium-gas pycnometry and Archimedes with ethanol gave similar and repeatable results, whereas using water resulted in much lower values. The density values were all in the range of reported values. However, Helium-gas pycnometry or Archimedes using ethanol are recommended for more precision in measuring the density of FFRP composites.*

1 INTRODUCTION

Towards increasing demand for replacing conventional synthetic fibers with natural fibers as reinforcement in fiber-reinforced polymer (FRP) composites, flax fibers have found their place in the industry to replace man-made glass fibers. Flax is one of the oldest plant-based fibers and together with hemp, jute, ramie and kenaf fibers are classified as bast fibers which are nowadays extensively used in the composite field [1, 2]. Flax fibers are extracted from the stems of the flax plant and are composed of about 64% of cellulose. They normally come in

bundles and at the mesoscopic level, a bundle contains 10 to 40 elementary fibers linked together by pectin. The elementary fibers, which have a 5-7-side polyhedron shape, have an extremely complex microstructure composed of concentric primary and secondary walls forming an open channel in the middle called lumen that contributes to water absorption [2, 3].

Flax fibers are used in different forms as reinforcement in polymer composites, for instance, monofilament fibers, mats, rovings, yarns and fabrics. Nowadays, various fabrication technics are used to manufacture polymer composites, e.g. resin transfer molding (RTM), vacuum infusion, hand lay-up, film stacking, compression molding, injection molding and pultrusion [2, 3]. In some studies, a variety of surface treatments have been applied to flax fibers to improve fiber-matrix adhesion, however, it is preferred to eliminate any extra procedure from the manufacturing process and use the fibers without any modifications [3-7]. J. Zhu [3] reported the resin transfer molding as a preferred processing method to produce high performance flax fiber-reinforced epoxy composites.

Flax has been used to reinforce many polymer matrices, including thermoplastics, thermosets and biopolymers, and each type has its advantages and disadvantages. Thermoset polymers are superior in terms of mechanical properties, chemical resistance, thermal stability and overall durability. As a thermoset polymer matrix, epoxy offers high mechanical performance and durability. It has attracted many researches and is the most commonly used matrix to produce flax fiber-reinforced polymer composites [2, 4, 8-10]. For that reason, epoxy has been chosen for matrix in the flax composite of this study.

Flax/epoxy composites have many environmental advantages, economic benefits, high-performance and low density, factors of the highest importance for many industries [2, 3, 11-13]. These composites, having specific properties comparable to those of glass fiber-reinforced polymer (GFRP) composites, are potential alternatives for GFRPs in many structural and non-structural applications. They have found their ever-widening applications in many industries, such as automotive, construction, packaging, sporting and leisure [2, 3, 14, 15]. Consequently, these composites need to be known very well in terms of physical and mechanical properties.

As a fundamental physical property of composites, density enters in many engineering design and quality control calculations and its value is a determining factor as to their application. Density determines one of the most important advantages of flax fiber-reinforced polymer (FFRP) composites, i.e. their relatively low weight leading to high specific properties. So we need precise material properties including density so as to develop efficient numerical models to these materials.

Although there are some works regarding the measurement of fiber density [16] and some others dedicated to the density measurement of flax fibers [17], the sensitivity of FFRP composites to different measurement methods has not been studied yet. The literature data are scattered, ranging from 1.117 to 1.32 g/cm^3 [2, 18] and considering the fact that the density value depends on factors like the fiber volume fraction, fabrication process, measurement method and the condition of fibers used, it is often not possible to use values published in other studies. For the Finite Element Modeling (FEM) of the machining process of the FFRP composites used in this study, and in order to have a precise density value for them, this study has been conducted. Three methods to determine the density of unidirectional flax composites are evaluated and compared: Helium-gas pycnometry and Archimedes using two different immersing liquids, water and ethanol. The values will be compared and the possible sources of variations will be discussed.

2 MATERIALS AND TEST SPECIMENS

Unidirectional flax fibers in the form of tapes with a surface density of 200 g/m^2, commercially named FlaxTape^{TM} (LINEO - France), were used as reinforcement and Marine 820 epoxy resin and Marine 824 hardener (ADTECH® Plastic Systems) as the polymer matrix to produce flax fiber-reinforced composite laminates. The flax/epoxy laminates were molded using the RTM process, as reported to be the preferred processing method to produce high-performance flax fiber-reinforced epoxy composites [3]. All laminates were molded in 300 mm × 300 mm dimensions, with $[0]_n$ and $[0/90]_n$ stacking sequences for the preparation of the test specimens. The thicknesses of the laminates were precisely calculated and controlled to result in a fiber volume fraction of 41% for all composites. The laminates were post-cured at 70°C and prepared for the cutting of specimens.

The test specimens were cut to fit in the considered location of test equipment and 5 specimens were prepared from identical laminates to check the repeatability of the tests. The samples were all stored in room conditions for 24 hours before testing to stabilize the temperature and humidity levels.

3 EXPERIMENTAL PROCEDURES

Three conventional methods, which are frequently used by researchers to determine the density of composites, were applied to measure the density of the FFRP composites: Helium-gas pycnometry, Archimedes (water used as immersing liquid) and Archimedes (ethanol used as immersing liquid).

3.1 Helium-gas pycnometry

Helium-gas pycnometry is a very quick, clean and convenient density measurement method, based on which some commercially available equipment and the ASTM-D4892 [19] standard test method are developed. In this method, based on the volume of displaced gas and Boyle's law, the solid phase volume of a material sample of known mass is measured and accordingly the density is calculated. For this purpose, two chambers are used and the solid volume of the specimen is calculated based on equation 1;

$$V_s = V_c - \frac{V_x}{\frac{P_1}{P_2} - 1} \tag{1}$$

where the subscript V_s refers to the sample volume, V_c to the sample chamber volume, V_x to the expansion chamber volume, P_1 and P_2 to the pressures after fill and after expansion respectively.

The disadvantage of this method is that from a certain level of pressure, Helium can enter into the open cavities so as to measure the density of the constituent materials of the composite rather than the composite density in its specific form and configuration. This issue will be evaluated by comparing the results with those of other methods.

An ACCUPYC® II gas displacement pycnometer device (a product of Micromeritics Instrument Corporation) was used in this work. The specimens and equipment are shown in figure 1. The test was automatically repeated by the equipment 10 times for each sample, the average value was taken as the density of composite and the standard deviation was calculated.

3.2 Archimedes method

This is a buoyancy method working based on the Archimedes' principle. It is simple to implement and has been traditionally used for measuring the density of materials. The ASTM D792 standard test method [20] has been developed based on this principle and is recommended for measuring the density of plastic materials. It has been used for measuring the density of composite in some works [21, 22]. A Sartorius YDK03 density measurement kit was used in this study, as shown in Figure 2. The density was calculated according to equation 2;

$$\rho = \frac{W(a).[\rho(fl) - \rho(a)]}{W(a) - W(fl)} + \rho(a) \quad (2)$$

where ρ refers to the density, W refers to Weight, *(fl)* refers to immersion fluid and *(a)* to air. In order to monitor the absorption of liquid by the composite samples, the surface of the coupon was dried immediately after testing and the coupon reweighted.

3.2.1 Water used as immersing liquid

Water is the most commonly used liquid with this method. Due to the hydrophilic nature of natural fibers, immersing their composites in water may cause absorption of water by the fibers, thus affecting the value of measured density. In some studies water has been used to measure the density of natural fiber composites [21, 22]. In this method, the weight of the samples in the water started to increase without stabilizing. This is an evidence of absorbing water (rather than the removal of bubbles that stops in a short period of time) which was validated after testing by reweighting the samples. To avoid this problem, before immersing the samples, they were rapidly wetted to remove the air bubbles surrounding the sample and they were weighted in the water in a short time after immersion to avoid absorption. In this study, the validity of using water as immersing liquid for measuring FFRP composites will be investigated by comparing the three measuring methods.

Figure 1: ACCUPYC® II Helium Gas Pycnometer

Figure 2: Sartorius YDK03 density measurement kit

3.2.1 Ethanol used as immersing liquid

As an alternative to water, ethanol was used. It can be easily cleaned off, it doesn't affect the samples and it can be safely used in room conditions. It has been used by some researchers to measure the density of natural fibers [23, 24]. The weight of samples in the ethanol was very well stabilized after a reasonable immersion time.

9 RESULTS AND DISCUSSION

For each method at least 5 tests were performed and the mean value of the measured densities are summarized and reported in table 1. As can be seen, the gas pycnometry method resulted in nearly the same value for different samples.

Using Archimedes' method with water, in order to avoid the absorption of water by the samples, they were weighted in a short time after immersion. This resulted in lower specimen weight in the liquid (which may be due to remaining air bubbles) and consequently, in a lower density value (following Equation 2). Considering this issue and the fact that the samples need to be immersed in the fluid for a certain period of time to remove the air bubbles, it is concluded that measuring the density of FFRP composite by this method doesn't result in precise values.

Archimedes' method with ethanol allowed an immersion times long enough to remove the air bubbles and reach a stable weight. After testing, no weight change was observed, meaning that almost no ethanol was absorbed. Secondly, the very small coefficient of variation in Table 1 (for repeated samples) verify that a single physical property is measured. Finally, because the resulting value is very well correlated with the result of gas pycnometry method, this means both methods can be recommended to evaluate the density of natural fiber composites.

Table 1: Measured density values and its variations

Method	Gas Pycnometry (with Helium)	Archimedes (with water)	Archimedes (with ethanol)
Density (g/cm^3)	1.2813	1.2594	1.2804
Standard deviation	0.0005	0.0065	0.0009
Coefficient of variation† (%)	0.04	0.52	0.07

† Standard deviation/Mean value *100

11 CONCLUSION

The density of FFRP composites was measured by three different methods, the results were compared to each other and discussed. According to the findings of this study, Archimedes' method using water as immersion fluid is not recommended for measuring the density of FFRP composites. Instead, Archimedes' using ethanol and the gas pycnometry methods are recommended as the results obtained from these methods were nearly the same.

12 ACKNOWLEDGMENTS

This research was supported by the National Research Council of Canada. We sincerely thank Mr. Daniel Poirier and his colleagues from CDCQ (Centre de développement des composites du Québec) for samples preparation as well as Radu Romanica, and Nabil Mazeghrane, who provided technical assistance that greatly assisted us in this research.

REFERENCES

[1] Faruk, O., et al., Biocomposites reinforced with natural fibers: 2000–2010. *Progress in Polymer Science* (2012) **37**(11): 1552-1596.

[2] Yan, L., N. Chouw, and K. Jayaraman, Flax fibre and its composites–A review. *Composites Part B: Engineering* (2014) **56**: 296-317.

[3] Zhu, J., et al., Recent development of flax fibres and their reinforced composites based on different polymeric matrices. *Materials* (2013) **6**(11): 5171-5198.

[4] Yan, L., N. Chouw, and X. Yuan, Improving the mechanical properties of natural fibre fabric reinforced epoxy composites by alkali treatment. *Journal of Reinforced Plastics and Composites* (2012) **31**(6): 425-437.

[5] Van de Weyenberg, I., et al., Improving the properties of UD flax fibre reinforced composites by applying an alkaline fibre treatment. *Composites Part A: Applied Science and Manufacturing* (2006) **37**(9): 1368-1376.

[6] Zhang, Y., et al., Tensile and interfacial properties of unidirectional flax/glass fiber reinforced hybrid composites. *Composites Science and Technology* (2013) **88**: 172-177.

[7] Arbelaiz, A., et al., Flax fiber surface modifications: effects on fiber physico mechanical and flax/polypropylene interface properties. *Polymer composites* (2005) **26**(3): 324-332.

[8] El Sawi, I., et al., Influence of the Manufacturing Process on the Mechanical Properties of Flax/Epoxy Composites. *Journal of Biobased Materials and Bioenergy* (2014) **8**(1): 69-76.

[9] Charlet, K., et al., Mechanical properties of flax fibers and of the derived unidirectional composites. *Journal of Composite Materials* (2010) **44**(24): 2887-2896.

[10] Lefeuvre, A., A. Bourmaud, and C. Baley, Optimization of the mechanical performance of UD flax/epoxy composites by selection of fibres along the stem. *Composites Part A: Applied Science and Manufacturing* (2015) **77**: 204-208.

[11] Netravali, A.N. and S. Chabba, Composites get greener. *Materials Today* (2003) **6**(4): 22-29.

[12] Zini, E. and M. Scandola, Green composites: An overview. *Polymer Composites* (2011) **32**(12): 1905-1915.

[13] Wambua, P., J. Ivens, and I. Verpoest, Natural fibres: can they replace glass in fibre reinforced plastics? *composites science and technology* (2003) **63**(9): 1259-1264.

[14] Gurunathan, T., S. Mohanty, and S.K. Nayak, A review of the recent developments in biocomposites based on natural fibres and their application perspectives. *Composites Part A: Applied Science and Manufacturing* (2015) **77**: 1-25.

[15] Summerscales, J., et al., A review of bast fibres and their composites. Part 1–Fibres as reinforcements. C*omposites Part A: Applied Science and Manufacturing* (2010) **41**(10): 1329-1335.

[16] Rude, T.J., L.H. Strait, and L.A. Ruhala, Measurement of Fiber Density by Helium Pycnometry. *Journal of Composite Materials* (2000) **34**(22): 1948-1958.

[17] Amiri, A., et al., Standard density measurement method development for flax fiber. *Industrial Crops and Products* (2017) **96**: 196-202.

[18] Mahmoudi, S., et al., Experimental and numerical investigation of the damping of flax-epoxy composite plates. *Composite Structures* (2018) **208**: 426-433.

[19] ASTM, D4892-Standard Test Method for Density of Solid Pitch (Helium Pycnometer Method).

[20] ASTM, D792- Standard Test Methods for Density and Specific Gravity (Relative Density) of Plastics by Displacement.

[21] Madsen, B., *Properties of plant fibre yarn polymer composites*. Technical University of Denmark, (2004).

[22] Madsen, B. and H. Lilholt, Physical and mechanical properties of unidirectional plant fibre composites-an evaluation of the influence of porosity. *Composites Science and Technology* (2003) **63**(9): 1265-1272.

[23] Truong, M., et al., A comparative study on natural fibre density measurement. *The Journal of The Textile Institute* (2009) **100**(6): 525-529.

[24] Le Gall, M., et al., Recommended flax fibre density values for composite property predictions. *Industrial Crops and Products* (2018) **114**: 52-58.

European Conference on Multifunctional Structures
EMuS 2019
X. Martinez and H. Schippers (Eds)

ELECTRICAL CONDUCTIVITY AND ELECTROMAGNETIC SHIELDING EFFECTIVENESS OF BIO-COMPOSITES

EMUS 2019

KONSTANTINOS TSERPES[*], VASILEIOS TZATZADAKIS[*] AND JENS BACHMANN[†]

[*] Laboratory of Technology & Strength of Materials (LTSM)
Department of Mechanical Engineering & Aeronautics
University of Patras
Patras, 26504, Patras, Greece
e-mail: kitserpes@upatras.gr
e-mail: mead6256@upnet.gr

[†] German Aerospace Center (DLR)
Institute of Composite Structures and Adaptive Systems
Lilienthalplatz 7, 38108 Braunschweig, Germany
e-mail: jens.bachmann@dlr.de

Key words: Bio-composites, Electrical conductivity, Electromagnetic shielding effectiveness

Abstract. In this paper, electrical conductivity and electromagnetic shielding effectiveness of two bio-composites have been studied by tests and numerical models. Two monolithic composites with partly bio-based content were manufactured. The first bio-composite is made of a carbon fibre fabric prepreg and a partly bio-based (rosin) epoxy resin (CF/Rosin). The second bio-composite is a combination of prepregs of carbon fibre fabric / epoxy resin and flax fibre fabric / epoxy resin (CF-Flax/Epoxy). A single line infusion process has been used prior to the curing step in the autoclave. Both variants are exemplary for the possibility of introducing bio-based materials in high performance CFRP. In-plane and out-of-plane electrical conductivity tests have been conducted according to Airbus standards AITM2 0064 and AITM2 0065, respectively. Electromagnetic shielding effectiveness tests have been conducted based on the standard ASTM D 4935-10. Materials were prepared at the German Aerospace Center (DLR) while characterization tests were conducted at the University of Patras. In addition to the tests, numerical models of representative volume elements have been developed using the DIGIMAT software to predict the electrical conductivity of the two bio-composites. The preliminary numerical results show a good agreement with the experimental results.

1 INTRODUCTION

Carbon-fiber reinforced plastics (CFRPs) are increasingly replacing metallic materials in lightweight structures. Bio-composite materials derived from natural, renewable sources such as bio-fibers and bio-resin have received significant interest in recent years, mainly due to the increased awareness of environmentally sustainable technologies, the weight reduction they offer, the added functionality and the occupational health benefits. However, they have not yet found their way in aircraft structures mainly due to their low mechanical properties, the lack of

experience and confidence regarding their durability and the unknown electromagnetic properties [1,2].

Electromagnetic (EM) penetration of aircrafts mainly comes from lightning effects. On the other hand, lightning discharges do not necessarily have to hit the aircraft structure directly to create EM fields. Intracloud discharges for example might produce intense high frequency radiation [3]. Additionally, to the lightning effects, an electromagnetically disturbed environment for the aircraft is developed from the infrastructure of all communication, entertainment and surveillance. EM radiation penetrates the aircraft from outboard ground-based transmitters for navigation, communication, radar surveillance from other aircrafts or satellite propagation as well as from onboard generated interferences appearing by the carried onboard communication and entertainment equipment. Whereas a metallic aircraft fuselage principally counters these EM fields like a faraday cage -through its high electrical conductivity is able to deflect and absorb the radiation and provides an EM shield- a composite fuselage is not able to counter EM fields without enhancement [4].

When passengers are exposed to the EM waves, the network of veins in high risk organs such as eyes might be affected. This is due to heat build-up in the eyes by the EM waves which could not be easily dissipated. In order to avoid these hazards to passengers and to protect the sensitive equipment from undesired EM radiation [5], EM interference shielding is essential. In order to block the undesired EM radiation, one has to understand the electrical properties and EM behavior of structural materials. In this work, the electrical conductivity and electromagnetic shielding effectiveness (EMSE) of two bio-composites, which are destined for use in secondary aircraft structures, have been studied by tests and numerical models.

2 MATERIALS

The first bio-composite is made of a carbon woven fibre fabric prepreg and a partly bio-based (rosin) epoxy resin (CF/Rosin). The second bio-composite is a combination of prepregs of unidirectional carbon fibre fabric (5 layers in 0^o and 90^o direction) / epoxy resin and flax plain weave fibre fabric / epoxy resin (CF-Flax/Epoxy). The epoxy resin, which was used for the production of the second bio-composite, is the LY556 (HY+ DY). A single line infusion process has been used prior to the curing step in the autoclave at 80 ºC for 4 hours with a post-curing at 120 ºC for 4 hours. The prepreg layup of the first bio-composite was cured in the autoclave at 130 °C for 3 hours.

3 EXPERIMENTAL

3.1 Electrical conductivity tests

Electrical conductivity of bio-composites was derived from electrical resistivity. The electrical resistivity along X (longitudinal) and Z (normal) directions was measured according to AITM2-0064 [6] and AITM2-0065 standards [7], respectively. To this end, a plastic test-jig and a probe ohmmeter were used. Fig. 1(a) shows the specimen (coupon) used for the tests along X axis inside the test-jig while Fig. 1(b) shows the specimen (plate) used for the tests along Z axis in between two brass plates.


(a)
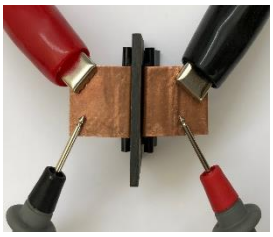
(b)

Figure 1: (a) The electrical resistivity test along X axis (b) the electrical resistivity test along Z axis

The resistance (in Ω) of a parallelepipedic sample made from an isotropic material may be expressed as follows:

$$R = \rho \times \frac{l}{s} = \rho \times \frac{l}{w \times t} \tag{1}$$

where ρ is the resistivity of the material, expressed in ohm meter (Ω m), s the cross-sectional area of the specimen, expressed in squared meters (m^2), l, w and t are respectively the length, the width and the thickness of the specimen, expressed in meters (m).

The resistivity is an intrinsic property of the bulk material and may be represented as the resistance between the opposite faces of a 1-meter edge cube from this material. The conductivity σ, expressed in Siemens (S) per meter (S m^{-1}), is the inverse of the resistivity:

$$\sigma = \frac{1}{\rho} \tag{2}$$

3.2 EMSE tests

EMSE tests were conducted according to ASTM D4935-10 standard [8]. For each material, a set of a reference and a load specimen of circular shape have been produced. The external diameter of the specimens is 133 mm, while the internal diameter of the reference specimen is 33 mm. The specimens used in the EMSE tests are shown in Fig. 2. Both bio-composites are electrically thin according to the measured frequency bandwidth.

Figure 2: The specimens used in the EMC tests (left: reference, right: load).

EMSE tests were conducted inside an anechoic chamber (Fig. 3) in order to ensure a clear environment from other EM interferences (noise-free environment). The EM wave was produced from a signal generator and was transmitted through a double-shielded cable. The specimens were placed into the specimen holder device. A set of N-type connectors were placed at both ends of the specimen holder to ensure a constant 50 Ohm impedance. The signal was finally received by a receiver device.

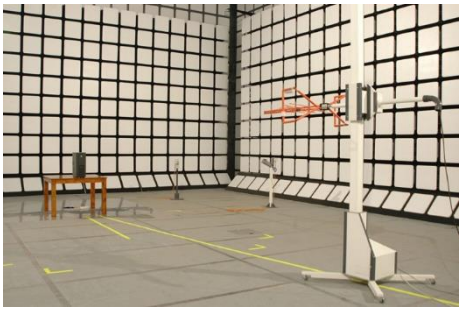

Figure 3: The anechoic chamber used for the EMSE tests.

The specimen holder (Fig. 4) is a bronze made apparatus manufactured according to the ASTM D 4935-10 standard. A coaxial signal transmission is realized, as the device has a constant 50 Ohm impedance through its perfectly symmetrical structure (calibration of the device is been a mandatory step) The mounting of the specimen with the holder is made through a set of four plastic fasteners. The leakage caused by the plastic fasteners is characterized as negligible.

Figure 4: The specimen holder used for the EMSE tests.

The signal generator has been set to produce an EM wave of 1 sec total duration, starting from 30 MHz to 1.5 GHz with a step increment of 0.5 MHz. The system is been calibrated in order to avoid an energy leakage or a component mismatch (a constant value of 50 Ohm is required). Inside the specimen holder (blank space) a far-field EM wave is formed that traverses through the testing material (load material case) in order to reach the holder's end. The receiver records the signal's power in dBm units (frequency bandwidth of 30 MHz to 1.5 GHz). The measurements are made for both reference and load specimens. Shielding Effectiveness (SE) can be calculated directly from the dBm values or through conversion to mWatt units

$$SE = -(\mathrm{dBm}_{ref} - \mathrm{dBm}_{load}) \tag{3}$$

4 NUMERICAL ANALYSIS

Additional to the tests, electrical conductivity of bio-composites was predicted by numerical analysis which is based on representative volume elements (RVEs). To this end, the DIGIMAT software was used. For the development of the RVEs, it was crucial to have information on the microstructure and electrical properties of the materials (Table 1). The developed RVEs are shown in Fig. 5. The RVEs were meshed using a built-in mesh generator, with second order tetrahedral elements, instead of voxel elements [9-10]. The FE meshes of the RVEs are also illustrated in Fig. 5. The RVEs were loaded using periodic boundary conditions to achieve homogenization.

Table 1: Physical and electrical properties of materials

Property	Carbon	Flax
Density (gr/cm^3)	1.8	1.54
Electrical conductivity (S/m)	70000	100
Dimensions of yarn (mm)	0.15 x 0.5	0.15 x 0.4

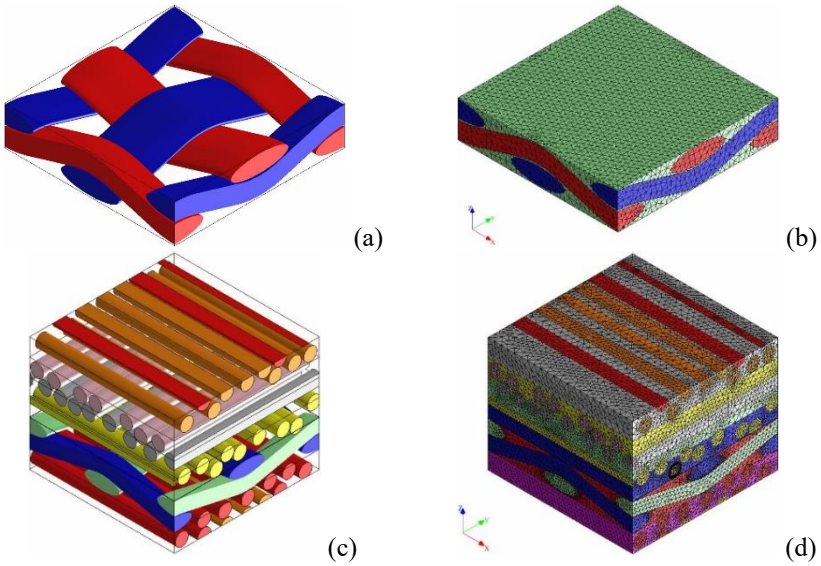

Figure 5: (a) RVE of CF/Rosin bio-composite (twill carbon fabric), (b) FE mesh of the RVE of CF/Rosin bio-composite, (c) RVE of CF/Flax-Resin bio-composite (d) FE mesh of the RVE of CF/Flax-Resin bio-composite.

5 EXPERIMENTAL RESULTS

5.1 Electrical conductivity

The measured electrical conductivity values of the bio-composites are displayed in Fig. 6. The average conductivity of the CF/Rosin bio-composite is 11491 S/m and the standard deviation is 558 S/m. The average conductivity of the CF/Flax-Epoxy bio-composite is 15104 S/m and the standard deviation is 4858 S/m. The relatively high standard deviation electrical conductivity for the CF/Flax-Epoxy material is due to the variation of metallization quality of the flax fiber surface and due to the variation of fiber volume fraction through the dimensions of the specimens. Fig. 7 shows a metallized flax fiber surface with many defects. The measured electrical conductivities of the bio-composites lie in the area of the lower limit of the electrical conductivity of CFRPs (~12,000 S/m) [11-12].

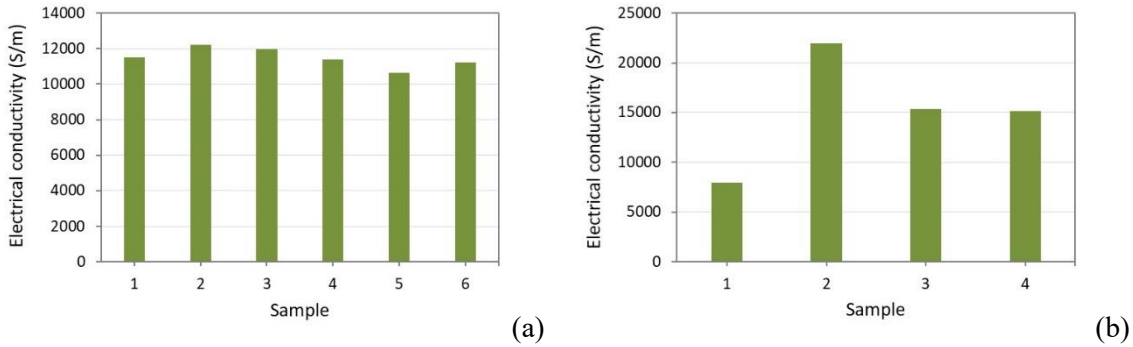

Figure 6: Electrical conductivity values of bio-composites: (a) CF-Rosin, (b) CF-Flax/Epoxy

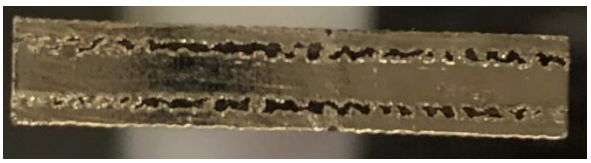

Figure 7: Metallization of the hybrid (Carbon\flax composite)

5.2 EMSE

EMSE tests were conducted under continuous loading, from 30 MHz and 1.5 GHz with increment step of 0.5 MHz for both reference and load specimens. Inside of the specimen holder a far-field wave is formed that propagates through the testing material (when load specimen is tested) and reaches the receiver which records the signal's power. The received signals are plotted in Figs. 8 and 9 in terms of signal's amplitude versus frequency. The SE is derived from Eq. (3). The results show that both materials exhibit a higher SE at high frequency EM waves. More specific, the maximum SE for the CF/Rosin material is 81.05 dB at 1363 MHz and for the CF/Flax-Epoxy material is 86.15 dB at 1417 MHz. The minimum SE values for the two materials is 38.89 dB and 36.68 dB, respectively, both achieved at 30MHz (low EM frequencies). The values above 60 dB (up to 90 dB) provide sufficient EM protection [13-14].

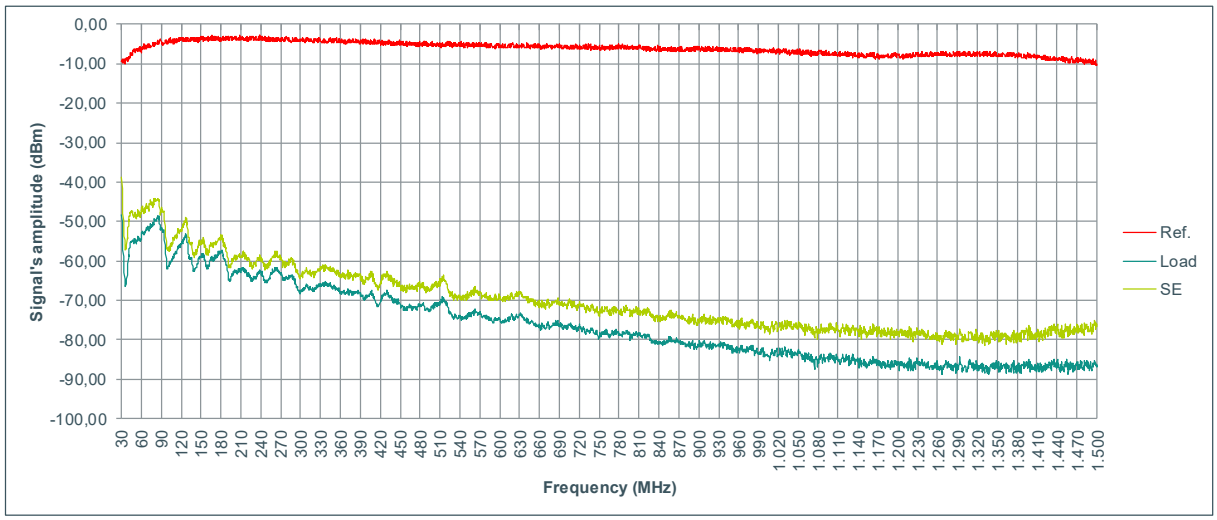

Figure 8: Signal' amplitude vs. frequency for the CF/Rosin bio-composite

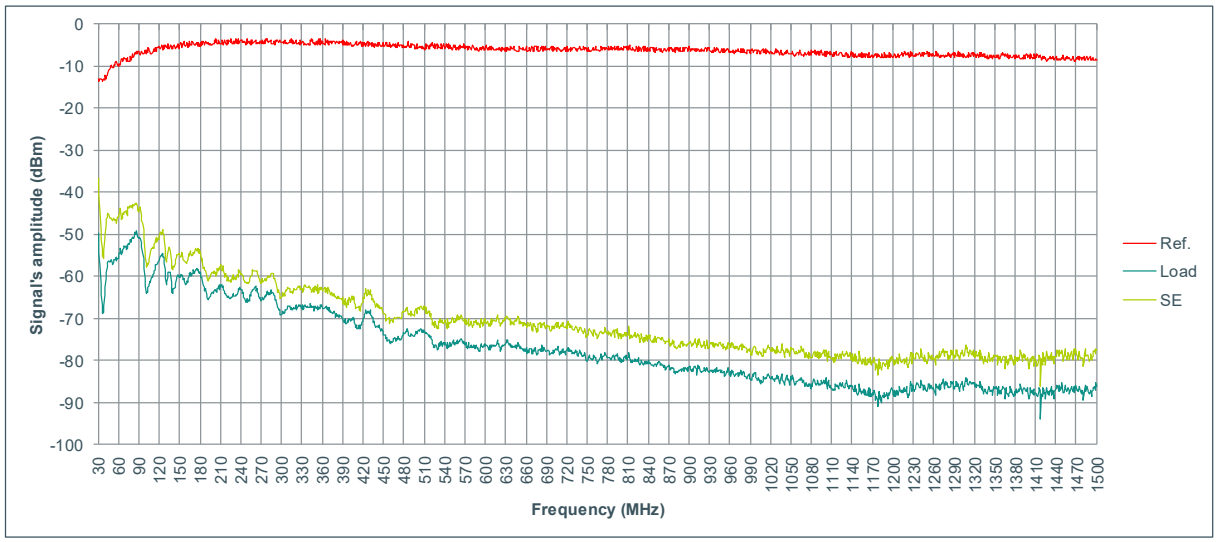

Figure 9: Signal' amplitude vs. frequency for the CF/Flax-Epoxy bio-composite

6 NUMERICAL RESULTS

The computed electrical conductivity is 12357 S/m for the CF/Rosin bio-composite and 14333 S/m for the CF/Flax-Epoxy bio-composite. Both predicted values compare very well with the average experimental values (11491 S/m and 15104 S/m, respectively).

7 CONCLUSIONS

In this paper, the electrical conductivity and EMSE of a CF/Rosin bio-composite and a CF/Flax-Epoxy bio-composite, which are intended for use in secondary aircraft structures, have been studied by tests and numerical models. The findings show a potential of the bio-composites since the measured electrical conductivities and the SE although being smaller than the

respective values of CFRPs, they are within the acceptable deviation range. Furthermore, the RVE-based numerical model has given very good predictions on electrical conductivity of the bio-composites.

ACKNOWLEDGEMENT

The work reported in this paper has received funding from the European Union's Horizon 2020 research and innovation programme ECO-COMPASS (Grant no. 690638).

REFERENCES

[1] Bachmann, J., Yi, X., Gong, H., Martinez, X., Bugeda, G., Oller, S., Tserpes, K., Ramon, E., Paris, C., Moreira, P., Fang, Z., Li, Y., Liu, Y., Liu, X., Xian, G., Tong, J., Wei, J., Zhang, X., Zhu, J., Ma, S. and Yu, T. (2018). Outlook on ecologically improved composites for aviation interior and secondary structures. *CEAS Aeronautical Journal*, 9(3), pp.533-543.

[2] Yi, X. and Tserpes, K. (2019). Special Issue "ECO-COMPASS: Ecological and Multifunctional Composites for Application in Aircraft Interior and Secondary Structures". *Aerospace*, 6(2), p.17.

[3] Rakov, V. and Rachidi, F. (2009). Overview of Recent Progress in Lightning Research and Lightning Protection. *IEEE Transactions on Electromagnetic Compatibility*, 51(3), pp.428-442.

[4] White, D. and Mardiguian, M. (1988). *Electromagnetic shielding*. Gainesville, Va.: Interference Control Technologies.

[5] Rifai, A. and Hakami, M. (2014). Health Hazards of Electromagnetic Radiation. *Journal of Biosciences and Medicines*, 02(08), pp.1-12.

[6] AITM 2-0064 – Airbus Test Method. Electrical resistance for a composite laminate with carbon fibre: Measurement along X or Y direction.

[7] AITM 2-0065 Airbus Test Method. Electrical resistance for a composite laminate with carbon fibre: Measurement along Z direction.

[8] ASTM D4935 - 10 Standard Test Method for Measuring the Electromagnetic Shielding Effectiveness of Planar Materials

[9] Zienkiewicz, O.C. and Taylor, R.L. *The finite element method*. McGraw Hill, Vol. I., (1989), Vol. II, (1991).

[10] Idelsohn, S.R. and Oñate, E. Finite element and finite volumes. Two good friends. *Int. J. Num. Meth. Engng* (1994) **37**:3323-3341.

[11] Alexandre Piche, Gilles Peres and Ivan Revel (2011). *Experimental and Numerical Methods to Characterize Electrical Behaviour of Carbon Fiber Composites Used in Aeronautic Industry*. INTECH Open Access Publisher.

[12] Si-Ping Gao, Hui Min Lee, Richard Xian-Ke Gao, Qi Feng Lim, Warintorn Thitsartarn, En-Xiao Liu and Ching Eng Png (2017). Effective Modeling of Multidirectional CFRP

Panels Based on Characterizing Unidirectional Samples for Studying the Lightning Direct Effect. [online] Available at: https://ieeexplore.ieee.org/document/8105177 [Accessed 18 Apr. 2019].

[13] Daniela Munalli, Dimitrios Chronopoulos and Steve Greedy (2018). Electromagnetic shielding effectiveness of fiber-reinforced composites: a preliminary study. In: *9th European Workshop on Structural Health Monitoring*. [online] Manchester, United Kingdom.

[14] Tugirumubano, A., Vijay, S., Go, S., Kwac, L. and Kim, H. (2018). Investigation of Mechanical and Electromagnetic Interference Shielding Properties of Nickel–CFRP Textile Composites. *Journal of Materials Engineering and Performance*, 27(5), pp.2255-2262.

Functionalization of carbon nanotubes and mechanical characterisation of bio-based epoxy nano-composites

A. Singh*, C. Sguazzo*, C.F.R.A.C. Lima†, L.M.N.B.F. Santos†, P.J.S. Tavares* and P.M.G.P. Moreira*

*Laboratory of Optics and Experimental Mechanics (LOME),
Institute of Science and Innovation in Mechanical and Industrial Engineering (INEGI)
Rua Dr. Roberto Frias, Campus da FEUP, 400 4200-465, Porto, Portugal
email: csguazzo@inegi.up.pt, webpage: http://www.inegi.up.pt

† Department of Chemistry and Biochemistry,
Faculty of Science of University of Porto,
R. Campo Alegre, 687, 4169-007 Porto, Portugal

Keywords: Carbon nanotubes, Composites, Functionalization, Mechanical Characterization, Polymers.

ABSTRACT

Chemical functionalization of multiwalled carbon nanotubes (MWCNTs) is important from the view point of polymer based composite manufacturing. As pristine MWCNTs has certain disadvantage such as they have lower dispersion, they are hydrophobic and are not readily soluble in a solvent, these characteristics makes them unreliable candidate for most of the industrial applications. By doing chemical functionalization of MWCNTs, these shortcomings can be overcome, and the MWCNTs can be used as a filler in composite manufacturing. This has the advantage of better nanofillers' dispersion and provide the better interfacial bonding.

In this study, MWCNTs are functionalized by the carboxylic group, chemical functionalization of MWCNTs is an optimization problem, governed by parameters like mixture acid concentration, temperature, time of heating and amount of MWCNTs used. Material characterization of MWCNTs is done and test specimens are manufactured according to different concentrations of MWCNTs within a bio-based epoxy resin. Mechanical properties are then compared according to different concentrations. These mechanical and material characterizations increase the understanding of chemical functionalization by carboxylic group and the influence of the concentration of MWCNTs dispersed within the bio-based resin matrix.

1 INTRODUCTION

Use of composite materials in aircraft industry comes with certain advantages such as light weight, high temperature resistant, high strength to weight ratio, resistant to corrosion, flexibility, in association with their design. Furthermore, the use of bio-based resins is on the rise to reduce the carbon footprints in different engineering fields [1], including the aeronautic sector. Recently, research is focused on the use of carbon nanotubes to be incorporated into the polymer matrix as a filler material to increase multiple physical properties. A significant boost in the carbon nanotubes research field [2] came after an impactful research paper by Sumio and Iijima in 1991 [3]. Carbon nanotubes are very promising candidates because of properties such as high strength, low density, high conductivity, chemical inertness and low-dimensionality, thus their use is open to diverse field applications [4]. Carbon nanotubes in its pristine form are difficult to disperse within the polymer matrix due to the presence of strong van der Waals forces, which keep them as an agglomerate [5]. To improve their dispersion capability within polymer matrices, chemical functionalization can be

applied. Modification techniques may be broadly categorized as covalent and non-covalent functionalization [6].
In this work, covalent functionalization was performed by using sulphuric and nitric acid (mixture acid), resulting in the functionalization of the surface of the MWCNTs by the carboxylic group, in order to improve the dispersion of pristine MWCNTs within an epoxy matrix. Indeed, the compatibility of carboxylic group with the epoxy molecules helps to increase the dispersion and the interfacial bonding with the epoxy matrix. Particularly, within the chemical functionalization by mixture acid, sulphuric acid creates a defect site at the surface of the MWCNTs and nitric acid oxidized these defects [7], thus, grafting the carboxylic group on the walls of carbon nanotubes. Furthermore, this changes the sp2 hybridization of multi-walled carbon nanotubes into sp3 hybridization and makes them more stable.
Different key points characterize the chemical functionalization such as: higher curvature MWCNTs are more reactive at the site, smaller diameter MWCNTs are easier to functionalize, ends of the MWCNTs are more reactive than the side walls, MWCNTs with defects are more susceptible to functionalization [4,7]. Furthermore, there are certain parameters that control the functionalization process which are the concentration of the acids used, the temperature of the solution, the duration of the acid treatment and the ratio of MWCNTs to acid.
In this work, bio-sourced epoxy resin was used as matrix for the nanocomposites to produce. Material characterization of the pristine and functionalized MWCNTs was carried out and the process of fabrication of the nanocomposite was optimized. Finally, tensile mechanical properties were analysed according to different concentrations of both pristine and functionalized MWCNTs.

2 MATERIALS AND METHODS

2.1 Multi-walled Carbon Nanotubes (MWCNTs) and its functionalization

MWCNTs synthetized by Catalytic Chemical Vapor Deposition (CCVD) of type NC7000™ process were supplied by NANOCYL® - Belgium [8]. They are recommended for applications in the transportation including the aeronautic sector and for EMI-shielding, because of their high electrical conductivity. This type of MWCNTs was provided in the pristine form and chemical functionalization was applied.
Pristine MWCNTs were functionalized in a mixture acid of 3 part of concentrated sulphuric acid and 1 part of concentrated nitric acid. A quantity of 100 ml of mixture acid was heated to a temperature of 90 °C and then maintained for a certain time. The pristine MWCNTs in a quantity of 1g was added to the mixture acid and five different synthesis were carried out using time of heating: 15, 30, 45, 60 and 90 minutes in a reflux [9,10]. After the synthesis, the sample was diluted in a deionized water (1L) and then filtered in a vacuum by means of a 0.22 µm membrane filter. The resultant solid was then washed with deionized water until the pH reached neutral value. Finally, MWCNTs were dried in oven at 60 °C for 24h and weighed afterwards. The dried MWCNTs were added to dimethylformamide (DMF) and the soluble part was then separated from the insoluble part.

2.2 Thermogravimetric Analysis (TGA)

The thermal behaviour of both pristine and functionalized MWCNTs was studied by means of TGA analysis. The samples of MWCNTs were heated from the room temperature to 900 ºC in a nitrogen atmosphere with a gas flow rate of 200ml/min characterised by a heating rate of 10ºC/min. Then an isotherm condition was kept at 900 ºC for 10 minutes and followed by cooling down to room temperature at a heating rate of 10ºC/min.

2.3 Scanning Electron Microscopy (SEM)

Both pristine and functionalized MWCNTs were prepared for the SEM analyses, which were performed at were performed at CEMUP (Centro de Materiais da Universidade do Porto), Porto, Portugal. To visualize the MWCNTs in the SEM, thin film of MWCNTs was deposited over the Indium Tin Oxide (ITO) coated glass (to make them conductive). The pristine MWCNTs and the ones functionalized in 45 minutes and 90 minutes were analysed at a scale of 2 μm.

2.4 Preparation of MWCNTs based epoxy nanocomposite

In this study the epoxy/hardner resin system used for producing the nanocomposites has the commercial name of SR GreenPoxy® 33/SZ 8525 and was supplied by Sicomin – France [11]. SR GreenPoxy® 33 has a bio-based carbon content with 35% of its molecular structure coming from plant origin. According to the TDS, viscosity of the resin at 20 °C and 25 °C is 3240 mPa·s and 1780 mPa·s respectively. Viscosity of the hardener at 20 °C and 30 °C is 33 mPa·s and 25 mPa·s respectively. In the following the description of the method developed for fabricating the resin-based nanocomposites id reported. MWCNTs were added to the acetone and sonicated for 30 minutes, for making them easy to disperse and for reducing the viscosity of the mixture with the epoxy resin. Epoxy was added to this mixture and sonication was carried out for another 30 minutes. After that, the mixture was subjected to magnetic stirring for 3h at 80 °C in order to completely remove the acetone from this mixture. Degassing of the mixture was done for 15 minutes to ensure the removal of any air bubbles trapped because of previous processes. At this step, hardener was added to the mixture and was magnetic stirred for 15 minutes without heating. Sonication was performed for another 2 minutes and then degassing was done for 5 minutes. The mixture was then poured into moulds and put into the oven at 120 °C for 45 minutes. Finally, the oven was turned off and allowed to cool slowly till room temperature.

3 RESULTS AND DISCUSSION

3.1 Yield Time vs the Time of Synthesis

With the increase of the time of functionalization (15, 30, 45, 60 and 90 minutes) the amount of yield of MWCNTs which was acquired after synthesis followed an exponential decay, which is in accordance with the first order reaction kinetics. This is shown in Figure 1. Exponential decay followed the Equation 1 below, where x is the time of synthesis and y is the amount of yield after the functionalization.

$$y = 973.21e^{-0.015x} \quad (1)$$

3.2 Hydrophilic behaviour of MWCNTs after functionalization

Hydrophilicity of MWCNTs was confirmed by mixing the pristine and functionalized MWCNTs into two separate bottles containing water and dichloromethane (DCM). Pristine MWCNTs showed to have an affinity towards DCM while MWCNTs showed to have a hydrophilic nature and got attracted towards water at the top. Thus, confirming the change of behaviour from hydrophobic to hydrophilic. This change of behaviour was also used to separate the non-functionalized part from the functionalized one. The functionalized product was dissolved in the DMF and then functionalized and non-functionalized parts were separated. Separated functionalized product gave the same percentage of functionalized product after each synthesis, which followed the previously reported exponential decay. This led to a conclusion that with the increase of time of synthesis, the overall yield of MWCNTs decreased but the percentage of functionalized product inside the yield quantity remained the same. It

was observed that the time of reaction consumed more pristine MWCNTs but did not change the final quantity of functionalized MWCNTs. Therefore, the first reproducible functionalization time of 30 minutes was chosen for producing the bulk functionalized MWCNTs. The time of 15 minutes of synthesis was not used as it was not as reproducible as the 30-minute functionalization reaction.

Table 1: Percentage of functionalized MWCNTs soluble in DMF

Functionalization Time (minute)	Percentage of pure functionalized MWCNTs
15	13 %
30	14 %
45	14 %
60	10 %
90	15 %

3.2 TGA results of pristine and functionalized MWCNTs

TGA results showed the degree of functionalization of MWCNTs with the carboxylic group and the results were compared with the pristine MWCNTs. Pristine MWCNTs showed a decrease of the weight to 13.74% whereas the functionalized MWCNTs weight decreased to 25.41%. This increase in weight loss from pristine to functionalized MWCNTs could be due to the presence of carboxylic group at the surface of MWCNTs. Figure 2 shows the mass loss for different samples.

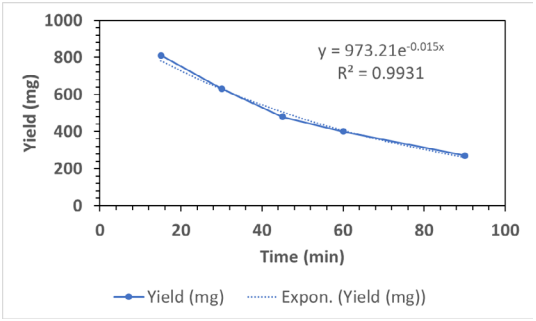

Figure 1: Amount of yield vs time of functionalization

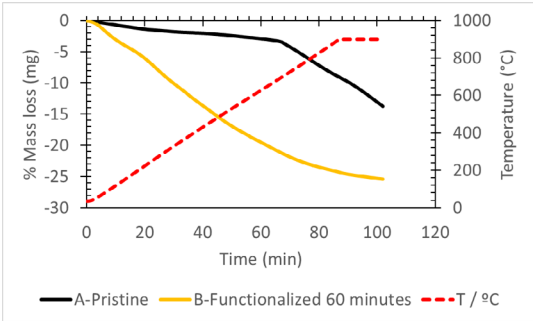

Figure 2: TGA results of pristine and functionalized MWCNTs

3.3 SEM analysis

The results of SEM analyses are reported in this paragraph. Figure 3a) shows the pristine MWCNTs at 2µm length scale: they appeared in the form of agglomerates, long seamless wires and appeared entangled together due to the weak van der Waals forces. Figure 3 b) and 3 c) shows SEM images of the 45-minute functionalized MWCNTs and 90-minute functionalized MWCNTs. From the figure, the MWCNTs appeared well dispersed and the length of the MWCNTs was shorter than the pristine ones. It was observed that the length of MWCNTs decreased after the acid treatment, but they were not anymore in the form of agglomerates, thus resulting well dispersed. Also, by increasing the time of functionalization from 45 minute to 90 minutes, the quantity of functionalized MWCNTs appeared to be reduced.

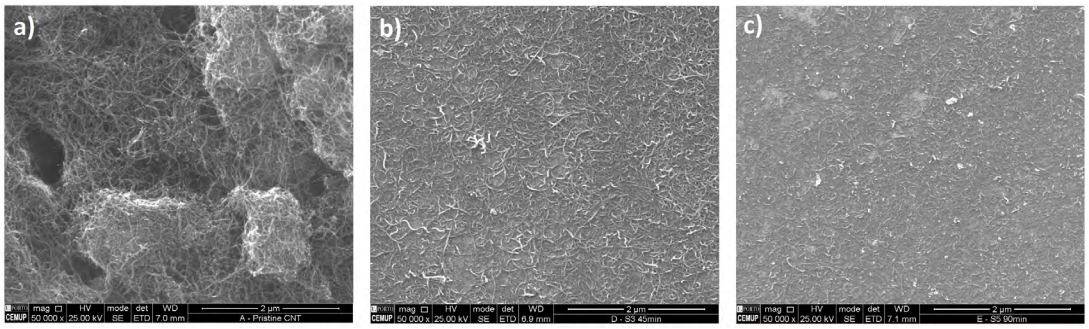

Figure 3: SEM analysis of a) pristine b) 45-minute functionalized MWCNTs and c) 90-minute functionalized MWCNTs

3.4 Mechanical properties of bio-based resin nano-composites

Nanocomposite samples were manufactured for the mechanical characterization containing different concentrations of pristine and 30 minutes functionalised MWCNTs. A digital image correlation system was used to detect the strain-field distribution during the experiments. The method previously described was applied for obtaining the specimens to characterise according to the ASTM D638 standard, with the aim of studying the influence of the MWCNTs type and concentration on the final mechanical properties of the nanocomposites. Neat resin samples of SR GreenPoxy® 33/SZ 8525 were also produced as benchmark case-study. In Figure 4 and Figure 5, the mechanical properties in terms of tensile stress at break and Elastic modulus are respectively reported. Particularly the mean values of the physical properties and the standard deviation are reported for the different concentrations analysed. The nanocomposites produced with pristine MWCNTs showed mean values of tensile stress at break and elastic modulus smaller than the neat resin samples and the nanocomposites produced with functionalized MWCNTs. The nanocomposites produced with functionalized MWCNTs showed comparable mechanical properties to the neat resin samples, both in terms of elastic modulus and tensile stress at break, when a percentage of 0.25% of functionalized NC7000 was considered, thus confirming the indication of the TDS of the product NC7000 of retention of the original mechanical properties of the final nanocomposite.

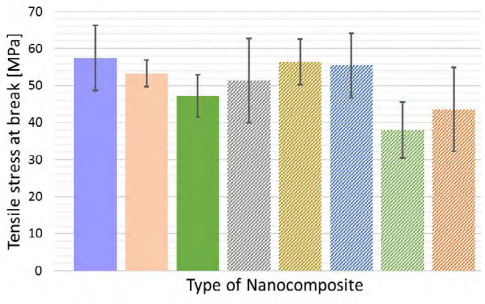

Figure 4: Mean values and standard deviation of tensile stress at break for neat resin, nanocomposites produced with pristine CNTs (MWCNTs) and with functionalized ones (fMWCNTs) at different concentrations.

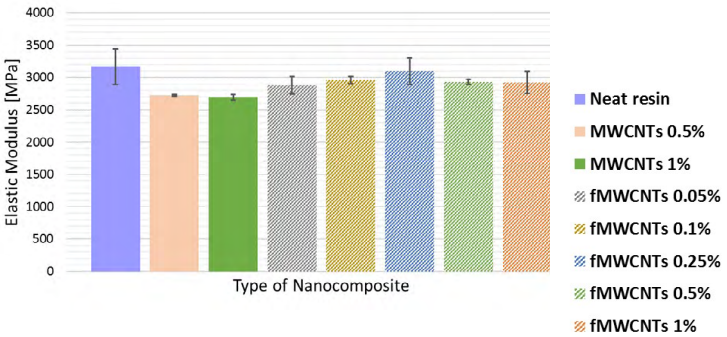

Figure 5: Mean values and standard deviation of Elastic modulus at break for neat resin, nanocomposites produced with pristine CNTs (MWCNTs) and with functionalized ones (fMWCNTs) at different concentrations.

4 CONCLUSIONS

In view of nanocomposite manufacturing, chemical functionalization by carboxylic group was performed on pristine MWCNTs by means of mixture acid to improve their dispersion within a bio-sourced resin system. It was observed that for the functionalized MWCNTs, a change of behaviour from hydrophobic to hydrophilic led to increase the solubility of MWCNTs within an organic solvent. DMF was used to differentiate the functionalized and non-functionalized part. Amount of yield versus time of functionalization followed the first order reaction kinetics and the graph was fit by an exponential decay, showing that the amount of functionalized product decreases with the time of functionalization. From the TGA curve, it was observed that the increase in weight loss from pristine to functionalized MWCNTs can be explained by the presence of carboxylic group at the surface of MWCNTs. SEM images showed that the MWCNTs were well dispersed but length of the MWCNTs was shorter than the pristine ones. The decrease in length of MWCNTs was attributed to the acid treatment; nevertheless, the functionalized MWCNTs were not in the form of agglomerates and were well dispersed into the resin. It was found out that with an increase of synthesis time, the overall yield decreases but the percentage of functionalized product inside the yield quantity remains the same. Therefore, the time of reaction consumed more pristine MWCNTs but did not change the final functionalized MWCNTs product. The functionalized MWCNTs based nanocomposites showed mechanical tensile properties higher than the pristine-based ones produced according to the same concentration. For specific concentrations both tensile elastic modulus and tensile stress at break were comparable to the ones of the neat resin samples.

This research was developed within the ECOCOMPASS project and has received the funding from the European Union's Horizon 2020 research and innovation program under grant agreement No. 690638.

REFERENCES

[1] Ramon, E.; Sguazzo, C.; Moreira, P. A Review of Recent Research on Bio-Based Epoxy Systems for Engineering Applications and Potentialities in the Aviation Sector. *Aerospace* **2018**, *5*, 110, doi:10.3390/aerospace5040110.

[2] Monthioux, M.; Kuznetsov, V. L. Who should be given the credit for the discovery of carbon nanotubes? *Carbon N. Y.* **2006**, *44*, 1621–1623, doi:10.1016/j.carbon.2006.03.019.

[3] Iijima, S. Helical microtubules of graphitic carbon. *Nature* **1991**, *354*, 56–58, doi:10.1038/354056a0.

[4] Grady, B. P. *Carbon Nanotube –Polymer Composites, Manufacture, Properties, and Applications*; 2011; ISBN 9780470596418.

[5] Sahoo, N. G.; Rana, S.; Cho, J. W.; Li, L.; Chan, S. H. Polymer nanocomposites based on functionalized carbon nanotubes. *Prog. Polym. Sci.* **2010**, *35*, 837–867, doi:10.1016/j.progpolymsci.2010.03.002.

[6] Mahmood, N.; Islam, M.; Hameed, A.; Saeed, S.; Khan, A. N. Polyamide-6-based composites reinforced with pristine or functionalized multi-walled carbon nanotubes produced using melt extrusion technique. *J. Compos. Mater.* **2014**, *48*, 1197–1207, doi:10.1177/0021998313484779.

[7] Ma, P.-C.; Siddiqui, N. A.; Marom, G.; Kim, J.-K. Dispersion and functionalization of carbon nanotubes for polymer-based nanocomposites: A review. *Compos. Part A Appl. Sci. Manuf.* **2010**, *41*, 1345–1367, doi:10.1016/J.COMPOSITESA.2010.07.003.

[8] Nanocyl TDS - NanoCyl NC7000 Available online: https://www.nanocyl.com/wp-content/uploads/2016/07/DM-TI-02-TDS-NC7000-V08.pdf (accessed on Apr 1, 2019).

[9] Osorio, A. G.; Silveira, I. C. L.; Bueno, V. L.; Bergmann, C. P. H2SO4/HNO3/HCl—Functionalization and its effect on dispersion of carbon nanotubes in aqueous media. *Appl. Surf. Sci.* **2008**, *255*, 2485–2489, doi:10.1016/j.apsusc.2008.07.144.

[10] Men, X. H.; Zhang, Z. Z.; Song, H. J.; Wang, K.; Jiang, W. Functionalization of carbon nanotubes to improve the tribological properties of poly(furfuryl alcohol) composite coatings. *Compos. Sci. Technol.* **2008**, *68*, 1042–1049, doi:10.1016/j.compscitech.2007.07.008.

[11] Sicomin TDS - SR GreenPoxy 33 / SZ 8525 Available online: http://www.sicomin.com/datasheets/product-pdf1165.pdf.

European Conference on Multifunctional Structures
EMuS 2019
X. Martinez and H. Schippers (Eds)

The ECO-COMPASS EU-China Project

EMUS 2019

JENS BACHMANN*, XIAOSU YI†

* German Aerospace Center (DLR)
Institute of Composite Structures and Adaptive Systems
Lilienthalplatz 7, 38108 Braunschweig, Germany
e-mail: jens.bachmann@dlr.de, www.dlr.de/en

† AVIC Beijing Institute of Aeronautical Materials (BIAM) /ACCT
University of Nottingham Ningbo China (UNNC)
e-mail: xiaosu.yi@nottingham.edu.cn

Key words: Composite, bio-based, flax, ramie, recycling, epoxy, honeycomb

Abstract. Fibre reinforced polymers are important materials used in aviation due to their excellent specific properties enabling the reduction of fuel consumption. For example, carbon fibre reinforced epoxy resins are used in fuselage and wing structures. Glass fibre reinforced phenolic resins are mainly used for the interior panels due to their low weight and favourable fire properties. All these composite materials used in aviation have one thing in common: they are man-made. Renewable materials like bio-fibres and bio-resins are under investigation for a long time for composites but they did not made it into modern aircraft in high amounts yet.

The project ECO-COMPASS under Horizon 2020 aims to bundle the knowledge of 17 partners from China and Europe to develop ecological improved composites for the use in aircraft interior and secondary structures [1]. Bio-based reinforcements, epoxy resin and sandwich cores are developed and improved for their application in aviation. Furthermore the use of recycled carbon fibres to increase the mechanical strength and multifunctional aspects of bio-composites are evaluated. In order to withstand the special stresses in aviation environment, protection technologies to mitigate the risks of fire, lightning and moisture uptake are under investigation. An adapted modelling and simulation will enable the optimization of the composite design. Electrical conductive composites for electromagnetic interference shielding and lightning strike protection are under investigation in ECO-COMPASS as well. The cooperation includes the exchange of knowledge and materials in order to optimize the development of ecological friendly composites.

1 INTRODUCTION

Lightweight structures made from composite materials have gained in importance due to

their excellent mechanical properties combined with relatively low weight. Fibre Reinforced Polymers (FRP) enable the construction of lighter and more efficient aircrafts resulting in the reduction of fuel consumption and increased payloads. High performance composites like carbon-fibre reinforced plastics (CFRP) are used in primary structures of modern aircrafts like Airbus A350. Sandwich structures made of glass and aramid fibres with phenolic resins as matrix system find their application in the interior due to their low weight to stiffness ratio. But all these composite materials currently used in aviation have are synthetic and energy intensive in their production. Renewable materials like bio-based fibres and bio-based resin systems are under development and already used in other industries such as automotive. But they have not been introduced into a modern aircraft in noticeable amounts yet [1].

As safety is of primary importance in aviation, the lack of experience and confidence in the long-term performance and mechanical properties of composites made of renewable materials is still an obstacle for their usage. It is therefore at the moment out of scope to substitute high performance and safety-relevant composites like CFRP in primary structural parts of the aircraft, for example the fuselage frame and the outer wing box, with bio-based materials. On the other side, secondary structures and interior composites which are not stressed on such high levels offer possible areas of application. Examples for secondary structural parts are fairings and the landing gear doors. In the interior, cabin ceiling panels, sidewalls and floor panels are aims for the substitution of glass fibres and phenolic resins with ecological improved developments.

The composites under investigation in the ECO-COMPASS project are made from bio-based renewable resources like plants (e.g. flax, ramie, pine) as well as recycled carbon fibres. Added functionality like improved acoustic, vibration and electrical behaviour can be tuned according to design needs. Secondary and interior structures for aircraft were trial-manufactured by using these material systems in different combinations thereof. The threshold for the introduction of new materials in aviation is comparatively high because of the challenging safety requirements. An important example is the fire performance criteria for materials used in the cabin environment. The following chapter gives an overview of materials and results obtained in the ECO-COMPASS EU-China international collaboration project.

2 ECO-COMPOSITES

Today, thermosets are the most important polymer family used in the aviation industry, due to their versatility, high performance and the wide span of applications they comprise. However, their petrochemical base and the difficulty of thermosets to be recycled, forces the industry to seek for feasible alternatives that can reduce the ecological footprint associated to their production. Bio-based resin systems are gaining in attraction in order to replace the traditionally used petrol-based resin systems. For aviation it is important to develop bio-based high-performance resins which are able to substitute the traditional epoxies for use in structural applications. A comprehensive review article of bio-based resin system available and under research has been prepared in the ECO-COMPASS project by Ramon et al [2]. Furthermore, rosin acid [3] and itaconic acid [4] have been synthesized, and formulated partly

bio-based epoxy resins have been used to produce composites that can be compared to state of the art petrol-based epoxy resins [5]. Additionally, intrinsically flame retardant epoxy resin from renewable daidzein (diglycidyl ether of daidzein (DGED)) has been synthesized without addition of any flame-retardant element [6].

Further activities related to the bio-resins have focused on the introduction of nano fillers into the bio-based epoxy matrix and the preparation of specimens for mechanical and fire retardant testing. Silicon carbide nanoparticles, carbon nanotubes and nano clays have been selected as nano fillers to improve thermal, mechanical and conductive performance of the cured thermosets. High speed mixing followed by sonication has been used to disperse the previously functionalized nano fillers. After thermal and dispersion characterization, neat resin and nano modified resin tensile, compression and fire test specimens have been developed. Tensile and compressive tests have been performed to the neat resins showing values comparable to the currently used epoxies in this field.

A multitude of bio-based fibres is available on the world market. In Europe, flax and hemp fibres are the most common bast-fibres used to reinforce composites while ramie fibres that are grown in China are another suitable candidate. An important challenge of natural fibre reinforced polymers (NFRP) is their lack of strength compared to GFRP and especially CFRP. In theory, natural fibres can reach tensile strength of up to 1000Mpa while imperfections such as kink bands and the poor interfacial bonding properties between hydrophilic natural fibres and hydrophobic polymers lead to low mechanical properties of NFRP. Improving the interfacial strength and toughness is necessary in order to facilitate their full potential. On the other side, the low density of bio-fibres leads to beneficial specific stiffness values comparable to that of GFRP. Further advantages are their multifunctional aspects like acoustic and thermal damping due to the hollow fibre structure [7]. A multi-scale shear lag model was used to take the full advantages of the hierarchical structure of the NFRP [10, 11]. Component hybridization, nanoparticle grafting and nano modification have been utilised in ECO-COMPASS to improve the fracture toughness, interfacial shear strength, tensile strength and modulus of bio-based fibres. Fire retardation and the anti-microbial performances could be improved as well [8], [9].

Another topic of ECO-COMPASS was the utilisation of recycled carbon fibres (rCF). Virgin carbon fibres (vCF) are very expensive due to their energy intensive production process. It is therefore of high importance to reuse these valuable fibres in order to save energy, raw materials and cost. Pyrolysed rCF are available in milled and chopped form. A restricted length and the removal of the fibre sizing are their main drawbacks compared to vCF [10]. It is therefore at the moment not possible to give these “downcycled” fibres the same function as vCF. Therefore, an alternative way to improve the properties of pure NFRP by adding rCF has been assessed. Wet-laid [11] and carded [12] hybrid nonwoven of flax and rCF were produced on a small scale. Positive effects on the flexural properties on composite level can be observed by adding even small amounts of rCF. Furthermore, a honeycomb sandwich core was made of plant fibre hybrid paper containing 20% plant fibres and 80% chemical fibres (Green Honeycomb). The preparation process was similar to NOMEX® honeycomb and the developed material exhibits high strength and toughness in a small cell

with low density.

In order for eco-composites to be a real alternative to synthetic composites, it is necessary to improve the existing knowledge about them, as well as to have analysis and simulation tools capable of representing accurately their structural performance. This will ensure that the structures designed with them comply with the required security, functionality and quality standards. The mechanical-numerical proposal for such purpose consists of the adaptation of generalized mixing theory and/or multiple scale homogenization theory [13], derived from the formulations for the classical composite material, and all these mechanical formulation within a framework provided by the genetic algorithms optimization [14]. So, the proposed procedure promises a detailed behaviour study of the whole composite, starting from each one's simple component behaviour. As an example, a ramie-woven sandwich laminate was analysed with a full numerical homogenization approach. The numerical procedure developed has been applied to improve the design of a cabin luggage bin (hatrack).

An important aspect for composites used in aircraft is the material multifunctionality. Examples are the electrical conductivity for structural composites in order to detect cracking [15], shield the electromagnetic interference and lightning strike protection (LSP). The Functionalized Interlayer Technology (FIT) was proposed in order to simultaneously increase the electrical conductivity and the interlaminar fracture toughness [16]. A coupled electrical-thermal-pyrolytic model shows that the lightning strike damage is strongly governed by the anisotropic electrical properties of the carbon fibre composite. A lightning damage criterion was proposed to evaluate the in-plane damage by temperature dependent model and to estimate the in-depth damage by pyrolysis dependent model [17]. Further investigation is going to quantitatively understand the mechanism of the lightning strike on the composite laminates, supported by the experimental lightning strike test.

3 CONCLUSIONS

Bio-based and multifunctional composites offer unique alternatives for aeronautical structures and can also expand state-of-the-art technologies. Based on the current results with the materials considered in ECO-COMPASS, partly bio-based epoxy resin systems have the highest potential for a successful application in aviation. Their properties approach the performance of the fully petrol-based epoxy resins used today. A case study from the ECO-COMPASS project demonstrates the manufacturing of an empennage side panel based on state of the art carbon fibre and partly bio-based epoxy resin including lightning strike protection. Improvements of resin properties such as conductivity and flammability with adapted flame retardants such as DOPO-MA and different nano fillers are under development. Green Honeycomb with small amount of natural fibre mixed with classic aramid fibre can be another technology with high potential for the introduction of bio-based materials in aviation composite structures.

Natural fibres such as ramie and flax have a high potential for weight reduction due to their low density and good damping properties. However, their long-term behaviour and mechanical properties need to be further improved. Potential technologies are under

development, such as cellulose nanocrystal coating, plasma treatment and hybridization with recycled carbon fibres. Fire properties of NFRP with natural fibres and epoxy resin are a challenge the application in the cabin interior and baggage compartment. While flammability and toxicity are already under control for the combination of natural fibres and epoxy resin, the heat release and smoke density properties need further improvement.

Different numerical methods developed within ECO-COMPASS have been used to gain a better understanding of the performance of eco-composites, and can be used to predict the response of these materials when used in aerospace applications. A good design of an aerospace structure made with eco-composites will require accounting for the different aspects considered, from mechanical characterization to resistance to a lighting strike. The presented results highlight materials-enabled potential, and an alternative solution to reduce environmental impacts of aviation within the CLEAN SKY target. Research and development needs to be continued in order to understand the fundamental issues affecting the performance of these material systems. Life Cycle Assessment needs to be intensified in order to further reduce ecological impacts using bio-based materials with suitable technologies to improve their properties.

(a) (b) (c)

Figure 1: Examples of demonstrators from ECO-COMPASS Project: Generic secondary (a) and interior (b) sandwich panels with Green Honeycomb core; trailing edge panel of a horizontal tail made of carbon fibre with epoxy including rosin-based curing agent (c).

AKNOWLEDGEMENT

This project was supported by the European Union's Horizon 2020 research and innovation programme (Grant No. 690638), and the Ministry for Industry and Information of the People's Republic of China (Grant No. [2016]92).

REFERENCES

[1] Bachmann J, Yi X, Gong H, et al. Outlook on ecologically improved composites for aviation interior and secondary structures. *CEAS Aeronaut J* (2018) 9: 533-543.

[2] Ramon E, Sguazzo C, Moreira PMGP. A Review of Recent Research on Bio-Based Epoxy Systems for Engineering Applications and Potentialities in the Aviation Sector. *Aerospace*. 2018; 5(4):110.

[3] Li C, Liu X, Zhu J, Zhang C, Guo J. Synthesis, Characterization of a Rosin-based Epoxy

Monomer and its Comparison with a Petroleum-based Counterpart, *Journal of Macromolecular Science, Part A: Pure and Applied Chemistry*, (2013) 50, 321–329

[4] Ma S, Liu X, Jiang Y, Tang Z, Zhang C, Zhu J. Bio-based epoxy resin from itaconic acid and its thermosets cured with anhydride and comonomers, *Green Chemistry*, 2013, 15, 245–254

[5] Dai J, Peng Y, Teng N, Liu Y, Liu C, Shen X, Mahmud S, Zhu J, Liu X. High-Performing and Fire-Resistant Biobased Epoxy Resin from Renewable Sources, *ACS Sustainable Chemistry and Engineering* 2018, 6, 7589−7599

[6] Yi X, Zhang X, Ding F, Tong J. Development of Bio-Sourced Epoxies for Bio-Composites. *Aerospace*, 2018; 5(2):65

[7] Zhang J, Shen Y, Jiang B, Li Y. Sound Absorption Characterization of Natural Materials and Sandwich Structure Composites. *Aerospace*, 2018; 5(3):75.

[8] Wang H, Xian G, Li H, Grafting of nano-TiO2 onto flax fibers and the enhancement of the mechanical properties of the flax fiber and flax fiber/epoxy composite, *Composites Part A -Applied Science and Manufacturing* 76 (2015) 172-180.

[9] Li Y, Yi X, Yu T, Xian G, An overview of structural-functional-integrated composites based on the hierarchical microstructures of plant fibers, *Advanced Composites and Hybrid Materials*, June 2018, 1(2), 231-246

[10] Fischer, H. & Schmid, H.G. (2013). Quality control for recycled carbon fibres. *Polymers* 11/2013, pp. 88-91

[11] Tse B, Yu X, Gong H, Soutis C. Flexural Properties of Wet-Laid Hybrid Nonwoven Recycled Carbon and Flax Fibre Composites in Poly-Lactic Acid Matrix. *Aerospace*, 2018; 5(4):120.

[12] Bachmann, J. and Wiedemann, M. Flexural Mechanical Properties of Hybrid Epoxy Composites Reinforced with Nonwoven Made of Flax Fibres and Recycled Carbon Fibres. *Aerospace*, 2018; 5(4):107.

[13] Otero, F., Martinez, X., Oller, S., Salomón, S. (2015). An efficient multi-scale method for non-linear analysis of composite structures, *Composite Structures*, Vol. 131, pp. 707-719.

[14] Lee, D.S., Morillo, G., Bugeda, G., Oller, S.,Onate, E. (2013). Robust design optimisation of advance hybrid (fiber–metal) composite structures, *Composite Structures*, Volume 99, 2013, Pages 181-192. ISSN: 0263-8223

[15] Tserpes K, Kora C. A Multi-Scale Modeling Approach for Simulating Crack Sensing in Polymer Fibrous Composites Using Electrically Conductive Carbon Nanotube Networks. Part II: Meso- and Macro-Scale Analyses. *Aerospace*, 2018; 5(4):106.

[16] Lin, YE. Functionalized interleaf technology in carbon-fibre-reinforced composites for aircraft applications. *National Science Review*, 2014, 01, 00: 1-2, 2013. doi: 10.1093/nsr/nwt005.

[17] Guo, Y L, Dong Q, Chen J L, et al. Comparison between temperature and pyrolysis dependent models to evaluate the lightning strike damage of carbon fiber composite laminates. *Comp Part A-Appl S*, 2017, 97: 10-18.

INTEGRATING ELECTROMAGNETIC FUNCTIONS INTO FIBER METAL LAMINATES – THE STRUCTURAL CHALLENGE

– EMuS 2019 -

CEES VAN HENGEL[*], CHARLY HEUTS[†] AND JACO VERPOORTE[¤]

[*] Fokker Aerostructures
Industrieweg 4, 3351 LB Papendrecht, Netherlands
cees.vanhengel@fokker.com

[†] Fokker Elmo
Aviolandalaan 33m 4631 RP, Netherlands
charly.heuts@fokker.com

[¤] Netherlands Aerospace Centre (NLR)
Voorsterweg 31, 8316 PR Marknesse, Netherlands
jaco.verpoorte@nlr.nl

Keywords: GNSS, VHF, FML, Integrated Antenna, Glare

Abstract:

This paper outlines aspects, outcome and prospects of full integration of antennas into structural elements of aircraft, from a structural design perspective.

1 INTRODUCTION

Currently, antennas on civil aircraft are typically not integrated but externally mounted items. Firstly this causes aerodynamic drag resulting in increased fuel use. Secondly, conventional antennas are subject to in-flight damage by hail, lightning strike and also by ground handling. Integration of antennas holds the potential to remove the drag issue, and reduce the impact damage sensitivity as well. Thirdly, a smooth fuselage may also offer esthetic appeal which may be appreciated by discerning customers of top level business jets.

In view of these benefits, integration of antennas is the subject of research such as in the European ACASIAS project. The aim is ***full*** integration, i.e. to making the antenna function an integral part of the structural component. Structural components in this regard are meant to be structural aircraft elements that fulfil a load-bearing function.

A particularily interesting material type for the antenna integration purpose are Fiber Metal Laminates or FMLs. An FML is a hybrid composite aircraft construction material, consisting

of fiber layers that are bonded together with metal layers to form a cohesive laminate. This construction material has been developed especially to improve metal fatigue properties of aircraft construction material. As it turns out, this material also lends itself to be morphed into an antenna. However, the electromagnetic functioning of an antenna, and its associated design, are outside the scope of the present paper.

Two types of antenna, which enable integration within an aircraft fuselage skin, have been chosen for the present research; each antenna for a different application in terms of operating frequency and direction of radio wave propagation. The smaller of the two is a GNSS (Global Navigation Satellite System) antenna, as described in the paper by Konter et.al. [1]. This antenna is of limited structural complexity and will not be further discussed here. The larger of the two is a VHF antenna, which has the potential to cause major disruption to the fuselage structure, making the integration significantly more challenging. The structural integration of the VHF antenna will therefore be the main topic of this paper.

2 FMLs- A BRIEF INTRODUCTION

Fiber Metal Laminates are a class of hybrid materials consisting of aluminium layers bonded together with epoxy adhesive reinforced by high strength unidirectional glass fibres, see Fig. 1. The material is produced in a composite like process, namely by precisely placing the ingredient aluminium and glass-fibre prepreg plies in a predefined way on top of each other on a curved aluminium lay-up mold. Following lay-up, the laminate is consolidated in an autoclave by curing under pressure and temperature. The resulting material has aluminium-like characteristics, making it suitable for adoption in aluminium oriented production processes such as used in the aircraft industry.

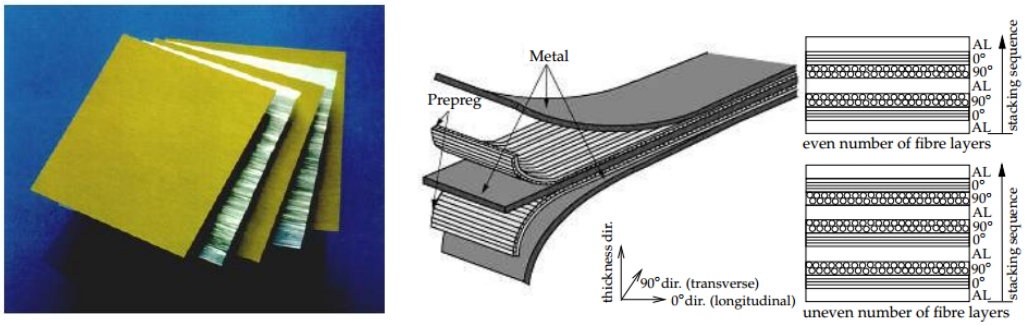

Figure 1: FML laminate ingredients (left) and typical laminate lay-up and stacking sequence

The mechanical properties that result from the judicious combination of the aluminium and GRP layers include very slow fatigue crack growth, high static strength and high impact resistance. In addition, the electrical conductivity of the metal layers provides lightning protection and EMI shielding. Furthermore, the glass-epoxy layers provide corrosion resistance and aid burn-through resistance (Fig. 2).

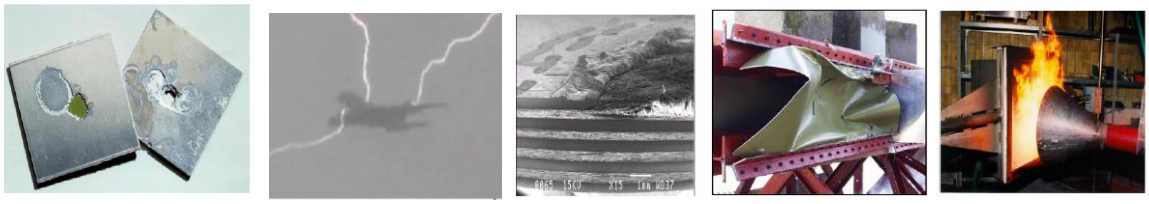

Figure 2: FML materials property illustrations (from left): corrosion resistance, lightning strike event and localized material damage, impact resistance (leading edge development test), and burn-through resistance

Also, the composite-like nature of the FML material concept provides a composite-like design freedom with respect to fiber orientation and laminate thickness variation. As demonstrated on the Airbus A380, where approx. 460 m^2 of the material is applied as 27 large fuselage skin panels, the combination of this design freedom, the FML material properties, and the manufacturing process enable aircraft designers to achieve significant weight savings at costs that are competitive with aluminium [2, 3].

Last but not least the aluminium-like character of FMLs also brings with it another benefit. As demonstrated by many years of flight testing on an Airbus A310 of the German Air Force during the development of FML in the late 90's and early 00's, the aluminium-like characteristic of FML material makes it relatively easy to replace an aluminium skin panel of an existing aircraft by an FML panel (Fig. 3). This fact may greatly simplify the future introduction for testing or operational use of integrated antennas on existing aircraft.

All in all, FMLs make promising candidate material for the integration of antennas in the structure

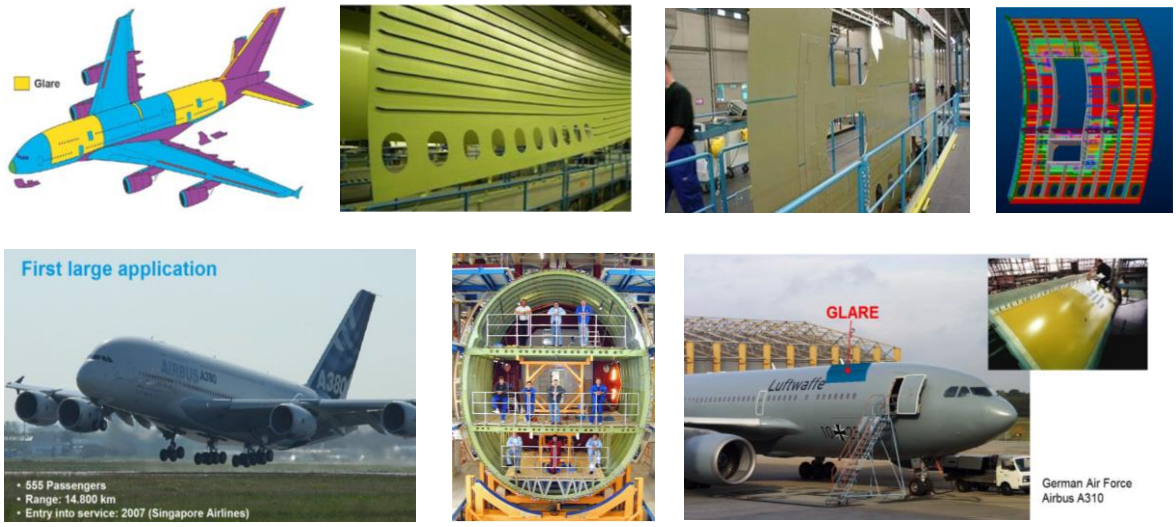

Figure 3: FML Glare application examples (clockwise from top left): Glare FML panels on A380, FML panel with stringers and window cut-outs, FML door panel, door panel design, developmental Glare test panel flown on A310, A380 fuselage cross section (Megaliner Barrel test), A380 take-off

3 VHF ANTENNA: CUT-OUT GEOMETRY

From an antenna design perspective, a slot antenna is an elegant solution to enable a flush (non-protruding) antenna. Since for VHF-COM the electromagnetic fields needs to be vertically polarized, the laws of electromagnetism require that the slot is oriented horizontally. This kind of geometry is show in Fig. 4. A VHF antenna operates at a relatively low electromagnetic frequency (approx. 100 MHz) and since the slot length is determined primarily by the frequency, this results in a slot length of approx. 0.8 to 1.2 m depending on the antenna materials. Aircraft fuselages are typically semi-monocoque structures, where circular frames and straight stringers support the skin which is the main load carrying structural element. For commercial aircraft that fly at a height of approx. 10 km, the cabin section of the fuselage is pressurized to approx. 0.5 bar or more of overpressure in flight, which results in high *circumferential* (and lesser axial) loads in the skin.

In these circumstances, from a structural perspective, creating a *horizontal* slot in the skin is about the worst possible "damage" that can be done to the structure. Detailed FEM analyses [2] of early design studies showed the high deformations and stresses that can occur due to the pressurization load, and highlighted the need for proper attachment of stringers and frames in the cut-out area.

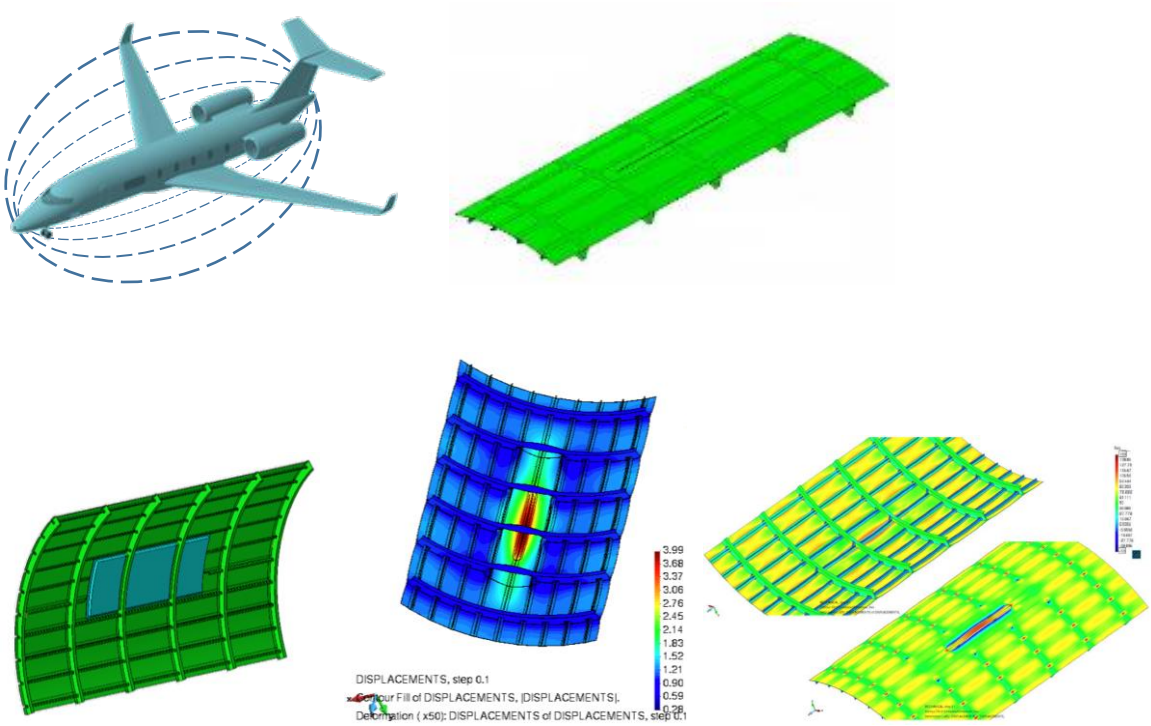

Figure 4: Slot antenna lay-out (early concept studies and FEM analyses [4])

4 SKIN LOAD PATH CONTINUITY

A fuselage typically contains many cut-outs, such as passenger doors, emergency exits and windows, so the antenna slot is not unique in disturbing skin load path continuity. However, to keep the antenna commercially attractive, the added weight and cost of integration must be kept small, and therefore the kind of reinforcements needed for doors etc. are not acceptable. Fortunately the antenna slot needs only to be present in the aluminium part of the FML layers, and the slot gap can therefore be bridged by continuous glass layers since these are electromagnetically transparent. Additional glass layers are added for sufficient strength (Fig. 5). The most effective build-up is currently under investigation.

Figure 5: Transition from FML to «full glass» GFRP to FML (concept)

5 CERTIFICATION ASPECTS

Aircraft need to meet stringent airworthiness requirements before they are allowed to fly. Since an integrated slot antenna, if ever applied, will definitely come under the scrutiny of the airworthiness authorities, it is wise to consider the airworthiness requirements early in the development. A time proven approach to meet strength requirements is the so-called Building Block testing pyramid approach as shown in fig. 6. This approach goes from testing a large number of (cheap) small test specimens at the material level, up to testing only one or two very large and expensive test specimens at the component level (such as a wing or fuselage section).

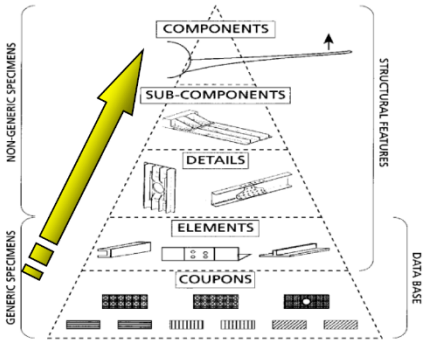

Figure 6: Building Block test Pyramid

This approach will also be followed for structural testing of the integrated antenna. In line with the low-TRL level of the current project, the anticipated highest level is that of “details” (Fig. 7).

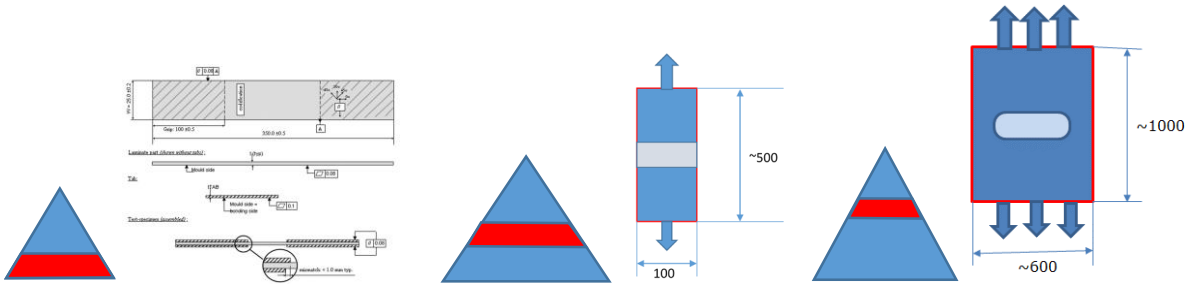

Figure 7: Building Block tests planned for Integrated Antenna (from left): coupon testing for material characterization, structural element testing of FML-GFRP-FML transition, «full scale» panel test

6 CONCLUDING REMARKS

The structural aspects have been outlined of an Integrated Slot Antenna in an FML fuselage skin. As has been shown, the FML material offers numerous advantages to the realization of this concept, such as the possibility for a smooth transition from FML to full glass-fiber reinforced composite and back. The development approach selected takes into account the possibility of future airworthiness certification.

ACKNOWLEDGEMENTS

The support of CIMNE in the preparation of this paper is gratefully acknowledged.
All work described in this paper has received funding from the European Union's Horizon 2020 research and innovation programme under grant agreement No. 723167, ACASIAS project.

REFERENCES

[1] Yuri E. Konter†, Charly Heuts and Cees van Hengel "Exploration Of Radiating Aerostructures Ultimate Antenna And Structure Integration" – EMuS 2019, June, BARCELONA, Spain

[2] Hinrichsen, J.: "The Material Down-selection Process for A3XX"; Keynote Address to the "19th European Conference on Materials for Aerospace Applications", Confederation of European Aerospace Societies (CEAS), Munich, Germany Dec. 6th – 8th, 2000.

[3] Dr.-Ing. Thomas Beumler,: "Airbus Fiber Metal Laminate Structures – from Laboratory to Application", Lecture to RAeS Hamburg Branch, 29 October 2009, https://www.fzt.haw-hamburg.de//pers/Scholz/dglr/hh/text_2009_10_29_Fiber_Metal_Laminates.pdf

[4] Xavier Martinez, FrancescTuron & Fermin Otero "Homogenization procedure for the structural design of smart fuselage panels", 8TH EASN-CEAS International workshop on manufacturing for growth and innovation, September 5TH, 2018, GLASGOW, UK

European Conference on Multifunctional Structures
EMuS 2019
X. Martinez and H. Schippers (Eds)

EXPLORATION OF RADIATING AEROSTRUCTURES ULTIMATE ANTENNA AND STRUCTURE INTEGRATION – EMUS 2019

YURI E. J. KONTER[†], CHARLY HEUTS[*] AND CEES VAN HENGEL [n]

[†] Netherlands Aerospace Centre (NLR)
Voorsterweg 31, 8316 PR Marknesse, Netherlands

[*] Fokker Elmo
Aviolandalaan 33, 4631 RP, Netherlands

[n] Fokker Aerostructures
Industrieweg 4, 3351 LB Papendrecht, Netherlands

Key words: GNSS, VHF, FML, Integration, GLARE

Abstract. Two antenna designs are described that are both fully integrated into Fiber Metal Laminate fuselage panels. Full integration in this context means that the antennas are flush with the fuselage skin on the outside of the aero structure, while maintaining the structural properties of the FML panel. The antennas are designed to resonate at GNSS and at VHF frequency bands. Design considerations are discussed and preliminary results are presented.

1 INTRODUCTION

Currently antennas are mounted as separate components onto the exterior of fuselages. These antennas protrude into the airflow around an aircraft which produces drag during flight. Integration of the antennas into the fuselage will further smoothen the outside of aero planes and thus reduce the aerodynamic drag.

Fiber Metal Laminate (FML) is a composite aircraft construction material, consisting of metal layers bound together by glass fiber layers and resin to form a cohesive laminate. Since the glass fiber layers are electrically insulating, applying RF currents onto the metal layers will cause electric fields which can be used to create antennas.

This paper discusses integration of a global navigation satellite system (GNSS) antenna and a VHF antenna into FML panels. The antennas are realized as a double patch antenna and a slot antenna respectively. Stacked patch antennas share many similarities with FML panels in terms of buildup and the electric properties of the used materials. Consequently, an antenna can be made directly in the FML panel with slight modifications to the buildup of the FML layers. Integration of the GNSS antenna is described in section two. Alternatively, a hole can be made in a metal layer which will operate as a slot antenna. A slot can be used to create a VHF antenna. The integration of such a slot antenna into a FML panel is described in section three.

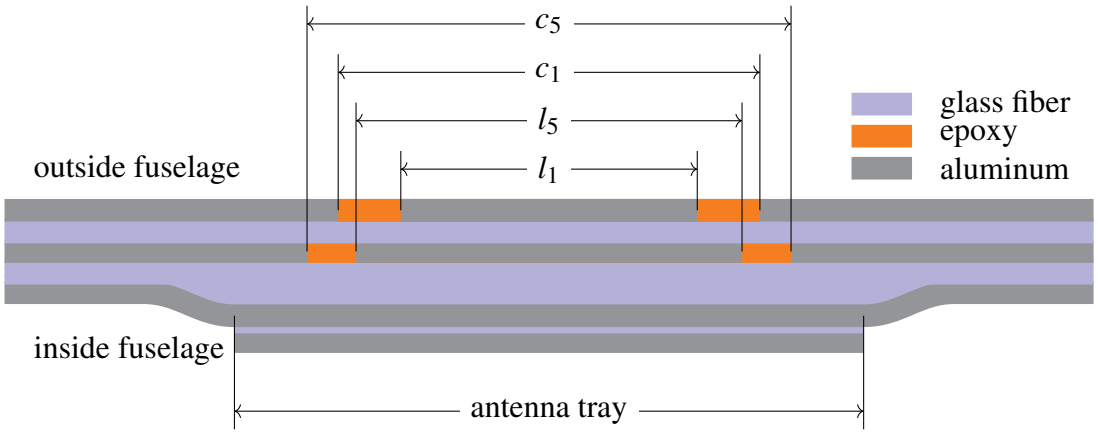

Figure 1: Cross section of the circular double patch GNSS antenna integrated into a FML panel. The inner aluminum layer of the FML panel is bend to create a tray for the antenna. The two radiating patches are created in-plane with the two outer aluminum layers.

2 Integration of a double stack GNSS antenna into FML

GNSS antennas used for aviation are Right Handed Circular Polarized (RHCP) and operate in both the L1 and the L5 bands. Therefore, a double stacked patch antenna is designed such that each of the stacked patches radiates in one of the bands. As discussed in [1], four probes are used in order to meet the polarization requirements of the GNSS antenna. By doing so, a good axial ratio is guaranteed for a broad viewing angle, whilst keeping the antenna design robust enough for integration in FML panels.

The antenna is integrated in GLARE G-4B-3/2-0.3 fuselage, a composite material build up from three aluminum layers bound together with layers of glass fiber and resin. A circular dent is introduced in the inner aluminum layer creating a thicker glass fiber layer between the inner and middle layers. This inner metal layer will function as an electrical ground-plane for the stacked patch antenna. Concentric circular patches are created in the middle and outer aluminum layers resulting in the FML stack shown in figure 1. The l_1 and l_5 patches will attribute to radiation in the L1 and L5 bands respectively. An additional aluminum layer is added on the inside of the dent to provide additional strength to the fuselage. This aluminum layer has no effect on the electrical performance of the integrated antenna.

2.1 Fabrication tolerances

The GNSS antenna is made by placing the circular patches in an autoclave together with the fuselage panels. In doing so, the antenna becomes a flush integral part of a fuselage panel. During this manufacturing process, the metal components responsible for the antenna function of the fuselage panel can drift. Two fabrication artifacts are of particular interest. The centers of the circular patches can be misaligned (figure 2a) and fuselage can drift towards the antenna patches (figure 2b). The effect of these deviations are shown in figure 3. The FML panels can drift several millimeters with no significant consequence on the antenna performance. Drifts of the FML panels relative to the circular antenna patches primarily affect antenna performance

(a) The two circular metal patches can show some misalignment resulting in degradation of antenna performance.

(b) The circular antenna patches can drift towards the fuselage panel which can lead to unwanted electrical coupling between the patch and the fuselage panel.

Figure 2: Examples of misalignment resulting from the fabrication process.

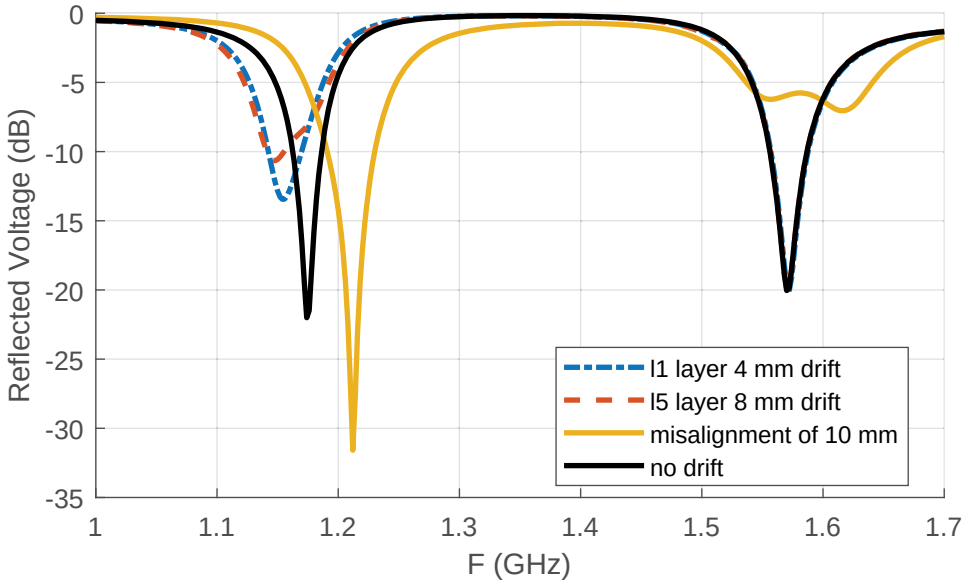

Figure 3: The effect of misalignment on the reflected voltage of the integrated antenna. The two resonance peaks correspond to the L5 band (left) and the L1 band (right). The reflected voltage subject to drifts of the middle FML metal layer and outer FML metal layer are shown in blue and red respectively. The effect of misalignment of the circular patches is shown in yellow.

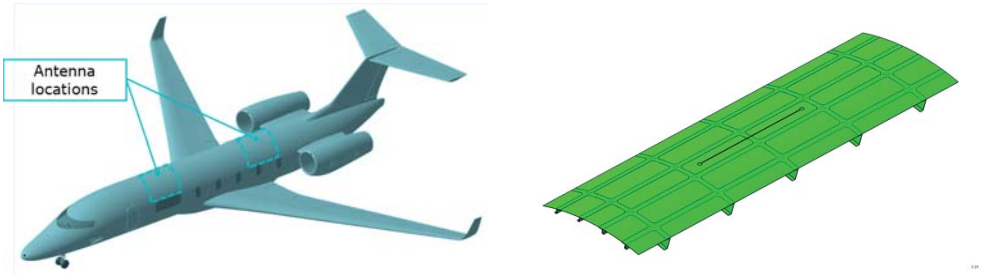

(a) Location of VHF slot antennas on outside of aircraft.

(b) VHF slot antenna integrated between frames and stringers of GLARE fuselage panel.

Figure 4: Integration of VHF slot antenna.

in the L5 band. The loss in performance due to drifts of the middle FML metal layer is due to coupling between the L5 radiating patch and the fuselage. The performance loss caused by drifts of the outer metal layer is caused by the outer FML metal layer which partially covers the lower circular patch. Misalignment of the two antenna patches increases the parasitic coupling between the two patches, improving the performance of the inner patch. However, the resonant frequency of the l_5 patch shifts out of the L5 band. Loss of L1 band performance is also seen when the L1 circular patch is misaligned such that it no longer sits fully on top of the lower patch.

The observed detrimental results are not gradual effects, but instead happen only if drifts are large enough. These thresholds result in the fabrication tolerances for the integrated GNSS antenna. The imposed tolerances can be made more lenient by increasing the diameter of the epoxy rings shown in figure 1, which will result in an overall larger antenna design.

3 Integration of a VHF slot antenna into FML

The larger wavelength, and therefore larger antenna sizes, make that VHF antennas are of particular interest for miniaturization. A slot antenna allows flush integration of antennas into the fuselage regardless of the operating frequency and wavelength. Moreover, FML has a large metal area on the outside of the fuselage which is required for proper operation of a slot antenna.

Slot antennas radiate in both directions away from the conducting surface, resulting in unwanted radiation into the inside of the aircraft. The inward radiation can be suppressed by introducing a ground plane shield a quarter wavelength (75 cm) behind the antenna. This required length can be reduced significantly by applying a parallel plate resonator as radiation shield [2]. Additionally, the bandwidth of a slot antenna is improved by applying a feed technique where two separate modes of the slot are excited [3].

3.1 Integration of the VHF antenna

Vertical polarization is achieved with a horizontally oriented slot antenna placed on the sides of an aircraft as shown in figure 4a. Due to the length of the slot needed for VHF radiation, the slot will run through one of the frames as shown in figure 4b. Modification to the frames

(a) Slot antenna with a folded parallel plate resonator. The antenna is made using standard FR4 as dielectric with copper plating. The rectangular slot is visible as the shaded area in the top FR4 layer.

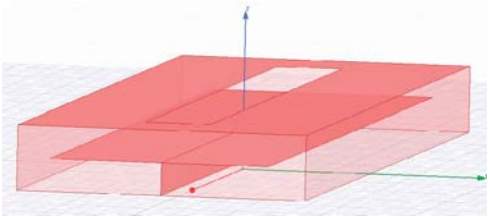

(b) Design showing fold of the PPR. The PPR fold is created by placing a T-shaped copper structure underneath the slot.

Figure 5: 300 MHz slot antenna with PPR to suppress back radiation.

are required to fit the PPR behind the slot on the inside of the fuselage. These modifications should preserve both the electrical function of the PPR and the local structural properties of the fuselage panel.

3.2 Verification of simulations

A 300 MHz version of the slot antenna was used to validate our simulations. The antenna was made using FR4 materials as shown in figure 5a). The PPR is folded according to figure 5b. The reflected voltage of the antenna design is shown in figure 6 together with the simulation results created in FEKO. The two resonant modes required to broaden the bandwidth are recognizable by the valleys in reflected voltages. Increasing the length of the stub reduces the reflected voltage for the lower resonant frequency of about 270 MHz but increases the reflected voltage of the higher resonant frequency at about 340 MHz. Thus, a trade-off is made resulting in the broadest possible bandwidth.

4 Conclusion

Two fully integrated antenna concepts are presented, both with a flush finish on the outside of the fuselage. Effects of integration on electrical performance have been simulated resulting in fabrication limits for the antenna designs. The performance of the VHF slot antenna with a PPR has been demonstrated with a prototype. Measurements of the prototype show good correspondence with the simulations results. The antennas will further improve aerodynamic properties of aero structures by replacing protruding electrical components with flush integrated antenna solutions.

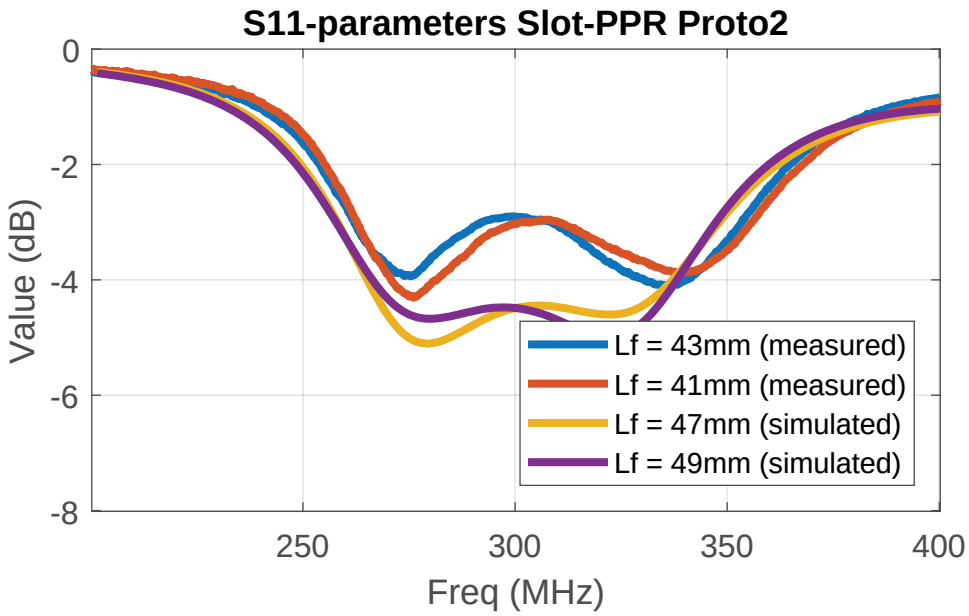

Figure 6: Simulated and measured reflected voltage the 300 MHz slot antenna with a folded parallel plate resonator as shield. The length of the stub is given by Lf.

Acknowledgements

This project has received funding from the European Union's Horizon 2020 research and innovation programme under grant agreement No. 723167.

REFERENCES

[1] K. Yinusa, "A Dual-Band Conformal Antenna for GNSS Applications in Small Cylindrical Structures," *IEEE Antennas and Wireless Propagation Letters*, pp. 1–1, 2018.

[2] W. Hong and K. Sarabandi, "Platform Embedded Slot Antenna Backed by Shielded Parallel Plate Resonator," *IEEE Transactions on Antennas and Propagation*, vol. 58, pp. 2850–2857, Sept. 2010.

[3] N. Behdad and K. Sarabandi, "A wide-band slot antenna design employing a fictitious short circuit concept," *IEEE Transactions on Antennas and Propagation*, vol. 53, pp. 475–482, Jan. 2005.

European Conference on Multifunctional Structures
EMuS 2019
X. Martinez and H. Schippers (Eds)

ANALYSIS OF RADAR ABSORBING FSS ON FOLDCORES AND HONEYCOMBS

J.J.P. VAN ES[*], A. HULZINGA[*], P. TENSEN[*], H. SCHIPPERS[*], R.M.H. HEIJMANS[†], M.J.G. JOURNEE[†]

[*] Netherlands Aerospace Centre (NLR)
Voorsterweg 31, 8316 PR Marknesse, The Netherlands
e-mail: Jan-Joris.van.Es@nlr.nl, www.nlr.nl

[†] Teijin Aramid B.V.
Velperweg 76, 6824 BM Arnhem, The Netherlands
email: Ruud.Heijmans@Teijinaramid.com, www.teijinaramid.com

Key words: Computational Methods, Metamaterials, Radar absorption

Abstract: The objective of the paper is to investigate the radar absorption of honeycombs and foldcores with printed conductive patterns. These structures can be manufactured by first printing conductive Frequency Selective Surfaces (FSS) on planar substrates, which then can be used to shape foldcores and honeycombs by means of specific manufacturing technologies. Foldcores can be considered as intermediate shapes between planar sheets (where the printed patterns are perpendicular to the impinging radar waves) and honeycombs (where the printed patterns are parallel to the impinging radar wave). It is shown that the radar absorbing properties of the design strongly depend on the electrical conductivity of the paint, the size of the printed patterns and the orientation of the printed patterns with respect to the impinging wave. It is shown that a planar FSS has a maximum absorption of 50%, while foldcores and honeycombs may obtain a higher absorption due to the fact that the patterns are orientated under an angle with respect to the propagation direction of the wave.

1 INTRODUCTION

This research deals with the development of advanced radar absorbing structures with artificial structured metamaterials. These materials can be realised by printing arrays of electrically conducting patterns (such as Split-Ring resonators) on non-conducting sheets. The goal of the conducting patterns is to modify the EM properties of the structure and to influence the way incident EM waves are reflected and transmitted. The structure can be made lossy, i.e. absorbing EM energy, by applying the right patterns and right electric conductivity.

The challenge is two-fold. There is the question of how the conducting patterns should look and what size they should have in order to obtain the desired EM properties. On the other hand there is the question of actually fabricating such a structure. Screen printing and inkjet printing with electrically conducting ink appear valid options to produce the desired shapes. The substrates can be FR4 glass epoxy, aramid honeycomb papers, or other non-conducting sheets. Once successful the printed 2D sheets can be used to create 3D structures such as honeycombs and foldcores with tailored EM properties.

The subject of tailoring the EM properties of 3D arrangements of electrically conducting patterns is not new and has been the topic of earlier research [1,2,3]. In these earlier publications the emphasis is on achieving particular values of permittivity and permeability. In the current work we focus on the radar absorbing properties of the materials and the optimisation of the conductivity to maximise absorption.

2 GEOMETRIES

The electrically conducting patterns in this research are circular rings and split-ring resonators (SRR). The conducting patterns are repeated in a regular way to form an infinite sheet. Depending on the orientation of the pattern in the unit cell and the repetition vector, the sheet can be an infinitely thin FSS, a honeycomb or a foldcore (**Figure 1**).

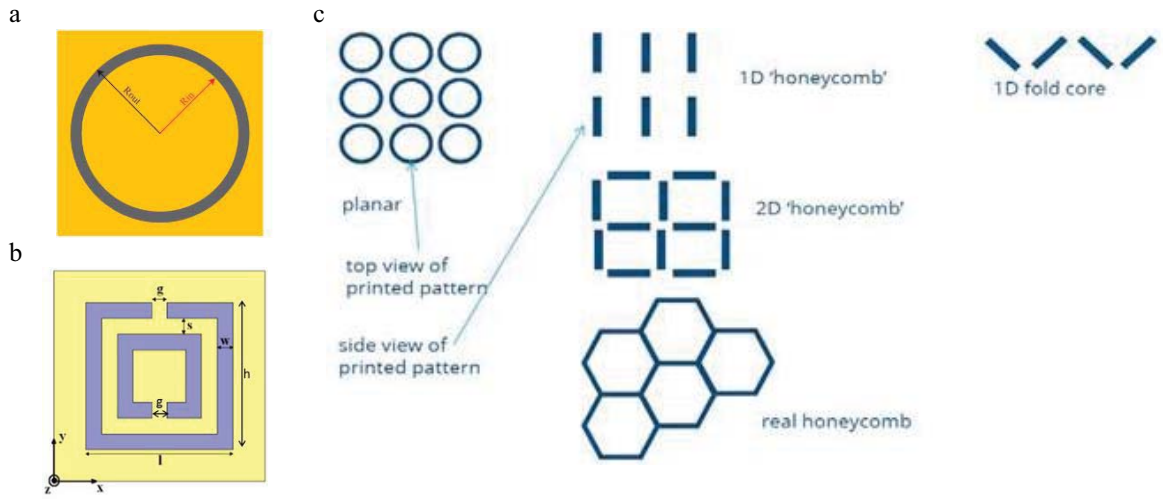

Figure 1: Conducting patterns ring (a) and split-ring resonantor (SRR) (b). Extension of primary periodic cells to sheets, honeycombs or foldcores (c)

3 SIMULATION RESULTS

The electromagnetic properties of the conducting patterns are determined by simulating the interaction between an infinite sheet of repeated patterns and impinging planar waves. The reflection and transmission coefficients of the waves due to the presence of the sheet are simulated in Ansys HFSS. In this software package a single conductive element embedded in a unit cell with periodic boundary conditions generates the regular array. In the simulations only the conductors are considered. Substrates, part of any practical material, are ignored as they are thin and have little impact on the final EM properties.

3.1 Size

The size and the exact shape of the conducting patterns determine the resonant behaviour. In the current work the conducting patterns are designed for maximum effect in X-band (8.2-12.4 GHz). The SRR has a 4 mm width (l), 3 mm height (h), 0.5 mm spacing between the rings (s), 0.5 mm gap (g) and 0.3 mm trace width (w). The conducting rings have an inner radius of 4.2 mm and an outer radius of 4.8 mm (**Figure 1 a and b**).

3.2 Electric conductivity

The impinging EM waves induce currents in the conducting patterns. These currents experience Ohmic losses which gives rise to the radar absorbing effect. The rings need to have a specific conductivity for optimum absorption. If the electric conductivity is too high currents will be induced in the patterns, but the currents will experience little losses. If the conductivity is too low little currents will be induced and the waves will propagate unobstructed. The absorption, *A*, is calculated from the (complex-valued) transmission, *T*, and reflection, *R*, coefficients in the HFSS simulation results as

$$A = 1 - RR^* - TT^* \tag{1}$$

To illustrate the importance of the value of the conductivity, the reflection and transmission coefficients have been computed for perfectly conducting rings in a planar sheet FSS. The results are shown in **Figure 2**. Obviously the rings are resonant at 12 GHz. For these perfectly conducting rings there is no absorption. Next the absorption coefficient is computed in relation to the conductivity of these rings. From **Figure 3** it is concluded that the amount of absorption strongly depends on the conductivity. The conductivity of the rings can be quantified in different ways. It can be given as the sheet resistivity (R_s), the parallel resistance ($R_{||}$) of two half rings when measured across with two probes or as the resistance of the whole ring when it would be interrupted by an infinitely narrow slit ($R=4\ R_{||}$). R_s and $R_{||}$ relate as

$$R_{||} = R_s\ (\pi/4)\ (r_o + r_i)/\ (r_o - r_i) \tag{2}$$

For the given size of the rings, simulations show that the optimum absorption is obtained for $R_{||}$=140 Ω and R_s=12 Ω/sq. $R_{||}$ is almost frequency invariant.

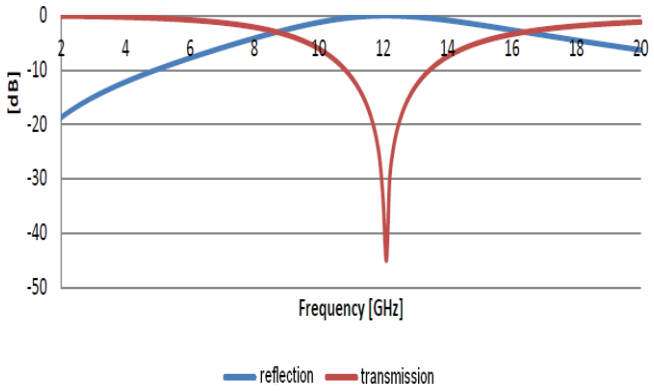

Figure 2: Reflection and transmission coefficient of planar sheet with perfectly conducting rings; (inner radius : 4.2 mm, outer radius 4.8 mm, cell size 11 mm)

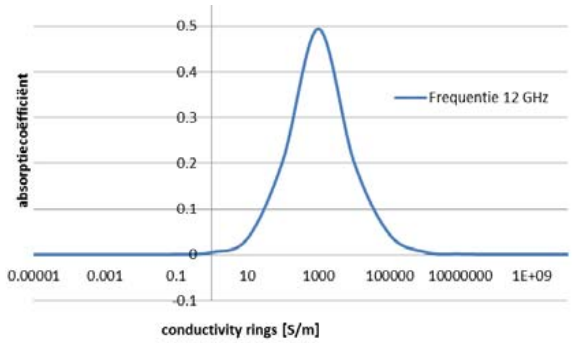

Figure 3: Absorption coefficient of planar sheet with conducting rings at 12 GHz as function of the bulk conductivity of the rings

3.3 Orientation

For planar sheets of conducting patterns with zero thickness the maximum absorption is found to be 0.5 (-3 dB) (**Figure 3**). Using transmission line theory, this case can be modelled as a lumped impedance Z_L in parallel with the wave impedance of the propagation medium Z_0. In this case the reflection and transmission coefficients are given as

$$R = -Z_0 / (Z_0 + 2Z_L) \tag{3}$$

$$T = 2\,Z_L / (Z_0 + 2Z_L) \tag{4}$$

such that indeed the absorption is 0.5 when $Z_L = Z_0/2$. Only in the case when the conducting patterns are oriented out-of-plane higher absorption is observed.

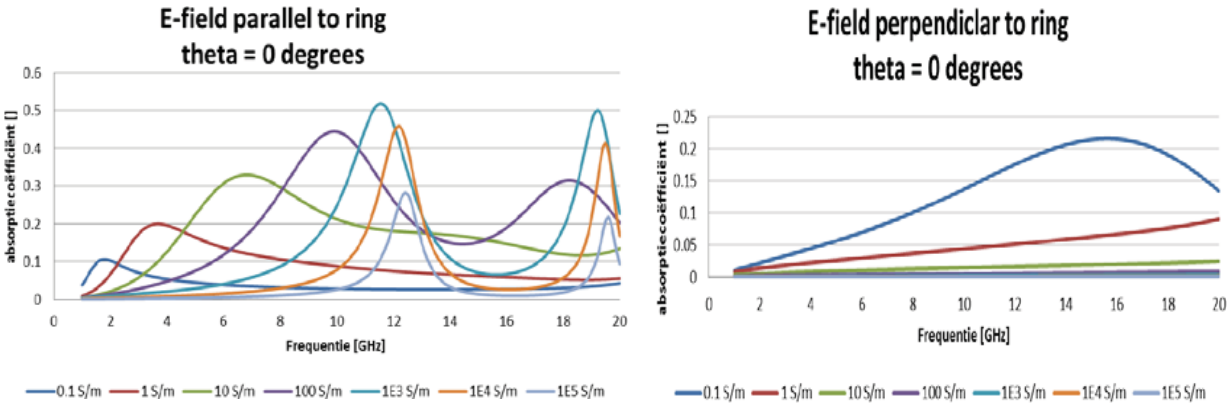

Figure 4: Absorption of 1D honeycomb with rings for different conductivities; direction E-field parallel to the rings (left), direction of E-field perpendicular to the rings (right)

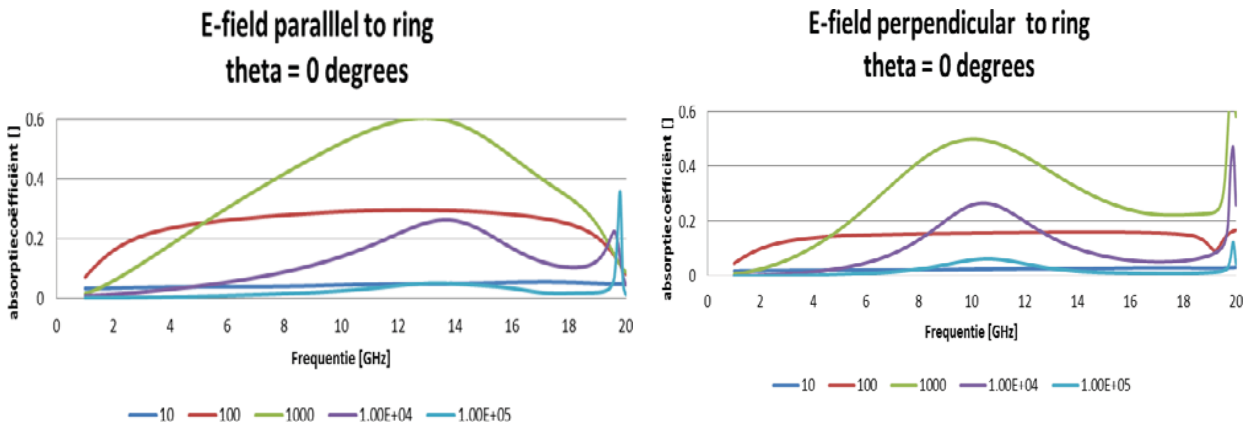

Figure 5: Absorption of 1D foldcore with rings for different conductivities;
direction E-field parallel to the rings (left), direction of E-field perpendicular to the rings (right)

The orientation of the conducting patterns with respect to the E-field of the impinging influences the magnitude of the induced current in the patterns and thus the absorption. The induced current and the losses are largest with the conductors parallel to the electric field vector. This effect is nicely illustrated in a 1D honeycomb with conducting rings (**Figure 4**). The different colours in this figure indicate different values of the conductivity. Generally the variation in absorption is smaller in foldcores, because the patterns are oriented in two or more angles out of plane (**Figure 5**).

4 FABRICATION OF TEST SAMPLES

4.1 Foldcores

Samples of foldcores with conducting patterns were made to allow RF measurements of the absorbing properties (**Figure 6**). First the conducting patterns were printed on 54 g/m2 aramid paper which was impregnated with 61 g/m2 phenolic resin to a total weight of 115 g/m2. The patterns were applied with 120 mesh screen printing of electrically conducting ink. The conductivity of the patterns was tuned to the desired value by blending a low and a high-conductivity ink to the desired value. In some cases the conductivity of the patterns was increased by printing multiple (two) layers of the same ink.

After printing and drying, the paper was folded into the desired foldcore shape or honeycomb shape. Finally the foldcores were cured for about 1 hour at 150ºC to secure the shape. The curing also improved the conductivity of the printed patterns. The exact curing duration and temperature were used to optimise the conductivity.

Finally, the conductivity of the conducting rings was characterized through measurement of the resistance ($R_{||}$) between the two sides of the rings using a two-probe method. The ring resistance typically shows a variation in the order of 10%. The foldcore samples have a size of about 25 x 16 cm and a height of 2 cm.

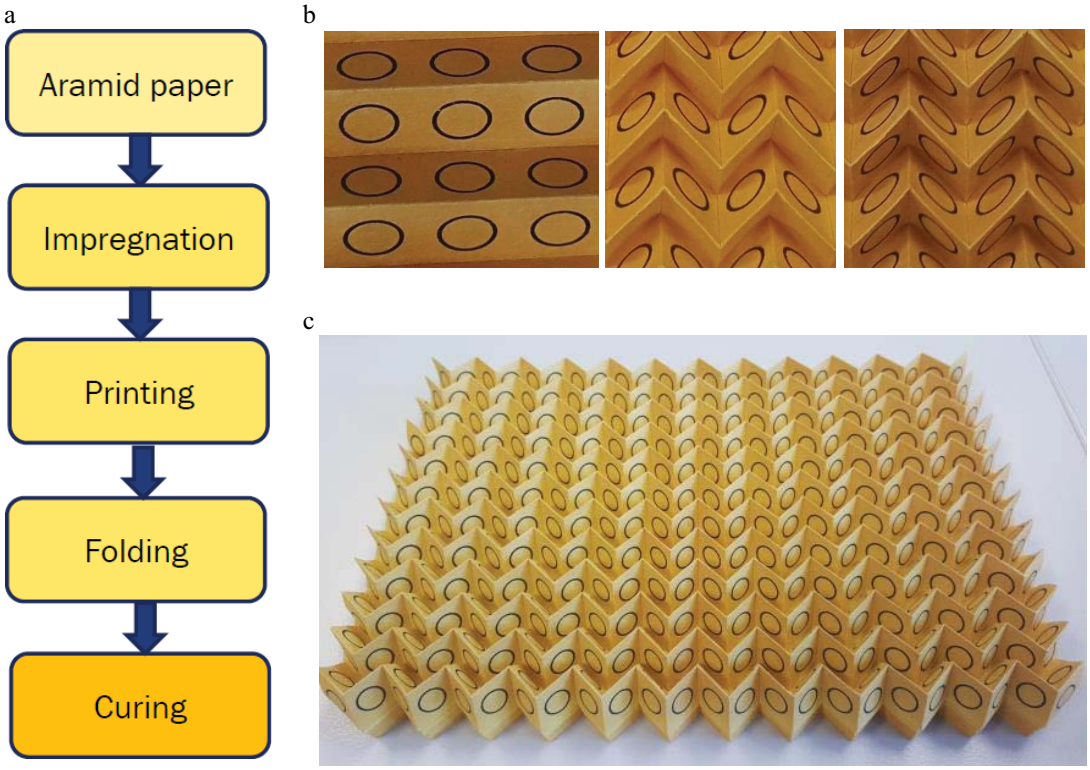

Figure 6: Foldcore and honeycomb fabrication
a: fabrication process, b: different printing and folding patterns, c : final product

4.2 Honeycombs

Honeycomb samples with SRRs were fabricated in a similar way as the foldcore samples. The honeycombs were folded from a single printed sheet (unlike in large-scale honeycomb fabrication). The samples measure 7.5 cm x 4 cm and have a thickness of 0.5 cm. Samples with carbon ink (236 Ohm/sq) and silver ink (0.05 Ohm/sq) were made (**Figure 7**).

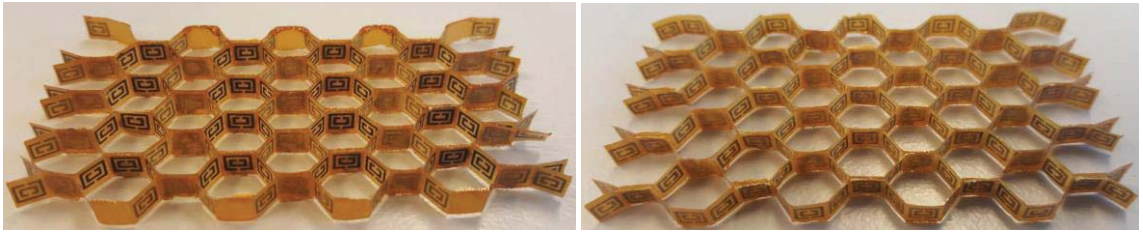

Figure 7: Honeycomb samples with SRR rings
in carbon (left) and silver ink (right)

5 MEASUREMENT RESULTS

Both foldcore and honeycomb samples were measured in the frequency range between 1 and 20 GHz in free-space reflection-transmission setups to determine the absorption. For these measurements six foldcore samples were combined in a single panel of 50 cm x 50 cm

on a Styrofoam substrate. The honeycomb samples were measured individually, placed in an aperture in an absorbing plate (**Figure 8**). All measurements were performed with normal incidence.

Figure 8: Final 50x50 cm foldcore panel (left) and honeycomb sample (right) during measurement

5.1 Foldcores

Foldcore samples with rings with two different conductivities (120 Ω/sq and 12 Ω/sq) were fabricated and measured (**Figure 9**). The conductivity of 12 Ω/sq is approximately optimal and yields an absorption of 0.55; nearly the simulated value of 0.6. The maximum is found for HH polarization where the E-field vector is best aligned with the conducting patterns. The conductivity of 120 Ω/sq is sub-optimal and yields reduced absorption.

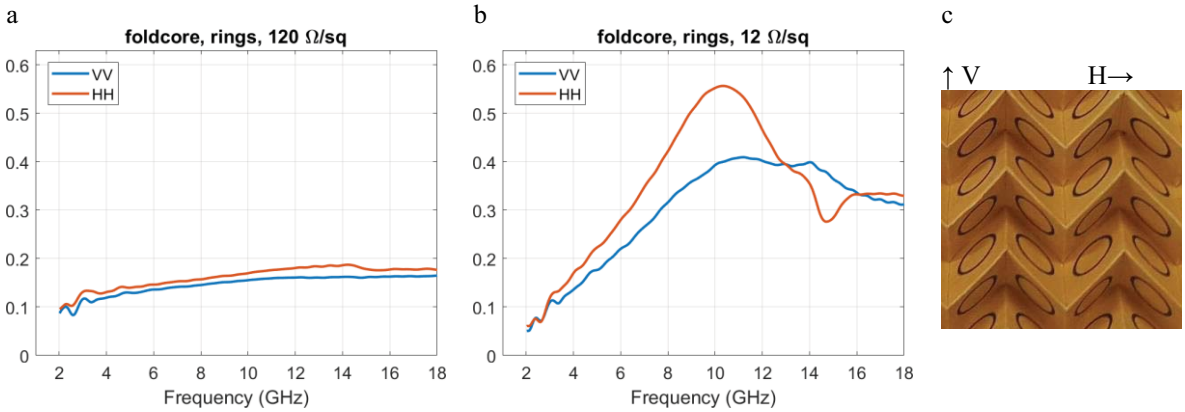

Figure 9: Measured absorption in (a) foldcore with rings Rs = 120 Ω/sq and (b) foldcore with rings Rs = 12 Ω/sq. The polarization is indicated in (c).

5.2 Honeycombs

The honeycomb measurement results show the importance of the conductivity of the patterns (**Figure 10**). The carbon ink (236 Ω/sq) has too low conductivity to yield a significant effect and the radar wave passes through the sample without much interaction. The high conductivity silver ink (0.05 Ω/sq) makes visible the double resonant structure of the SRR. It has a maximum absorption of 0.67 (-1.7 dB) with HH polarization at 9.65 GHz.

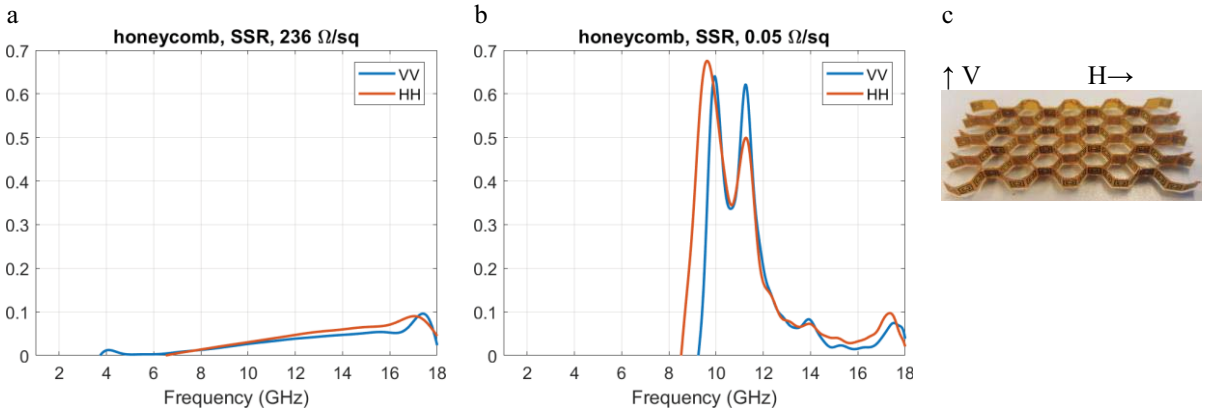

Figure 10: Measured absorption (A) of honeycomb with SRR in carbon ink (236 Ω/sq) (a) and in silver ink (0.05 Ω/sq) (b). The polarization is indicated in (c).

6 CONCLUSIONS

This paper investigates radar absorbing structures based on foldcore and honeycomb sandwich cores with printed electrically conducting patterns. RF absorption is created by Ohmic losses of currents induced in the patterns. To achieve optimal absorption it is necessary that the E-field of the incident wave is parallel to the conducting pattern and that the conductivity has a specific value. Honeycomb and foldcore samples with patterns with the desired conductivity were fabricated and measured. The samples were shown to have high losses. The lossy foldcore and honeycomb materials can be used as core materials to produce lightweight structures with tailored EM properties. The current work focused on conducting patterns consisting of SRRs and rings resonant at X-band. The patterns can be engineered to further optimise the EM properties at X-band or at other frequencies.

7 ACKNOWLEDGEMENTS

The authors acknowledge the kind support from Matthias Jansen (Airbus Defence and Space) in the measurement of the honeycomb samples.

REFERENCES

[1] Diaz, Rodolfo E. *Material with artificial dielectric constant* United States Patent 5662982, 2 Sept 1997.

[2] Houck, Andrew A.; Brock, Jeffrey B.; Chuang, Isaac L. *Experimental observations of a left-handed material that obeys Snell's law* Phys. Rev. Lett. 90(13), 137401, 2003.

[3] Ekmekci E.; Turhan-Sayan G. *Comparative investigation of resonance characteristics and electrical size of the double-sided SRR, BC-SRR and conventional SRR type metamaterials for varying substrate parameters* Progress In Electromagnetics Research B, Vol. 12, 35-62, 2009.

European Conference on Multifunctional Structures
EMuS 2019
X. Martinez and H. Schippers (Eds)

Development of multifunctional materials and structures with improved capacities in aerodynamics, de-icing, acoustics or electromagnetism for civil and military aircraft

EMUS 2019

BENOIT BERTON

Dassault Aviation
78 quai M. Dassault
92552 St Cloud Cedex, France
e-mail: benoit.berton@dassault-aviation.com

Key words: multifunctional structures, smart materials, acoustics, icing protection, antennas

Abstract.

For several years, either in the frame of research projects (French, European), or for direct application on aircraft programs, Dassault Aviation has developed multifunctional materials and structures (MMS) with specific benefits in aerodynamics, de-icing, acoustic or electromagnetisms. The main challenge is to get the best compromise between the high functional performances desired and the mechanical and aeronautic environment resistance needed for the application. This presentation will review some examples of development performed in the recent years for aircraft aerodynamics improvement, icing protection, acoustics and new antenna radomes.

1 INTRODUCTION

The design of advanced multifunctional materials and structures is really a challenge for the aerospace industry. Indeed, aeronautic structures that combine mechanical and aeronautic environment resistance with a specific functional property like acoustic, aerodynamic, electromagnetism…. are gathering more and more attention. Such materials and structures can only be passive but can also present some active characteristics, including sensors, actuators and processors, leading to the smart materials and structures (SMS) concept. Innovation also comes from new manufacturing and modelling techniques, especially in the composites domain which provide opportunities for integration of dedicated functional components.
In the following sections, examples of such development carried out at Dassault Aviation will be given.

2 GENERAL SPECIFICATIONS FOR AERONAUTIC APPLICATIONS

As reminded in the introduction, multifunctional materials and structures can be defined as materials that exhibit a specific functionality in addition to resistance to aeronautic environment. Consequently, it is important to describe the multiple constraints that must be fulfilled in order to be implemented in an aircraft like the Falcon 7X (Figure 1).

Figure 1 : Falcon 7X bizz jet

Such general constraints are the following :

- Weight : to be minimized
- Life cycle = 30 years
- Temperature range : -50°C /+ 80°C (general case)
- Mechanical :
  - compatibility of deformation with the aircraft structure (5000 µdef minimum)
  - fatigue life : 10^6 cycles @ 1000 µdef
- Aircraft environment :
  - wet aging (70°C, 85%RH), salt spray …
  - resistance to aeronautic fluids : cleaning fluids, fuel, hydraulic fluids, grease, de-icing fluids,…
  - erosion resistance (rain, sands)
- Electromagnetic compatibility, lightning, high intensity fields
- Manufacturing aspects
  - Withstand the bonding cycle on metal or co-curing cycle in composites @ 180°C
- ….

3 MULTIFUNCTIONAL STRUCTURES

Examples of multifunctional structures developed at Dassault Aviation for some years are presented below:

3.1 Aerodynamics functionalities

Aerodynamic optimization of the airfoil design is of course a key point of every new aircraft programs. Especially, for Falcon business jets that are devoted to long range operations, improvement of aerodynamic characteristics such as the drag in cruise is a regular effort of engineers. In the following sections, two examples of application of MMS are presented.

3.1.1 Trailing edge shape control with smart materials

For civil aircraft and long endurance UAV, aerodynamic optimisation of the wings is important in order to enhance the endurance. Especially, the capability to reduce the wave drag in transonic cruise at flight altitude without increasing the drag at lower Cl or lower Mach number can be very promising. This can be achieved by modifying the shape of the trailing edge from a divergent one at flight altitude to a straight one in the transition regimes.

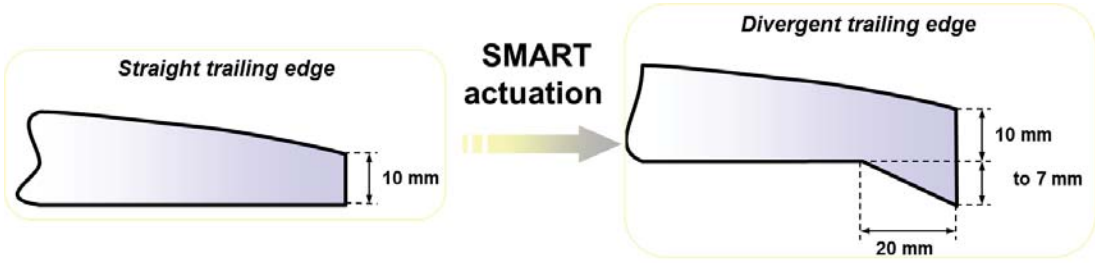

To achieve this shape modification, we have considered a smart structure using shape memory alloys (SMA) as actuators. Ni-Ti wires with two-way effect respond to a heat stimulus resulting in a crystalline transition and a length modification. Such development has been launched at Dassault in the frame of an European EUCLID research program: CASS.

A demonstrator has been manufactured based on the generic geometry of a wing aileron. External dimensions are 300 mm along the chord and 500 mm along the span. This aileron is split in 2 parts as shown on figure 2 :

- a forward box with the main function is to withstand the structural loads (200 mm along the chord).
- a rearward box with the adaptive part and the actuation system (100 mm along the chord). However, for spacing reasons, the SMA wires are located in the forward box (fig 2). The actuation system has been designed to fulfil the aerodynamic specification

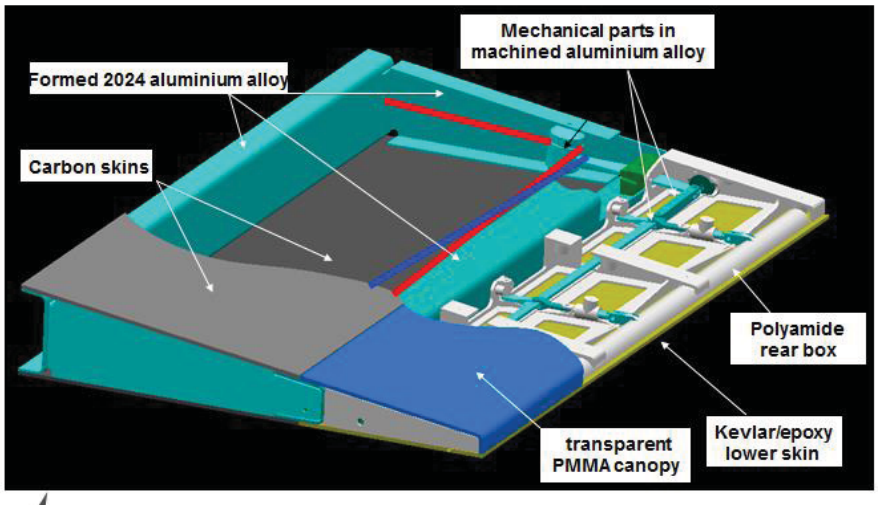

Figure 2 : divergent trailing edge demonstrator design

This demonstrator has been tested in Dassault lab regarding its functional performance at virgin state and under environment (figure 3). Especially, the SMA actuators reliability has been verified at low and high temperature and under repetitive temperature cycling. Specifications have been demonstrated in terms of deflection and response time.

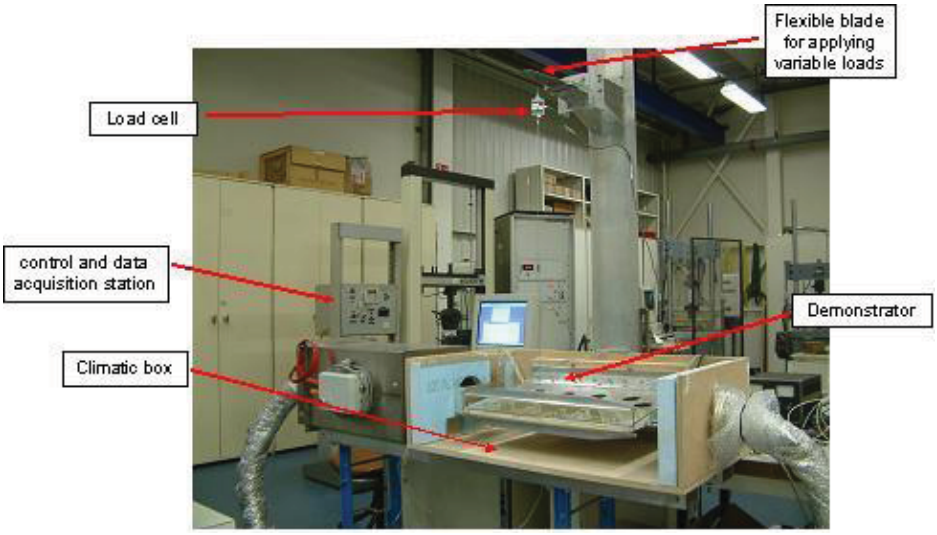

Figure 3 : functional ground test of the smart demonstrator

3.1.2 Multifunctional materials for laminar surfaces

Laminar flow technologies that exploit the low drag characteristics of laminar boundary layers on aircraft surfaces, such as wings, engine nacelles and empennage, have the potential to produce a significant reduction in drag. However, the application of these laminar flow

technologies in a commercial environment is still hindered by unanswered questions regarding its operational reliability. Contamination of leading edges by insects is a concern as excrescences can cause transition of the boundary layer, as ice accretion, reducing the potential drag benefit. Another cause of premature transition is surface roughness; poor durability of leading edge coatings and materials is thus another concern. Prolonged exposure to high velocity water impact (flight through rain) can cause erosion of anti-contamination surfaces, leading to a temporary or complete loss of laminar flow. These topics have been studied through a combination of flight and laboratory test campaigns, in part, within the European Commission funded AEROMUCO project.

In particular, several multifunctional coatings have been developed by members of the consortium with different approaches. These new materials have been characterized regarding laminar functionalities (contamination, erosion, icing) and aeronautic specifications.

Then, Dassault was in charge of a flight test campaign conducted in 2013 at the Istres Dassault Flight Center to evaluate the most interesting materials. Candidate surface preparations were applied to strips of tape. Two types of tape were used: aluminium foil (3M) and PET-Polyethylene Terephthalate tape. The tape was adhered to the leading edge of the horizontal tail plane of a Falcon 7X (Figure 4).

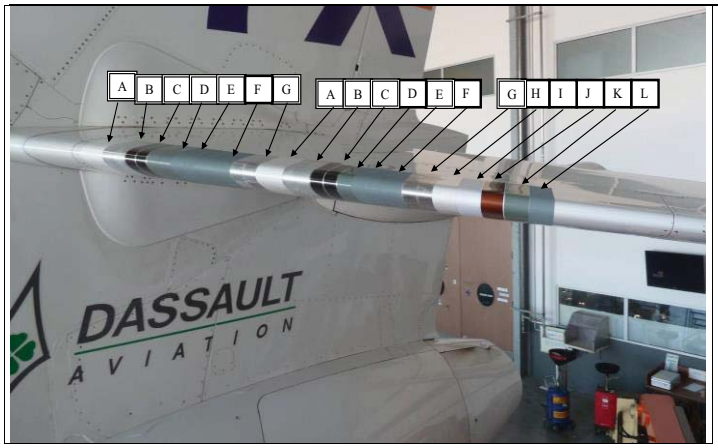

Figure 4 : laminar coatings installed on the horizontal tail plane of a Falcon 7X

Materials samples have been let on the aircraft during several months. Therefore, their durability in real flight environment could be evaluated. Moreover, their efficiency towards leading edge contamination could be assessed. In the tested conditions, most of materials avoid the presence of contamination above the transition criteria.

3.2 Icing protection functionalities

Icing of aircraft aerodynamic surfaces and engines is a complex and demanding challenge, and several research activities have already addressed the issue of ice accretion because of the threat to aviation safety. These difficulties are increased by the recent changes in certification regulations, which will require manufacturers to certify their products against more stringent requirements.

Dassault Aviation is fully involved in this problematic to optimize the icing protection of Falcon business jets (figure 5).

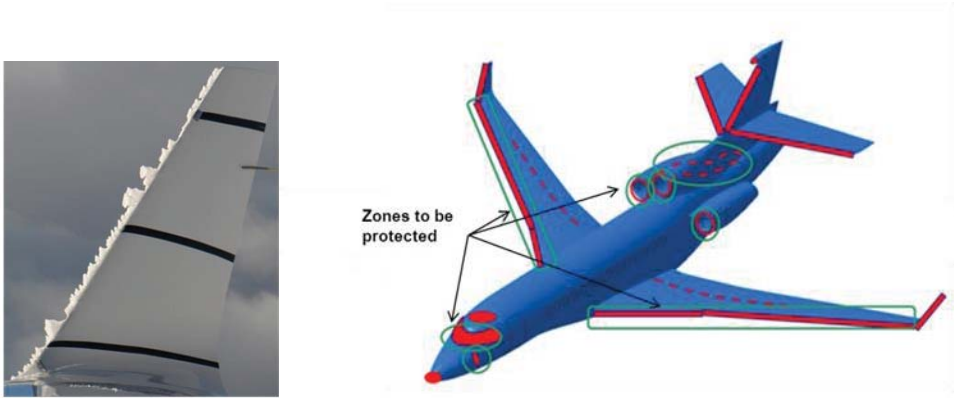

Figure 5 : ice accretion zones (in red) of a Falcon jet and protected areas.

Indeed, Dassault participates to research projects with industries and research organizations to develop new technologies for wing ice protection systems (WIPS), as Clean sky, HAIC, Jedi Ace EU projects...Even if the existing technologies, like bleed air, have worked well for decades in aircraft systems, the potential to further improve aircraft safety and reduce energy consumption with these new technologies is rather high. In particular, anti-icing coatings ("icephobics") combined with electro-thermal system appears to be extremely promising.

Such combined icing protection system have been characterized on mock-ups defined by Dassault in icing wind tunnel showing significant energy saving (> 50%) thanks to some icephobic coatings.

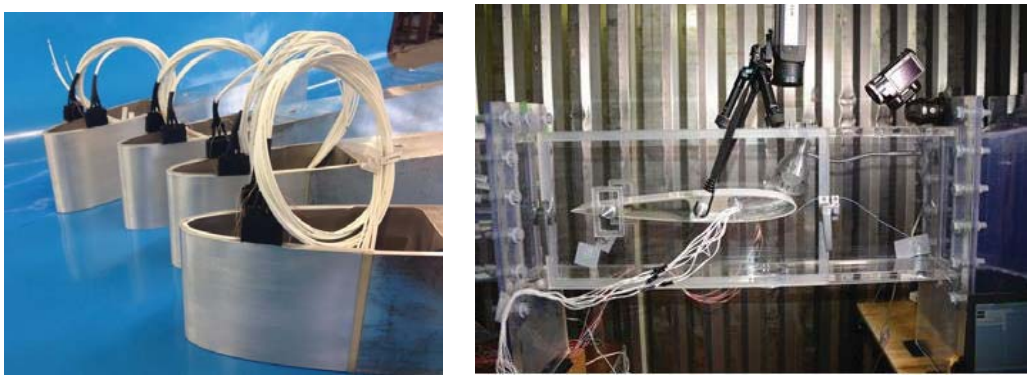

Figure 6 : airfoil mock-up equipped with electrothermal mats and icephobic coatings in icing wind tunnel.

3.3 Acoustic functionalities

Acoustic comfort of business jets is also an important design criterion for structure engineers as the noise level inside the cabin during flight is clearly a criteria of choice to buy a new aircraft. In that sense, Falcon 7X and 8X appear to be amongst the most silent aircrafts on the market.

Consequently, a large effort is put at Dassault to optimize the acoustic protection of the

cabin. Based on vibro-acoustic simulations of the aircraft, absorbing and damping materials are added on dedicated zones of the fuselage and trim panels with a constant effort to minimize the weight. In that sense, it can be worthwhile to integrate the damping component within the composite structures to optimize the weight added. Such approach has been followed some years ago in the frame of carbon composite fuselage development (FUBACOMP and FACE projects- figure 7).

Figure 7 : Fubacomp demonstrator

In cooperation with a material manufacturer, Dassault has developed a damped composite material with integration of a viscoelastic layer between two carbon composite skins (figure 8). Definition of the materials of the skins and of the corresponding thicknesses has been done to get the best compromise between the vibro-acoustic properties and the mechanical resistance (shear). Another challenge comes from the manufacturing process that shall combine right curing of the carbon composite skin with the good integration of the damping layer.

Figure 8 : damped composite architecture

The new composite material has been characterized in damping properties (Oberst test – figure 9) with damping up to 50% in the 1000-2000 Hz range.

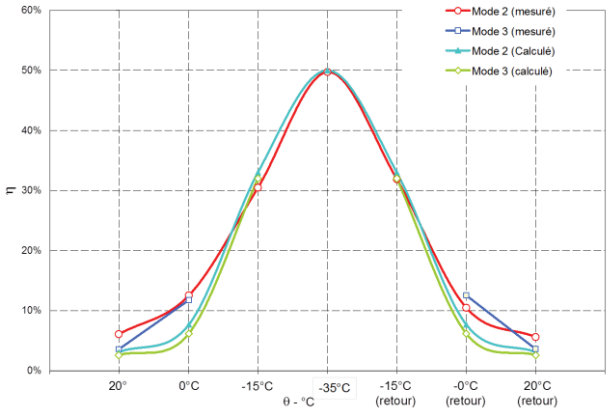

Figure 9 : damping properties of the composite

Similarly, mechanical tests were conducted on the damped composite material as the 4 points bending test, shown on figure 10, and buckling test. Finite element models have been developed to simulate the behavior of this new composite.

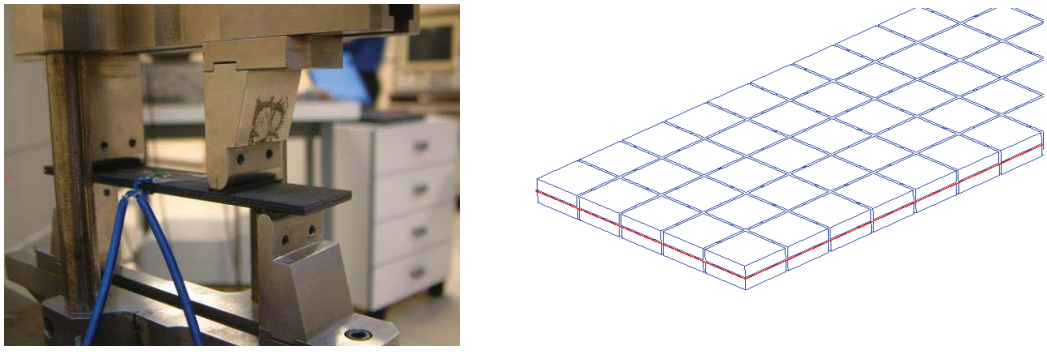

Figure 10 : experimental and simulation results of composite bending test

3.4 Electromagnetic functionalities

Electromagnetic functionality is also an important application case of MMS as illustrated on the two examples below.

3.4.1 Antennas application

Recent aircraft integrate more and more antenna systems that cover different functions and work in different frequency ranges.

To deal with the multiplication of antenna embarked in future aircraft, Dassault aviation evaluate the interest of conformal and integrated antennas in composite structures. At this time, we are still at a development stage for civil application.

Regarding new antenna systems which operate in novel frequencies ranges, that induce the needs of specific radomes. Such problematic has been recently encountered for a new Satcom

communication system for Falcon jets, where Dassault has launched the development of a new radome part. As presented in figure 11, different architectures of radomes can be considered with different bandwidth and attenuation performances. These architectures consist in superposition of alternate layers of “high” permittivity and low permittivity materials.

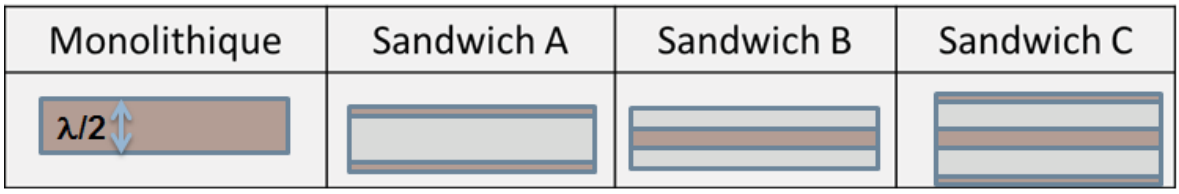

Figure 11 : different types of antenna radome architectures

Therefore, for this new radome development, Dassault has prospected and evaluated a lot of low permittivity and low loss materials. Such materials have been characterized on a free space test rig (figure 12) in Dassault lab. This test campaign has allowed to select the best candidate materials and to design the sandwich structure suitable for the antenna system and compatible with the functional and operational requirements.

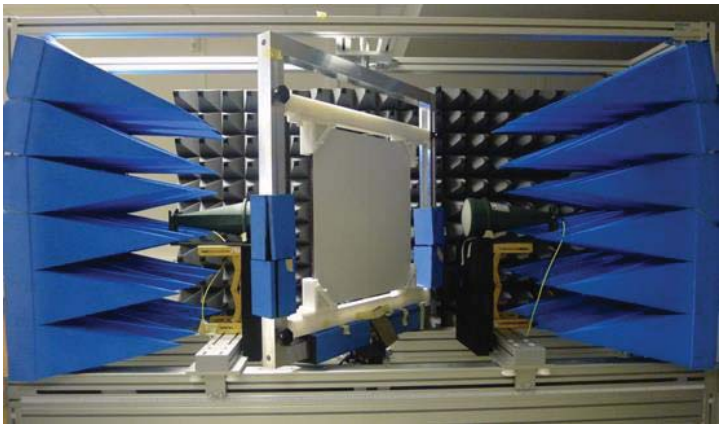

Figure 12 : EM transparency test in Dassault lab

3.4.2 Low observability MMS

Although the previous illustrations were principally oriented to civil application, Dassault Aviation is of course also largely involved in military aircraft. Consequently, for decades, the company has developed Low Observability concepts, acting on the aircraft shapes but also on different absorbing materials as well. This approach has mainly been applied on the Rafale fighter and to a larger extent on the Neuron UCAV demonstrator that first flew in 2012 (figure 13 below).

If details of such low observability materials and structures cannot be revealed, the development principles are similar to the examples presented above, resulting in multi-layers

composite structures.

Figure 13 : Neuron low observability demonstrator

4 CONCLUSIONS

Different types of multifunctional materials and structures have been developed at Dassault Aviation during the recent years. Maturity of these solutions ranges from medium TRL development to serial production. If the applications appear to be very diverse, the development principles are in general similar. In particular, two common features are present in all these developments:

- a strong implication of physics simulation (acoustic, electromagnetism…) in order to optimize the multifunctional structures regarding the different constraints
- the use of composite manufacturing processes that allow to integrate different components and materials, specifically designed to achieve the final performance of the structure

REFERENCES

[1] Berton B. – *Shape Memory Applications Trailing edge shape control* – RTO conference - AVT – 141 Multifunctional Structures - 2006

[2] Berton B. & al - *Evaluation of functional coatings for laminar flow applications on future business jets through ground and flight testing*- conference AIAA – ATO 2014

[3] Rehfeld N. & al - *JediAce: Japanese-European De-icing Aircraft Collaborative Exploration* – Conference Aerodays – London - 2016

New Enhanced Acoustic Damping Composite Material for the Aeronautics Industry

EMUS 2019

D. PASTORINO[*], J. DI LORENZO[†], B. LÓPEZ-ROMANO[*], P. HADLEY[†] AND T. BLANCO[§]

[*] FIDAMC, Foundation for the Research, Development and Application of Composite Materials, Avda. Rita Levi Montalcini 29, 28906 Getafe, Madrid, Spain

[†] Hexcel Composites, Ickleton Road, Duxford, Cambridge, CB22 4QB United Kingdom

[§] Airbus Operations, S.L., Paseo de John Lennon, S/N, 28906 Getafe

Key words: Aerospace, acoustic performance, composite material

Abstract. The present article investigates an innovative structural composite material concept with the additional functionality of acoustic damping. It is achieved by introducing an embedded elastomeric layer within the composite laminate, which constitutes a constrained layer damping (CLD) system. The main objective is to increase the acoustic performance of the baseline material, while its mechanical properties are maintained. In addition, material processability and inspectability have been considered as important drivers for the technology development. In order to identify the most promising candidate, a set of alternatives has been explored and analysed, giving rise to a compromise solution between the enhanced acoustic performance and the structural properties of the baseline material.

1 INTRODUCTION

The aim of the present study is to investigate a structural composite material concept with the additional functionality of acoustic damping. To this end, a standard modulus Carbon Fiber Reinforced Plastic (CFRP) prepreg is used as the baseline material. The damping performance of this substrate prepreg is enhanced by the addition of an elastomeric layer (EL), which becomes embedded in the composite structure when formed. The elastomeric layer, which is designed to co-cure with the thermoset prepreg, acts as part of a constrained layer damping (CLD) system. This confers vibration damping performance on the cured laminate.

The target application of the present study is the fuselage skin. The existing solution requires the manual addition of heavyweight, bespoke damping elements that are applied following part production and assembly. Such an approach adds inventory, time, weight and, ultimately, cost. The main drivers for the exploration of this technology are the potential for weight saving, maintaining or increasing production rate and the cost savings associated with these benefits. These are all key targets in the commercial aerospace sector. Weight savings and cost reductions are delivered in part by the embedded nature of the damping solution. The modified prepreg can be processed using established manufacturing techniques such as

Automated Fibre Placement (AFP) or Automated Tape Laying (ATL). This allows for high production rates.

Acoustic performance of a range of elastomers and composite structures was assessed within the range -55°C to 70°C using a modified Oberst beam test. Modal analysis was performed on the resonant peaks of test specimens, and the loss factor for the second and third resonant modes were determined using the half-power bandwidth method.

With regard to structural performance, it would be desirable to maintain substantially the same level of performance as the reference CFRP. The introduction of a rubbery layer within a laminate is likely to have a detrimental effect on its mechanical performance. However, it is recognised that a decrease in mechanical performance may be tolerable if a substantial weight saving or cost decrease can be achieved. Additional measures may then be taken to recover performance. A mechanical test campaign has been performed in order to quantify the structural behaviour of the multifunctional solution proposed.

It has been demonstrated that damping effectiveness is related to the relative amount of shear stress in the x-y plane, the best damping performance being associated with the positioning of the damping element at the location of maximum shear during bending. Placing the damping element centrally within the simple test specimen of this study was found optimal from a damping perspective, but then delivered the poorest mechanical performance. Strategies to mitigate this contradiction were explored.

2 CLD SYSTEM

The present technology is conceived to enhance the acoustic damping performance of a structural layered CFRP. The elastomeric layer is deposited uncured over a thermoset prepreg CFRP layer as shown in Figure 1. In this way, the hybrid material is readily processable and is suitable to be used in ATL and AFP processes.

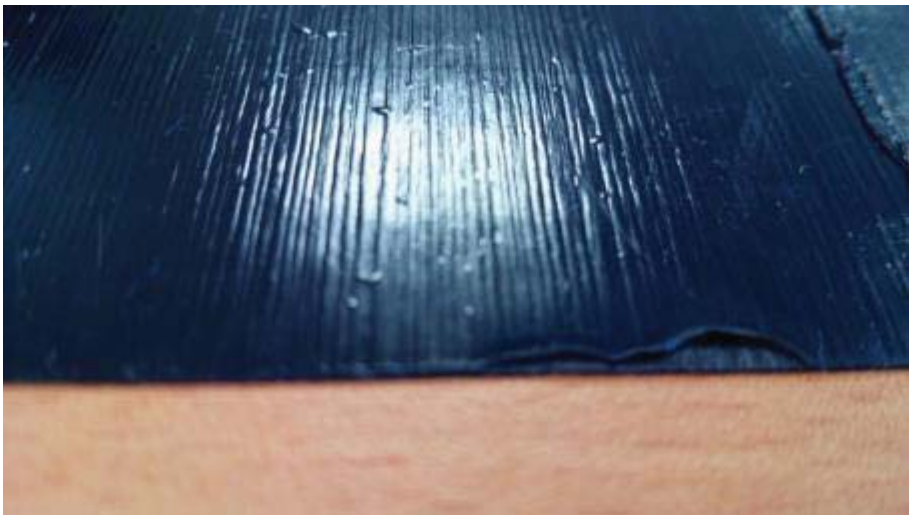

Figure 1: Detail of the elastomeric layer, deposited over a CFRP layer.

Figure 2 shows a laminate cross section, where the EL is perfectly visible at the centre of a composite panel.

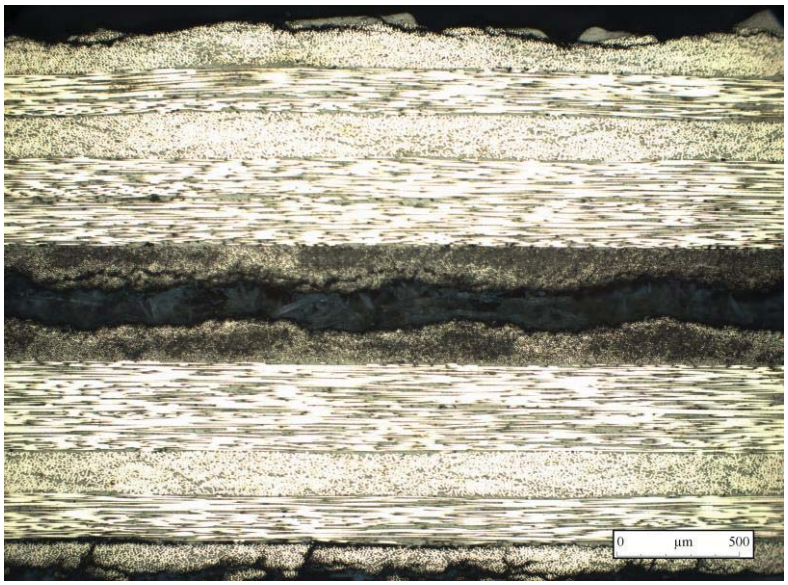

Figure 2: Microscopy of the transverse section of a coupon with a centred elastomeric layer.

2.1 Elastomer formulation

A polyisoprene based rubber was selected following the preliminary screening of three engineered rubber compounds: a nitrile rubber compound (NBR), an ethylene propylene diene monomer rubber compound (EPDM), and a polyisoprene based rubber compound. For the temperature range of particular interest, -30°C to 20°C, the polyisoprene based rubber compound performed the best, with the highest loss factor for resonant mode 2 in the range 800 Hz to 1100 Hz.

The elastomer is formulated to vulcanize, and thus co-cure, in the same conditions as Hexcel's 180°C epoxy prepreg systems. The novel use of an unvulcanised system takes advantage of the adhesion properties of the material to give benefits in automatic processability.

2.2 Laminate architecture

One of the most critical decisions of the present research project has been to propose a laminate architecture that fulfils both acoustic and mechanical requirements. To this end, a [+45/0/-45/0/0/90]s laminate is used as the reference lay-up. On this basis, one or more elastomeric layers have to be embedded within the reference lay-up in order to maximise the acoustic performance with the minimum effect on the mechanical properties.

In a first phase, the main driver for the selection of the laminate architecture was the fulfilment of the acoustic performance at minimal additional weight. Subsequently, several alternatives have been tested in order to keep the mechanical performance above an acceptable level. The definition of each architecture contemplates the following modifiable parameters:

- Position of the EL. The EL is placed at a certain distance from the laminate mid-plane.
- Thickness of the EL. Normally, an elastomeric layer thickness increment implies

better acoustic performance, compared with thinner layer in same position, penalizing weight.

- Number of EL. The usual configuration involves just one elastomeric layer. However, a trial has been carried out considering two symmetric off-centred films inserted within the laminate.

3 TEST PLAN

After a preliminary phase in which a great number of alternatives were proposed and investigated, a concise test plan is conceived, in which the most promising laminate architectures are considered. The test plan is conducted in order to achieve the best combination of mechanical and acoustic performances. Although other targets are sought and analysed, as processability and non-destructive inspectability, the preferred laminate architecture is selected just in view of the mechanical and acoustic results. The alternatives analysed in the test plan are shown in Table 1.

Table 1: List of tested configurations

Code	Designation	EL formulation	EL thickness	Lay-up	Additional weight (gsm) [(1)]
REF	Reference	--	--	[+45/0/-45/0/0/90]s	0
ARC-01	Centred	E11516/9	100 µm	[+45/0/-45/0/0/(90/EL)/90/0/0/-45/0/+45]	120
ARC-02	External with four constraining plies (100 µm)	E11516/9	100 µm	[-45/+45/+45/(-45/EL)/+45/0/-45/0/0/90/90/0/0/-45/0/+45]	1296
ARC-03	External with four constraining plies (200 µm)	E11516/9	200 µm	[-45/+45/+45/(-45/EL)/(EL/+45)/0/-45/0/0/90/90/0/0/-45/0/+45]	1416
ARC-04	Two symmetric EL	E11516/9	2x100 µm	[+45/(0/EL)/-45/0/0/90/90/0/0/-45/(EL/0)/+45]	240

[(1)] With respect to the reference architecture. Current SoA implies approximately 3000gsm.

It should be noted that the architectures that require the use of constraining plies (ARC-02 and ARC-03) are heavier (with respect to the reference laminate). However, these architectures are optimal for the structural performance, since the EL is moved outside from the coupon centre.

3.1 Acoustic performance

As a target for the investigation a temperature range of interest of -30°C to 20°C, and a loss factor of ≥0.05 for the second and third resonant modes was defined in agreement with the Airbus S.L. The targets reflect the early technology stage of the concept, and do not

constitute a full specification for the damping requirements of an aircraft.

Acoustic performance is assessed using a modified Oberst test method. The method is based upon the testing standard ISO 16940 [1], with two modifications: i) the representative layup is used instead of a 4mm thick beam, ii) the test is performed at multiple temperature ranges in 5°C ± 1°C intervals. To accomplish this, a 300 mm steel stinger rod at 5 mm diameter is used to hold the sample in an environment chamber for testing. The stinger rod has an undesirable contribution effect to the results at 600 Hz, 700 Hz and 950 Hz, but is sufficient for the benchmarking and comparison purposes of this study. The results of acoustic testing of resonant mode 2 are shown in Figures 3 and 4.

From the results, two important design variables for a successful CLD approach can be extracted; the thickness of elastomeric layer, and the proximity of the EL to the central axis of the material.

In the interest of minimizing the additional weight of any new structural material, it is clear from the results that for a given material the proximity to the central axis is important for achieving the maximum damping potential of this technology. ARC-01 has the highest peak loss factor performance of all the samples tested with the smallest amount of additional weight. This is because the elastomeric layer is placed in the location of the laminate that experiences the highest shear stress during bending, maximizing the potential for energy dissipation through shear deformation. Whilst the correlation between shear stress and damping performance was not explicitly investigated as part of this study, this is a reasonable conclusion when one considers that the primary mechanism for energy loss in CLD systems is shear deformation.

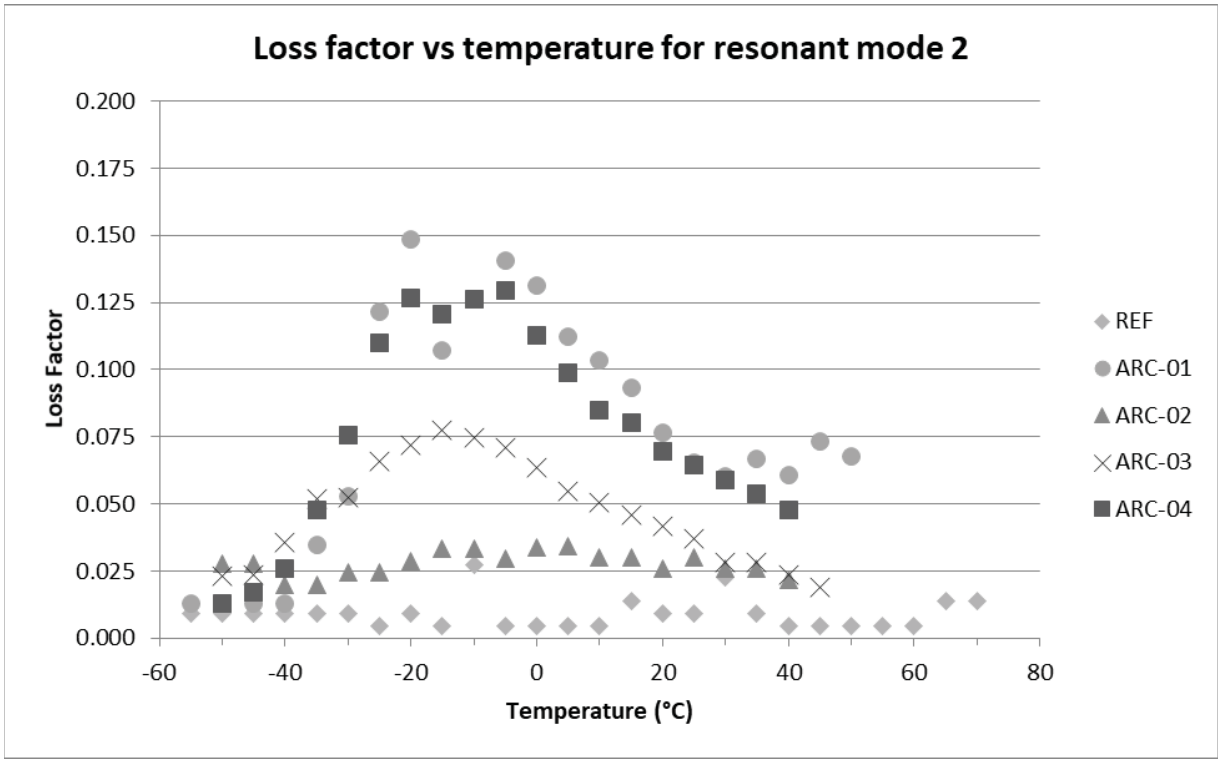

Figure 3: Loss factor vs temperature for the second resonant mode of tested samples.

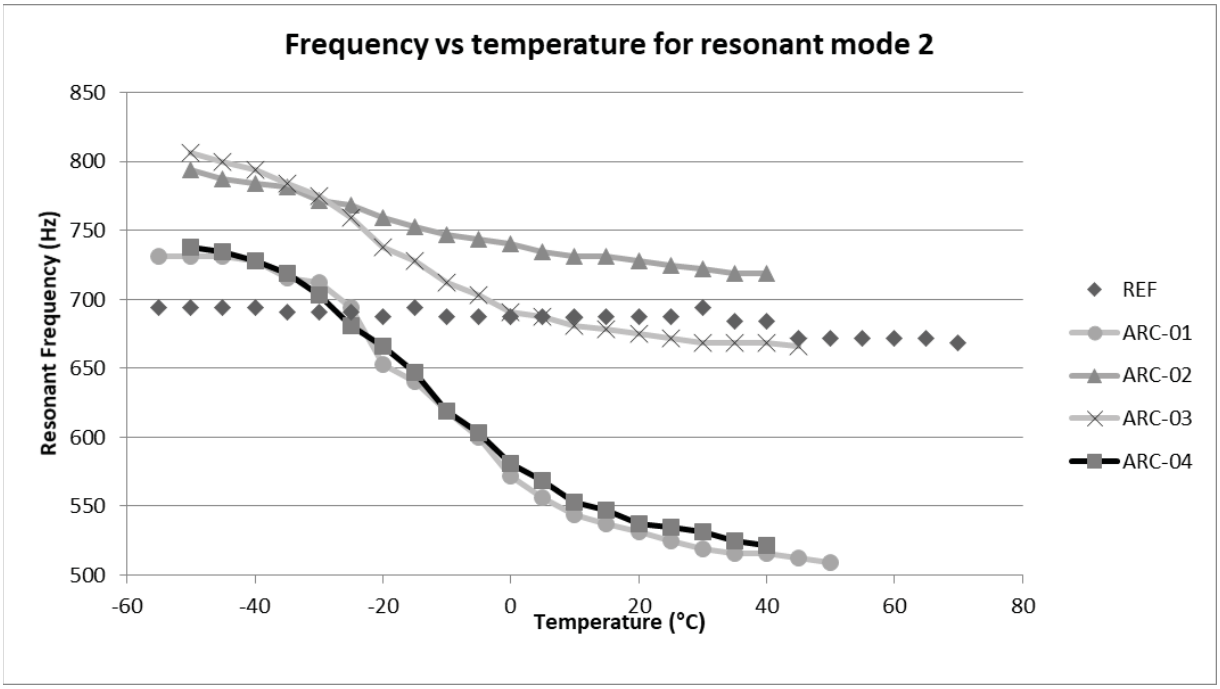

Figure 4: Resonant frequency vs temperature for the second resonant mode of tested samples.

3.2 Mechanical performance

From the requirements presented in the introduction, the mechanical performance of the laminate should remain at the same level as the reference, or slightly below if provided a significant improvement on the component weight with respect to the current state of the art (~3000 gsm).

Mechanically, the elastomeric layer acts as a physical division or barrier inside the laminate. The shear loading capacity of the elastomer is very limited due to its low stiffness. In fact, this is why the elastomeric layer has an outstanding acoustic performance. Clearly, this effect is counterproductive from the mechanical point of view, and hence it is desirable to have the EL as far away from the laminate centre as possible.

In order to test the influence of the elastomeric layer in the laminate a mechanical test campaign is conducted. Although a complete characterization has been performed, it was the 3-point bending test (acc. to EN2562 type A [2]) that leads to the most valuable results. The results are compared with respect to the reference in Table 2.

Table 2: Mechanical performance of the laminate architectures tested, with respect to the reference, based on 3-point bending test

Code	3-point bending test strength (%) (1)	Failure mode
REF	100	Bending
ARC-01	50.5 (2)	Out-of-plane shear

ARC-02	102	Out-of-plane shear
ARC-03	117.8	Out-of-plane shear
ARC-04	47.3	Out-of-plane shear
[1] With respect to the reference coupons. [2] The test have been carried out with Uni-Directional coupons (UD), the results are compared with a UD CFRP set of coupons.		

Here, architectures ARC-02 & ARC-03 show an improved mechanical strength with respect to the reference, which is expected since it is the same laminate with an extra EL and 4 additional plies. The coupons with 200 μm of EL thickness show higher strength than the coupons with 100 μm EL.

Finally, it should be mentioned that the failure mode changes with the inclusion of the elastomeric layer. The coupons with elastomeric layers normally fail by a combination of out-of-plane shear and bending, while the failure of the reference coupons is caused by pure bending. Figure 5 shows the differences on the failure of both configurations, the out-of-plane shear failure affects uniquely to the interface of the elastomeric layer with the adjacent CFRP layers, causing a slippage phenomenon during the test. This phenomenon causes the early failure of specimens with architectures ARC-01 and ARC-04.

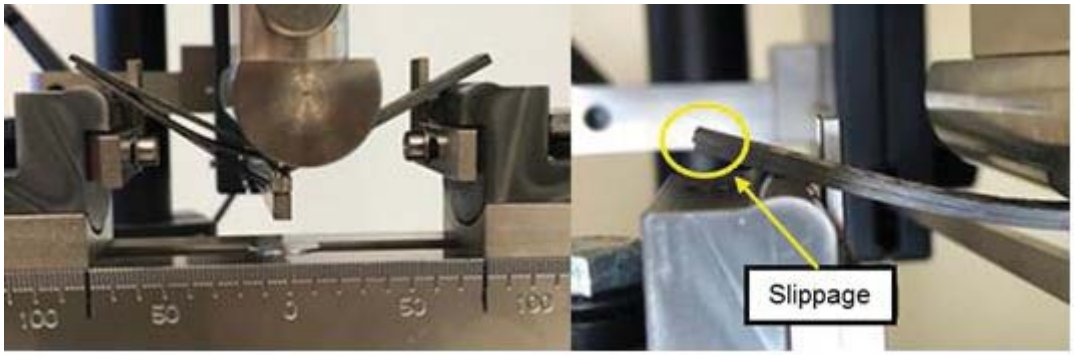

Figure 5: Bending failure mode of a reference coupon (left) and slippage phenomenon on a coupon with elastomeric layer (right).

3.3 Overall performance

The following conclusions are extracted by comparing the hybrid laminates with respect to the reference:

- The elastomer placed centrally gives rise to the best acoustic performance at the expense of reducing substantially the mechanical performance. The best solution from the structural point of view is to position the elastomeric layer near one of the external faces, under some constraining plies.
- Using a thicker elastomeric layer is beneficial from the acoustic point of view, and has been reported not to affect the mechanical performance negatively. Elastomeric layers up to 200 μm have been analysed.

- The use of two symmetrical elastomeric layers enhances the acoustic performance, but the mechanical performance is excessively poor.

Thus, the best combination of mechanical and acoustic performances is reached by using the configuration designated as ARC-03. A 200 μm EL is placed off-centre under 4 constraining plies.

5 OTHER ASPECTS OF PERFORMANCE

5.1 Processability

The material has been slit to 300 mm, 150 mm and 75 mm for Automated Tape Laying (ATL) production, using a release liner to avoid the self-bond of the material. It is always laid-up with the EL positioned upwards, and the CFRP ply downwards.

ATL manufacturing trials demonstrated that the adhesion of the EL to the next ply of CFRP is high enough to facilitate standard lay-up processes. In addition, the automated trimming systems have demonstrated an excellent performance with the hybrid material.

Figure 6: Automated deposition of the hybrid material by using ATL.

In addition to ATL material, it has been produced slit-tape material for Automated Fibre Placement (AFP) lay-up processes. However, no manufacturing trials have been performed for the time being.

5.2 Non-destructive testing (NDT)

In CFRP laminated composites, it is essential to be able to detect internal defects in the laminate, since hidden damage could lead to an unexpected failure of the structure. Usually, the detection and characterisation of defects is performed by using non-invasive techniques, such as the ultrasonic inspection (US).

Some interesting conclusions are drawn from the analysis of inspected CLD specimens. The elastomeric layer embedded into the laminate behaves as a damper that attenuates the ultrasonic wave. In fact, an attenuation of approximately 6 dB is found on the CLD specimens with respect to the reference (just CFRP) specimens. This attenuation is not worrisome, since it is uniform and well distributed over the surface.

In addition, a 4-step flat panel with thicknesses of 2.308, 3.412, 4.516 and 5.620 mm respectively and Armalon inserts of 4x4 mm and 6x6 mm as defects has been manufactured

and US inspected. The conclusions obtained are that the defects are detectable by manual and automatic inspection. However, the depth of the defects is hardly identifiable due to the elastomer insertion into the laminate, see Figure 7.

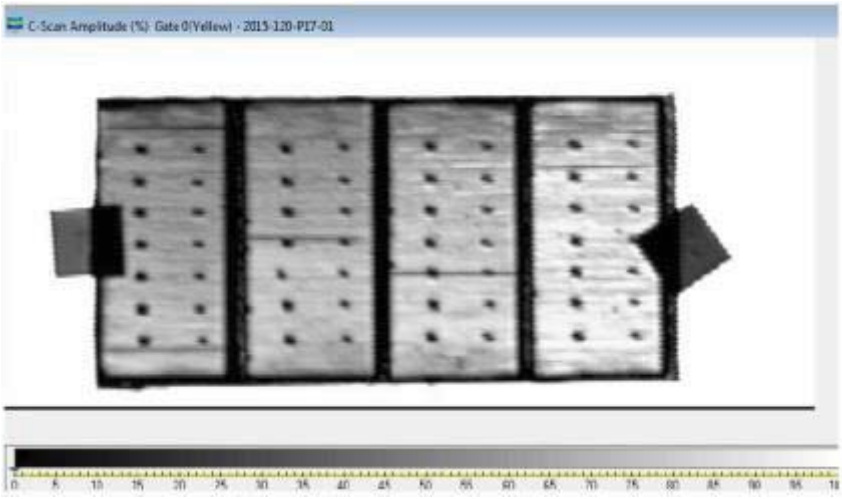

Figure 7: Amplitude C-Scan for a 4-step flat panel manufactured. Intentionally introduced defects are visible as dark spots.

6 CONCLUSIONS

The best acoustic performance is reached by placing the EL centred with respect to the laminate thickness. In this way, the energy dissipation provided by the EL is maximised, and thus the performance of the damping is optimal. On the contrary, the mechanical performance is benefited by a laminate architecture in which the EL does not interfere with the load path. This is achieved by positioning the EL outside of the load path of the structural laminate, and by introducing additional constraining plies to ensure that the EL experiences the required shear deformation during bending. In this way, the CFRP plies placed beyond the "structural part" of the laminate are important design variables, along with EL thickness and the type of EL, for achieving any specified level of acoustic performance.

A compromise solution for acoustic and mechanical performance has been found, which consists of placing an elastomeric layer of 200 μm thick externally under four constraining plies. The multifunctional material developed has proven itself interesting for the aerospace industry in terms of acoustic and mechanical performance. Additionally, the automated processability of the CLD system has been demonstrated, as well as its inspectability by means of NDT.

Finally, the drivers initially suggested for this development are completely fulfilled. In the first place, a potential weight saving is foreseen with the chosen architecture with respect to the current SoA. Secondly, the production rate could be significantly improved, since the investigated CLD system is suitable for automated lay-up processes, while the current reference requires a manual installation process. Improvements in production rate yield a significant reduction in the cost of the finished component.

The present study has been carried out under NEODAMP (New Enhanced acOustic DAMPing composite material) project. The NEODAMP project has been funded by the

European Union's Horizon 2020 and by Clean Sky Joint Technology Initiative under grant agreement number GA: 686374.

REFERENCES

[1] ISO 16940. Glass in building glazing and airborne sound insulation. Measurement of the mechanical impedance of laminated glass: 2008. Standard commonly known as Centre Impedance Method or Modified Oberst Test.

[2] EN2562. Aerospace series. Carbon fibre reinforced plastics. Unidirectional laminates flexural test parallel to the fibre direction.

European Conference on Multifunctional Structures
EMuS 2019
X. Martinez and H. Schippers (Eds)

TEXTILE-INTEGRATED TRANSMITTING UNIT

MIROSLAV CUPAL[*], JIŘÍ DŘÍNOVSKÝ[+], TOMÁŠ GÖTTHANS[+], JAROSLAV LÁČÍK[+], JAN PRÁŠEK[+], ZBYNĚK RAIDA[+], DITA KRÁČALOVÁ[†], ZDEŇKA LEDROVÁ[†], JIŘÍ PROCHÁZKA[†], DAVID KRUTÍLEK[^], AND ZDENĚK ŘEZNÍČEK

[* +] SIX Research Center, Brno University of Technology
Technická 10, 616 00 Brno, Czech Republic
e-mail: cupalm@phd.feec.vutbr.cz, web page: www.six.feec.vutbr.cz/

[†] SINTEX a.s.
Moravská 1078, 560 02 Česká Třebová, Czech Republic
e-mail: prochazka@sintex.cz, web page: www.sintex.cz/

[^] Evektor spol. s r.o.
Letecká 1008, 686 04 Kunovice, Czech Republic
e-mail: zreznicek@evektor.cz, web page: www.evektor.cz

Key words: Textile-integrated antenna, screen printing, 3D knitted fabric

Abstract. This contribution deals with the main parts of the textile-integrated transmitting unit, a transmitter and an antenna, operating in the ISM 5.8 GHz band. The transmitter is based on commercially available WLAN UART Serial Port OWS451 and it is controlled via the UART interface by microprocessor ATmega328. The antenna is based on the circular ring-slot concept and it is able to provide monopolar radiation pattern to ensure maximum coverage of the unit. The unit will be integrated in a seat cover and it will transmit the telemetry of sensors integrated in the seat (temperature, pressure…).

1 INTRODUCTION

In order to reduce weight of small airplanes and consequently decrease their fuel consumption, there is strong motivation to develop and use multifunctional structures. E.g. if textile materials are used, they can fulfill different functions. Apart from their conventional roles of seat or upholstery covers, they can be considered for thermal insulation or mechanical attenuation. In addition, textile materials are nowadays very popular for development of electronic components where they usually play the role of a substrate [1], [2].

In our previous work [2], the attention was focused on the integration of wireless sensor network components into 3 dimensional (3D) knitted fabrics (produced by SINTEX) exploited on a board of a small airplane EV-55 (developed by EVEKTOR) with particular attention on optimized 3D knitted fabric and textile-integrated receiver. In this paper, we will describe the main parts of the textile-integrated transmitting unit, a transmitter and an antenna, operating in the ISM 5.8 GHz band.

2 TRANSMITTER

The transmitter is based on IEEE 802.11a standard that can communicate over the 5 GHz frequency band [3]. The WLAN UART Serial Port OWS451 module has UART interface and fully embedded TCP/IP stack and driver. For real-time data acquisition, due to the dimensions and the selected frequency band, it seems to be the best choice. The module itself is controlled via the UART interface by microprocessor ATmega328. The microprocessor is as well connected through A/D converters to a sensor matrix for mechanical pressure sensing. The pressure sensors are piezoresistive fabrics that are made by coating regular fabrics in an inherently conductive polymer. In order to provide data to user, the wireless module is then connected to an AP (Access Point) router or ad-hoc network. Sensor data is sent to a user application that communicates using UDP (User Datagram Protocol). A Python visualization program is created on the user side.

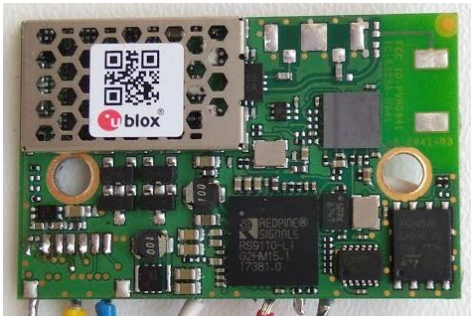

Figure 1: Photo of transmitter.

3 ANTENNA

To ensure maximum coverage of the unit, a ring slot antenna [4] was used and integrated in a broader wall of the substrate integrated waveguide. The antenna is able to provide monopole-like radiation pattern. However, in comparison to the antenna with shorting vias [5], the designed antenna is free of vias since the monopole-like radiation pattern is generated by the excitation of higher order mode in the slot. On the other hand, it is larger than it could be if the shorting vias were used.

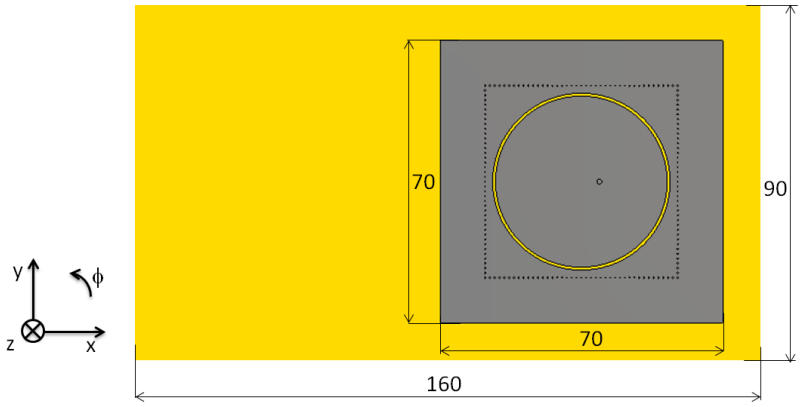

Figure 2: Top view of antenna realized on 3D knitted fabric.

The geometric configuration of the substrate integrated waveguide (SIW) circular ring-slot antenna is depicted in Figure 2. The antenna is designed on 3D knitted fabric of the thickness 3.4 mm and the relative permittivity 1.2. The fabric is from both sides covered by Digiflex – Master foil from the company Alphaset. The foil was ironed on the fabric. The radiator was screen printed on the top side of the fabric covered be the foil using Aurel mod. C880 semiautomatic screen printer. For the printing, the ESL 1901-S polymer silver conductor paste with good electrical conductivity was used. The same procedure was applied on the bottom side of the fabric covered by the foil to create continues conductive surface of the same size and position, but without the circular slot. To create the vertical walls of the SIW cavity, conductive thread ELITEX® Art, SC 110/f34_PA/Ag was used. To experimentally verify the properties of the antenna, it is equipped by SMA connector. In the final phase, the SMA connector will be replaced by UFL one and the antenna will be connected by a coaxial cable with the transmitter. The fabricated sample of the antenna is depicted in Figure 3.

Figure 3: Fabricated sample of the antenna (left) and the antenna with connected trensmitter (right).

The reflection coefficient of the antenna is depicted in Figure 4. Although the measured data shows narrower band response than the simulated one, the antenna is still very well matched in the desired ISM 5.8 GHz band (5.725 – 5.875 GHz). The difference of simulated and measured response is probably caused due to manufacturing tolerances.

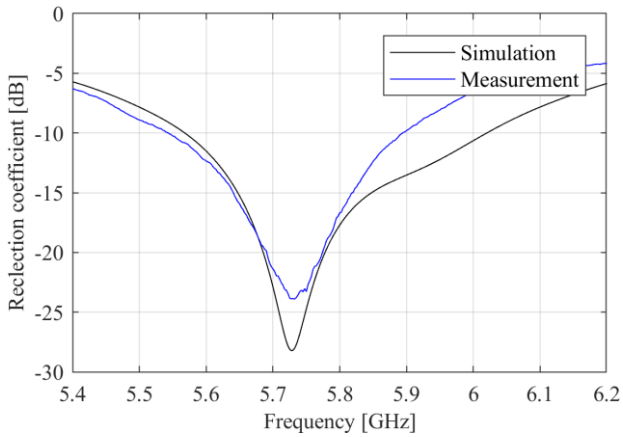

Figure 4: Reflection coefficient of simulated and measured antenna.

The simulated and measured radiation gain patterns are depicted in Figure 5. We can observe that the antenna is able to provide monopole like radiation pattern. The agreement of simulated and measured results is satisfactory. The measured peak gain of the antenna is about 5 dBi.

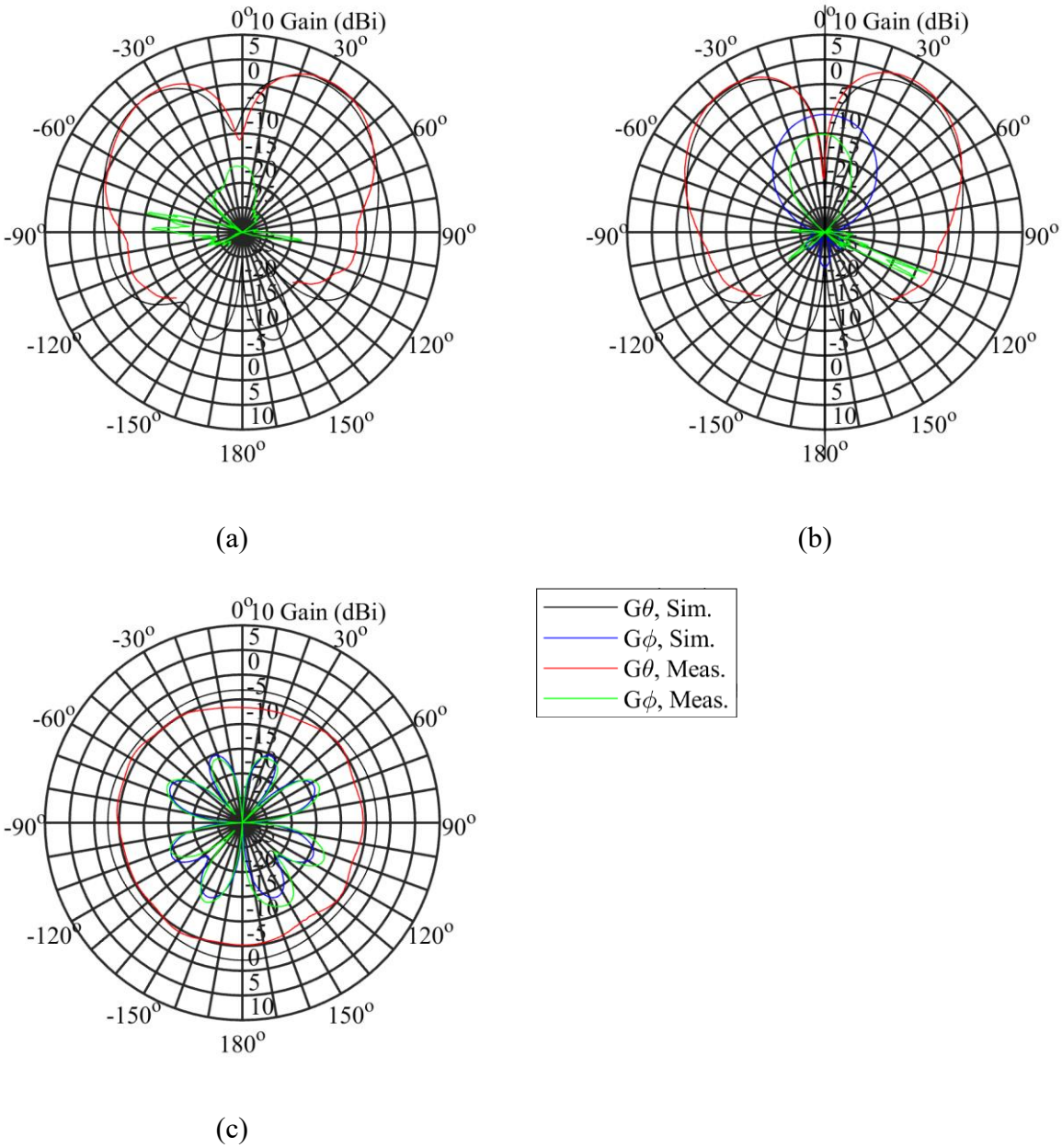

Figure 5: Radiation gain pattern of antenna at freqeuncy of 5.8 GHz in xz-plane (a), yz-plane (b), and xy-plane(c).

4 CONCLUSIONS

In this contribution, the main parts of the textile-integrated transmitting unit, the transmitter and the antenna, operating in the ISM 5.8 GHz band has been described. Now both those parts are being integrated. The final data of the unit will be presented at the conference.

ACKNOWLEDGEMENT

The described development has been supported by the Czech Ministry of Industry and Trade by the grant FV10087 Intelligent upholstery of vehicles.

REFERENCES

[1] A. Kiourti, Textile-Based Flexible Electronics for Wearable Applications: From Antennas to Batteries, *2018 2nd URSI Atlantic Radio Science Meeting (AT-RASC)*, Meloneras, 2018, pp. 1-4.

[2] M. Cupal et al., Textile-integrated electronics for small airplanes, *12th European Conference on Antennas and Propagation (EuCAP 2018)*, London, 2018, pp. 1-5.

[3] https://www.u-blox.com/sites/default/files/OWL253_ProductSummary_(UBX-14006701).pdf

[4] A. A. Serra, A. R. Guraliuc, P. Nepa, G. Manara, I. Khan and P. S. Hall, Dual-polarisation and dual-pattern planar antenna for diversity in bodycentric communications. *IET Microwave, Antennas and Propagation*, 2010, vol. 4, no. 1, pp. 106-112.

[5] J. Lacik et al., Substrate Integrated Waveguide Monopolar Ring-Slot Antenna, *Microwave and Optical Technology Letters*, vol. 56, no. 8, pp 1865-1869, 2014.

European Conference on Multifunctional Structures
EMuS 2019
X. Martinez and H. Schippers (Eds)

Cooling of Active Components in Structurally Integrated Phased Arrays Antennas

– EMuS 2019 -

Jens Leiß*, Thomas Ebert†, Marta Martínez-Vázquez†† and Rens Baggen††

*, ††IMST GmbH
Carl-Friedrich-Gauß-Str. 2-4, 47475 Kamp-Lintfort
e-mail: leiss@imst.de, web page: http://www.imst.com

†IQ evolution GmbH
Steinbachstraße 15, 52074 Aachen
Email: t.ebert@iq-evolution.com, web page: http://www. iq-evolution.com

Key words: 3D printing, embedded cooling, additive manufacturing, 5G, Satcom

Abstract. This paper presents an innovative cooling solution for active phased array antennas, using a 3D printed liquid cooling device integrated in the structure's PCB.

1. INTRODUCTION

The need for higher integration of active components on multilayer printed circuit boards (PCB) has dramatically increased over the last decades. In particular, the demand for steerability of the antennas used for communication systems and the increase in their opering frequencies has brought phased arrays antennas into the forefront of antenna development. Unfortunately the efficiency of these components for higher frequencies is very low, so that only 5 to 10% of the consumed power is used for the radiated signal. The rest is dissipated as thermal losses. The result is a higher integration density of active components with low efficiency, which in turn means a higher density of thermal discharge in a very small area.

This heat produced by the active components needs to be dissipated from the circuits, to avoid damages. The common way to do this is by integrating a heat-spreader, mounting passive or active coolers onto the devices or to integrate a copper core in the PCB (Printed Circuit Board). These solutions limit the space available for routing, or are bulky and heavy. In this work an alternative solution for the thermal management of an active array in the X-band (8-12GHz) antenna PCB is introduced. This array is to be integrated in the structure of an aircraft, in the frame of the Horizon 2020 project ACASIAS [1]. The idea is to integrate a 3D-printed active cooling structure directly into the PCB. This printed structure can be custom tailored to the needs of the active Radio Frequency (RF) circuits.

A nickel-based cooler is manufactured using a Selective Laser Melting (SLM) process and integrated in a standard RF- multilayer PCB. A cooling liquid (e.g. deionised water) can then be pumped in the cooler to transfers the heat from the critical points of RF-circuits to a radiator outside of the antenna. This solution allows really high power dissipation (up to 1

kW). This paper also presents the measurements of the first prototype of a PCB with embedded the liquid-cooling.

2. 3D – METAL PRINTING – THE SLM–PROCESS

In the Selective Laser Melting (SLM) process, summarised in Figure 1, 3D-metallic components are produced from a metal powder bed. A metal powder, in this case nickel (Ni), is applied layer by layer in an isolated chamber. Each powder layer is around 30µm in thickness. A laser beam moves over the powder layers, causing the material to melt locally to create solid metal corresponding to shapes of the 3D CAD model of the component. After one laser sweep, the manufacturing platform is lowered and a new powder layer is applied. Step by step, layer by layer, a homogeneous metal structure is build. With this process it is possible to build high resolution, completely closed structures, which would be impossible using other manufacturing processes [2], [3].

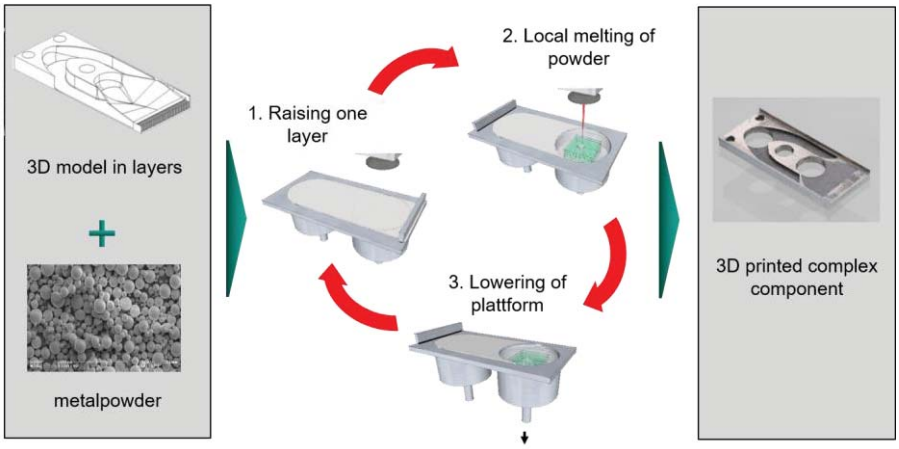

Figure 1: SLM-process – Manufacturing principle.

3. PCB WITH EMBEDED Ni-COOLER

A Ni-cooler with high thermal dissipation capability was manufactured (Figure 2) using the SLM process. This cooler can be embedded in FR4 material and integrated into a multilayer PCB structure, as needed for the implementation of an active phased array. The device must be robust enough to survive standard processes of the PCB industry, in particular, the different pressing cycles. Also, it has to allow for electrical connections between the PCB layers and be thin enough to be laminated in the PCB and to keep the inter-layer RF connections as short as possible.

Figure 2: Left: 800µm-thick 3D-SLM-printed Ni-cooler; Right: 3D-SLM-liquidconnector

The advantage of these 3D Ni-coolers is that they can be customised taking into account the placement of the active components on the PCB. It is possible then to place the cooling channels directly under the components that are generating the heat, while still leaving enough space for routing and interconnections. Figure 3 shows the schematic buildup of a PCB with the integrated liquid cooling system. In- and outlet connections used to pump the cooling liquid (deionized water) into the system are placed in the top side of the PCB. The Ni-cooler is placed under the active, heating components, in this case RF power amplifiers (PA). The top and bottom layers of the PCB are connected with different types of metallized via holes, for signal and ground connections.

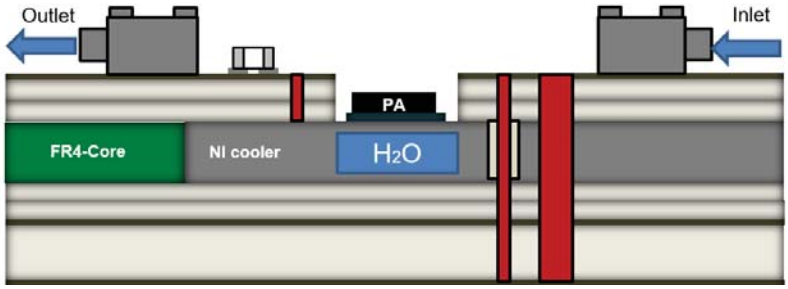

Figure 3: Multilayer PCB with 800µm-thick embedded 3D-SLM-printed Ni-cooler

A test board was manufactured using a standard multilayer process to assess the performance of the integrated cooler. The schematic of the test board and the manufactured prototype with liquid cooling are shown in Figure 4.

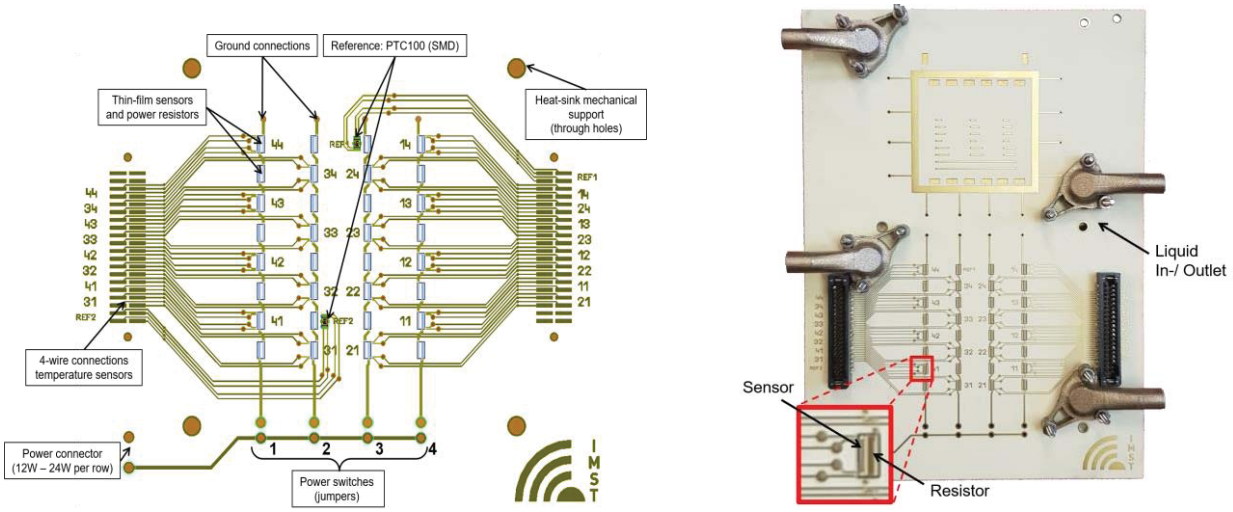

Figure 4: Left: Layout schematic of the thermal test boards; Right: Thermal test board with integrated liquid cooling

The inner core, in which the integrated Ni-cooler is embedded, is made out of standard FR4 material. Layers of Panasonic Megtron 6 RF-substrate (core and prepreg) are laminated onto it, to provide space for RF routing. SiO2 thin film resistors were glued to the surface of

the cooler in cavities foreseen in the PCB. These resistors simulate the effect of the active components, especially the power amplifiers, on a real PCB. The thin film resistors were dimensioned to provide the same heat as the PAs to be used in the ACASIAS project. In total, 64 of these heat sources were assembled, distributed in four rows of 8 resistors. The dissipated power can be controlled by adjusting the current and voltage delivered to the circuit. Small temperature-dependent resistors were assembled in the vicinity of some of the thin-film resistors, to sense the temperature variations. Two PTC100 temperature sensors are clamped onto the PCB at the end of the Ni-cooler as a reference.

4. MEASUREMENT RESULTS AND COMPARISON

The performance of the thermal demonstrator was measured in a temperature-controlled environment. The obtained results were compared to those obtained for a similar test board with a conventional heat dissipation strategy, namely a copper core embedded in the PCB stack. As a first step, a single row of resistors was activated. The temperature on the PCB was monitored using a thermal imaging camera and the temperature sensors assembled in the PCB. Figure 5 shows the heat distribution on the PCB, after switching on the resistors behaviour (left) and after switching on the pump for the liquid cooling. It is clearly seen that the liquid cooling of the PCB has a very quick temperature response and a high cooling capability. The thermal images show that the cooling system is both quick and effective.

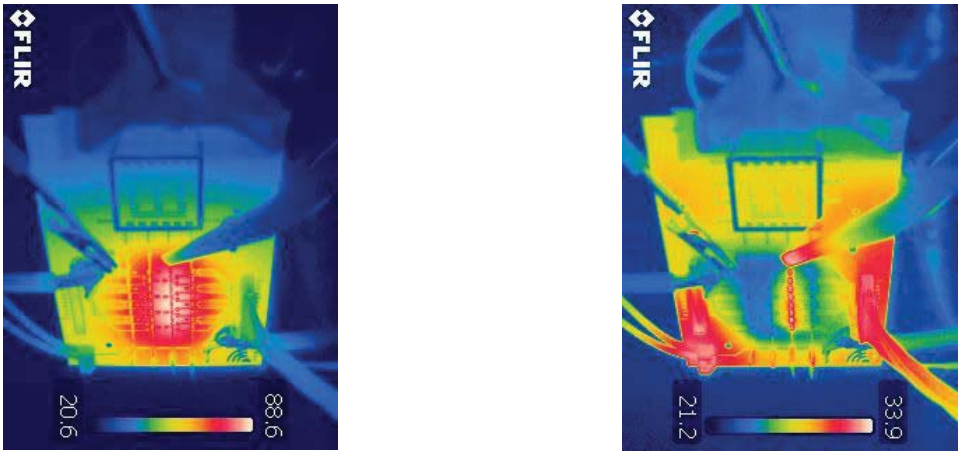

Figure 5: Temperature behaviour of the demonstrator after turning on one row of resistors, before (left) and 5 seconds after turning on the liquid cooling system (right). 12W dissipated power, 1 bar pressure (cooling fluid.)

Figure 6 (left) displays the evolution of the temperature detected by the on-board sensors as a function of time. The sensors T11- T14 are located along the active row, while T22 – T24 are along the parallel row, about 1cm away from the active heating components. The results show how the temperature quickly raises from the moment the resistors are activated on until t=220s, when the cooling system is turned on. At that point, the maximum temperature in the PCB has reached the steady state of 90°C. The temperature decreases quickly once the liquid cooling is activated, to reach a steady state of 38°C. Increasing the thermal dissipation does not significantly increase this steady state temperature, as shown in Figure 6 (right): multiplying the power by 4, to 48W, causes only 1°C increase in temperature; doubling it

again to 96W shifts the steady state to only 51°C, which is still within the operating margin of MMIC components.

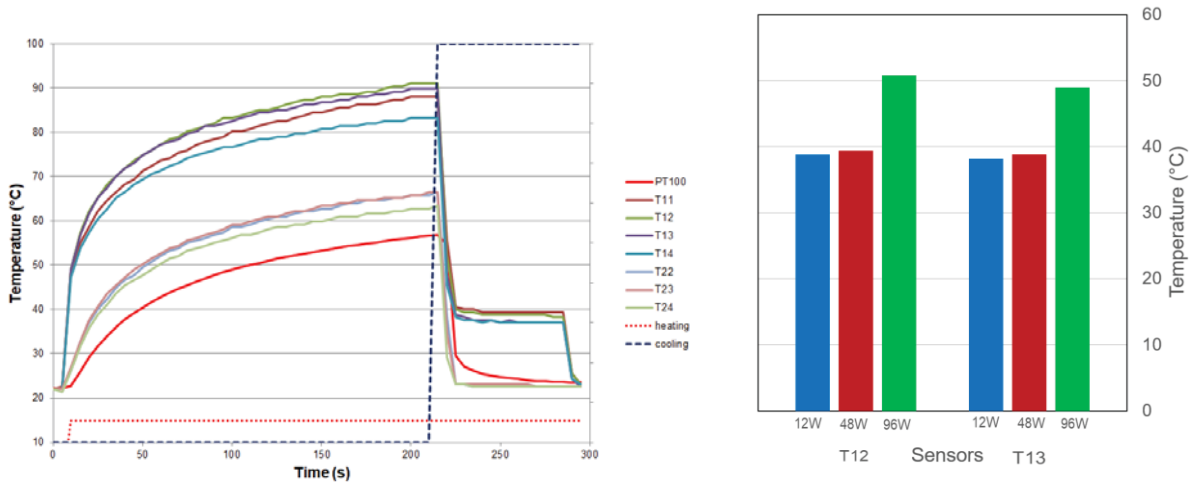

Figure 6: Left: Temperature detected by the on-board temperature sensors, with one row activated, 12W dissipated power; Right: Temperature detected by the sensors T12 and T13 vs. dissipated power.

A comparison, the experiment was repeated with the same layout, but on a PCB with a copper core. In this second case, the maximum temperature reached without additional cooling is around 73°C, clearly lower than the 90°C reached with the previous PCB. This is due to the fact that the copper PCB core has a high thermal conductivity, and spreads the heat over the whole area of the PCB. Figure 7 and Figure 8 shows the performance comparison between the two thermal demonstrators: copper core, a rib-cooler and a fan and with the liquid cooling for the same level of applied power (48W, four active rows), and the same ambient conditions. The liquid cooling allows decreasing the PCB temperature 34°C more than the passive conventional solution. The copper core, in this case, has reached the limit of its possibilities, even with an external airflow. The liquid cooling is operated with a pressure of 1 bar, far from its limit: The embedded nickel cooler is tested up to 4 bar pressure, so the device has much cooling reserve left.

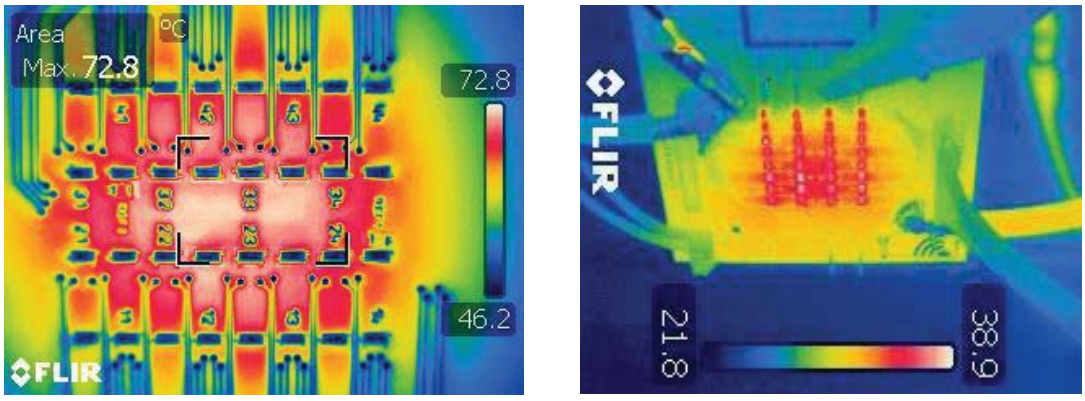

Figure 7: comparison between conventional copper core PCB with rib-cooler & fan (left) and PCB with liquid cooling system (right), 4 active rows, 48W dissipated power, 1 bar pressure (cooling fluid.)

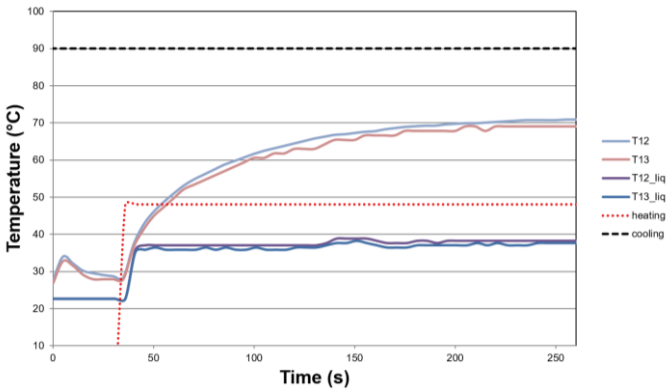

Figure 8: Performance comparison between the PCB with copper core vs. PCB with liquid cooling

The results highlight the superior cooling performance of the integrated Ni-cooler for the heat management of the PCB. It allows reaching quickly the steady state, so that the working point of the RF-circuits can be adjusted.

5. CONCLUSIONS

In this paper the manufacturing and measurements off an innovative embedded PCB-liquid cooling is presented. It shows the high potential of this technology for future buildups of active phased array antennas with a focus of on power dissipation and RF-routing capabilities. It is shown that such a device is manufacturable in a standard multilayer PCB technology. The cooling devices can be customised and accommodated to any kind of PCBs and applications, such as 5G and satellite communication.

ACKNOWLEDGEMENT

The work described in this paper has received funding from the European Union's Horizon 2020 research and innovation programme under grant agreement No 723167, ACASIAS project. The authors want to thank Elekonta Marek GmbH for their assistance in the manufacturing of the prototypes, and Uwe Gollor and Winfried Simon for their help with the thermal measurements.

REFERENCES

[1] "Advanced Concepts for Aero-Structures with Integrated Antennas and Sensors", http://www.acasias-project.eu/

[2] Ebert, T., „Metallkühler für Leistungsbauteile aus dem 3D-Laserdrucker", *Elektronik Praxis: Sonderheft Leistungselektronik* (2018), 20 -22.

[3] Wienhausen, A.H., Sewergin, A., de Doncker, R., Highly Integrated Two-Phase SiC Boost Converter with 3D Printed Fluid Coolers and 3D Printed Inductor Bobbins, *Proc. PCIM Europe; Int. Exhibition & Conf. Power Electr., Intelligent Motion, Renewable Energy & Energy Mgmt* (2018) 1-8.

[4] Curran, B., Reyes, J., Tschoban, C., Höfer, J., Grams, A., Wüst, F., Hutter, M., Leiß, J., Martinez-Vazquez, M., Baggen, R., Ndip, I., Lang, K-D., "Development and Validation of a Chip Integration Concept for Multi-Die GaAs Front-Ends for Phased Arrays up to 60 GHz", *IEEE Trans. Comp., Packaging & Manufacturing Techn.* (2018), **8:**1231-1240.

From design towards manufacturing of winglets with integrated VHF antenna

EMUS 2019

KAI GONET[*], STEFAN STEEGER[*], ZDENĚK ŘEZNÍČEK[†] MARTA MARTÍNEZ-VÁZQUEZ[††], JORDI BALCELLS-VENTURA[††], PETR VRCHOTA[†††], VICTOR LUNGAHO[††††]

[*] INVENT GmbH
38112 Braunschweig, Germany
e-mail: kai.gonet@invent-gmbh.de, http://www.invent-gmbh.de

[†] Evektor
686 04, Kunovice, Czech Republic
e-mail: engineering@evektor.cz, www.evektor.cz

[††] IMST GmbH
47475 Kamp-Lintfort, Germany,
email: contact@imst.com, www.imst.com

[†††] VZLU – Czech Aerospace Research Centre
19905 Prague, Czech Republic
e-mail: vrchota@vzlu.cz, web page: http://www.vzlu.cz

[††††] Trackwise
Gloucestershire GL20 8NB
United Kingdom
e-mail: victor.lungaho@trackwise.co.uk - web page: www.trackwise.co.uk

Key words: Integral Construction, Notch Antenna, Winglet, Aviation Engineering

Abstract. This paper shows the technical aspects and the progress of manufacturing a winglet concept with integrated VHF antenna.

1 INTRODUCTION

Reducing fuel burn emissions is one of the most important aims in aircraft design nowadays. One possibility for reducing the aerodynamic drag of airplanes is to reduce the number of protruding parts as antennas. One possible design concept is to move the antenna within the winglet and to integrate the transceiver of electromagnetic radiation into the aerodynamically optimized structure [1]. The challenge of this goal is to build the VHF antenna with its wavelength defined size into a winglet. The winglet designed in ACASIAS is for a small transport aircraft of the type Evektor EV55. This small size makes the integration in the small installation space a demanding task. This construction method shown here can also be easily used on larger aircraft. Another challenge of the design process is that the

winglet must be certifiable, maintainable, and repairable at the final stage for all systems and structure.

2 WINGLET DESIGN

Neither a high-quality winglet nor a VHF antenna is a revolutionary new idea. In aviation, however, assemblies are usually separated according to their function. Functional integration is unusual. In this chapter the structural design and the necessary boundary conditions will be discussed.

Several aspects of the winglet design have to be considered. First of all, it should apply the aerodynamically optimized shape for reducing the vortex drag at the tip of the wing, as well as it should fulfill the structural need for inducing aerodynamic forces and moments to the wing, remain stable in the event of bird strikes, and it should resist lightning strikes. The integrated antenna should be able to transmit VHF (very high frequency) radio communication to and from other air or ground stations.

Therefore, it is inevitable that the signals from the integrated antenna within the CFRP structure (Carbon Fiber Reinforced Plastic) are erased by a GFRP (Glass Fiber Reinforced Structure) “window” inside the winglet. CFRP does not allow electromagnetic radiation to pass through. The boundary conditions for an antenna is summarized in [2] and [3].

Figure1: Cross-section of scarfed GFRP “window” (flare) of the winglet

The notch antenna design itself was delivered by IMST, which is responsible for this topic. The production of the antenna itself is done by TRACKWISE, who create a thin, flexible PCB (Printed Circuit Board) which can be integrated within the winglet. The electromagnetic design is given in [4].

The position of the notch fiberglass antenna and "window" is very important for the reception and transmission of high frequency data.

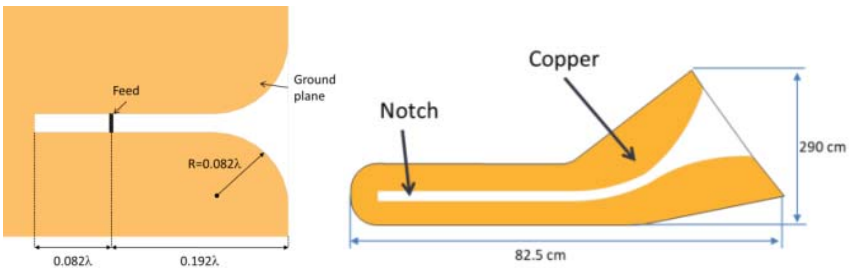

Figure2: Notch antenna. Left: Basic structure, Right: final geometry

2.1 Aerodynamic optimization

As mentioned, the Evektor EV55 is used for the EU project ACASIAS for the design. This aircraft was examined and optimized by VZLU under the aerodynamic conditions of the flight

envelope. The core of the optimization is the reduction of drag and the reduction of the number of attachments promoting drag. Two Evektor EV55 aircrafts are flying at the time of this study.

The optimization strategy is based on the Design of Experiment (DoE). The Response Surface Method (RSM) is also used. More detailed descriptions can be found in [5]. The optimization resulted in a winglet shape with the highest reduction of induced drag. The result is the yellow winglet shorn in Figure 3.

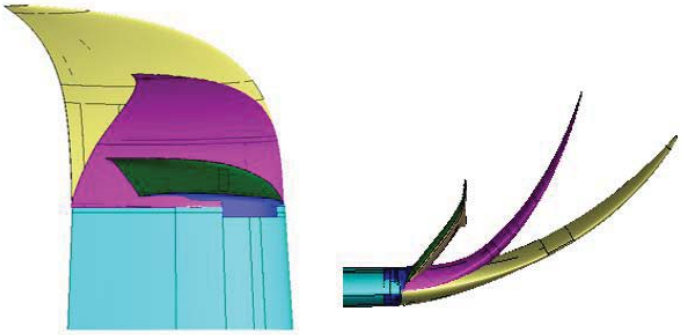

Figure 3: Stages of Optimization
(green = original, magenta = 1st optimization, yellow = 2nd optimization)

2.2 Structure simulation

With this aerodynamic design, structural investigations can follow. The dimensions of the winglet make it necessary that (as is usual in large wing constructions) a spar passes through the structure perpendicular to the plane of the wing in the area of the largest profile thickness. This beam absorbs a large portion of the load but reduces the installation area for the antenna. Therefore, the opening of the antenna is rotated so that the rear opening of the antenna terminates within the trailing edge of the winglet. The monolithic trailing edge in GFRP is a basic requirement for the functionality of the antenna. The beam, in the front area of the antenna, also limits the mounting position of the PCB sheet. With these boundary conditions, the antenna window (hereinafter referred to as “flare”) can be positioned.

The structure of the design concept was used to create a model for structural analysis. Before the structural investigation can be performed, the antenna notch must be positioned.

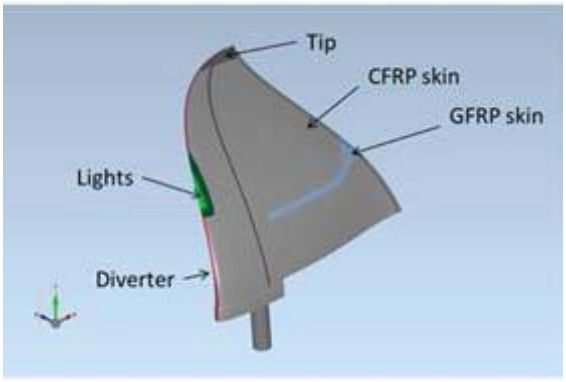

Figure: 4: Structure of winglet with notch antenna and the “flare” window

The stress on the winglet is calculated using the pressure distribution. In fact, the ultimate load factor must be taken into account. The winglet itself is made out of CFRP with a scarfed GFRP flare with dielectric properties for VHF antenna operation. The core of the winglet consists of a spar and a structural foam. The critical load case was considered by VZLU and EVEKTOR for an AoA of 17°. INVENT placed the pressure field (delivered by VZLU) on the structural model of the winglet. The ultimate load as a safety factor for individual parts were determined as followed:

- x 2.25 for composite parts
- x 1.5 for metallic components

The pressure distribution was also multiplied by this safety factor, as well as the acceleration due to gravity. The pressure distribution was projected onto the wetted winglet surface. The first structural model was based on a CFRP material thickness of 2.5mm, which corresponds to a plybook of 10 layers for the outer skin. The first estimation of material and thickness provided a total weight of 11.5kg.

The first iterations with the 11.5kg model showed that the winglet is far stronger than required. This led to weight optimization. In several successive steps, the influence of the reduction in material thickness and density was determined under the specific load. The structurally optimized winglet is a design with a lightweight foam core. The spar thickness is reduced. The material thickness of the outer skin was also reduced from 2.5mm to 1.7mm (corresponding to 7 layers). 2mm CFRP is applied only in the winglet root area. The final weight is around 8.5kg.

In the following the maximum principal stress of the upper side (left) and the lower side (right) of the winglet is shown. On the bottom side you can see the scarfed GFRP window, which has little influence on the strength of the winglet skins.

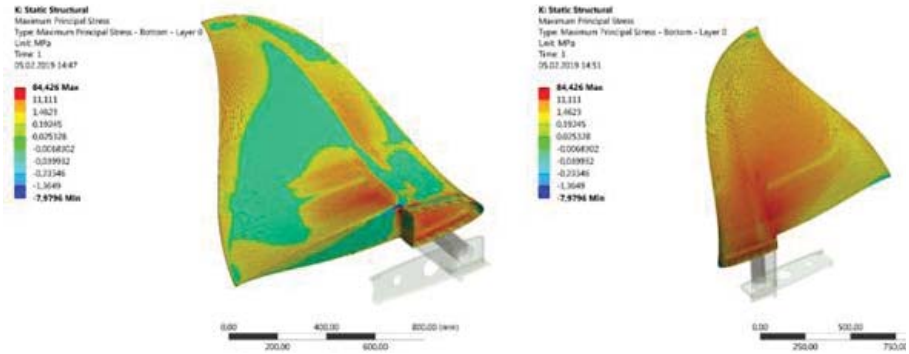

Figure 5: Maximum principal stress in logarithmic scale (Left: top side, Right: bottom side)

Within the optimization process the structure model could be further refined. For the calculation an Inverse Reserve Factor (IRF) with Tsai-Wu failure criteria was used. If the value of the IRF is less than one, there is no damage to the fiber composite structure.

The resulting IRF composite is 0.29 (usual: IRF = 1 = Failure). According to ultimate load.

$$\boldsymbol{IRF}/(\textbf{ultimate load}) = \mathbf{1}/(\mathbf{2.25}) = 0.57$$

is below IRF=1. Therefore, the winglet structure is safe.

The support reaction that are transferred into the wing was also calculated. For EVEKTOR these values are essential for the design of the wing itself. These values were delivered for re-dimensioning the wing spars and stringers.

Bird strike is also considered. The highest risk of a bird strike is the displacement of the trailing edge inwards towards the aileron. In the event of a bird strike, the winglet must not block the aileron. For cruising speed of 400 km/h and a bird weight of 2 kg the reaction force on the wing via the impact energy and the impulse were calculated. The calculation of this force applied to the outermost part of the structure results in a displacement of the trailing edge of 4mm. This displacement does not affect the aileron

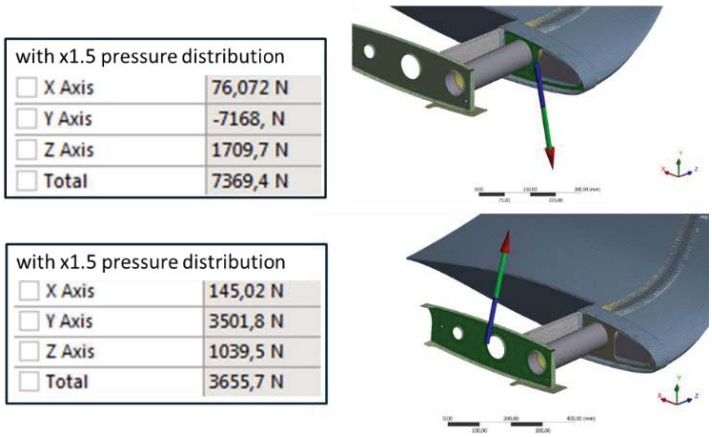

Figure 6: Resulting forces and moments on the joints between winglet and wing

4 TECHNICAL ISSUE ON THE WAY TO THE WINGLET

4.1 The scarfed shape GFRP window

The winglet is mainly made from CFRP. As mentioned, one characteristic of carbon fiber is shielding electromagnetic radiation. In addition, the outer layer of a winglet must be covered with a copper fabric in order to prevent lightning strike damage. Such a copper mesh also has a negative effect on the electromagnetic permeability. The antenna is constructed with a monolithic trailing edge in GFRP. This is necessary so that the antenna has the most suitable potential and thus the most optimum radiation of the radio signal.

In order to give the winglet composite structure, the necessary strength for the antenna in the area of the electromagnetically acceptable window, this area must be scarfed. This means that the size of the glass fiber cut-outs increases towards the inside of the winglet. Correspondingly, the opening of the carbon fabric becomes larger towards the inside. The resulting overlap creates a firm bond between the CFRP and the GFRP. This surface optimizes the emission of the electromagnetic radiation of the winglets and minimizes the surface without lightning protection on the outside.

Before a complete winglet is built, several panels were built for the technical realization of such a layer construction. In accordance with the shape of the winglet, INVENT built a specimen to provide information about the production process and thus the final structure of the winglet. The shafting was realized. A curved shape with the winglet radius and flat panels were sent to IMST for further investigations

4.2 Mold construction

The entire winglet is produced in one cycle and this has to be considered within the design process of the molds. This one cycle process production means cost-effective manufacturing, but requires a little more planning. At first, all necessary semi-finished products are prepared. The molds are wetted with a special varnish in order to release the winglet after production.

The skin layers are laid in the molds covered with a pre-impregnated resin system. A foam block milled to contour is then placed on the already prepared lower shell. This foam block also serves as a support to form the spar within the winglet. Both molds are then pressed together and cured at higher temperature by integrated heating pads.

The mold construction must be set with such precision so that the separation planes can release the winglet from the tooling negative forms after the curing of the resin. For this reason, we work with four molds. One heatable top and bottom and additionally two unheated side molds, which form the end rib facing towards the aircraft.

At first, the original forms are milled as positive (i.e. with the original contour). The negative tooling molds are then made from this positive. After preparing the milled master tooling foam, the heater mats are brought to the contour using a vacuum injection process. The necessary stability of the negative mold is then provided by applying prepreg and a specially knitted fabric (comparable to sandwich construction). Various tests must be carried out within these steps in order to document the functionality of the self-heating tools.

The geometry and the number of molds must be selected so that the molds can be separated after curing. For example, there must be no undercuts in the molded parts.

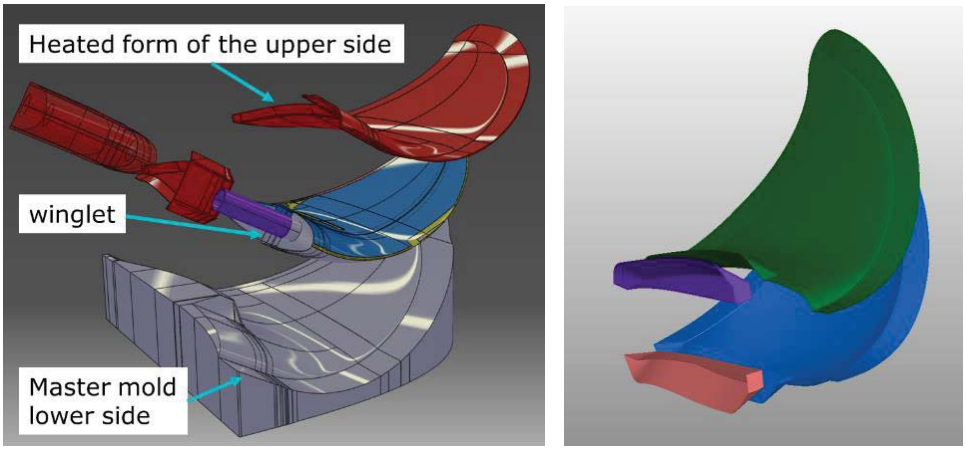

Figure 7: Left: the construction of molds and wing, Right: sepeartion area and the four mold elements for finals production process of winglet

4.3 Heated molds

In the ACASIAS project we are also aiming for self-heated mold production. For this purpose, it is necessary to produce special type of molds. INVENT strives for a heatable mold with specially defined heating surfaces that cure the material of the winglet at the required temperature. In this special case, we have to heat the mold up to 125°C.

INVENT pursues two strategies for heating the molds for the winglet. At first is the possibility of placing fabric embroidered with heating wires as a layer in the negative mold. This mat is then embedded in the fiber composite. The advantage of this manufacturing

process is that the heating mat can be prefabricated exactly to the geometry needed of the produced component. The other possibility is to use a special layer of CFRP, which is connected with wiring. The internal resistance of the CFRP causes this layer to heat up. With this variant, however, the effort required for assembly is somewhat higher. The heatable surface is divided into as many large rectangular surfaces as possible. These individual surfaces must then be electrically insulated from each other using GFRP. However, the winglet has a simplified triangular shape. Various geometries were taken into consideration for optimizing several divisions of a small number of independent heating areas . These are shown in the picture. In order to save heating surface three rectangular heating surfaces are favored. In the following picture these are outlined green.

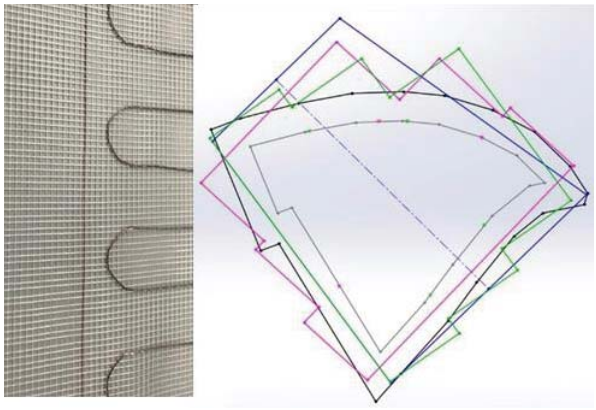

Figure 8: Left: Carrier fabric with embedded and embroidered heating filament, Right: Three possible designs for a heating field with different geometry

The structure of the heating surfaces is built up in an infusion process. This means that the top layer in the molds is a dry basalt layer, which serves as electrical insulation. This is followed by the heating layer with special carbon fabric, which is electrically connected at the edges with a wire mesh. A layer of fabric is applied on top of this for electrical insulation. This provides a molding tool that makes it possible to produce a component outside an autoclave or oven.

5 MAINTENANCE AND REPAIR

Maintenance and repair are a major focus for attention. The winglet presented here will be optimized for a smaller twin-engine 12-seater cruise aircraft. Due to the size of the aircraft, the construction volume of the winglet is very small compared to the winglet size on a large aircraft (CS-25). Due to the small construction volume and the special scarf shape GFRP flare, special repair measures are necessary.

The largest damage potential for the winglet would be: Lightning strike, collision damage, bird strike and electrically unusable/malfunction/damage antenna

For the first three types of damage, it can be assumed that the winglet would become aerodynamically and structurally unusable. This would result in a very costly repair and release to service. If the fiber composite in the area of the antenna is defective, there are different possibilities of repair. It would be possible to cut out and insert dry, large-area, prefabricated elements with the GFRP window in case of damage in the antenna area. The

scarfed flare is the biggest challenge in the production of such a patch. The ideal solution would be to replace the winglet. In the size segment of the aircraft class presented here (CS23), a new production might be cheaper than a repair.

For the repair of an electrically unusable antenna, the installation and handling space is not sufficient for the isolated repair of the antenna. Handhole covers would mean a considerable loss of the aerodynamic quality of the winglet for an aircraft of this size. One way to repair the antenna within the winglet would be to use position lights and ACL (Anti Collision Light) for opening the antenna mounting surface from the front of the winglet. For the best possibility of maintenance for the antenna would be a mounting, in which the flexible material could be slid into the final position.

The focus for the endurance tests should be a program for the durability of the solder joint for the antenna. The antenna is produced by TRACKWISE. There, the solder joints could also be made of flexible material and integrated into the manufacturing process of the antenna. The worst case for an electrical failure would be a cable break close to an edge near the wing root or a hidden cable break. These faults should be tested in a fatigue strength test and should lead separately to a special repair instruction.

For larger aircraft there are more possibilities to position the antenna with regard for a cheaper repair of the antenna itself. Unfortunately, the construction of the antenna depends on the fact that the flare must have a glass fiber edge at the end. Nevertheless, it would be possible to reach the antenna through an opening of the Leading Edge (through the holder of the position lights) by means of a special spar geometry in large aircraft.

Figure 9: Two different winglets with position lights and openings for possible antenna replacement (from internet picture research [10] and [11])

6 CONCLUSION AND OUTLOOK

The first results of the integration of a VHF notch antenna in an aircraft winglet have been presented. The antenna measured performance complies with the requirements in terms of bandwidth. The next steps include the measurement of the radiation patterns, and the adaption of the structure to the real, conformal winglet geometry.

Lightning protection will also be investigated in this context. Since the winglet is the component predestined for lightning strikes, this issue will be investigated further more. Especially with regard to the electrical components inside the winglet, it is necessary to discuss the rules and regulation for the certification and for increasing the TRLs.

13 ACKNOWLEDGEMENTS

All work described in this paper has received funding from the European Union's Horizon 2020 research and innovation programme under grant agreement No 723167, ACASIAS project.

REFERENCES

[1] "Advanced Concepts for Aero Structures with Integrated Antennas and Sensors", http://www.acasias-project.eu/
[2] J. Verpoorte, "Requirements and Specification Document", ACASIAS Deliverable 1.1, [online].
[3] Z. Reznicek , Towards Multi-objective Design of EV55 Winglet with integrated VHF antenna, EMUS2019, Barcelona
[4] Marta Martinez-Vásquez, Jord Balcells-Ventura, „VHF notch antenna integrated in an aircraft winglet", EMUS2019, Barcelona
[5] P. Vrchota, S. Steeger, M. Martinez-Vazquez, M. Svetlik, Z. Reznicek, "Aerodynamic and structural design of winglet with integrated VHF antenna", 8th EASN-CEAS Int. Workshop on Manufacturing for Growth & Innovation, 2018, Available: https://doi.org/10.1051/matecconf/201823300018
[6] R.A. Burberry, "VHF and UHF antennas", IEE Electromagnetic series 36, Peter Peregrinus, 1992.
[7] Empire XPU Manual, 2016, [online].
[8] CST, "Electromagnetic Simulation of Composite Materials and Cable Harnesses in Aircraft", [online].
[9] Elliot J. Riley, Erik H. Lenzing, Ram M. Narayanan, "Characterisation of carbon fiber composite materials for RF applications", Proc. Of SPIE, May 2014, DOI: 10.1117/12.2050132.
[10] Dieter Scholz, "Definition and discussion of the intrinsic efficiency of winglets", Aircraft Design and Systems Group (AERO),Hamburg University of Applied Sciences, Berliner Tor 9, 20099 Hamburg, Germany, [online]
[11] https://aegistg.com/how-the-59-caddy-saved-us-six-billion-gallons-of-gas

European Conference on Multifunctional Structures
EMuS 2019
X. Martinez and H. Schippers (Eds)

TOWARDS MULTI-OBJECTIVE DESIGN OF EV-55 WINGLET WITH INTEGRATED VHF ANTENNA

EMUS 2019

ZDENĚK ŘEZNÍČEK[*], STEFAN STEEGER[†], KAI GONET[†], MARTA MARTÍNEZ-VÁZQUEZ[††], JORDI BALCELLS-VENTURA[††], PETER VRCHOTA[†††], VICTOR LUNGAHO[††††]

[*] Evektor, spol. s r.o.
Letecká 1008, Kunovice, Czech Republic
e-mail: engineering@evektor.cz, www.evektor.cz

[†] INVENT GmbH
Christian-Pommer-Straße 34, 38112 Braunschweig
email: info@invent-gmbh.de, www.invent-gmbh.de

[††] IMST GmbH
Carl-Friedrich- Gauß-Str. 2-4, 40223 Kamp-Lintfort, Germany
email: contact@imst.com, www.imst.com

[†††] Czech Aerospace Research Centre (VZLU)
Beranovych 130, 199 05 Prague, Czech Republic
e-mail: vrchota@vzlu.cz, web page: http://www.vzlu.cz

[††††] Trackwise Designs plc
1 Ashvale Alexandra Way, Ashchurch, Tewkesbury, Gloucestershire, England
email: victor.lungaho@trackwise.co.uk, www.trackwise.co.uk

Key words: VHF antenna, electromagnetics, aerodynamics, stress analysis, winglet, aircraft

Abstract. The article is devoted to highlight the challenges, bottlenecks and possible solutions of VHF antenna integrated into a winglet from both the designer‘s and the airframer‘s perspective. We look into pros and cons specific for different antenna solutions and discuss ways how to protect them against possible electromagnetic environmental effects. As an outlook, a winglet with integrated VHF notch antenna designed within the ACASIAS project will be described in better detail.

1 INTRODUCTION

Modern winglet designs tend to introduce more functions than simply improving the efficiency of fixed-wing aircraft by reducing drag. As an example, integration of position and anti-collision lights represents one of the most common ways how to effectively utilize the winglet in more than one way. Hand in hand with new manufacturing technologies and materials, there is an increasing tendency to integrate different types of antennas into the winglet too. This is also the case for the ACASIAS project [1], where one of the systems to be

developed is a VHF antenna integrated into the winglet.

A successful design of winglets with integrated antennas is relatively complex and multidisciplinary task, especially when taking into consideration all possible technical trade-offs and bottlenecks [2], [3]. Biggest portion of possible difficulties usually falls into the following three fields of the design: aerodynamics, stress analysis and electromagnetics. However, the design of all such systems integrated in the winglet should be carried out in continuance of development of an aircraft, taking into consideration all system safety analyses at its beginning up to the certifiability, maintainability and repairability at the final stages.

The most basic problem is already to attach a winglet to a pre-existing wing of an aircraft to increase its performance and efficiency. When installing a new winglet to an aircraft, it is necessary to take into account possible additional reengineering and recertification works on a wing, which can be restrictive from time and economical perspective. This is why aftermarket installations are mostly viable only for large airplanes. The first main reason is possibility of adding originally unforeseen stress to a wing structure. The critical factor here is the influence of a winglet on load distribution along the wing, especially on bending moment distribution. In general, a winglet shifts resultant air force towards the tip of a wing and consequently increases its bending moment. The second is the above-mentioned change in aerodynamic performance of an aircraft, dictated by the final shape of a winglet and critical flight scenarios (i.e. load cases) specified for an aircraft. Both, levels of final loads introduced from the winglet to the wing structure and shape of the winglet, improving final aerodynamic performance of an aircraft, represents two contradicting design goals to be solved.

Another interesting challenge may represent physical dimensions of the winglet and the VHF antenna itself. VHF communication antennas operate on relatively low frequencies: 118 – 137/156 MHz ($\lambda \approx 2$ - 2.5 m). This is why design and integration of the VHF antenna into such small area may easily become a challenging engineering task from several reasons.

First reason is connected with the antenna performance. New unconventional designs may provide us with more spatially effective solutions without sacrificing necessary performance an antenna. However, some parameters applicable for airborne VHF communication specified in [4] are clearly in favour of standard monopole-like solutions where omnidirectional radiation pattern of an antenna is preferred in horizontal plane. Such a requirement is not feasible for any antenna situated at the tip of a wing due to obstruction caused by an airplane.

Logical solution to get omnidirectional-like pattern for a VHF comm. system is to place two separate antennas on both ends of a wing. The solution is technically valid because it rotates (rolls) the concept defined in [4] only by 90^o about the longitudinal axis of an aircraft. In addition, such a solution can be combined with the standard one to obtain better coverage.

However, such a choice for the antenna position also has its clear disadvantages. Winglet parts, as structural extremities, tend to attract a lightning and hold the lightning channel (at its trailing edge) and there is a high possibility that both winglets will become a part of the lightning channel at the same time. Therefore, winglet antenna will experience more severe and hazardous environment (zones 1A and 1B) and it is necessary to designed it in a way to overcome similar events without significant damage or damage to other systems behind it. This is why safe flight and landing without VHF COM antenna destroyed due to lightning has to be taken into account during aircraft safety analysis.

The last but equally important design challenges lies in the field of repairability and maintainability of the winglet antenna. Higher possibility of its damage due to a lightning

strike, as the negative aspect of its position on an aircraft, can be compensated by winglet design to allow possible repairs of the antenna element or the structure itself. Such measures will positively influence operational and maintenance costs of the whole system.

3 AERODYNAMIC DESIGN

Aerodynamic design of a new winglet has been done by means of the optimization method and numerical simulations. The cost function of the optimization was minimization of the induced drag. The flow conditions corresponded to the cruise regime of the EV55 aircraft. The RANS equations were solved in in-house CFD program. All simulations were run as a fully turbulent flow using k-ω EARSM turbulence model.

The optimization strategy is based on the Design of Experiment (DoE) in connection with Response Surface Method (RSM) to find out the optimal winglet's shape from the requirements point of views. Winglet itself was parameterized by elliptic curves. Six parameters in total were used for creation of the DoE matrix. The height, dihedral, twist and its combination defined the final winglet's shape. The number of parameters with the circumscribe type of DoE defined the total number of created and calculated geometries.

Several constrains have been introduced at the beginning of the optimization. The main constrains were the maximal increment of the bending moment due to the winglet and maximal loads of the end rib of the original wing. The another constrain was the size of the winglet itself. Larger winglet is better from the VHF antenna integration point of view. The winglet size was limited by the original on one side and by the large wetted surface (penalizing the friction drag) on the other side.

The calculated cases from DoE after some optimization loops resulted in the final shape of the winglet, which fulfil all requirements and constrains. The comparison of the original and optimized shape of the winglet is depicted in Fig. 1. More detail description can be found in [3]. The performance of the optimized winglet was compared with the baseline EV55 aircraft with winglet and with the EV55 with original winglet. It has been found that the new winglet decreased the drag by about 5 drag count compared with the baseline configuration without winglet and by about 2 drag count compared with the original winglet, respectively. The relatively small drag decrement is probably caused by the slot between the optimized winglet and aileron. This slot was not present in original winglet and has been modelled due to the horn aerodynamic balance of the aileron.

The additional critical cases were defined after the optimization to obtain the loading of the wing and winglet. The bending moment of the wing with new winglet together with the pressure distribution on the winglet's surface were calculated and exported for subsequent verification of wing's structure and structural design of the winglet itself.

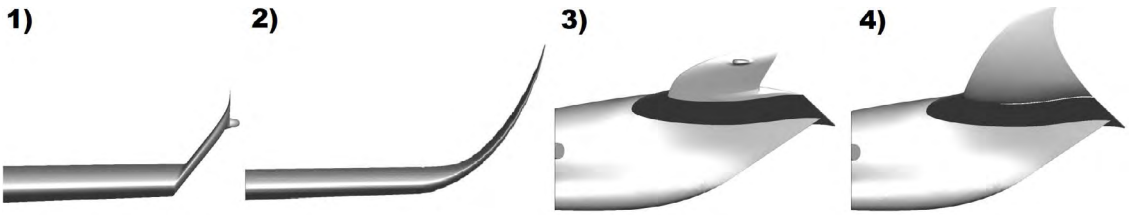

Figure 1: Comparison of the original (1, 3) and optimized (2, 4) shape of the winglet

4 STRUCTURAL DESIGN

Stress distribution, derived from pressure distribution obtained from CFD analyses, and resulting loads transferred from the winglet into the EV-55 wing have been taken into account during design and optimization of the winglet structure.
The critical load case was considered for an AoA (Angle of attack) of 17°. The ultimate loads as a safety factor for filing parts were determined as followed: 2.25 for composite parts and 1.5 for metallic components (CS 23.303). The pressure distribution was also multiplied by this safety factor, as was the acceleration due to gravity, and was projected onto the wetted winglet surface.
The first structural model was based on a CRFP material thickness of 2.5mm, which corresponds to a plybook of 10 layers for the outer skin, and the first estimation of material and thicknesses provided a total weight of 11,5kg. This resulted in first loop of the model refinement. For the calculation, an Inverse Reserve Factor (IRF) with Tsai-Wu failure Criteria was used. The first iterations showed that the winglet is far too strong than required. This led to weight optimization. In several successive steps, the influence of the reduction in material thickness and density under the specified load was determined.
The final design is a two-shell structure with a lightweight foam core. The material thickness of the outer skin was reduced from 2.5mm to 1.7mm (corresponding to 7 layers). Only in the area of the winglet root is applied with 2mm CFRP. The final weight is around 8,5kg. GFRP window enabling antenna to radiate has only little influence on the strength of the winglet.

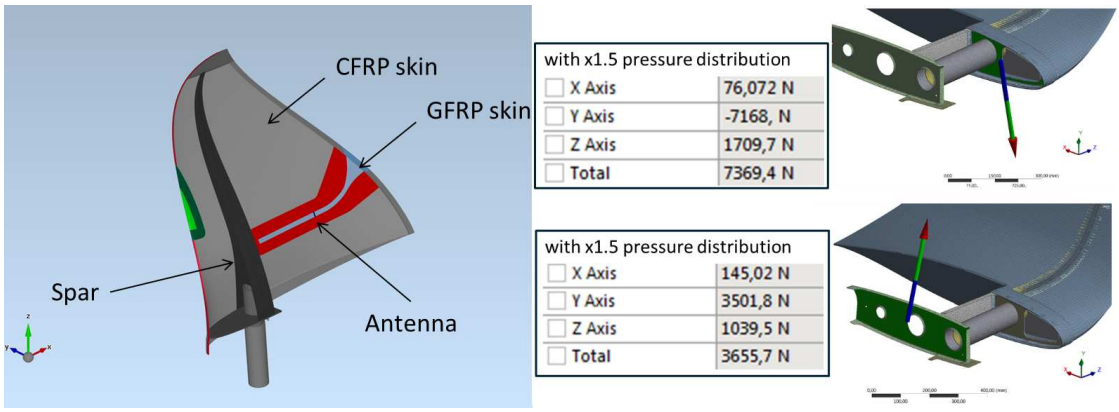

Figure 2: Main parts of the winglet, outer and inner layers (Rohacell and Cu mesh not shown for the sake of clarity), and support reactions transferred from the winglet into the last wing rib (green part)

The support reactions transferred from the winglet into the wing are shown in Fig. 2 (safety factor is 1.5). Assessment of the local effect of the winglet to the wing showed necessity of local structural modifications of the end part of the wing to transfer properly a local load generated by the winglet. In the further investigations, an iteration loop is once again run through in the event of bird strike. In first calculations the impulse of a bird strike on the outer tip of the winglet was applied. The deformation must not be so large that the trailing edge of the winglet may block the aileron connected to the wing. This calculation resulted in the displacement of the trailing edge by 4mm in the direction of the aileron. Since the gap dimension at this position is considerably larger, this position is also to be regarded as uncritical.

5 ANTENNA DESIGN

The preliminary design was performed for the basic VHF frequency band, 118 – 137 MHz. The antenna is integrated in the 3D volume of the winglet, taking into account the presence of other elements (e.g., lightning diverters and lights.) The winglet shell is made out of Carbon Fibre Reinforced Plastic (CFRP) covered with a copper mesh for lightning protection. A Glass Fibre Reinforced Plastic (GFRP) "window" is included to allow the antenna to radiate. The antenna itself is printed on flexible PCB (Printed Circuit Board) and placed between the CFRP/GFRP skins. The winglet is filled with foam material (Rohacell) for mechanical stability.

Different antenna concepts, namely a meandered monopole or a meandered slot (see Figure 3,) were considered for the project. To simplify the initial conceptual simulations, a planar projection of the winglet was considered, and metallic strips were added to account for the effect of the lightning diverters. Both concepts were discarded, as the required additional lightning protections on the winglet strongly degraded their performance.

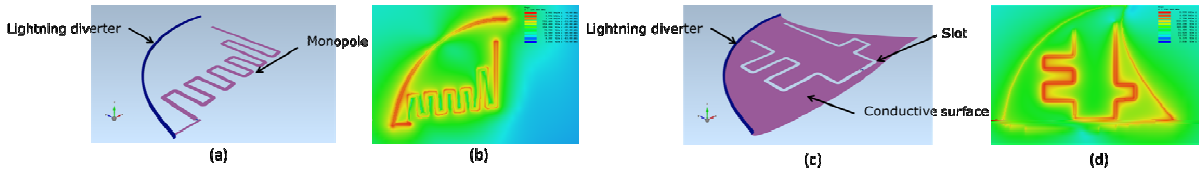

Figure 3: Initial antenna concepts for the winglet: meandered monopole (a) and its field distribution (b); and meandered slot antenna (c) and its field distribution (d)

In the end, a notch antenna [5] was selected. This structure is quite insensitive other metallic components in its vicinity. It consists of a slit in a ground plane, tapered at its open end, giving the shape of a trumpet, to increase the bandwidth.

The simulation model of the antenna, together with antenna's radiation field and S11 results is presented in Fig 5. The geometry is adapted to the shape and size of the winglet, and takes into consideration other elements, such as position lights and stiffeners. The S11 results can be compared with initial measurements of the antenna on a flat mockup reported in [2].

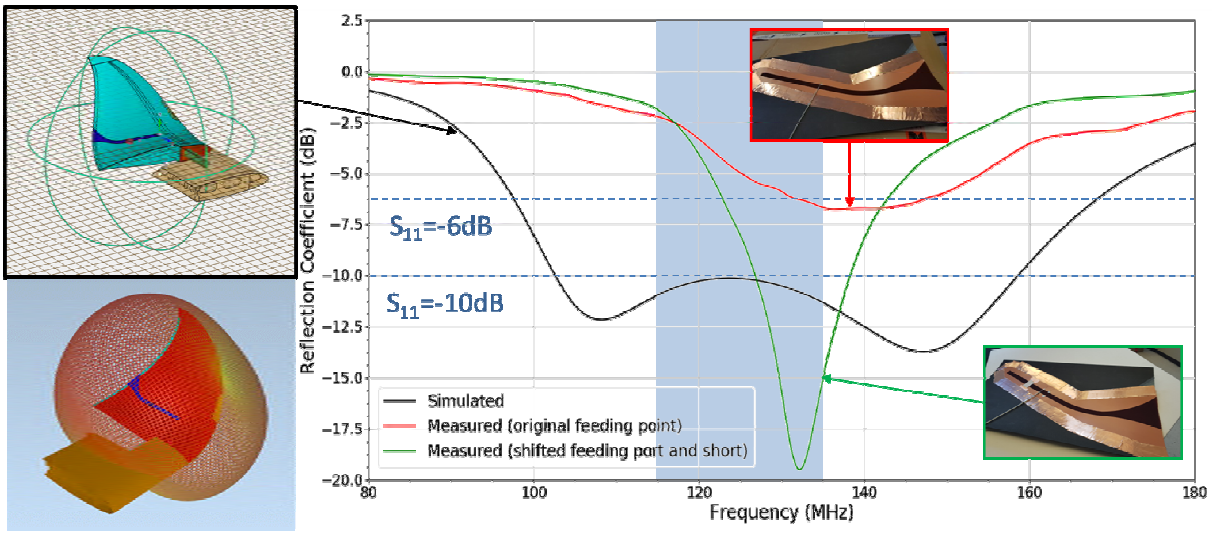

Figure 4: Simulation model representation, antenna far field and S11 results (simulation vs. mockup)

The notch antenna (mockup) was printed on a flexible PCB and fixed on conformal-shaped shell using adhesive copper tape. The feed consists of a semi-rigid cable with a SMA connector. When using the original feeding point (determined by simulation), the antenna does not comply with the bandwidth requirements, as the conformal shell, which acts as a ground plane, is smaller than the real winglet assumed in the simulation. This causes a shift of the resonance frequency and impedance matching. The antenna can easily be tuned to meet the requirements by slightly tuning the size of the notch and shifting the feeding point.
Future work will look at integrating a flexible circuit with the notch antenna in the right position as determined by the preliminary results. This should increase reliability and perfomance by eliminating the need for a joining mechanism between the feed line and the antenna.

6 SUMMARY

The complexity and multidisciplinary nature of the winglet with integrated VHF antenna has been discussed from several engineering perspectives. Finding optimal design solutions for both the winglet and the antenna without using modern simulation tools would significantly prolong the time and efforts necessary to reach the final design. This applies in general to all multifunctional structures offering us new possibilities in both avionic and automotive sector.

As the introductory discussion showed, the proposed design represents only first steps on the road towards the final (commercial) product. Other design aspects like reparability, maintainability, or potential to certify and operate the winglet still has to be addressed in detail.

ACKNOWLEDGEMENT

All work described in this paper has received funding from the European Union's Horizon 2020 research and innovation programme under grant agreement No 723167, ACASIAS project.

REFERENCES

[1] "Advanced Concepts for Aero-Structures with Integrated Antennas and Sensors", http://www.acasias-project.eu/

[2] M. Martínez-Vázquez, J. Balcells-Ventura, Z. Řezníček, K. Gonet, S. Steeger, P. Vrchota, V. Lungaho, „VHF notch antenna integrated in an aircraft winglet", submitted to IEEE Antennas & Propagation Society Symposium, Atlanta, US, 2019.

[3] P. Vrchota, S. Steeger, M. Martínez-Vázquez, M. Světlík, Z. Řezníček, "Aerodynamic and structural design of winglet with integrated VHF antenna", 8th EASN-CEAS Int. Workshop on Manufacturing for Growth & Innovation, 2018, Available: https://doi.org/10.1051/matecconf/201823300018

[4] RTCA DO-186B, Minimum Operational Performance Standards (MOPS) for Airborne Radio Communications Equipment Operating Within the Radio Frequency range 117.975 – 137.000 MHz

[5] R.A. Burberry, "VHF and UHF antennas", IEE Electromagnetic series 36, Peter Peregrinus, 1992.

AUTHORS INDEX

Abellán, J. M. 54
Algermissen, S. 30, 23, 36
Bachmann, J. 102, 87
Baggen, R. 153
Balcells-Ventura, J. 159, 168
Beauchamp, Y. 81
Berton, B. 128
Blanco, T. 138
Cano, F. 54
Chatelain, J-F. 81
Cupal, M. 148
Dřínovský, J. 148
Di Lorenzo, J. 138
Ebert, T. 153
Expósito, G. 54
Gal, A. 54
Gonet, K. 23, 36, 159
Gonnet, K. 168
Götthans, T. 148
Haase, T. 36
Hadley, P. 138
Heijmans, R.M.H. 120
Heuts, C. 108, 114
Hulzinga, A. 120, 74
Jiménez, A. E. 54
Jiménez, F. J. 54
Journee, M.J.G. 120
Kokott, A. 36
Konter, Y. 114
Krutílek, D. 148
Kráčalová, D. 148
Lebrun, G. 81
Ledrová, Z. 148
Leiß, J. 153
Lima, C.F.R.A.C. 96
Lungaho, V. 23, 36, 159, 168
Láčík, J. 148
López-Romano, B. 138
Martinez, X. 68
Martín, F. 54
Martínez-Vázquez , M. 159, 153, 168
Menéndez, J. 54
Middel, J. 44
Misol, M. 36, 30
Moreira, P.M.G.P. 96
Müller, J.M. 60
Nijhuis, P. 60
Otero, F. 68
Pastorino, D. 138
Prachař, A. 44
Procházka, J. 148
Prášek, J. 148
Raida, Z. 148
Řezníček, Z. 168, 159
Saadati, Y. 81
Santos, L.M.N.B.F. 96
Schippers, H. 120
Sguazzo, C. 96
Singh, A. 96
Šmíd, M. 44
Steeger, S. 168, 159, 23
Tavares, P.J.S. 96
Tensen, P. 120
Tserpes, K. 87
Turon, F. 68
Tzatzadakis, V. 87
van Es, J.J.P. 120
van Hengel, C. 114, 108
Verpoorte, J. 74, 108
Vrchota, P. 168, 44, 159
Yi, X. 102

CIMNE
International Centre
for Numerical Methods in Engineering